Galaxy Kinematics during the Peak Epoch of Cosmic Star Formation

Hannah Deborah Natalie Übler

SIGILL. UNIVERSI TAT. LUDOVIC. MAXIM.

München 2019

Galaxy Kinematics during the Peak Epoch of Cosmic Star Formation

---

Über die Kinematik von Galaxien während der Hochzeit der kosmischen Sternentstehung

Arbeit zur Erlangung des akademischen Grades
Doctor rerum naturalium
an der Fakultät für Physik
der Ludwig-Maximilians-Universität München

vorgelegt von
Hannah Deborah Natalie Übler, M.Sc., M.A.

Erstgutachter:	Prof. Dr. Reinhard Genzel, Max-Planck-Institut für extraterrestrische Physik
Zweitgutachter:	Prof. Dr. Andreas Burkert, Ludwig-Maximilians-Universität München
Vorgelegt am:	28. Mai 2019
Tag der mündlichen Prüfung:	19. Juli 2019

Zusammenfassung

Diese Arbeit befasst sich mit der Kinematik von Sterne bildenden Galaxien (SFGs) während der Hochzeit der kosmischen Sternentstehung, bei Rotverschiebungen $0.5 < z < 3$. Basierend auf den genommenen Beobachtungen wird abgeleitet, welche Massenkomponenten die Galaxien dynamisch stabilisieren, und wie sich deren Beitrag im Laufe von 6 Milliarden Jahren verändert.

Um einen Zusammenhang zwischen einerseits der beobachtbaren Masse in der Form von Sternen und Gas und andererseits der Dunklen Materie in Galaxien herzustellen, werden die Tully-Fisher-Beziehungen genutzt. Es zeigt sich, dass die dynamische Stabilität der SFGs bei $z \sim 2.3$ durch Gas und Sterne dominiert wird, während bei $z \sim 0.9$ Dunkle Materie relevanter wird. Bei gleichbleibender Kreisgeschwindigkeit haben SFGs bei $z \sim 2.3$ und $z \sim 0.9$ die gleiche stellare Masse, aber ihre Gasmasse ist bei höherer Rotverschiebung größer. Auf der Grundlage von vorhandenen Modellen der Galaxienentwicklung wird ein Toy-Modell entwickelt, das die zeitlichen Änderung in der stellaren und gasförmigen Masse typischer SFGs in Betracht zieht, um die beobachtete, nicht-monotone Entwicklung der Tully-Fisher-Beziehungen von $z \sim 2.3$ bis $z = 0$ zu erklären.

Durch die graduelle Umwandlung von Gas zu Sternen verändert sich das interstellare Medium und dessen Einfluss auf die Galaxienkinematik. Die Entwicklung der intrinsischen Geschwindigkeitsdispersion des ionisierten Gases in typischen SFGs wird diskutiert sowie die Streuung und mögliche Ursachen dieser turbulenten Bewegungen. Durch Beobachtungsdaten sowie theoretische Überlegungen wird gezeigt, dass die galaktische Turbulenz bei $z \gtrsim 2$ höchstwahrscheinlich durch gravitative Instabilitäten dominiert wird, während diese zu späterer kosmischer Zeit weniger bedeutsam werden, und so der Einfluss von stellaren Feedbackprozessen an Relevanz gewinnen kann.

Eine genauere Analyse der Kinematik individueller, massiver SFGs wird vorgenommen, um die Beiträge sichtbarer und Dunkler Materie zur Galaxiendynamik mit höherer räumlicher Auflösung und bis zu größeren galaktischen Radien zu untersuchen. Besonders bei $z \gtrsim 2$ finden sich sehr turbulente und extrem baryonisch dominierte Systeme mit fallenden Rotationskurven auf der Basis von ionisiertem Gas. In einer detaillierten Fallstudie, die Messungen des ionisierten sowie molekularen Gases kombiniert, wird gezeigt, dass die Kinematik dieser beiden Gasphasen ausgezeichnet übereinstimmt. Dieses Ergebnis ist eine wichtige Demonstration dessen, dass die Bewegungen des ionisiertes Gases das Gravitationspotential abbilden. Durch einen Vergleich der Beobachtungsdaten mit modernen kosmologischen Simula-

tionen werden Unterschiede im Gasgehalt und in der Kinematik massiver $z \sim 2$ SFGs identifiziert, die vermutlich auf Unzulänglichkeiten in den Simulationen aufgrund nicht aufgelöster physikalischer Prozesse im interstellaren Medium und deren Implementierung hinweisen.

Abstract

In this thesis we discuss the kinematics of star-forming galaxies (SFGs) during the peak epoch of cosmic star formation rate density, at redshifts $0.5 < z < 3$. Based on our observations, we deduce information on their mass budget and dynamical support, and we follow its evolution over 6 billion years of cosmic history.

We use the Tully-Fisher relations to connect the observable stellar and total baryonic mass to dark matter on galactic scales, and find that at $z \sim 2.3$ the galactic dynamical support is dominated by gas and stellar mass, while at $z \sim 0.9$ dark matter becomes more important. At fixed circular velocity, SFGs have the same amount of stellar mass at $z \sim 2.3$ and $z \sim 0.9$, but their gas masses are higher at higher redshift. Based on existing models of galaxy evolution, we develop a toy model taking into account changes in the stellar and gas content of typical SFGs, to explain the observed, non-monotonic evolution of the Tully-Fisher relations from $z \sim 2.6$ to $z = 0$.

Through the gradual conversion of gas into stars, the dynamical state of the interstellar medium and its impact on the galaxy kinematics changes. We discuss the evolution of the intrinsic velocity dispersion of ionized gas in typical SFGs, its scatter, and possible mechanisms driving these turbulent motions. Based on both observational and theoretical evidence we conclude that at $z \gtrsim 2$ gas turbulence is likely dominated by gravitational instabilities, while towards lower redshift these mechanisms become less important and therefore the impact of stellar feedback may become comparable.

We zoom in on the kinematics of individual, massive SFGs to investigate in more detail the dynamical contributions of luminous and dark matter with higher spatial resolution and out to larger galactic radii. Especially at $z \gtrsim 2$ we find very turbulent, strongly baryon-dominated systems with dropping outer rotation curves traced by ionized gas emission. In a detailed case study combining measurements from ionized and molecular gas, we show that the observed kinematics in both tracers are in excellent agreement. This result is an important demonstration that the ionized gas reliably traces the gravitational potential. Through comparison of our observations with modern cosmological simulations, we identify differences in gas content and kinematics of massive $z \sim 2$ SFGs that likely point towards shortcomings in the simulations introduced by unresolved physics in the interstellar medium, and their implementation via sub-grid recipes.

Publications

This dissertation is based on the following peer-reviewed journal articles, listed in chronological order:

P1 *Strongly Baryon-dominated Disk Galaxies at the Peak of Galaxy Formation Ten Billion Years Ago*
R. Genzel, N. M. Förster Schreiber, **H. Übler**, P. Lang, T. Naab, R. Bender, L. J. Tacconi, E. Wisnioski, S. Wuyts, T. Alexander, A. Beifiori, S. Belli, G. B. Brammer, A. Burkert, C. M. Carollo, J. Chan, R. I. Davies, M. Fossati, A. Galametz, S. Genel, O. Gerhard, D. Lutz, J. T. Mendel, I. G. Momcheva, E. J. Nelson, A. Renzini, R. P. Saglia, A. Sternberg, S. Tacchella, K. Tadaki, and D. J. Wilman
Nature 543, 397 (2017) Chapter 4.1

P2 *The Evolution of the Tully-Fisher Relation between* $z \sim 2.3$ *and* $z \sim 0.9$ *with* $KMOS^{3D}$
H. Übler, N. M. Förster Schreiber, R. Genzel, E. Wisnioski, S. Wuyts, P. Lang, T. Naab, A. Burkert, P. G. van Dokkum, L. J. Tacconi, D. J. Wilman, M. Fossati, J. T. Mendel, A. Beifiori, S. Belli, R. Bender, G. B. Brammer, J. Chan, R. I. Davies, M. Fabricius, A. Galametz, D. Lutz, I. G. Momcheva, E. J. Nelson, R. P. Saglia, S. Seitz, and K. Tadaki
ApJ 842, 121 (2017) Chapter 2

P3 *Ionized and Molecular Gas Kinematics in a* $z = 1.4$ *Star-forming Galaxy*
H. Übler, R. Genzel, L. J. Tacconi, N. M. Förster Schreiber, R. Neri, A. Contursi, S. Belli, E. J. Nelson, P. Lang, T. T. Shimizu, R. I. Davies, R. Herrera-Camus, D. Lutz, P. M. Plewa, S. H. Price, K. Schuster, A. Sternberg, K. Tadaki, E. Wisnioski, and S. Wuyts
ApJL 854, L24 (2018) Chapter 4.2

P4 *The Evolution and Origin of Ionized Gas Velocity Dispersion from* $z \sim 2.6$ *to* $z \sim 0.6$ *with* $KMOS^{3D}$
H. Übler, R. Genzel, E. Wisnioski, N. M. Förster Schreiber, T. T. Shimizu, S. H. Price, L. J. Tacconi, S. Belli, D. J. Wilman, M. Fossati, J. T. Mendel, R. L. Davies, A. Beifiori, R. Bender, G. B. Brammer, A. Burkert, J. Chan, R. I. Davies, M. Fabricius, A. Galametz, R. Herrera-Camus, P. Lang, D. Lutz, I. G. Momcheva, T. Naab, E. J. Nelson, R. P. Saglia, K. Tadaki, P. G. van Dokkum, and S. Wuyts
ApJ 880(1), 48 (2019) Chapter 3

Contents

List of Figures

List of Tables

Chapter 1

Introduction

This thesis addresses the kinematics and dynamical state of star-forming galaxies (SFGs) during and shortly after the peak epoch of cosmic star formation rate density at redshifts $0.5 < z < 3$, about $2 - 8.5$ Gyr after the Big Bang. It covers both population-integrated aspects through scaling relations, and detailed explorations of individual systems. This has become feasible only during the last decade, with the advent of efficient multi-object spectroscopy, and the targeted, time-intensive use of sensitive single-field instrumentation. The present work brings new insights and sets previous results on a more robust basis, through very high signal-to-noise (S/N) and quality data of individual galaxies, as well as statistics of large samples obtained with state-of-the-art instrumentation on ground-based telescopes.

The interpretation of the observational findings reported in this dissertation relies heavily on the current theoretical understanding of cosmic history on large scales, where the hierarchical structure formation of dark matter provides the precondition for galaxy formation. At the same time, the observational results pose a challenge to theoretical models describing the smaller scale interplay of baryons and dark matter.

To set the stage, we briefly summarize the theoretical framework of cosmological evolution with its primary agents, dark energy and dark matter, in Section 1.1. In Section 1.2 we give an overview of the known characteristics of star-forming galaxies at $0.5 < z < 3$, and we introduce the instrumentation used to obtain the data presented in this thesis in Section 1.3. In Section 1.4 we state relevant questions that are addressed in this work, and in Section 1.5 we outline the remainder of this thesis.

1.1 The ΛCDM cosmology

In current theory, our Universe is best described by the concordance cosmological model of ΛCDM, the ‘Standard Model’. Here, Λ is the cosmological constant,

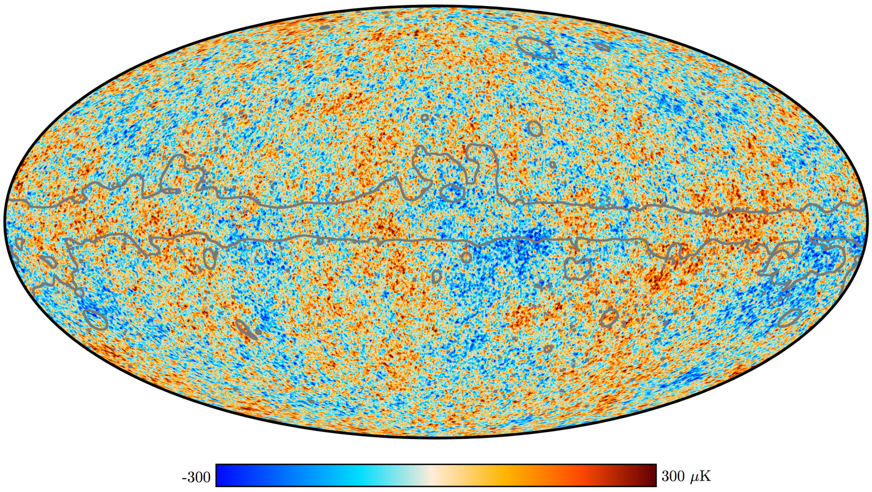

Figure 1.1: *CMB temperature anisotropy map obtained with the Planck satellite. The color scale shows deviations from the characteristic CMB blackbody-like temperature of* $T = 2.7255$ *K between* ± 300 μ*K. Regions within grey outlines are dominated by foreground emission, mostly from the galactic plane, and have been masked and inpainted. This figure is taken from Planck Collaboration et al. (2018a).*

associated with the vacuum energy, or dark energy responsible for the accelerated expansion of the Universe, and CDM stands for Cold Dark Matter. The ΛCDM model describes the evolution of structure formation after the Big Bang and inflation, and its success is largely based on its conformity with key observational findings from the past ~ 100 years.

The cosmic microwave background The discovery paper of the cosmic microwave background (CMB) by Penzias & Wilson (1965), resulting in the Nobel Prize in Physics 1978 *"for their discovery of cosmic microwave background radiation"*,[1] was accompanied by its interpretation as a cosmic blackbody radiation by Dicke et al. (1965). The existence of the CMB lends strong support to the ΛCDM model where such radiation is predicted as the afterglow of the very young (~ 375000 yr old) and hot Universe at the time of recombination, after the Big Bang and initial inflation period. Small temperature variations in the CMB reflect primordial fluctuations that have been amplified through inflation, and which are the precursors of the large scale structure of the present-day Universe.

Since its discovery, the CMB and its weak anisotropy have been studied in great detail in three dedicated missions: (i) COBE, the COsmic Background Explorer, operating from 1989 to 1993 (e.g. Smoot et al., 1992; Mather et al., 1994; Bennett et al., 1996; Fixsen et al., 1996). Work based on the COBE mission

---

[1] The Nobel Prize in Physics 1978. NobelPrize.org. Nobel Media AB 2019. Sat. 30 Mar 2019. `https://www.nobelprize.org/prizes/physics/1978/summary/`

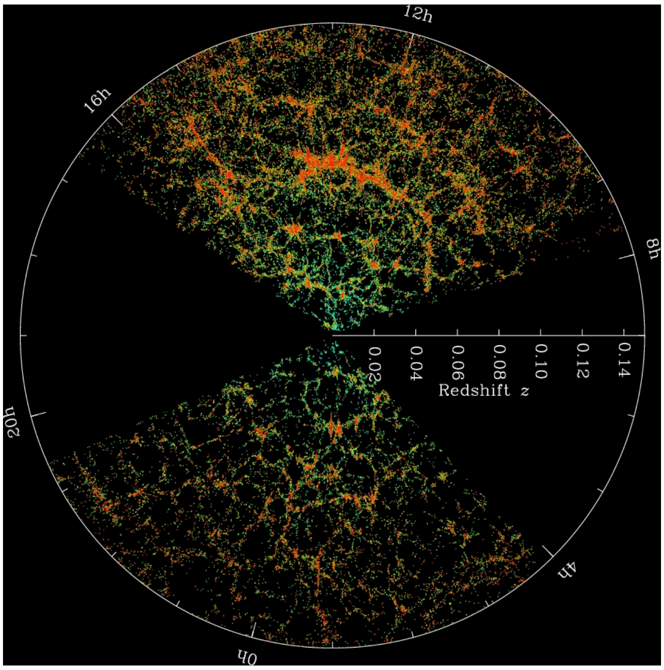

Figure 1.2: *SDSS map of the Universe out to* $z \approx 0.15$*. Each dot is a galaxy, where colors correspond to its* $g - r$ *color. Image credit: M. Blanton and SDSS.*

resulted in the Nobel Prize in Physics 2006 for J. Mather and G. Smoot *"for their discovery of the blackbody form and anisotropy of the cosmic microwave background radiation"*.[2] (ii) WMAP, the Wilkinson Microwave Anisotropy Probe, operating from 2001 to 2010 (e.g. Bennett et al., 2003; Spergel et al., 2003, 2007; Komatsu et al., 2009, 2011; Hinshaw et al., 2013); and (iii) the Planck satellite, operating from 2009 to 2013 (e.g. Planck Collaboration et al., 2014, 2016, 2018b). Figure 1.1 shows the most recent CMB temperature anisotropy map from the final Planck 2018 data release.

Large scale structure The large scale structure of the Universe observed through agglomerations and voids of baryonic matter up to scales of ~ 100 Mpc has been measured through the 2dF Galaxy Redshift Survey from 1997 to 2002 (e.g. Colless et al., 2001; Percival et al., 2001), and through the Sloan Digital Sky Survey (SDSS) from 2000 on (e.g. York et al., 2000; Abazajian et al., 2003, 2009; Aguado et al., 2019), as shown in Figure 1.2. A key discovery of these surveys was the detection of the baryon acoustic oscillations (Cole et al., 2005; Eisenstein et al., 2005), tracing back fluctuations in the photon-baryon fluid in the early Universe as predicted by ΛCDM.

---

[2] The Nobel Prize in Physics 2006. NobelPrize.org. Nobel Media AB 2019. Sat. 30 Mar 2019. `https://www.nobelprize.org/prizes/physics/2006/summary/`

In the ΛCDM model, structure formation is a consequence of small primordial perturbations in matter density in the early Universe which were subsequently blown up through the process of inflation. Gravity acting on the dissipationless dark matter component enhances these perturbations: small structures grow, and merge into larger objects via hierarchical clustering.

The expansion of the Universe The expansion of the Universe, first hinted at through redshifted emission lines of nearby galaxies (Slipher, 1913; Hubble, 1926), was discovered by Lemaître (1927) through the framework of the Friedmann equations describing the intrinsic expansion or contraction of space (Friedmann, 1922). The expansion history of the Universe was further constrained through observations of supernovae type Ia by S. Perlmutter, B. P. Schmidt, and A. G. Riess, who were awarded the Nobel Prize in Physics 2011 *"for the discovery of the accelerating expansion of the Universe through observations of distant supernovae"*.[3] The constraints obtained by Riess et al. (2004) are shown in Figure 1.3.

The expansion of the Universe is responsible for the 'cosmological redshift' whereby emitted light traveling towards us from distant galaxies is shifted to longer wavelengths:

$$\lambda_{\text{observed}} = (1+z)\cdot\lambda_{\text{rest}}, \tag{1.1}$$

where λ_{rest} is the wavelength of the emission in the source rest-frame. Through this effect, for instance, rest-frame optical radiation originating at $z \sim 2$ is observable locally at near-infrared wavelengths.

Together, these discoveries constrain the cosmological parameters, with the latest measurements from the Planck Collaboration et al. (2018b):

$$\begin{aligned}
\Omega_{\text{c}}h^2 &= 0.11933 \pm 0.00091 && \text{(comoving dark matter density)}\\
\Omega_{\text{b}}h^2 &= 0.02242 \pm 0.00014 && \text{(comoving baryon density)}\\
n_{\text{s}} &= 0.9665 \pm 0.0038 && \text{(spectral index)}\\
\tau &= 0.0561 \pm 0.0071 && \text{(optical depth)}
\end{aligned}$$

Assuming the standard ΛCDM cosmology, this gives the following constraints on present-day parameters:

---

[3] The Nobel Prize in Physics 2011. NobelPrize.org. Nobel Media AB 2019. Sun. 31 Mar 2019. `https://www.nobelprize.org/prizes/physics/2011/summary/`

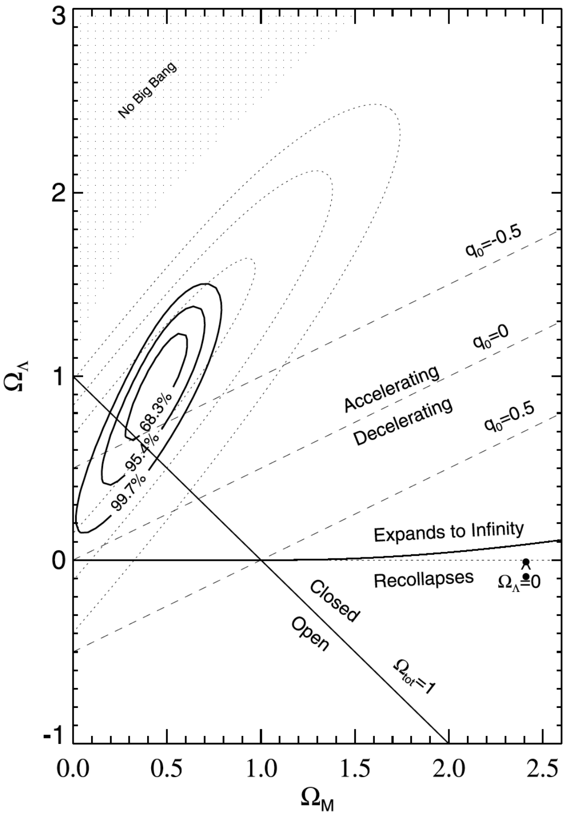

Figure 1.3: *Joint confidence intervals for the matter density* Ω_M *and dark energy density* Ω_Λ *from 157 supernovae type Ia. The expansion of the Universe is accelerating with* > 99 % *confidence since* $z \sim 0.5$. *This figure is taken from Riess et al. (2004).*

$$\begin{aligned}
H_0\ [\mathrm{kms^{-1}Mpc^{-1}}] &= 67.66 \pm 0.42 && \text{(Hubble constant)}\\
\Omega_\Lambda &= 0.6889 \pm 0.0056 && \text{(dark energy density)}\\
\Omega_\mathrm{M} &= 0.3111 \pm 0.0056 && \text{(matter density)}\\
z_\mathrm{re} &= 7.82 \pm 0.71 && \text{(redshift of re-ionization)}\\
\text{age [Gyr]} &= 13.787 \pm 0.020 && \text{(age of the Universe)}
\end{aligned}$$

In this framework, our Universe is dominated by dark energy (∼69%), followed by dark matter (∼26%), with a minor contribution from baryonic matter of <5%.

Halo and galaxy evolution in the context of ΛCDM The structure formation of the Universe is today accurately reproduced with the help of dark matter-only, collisionless $N-$body simulations, revealing a present-day net-like distribution of matter, with filamentary structures, sheets, and knots, known as

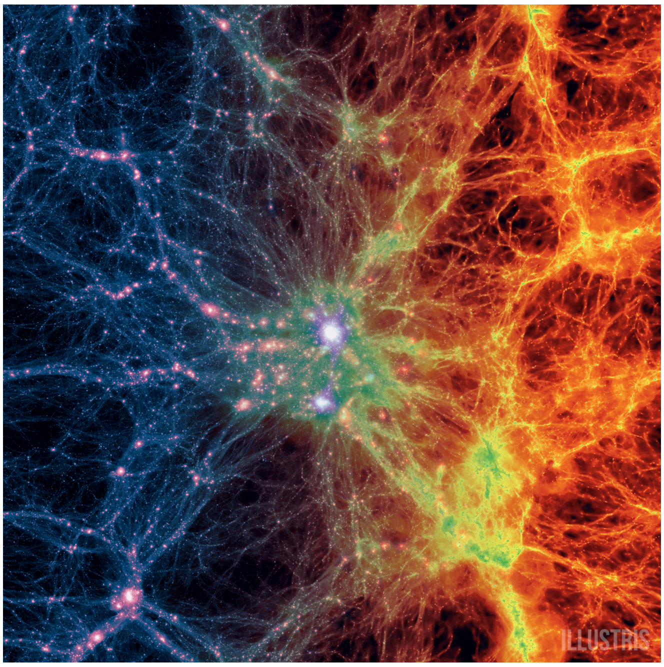

Figure 1.4: *Large scale projection through the Illustris simulation volume at $z = 0$ with colors showing dark matter density on the left and gas density on the right. Image credit: Illustris Collaboration.*

the cosmic web (e.g. Springel et al., 2005; Klypin, Trujillo-Gomez, & Primack, 2011; Angulo et al., 2012). The knots in this web are characterized by their overdensity, which is by convention taken as regions in excess of ~ 200 times the mean density, motivated by non-linear top-hat collapse models (Gunn & Gott, 1972). These overdensities, called haloes, show a typical scale-free density profile, prominently described e.g. through the Navarro-Frenk-White (NFW) profile (Navarro, Frenk, & White, 1996), or the Einasto profile (Einasto, 1965). The formation of galaxies is tightly connected to the formation and evolution of dark matter haloes. Dominating the mass budget, haloes provide the potential well for gas to cool into, where a fraction of it subsequently condenses into stars to form the first galaxies. The large scale distribution of dark matter and gas is illustrated in Figure 1.4, featuring the Illustris simulation (e.g. Vogelsberger et al., 2014).

Following the formation of galaxies including the dissipative nature of gas, however, requires a hydrodynamical treatment of the baryonic component. From the computational perspective this is expensive, such that cosmological simulations including baryons have much smaller volumes (typically $\sim (20-300\ \mathrm{Mpc})^3$) compared to pure $N-$body simulations (up to $\sim (10\ \mathrm{Gpc})^3$). This limitation hampers the consistent study of cosmological evolution covering at the same time large enough volumes to ensure appropriate structure formation and statistical properties, while also taking into account baryonic processes and their effect on the dark matter distribution. The relevant dynamic ranges go from the large scale cosmic structure on Gpc scales down to galaxy sizes on kpc scales, to the detailed ISM or black hole feedback physics on pc scales, and further down to the formation of individual stars. Even for a single galaxy the relevant dynamic and mass ranges are of the order $\mathcal{O}(10^{10-12})$. These and other challenges of modern galaxy formation theory are discussed in the review by Naab & Ostriker (2017).

1.2 Galaxies during the peak epoch of cosmic star formation

This dissertation focusses on SFGs at roughly $0.5 < z < 3$, during and shortly after the peak of cosmic star-formation rate density (Madau & Dickinson, 2014). During the last 15 years a plethora of observations of such objects have been collected. In particular through the multiplexing integral-field capabilities of second-generation instruments on the 8-10 m class telescopes both spatially and spectrally resolved data of over 1000 galaxies have been obtained (e.g. Genzel et al., 2006, 2008, 2014b; Förster Schreiber et al., 2006, 2009, 2018; Law et al., 2007, 2009; Epinat et al., 2009, 2012; Jones et al., 2010; Gnerucci et al., 2011; Wisnioski et al., 2011, 2015, 2019; Swinbank et al., 2012a; Contini et al., 2012; Stott et al., 2016; Turner et al., 2017). In addition, large data sets have been collected through long-slit surveys (e.g. Kassin et al., 2007, 2012; Kriek et al., 2015; Price et al., 2016, 2019; Simons et al., 2016, 2017). However, for the study of galaxy kinematics, spatially resolved information is crucial to robustly determine, for instance, a galaxy's kinematic position angle.

Salient findings from multi-wavelength lookback, imaging, and integral-field unit (IFU) surveys revealing general insights about the physical properties of the star-forming population in the early Universe are summarized in what follows, setting the observational framework for this thesis.

The peak epoch of cosmic star formation rate density Compilations of data tracing the amount of star formation from redshift $z = 0$ to $z = 8$ clearly show that there was a period of maximal cosmic star formation rate about 10 Gyr ago, at $z \approx 2$ (see review by Madau & Dickinson, 2014, and references therein; Figure 1.5). The era of high star formation activity at $1 < z < 3$ with typical rates up to a few hundred times higher compared to local SFGs has been dubbed 'cosmic noon'. Since this epoch is characterized through both rapid baryonic mass assembly and conversion of gas into stars at high rates, it represents a testbed for studying galaxy-scale baryonic processes and their impact on galaxy evolution.

It has further been established that out to at least $z \sim 5$ there exists a so-called 'main sequence' in the stellar mass – star formation rate plane such that at any given time, and over a wide range in masses and star-formation rates, the majority

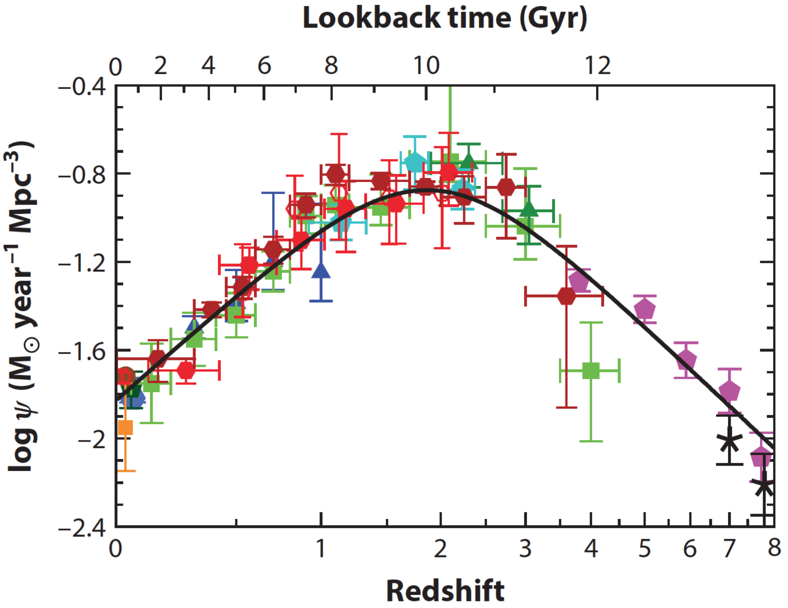

Figure 1.5: *The history of cosmic star-formation rate density ψ from rest-frame far-UV (green to black) and IR (orange to red) measurements, and the solid curve shows the best-fitting function $\psi(z)$. The time span at $1 < z < 3$ marks the era of highest star formation activity. This figure is taken from Madau & Dickinson (2014).*

of the star-forming population lies along a tight (±0.3 dex), approximately linear relation (e.g. Brinchmann et al., 2004; Daddi et al., 2007; Rodighiero et al., 2011; Whitaker et al., 2014; Speagle et al., 2014; Tomczak et al., 2016; Santini et al., 2017; Pearson et al., 2018). At $z \sim 2$, for instance, the main sequence encompasses about 95% of SFGs, accountable for about 90% of the star-formation rate density (Rodighiero et al., 2011). Main sequence fits between $z = 0.5$ and $z = 4$ are shown exemplarily in Figure 1.6.

Gas masses and depletion time scales The elevated star formation rates during cosmic noon are naturally connected to the available amount of cold gas from which the stars form. In the local Universe, this is captured by the Kennicutt-Schmidt relation between the star-formation rate surface density Σ_{SFR} and the gas mass surface density Σ_{gas} (Schmidt, 1959; Kennicutt, Jr., 1998). Through targeted, time-intensive studies (Tacconi et al., 2010, 2013; Daddi et al., 2010; Genzel et al., 2010; Magdis et al., 2012; Sargent et al., 2014; Béthermin et al., 2015) it has been shown that this relation is valid also at higher redshifts. This realization allowed for the derivation of scaling relations up to $z \sim 4$ that can be used to estimate galactic gas masses based on stellar mass, specific star formation rate, and redshift, as well as gas depletion time scales (Genzel et al., 2015; Scoville et al., 2017; Tacconi et al., 2018). Such relationships are extremely

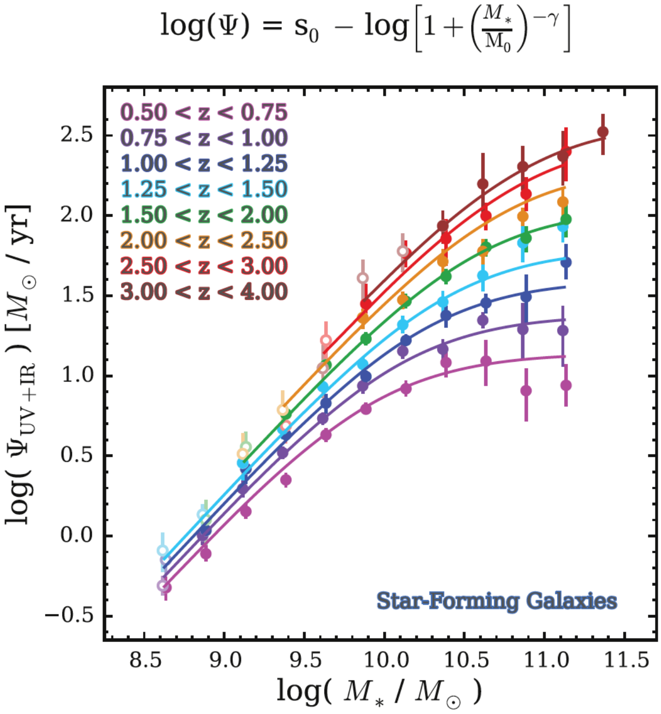

Figure 1.6: *Stacked star-formation rates* Ψ *as a function of stellar mass for SFGs in different redshift bins (colored points with error bars). Lines show fits according to the parametrization given at the top, with* $s_0 = 0.448 + 1.220z - 0.174z^2$, $\log(M_0) = 9.458 + 0.865z - 0.132z^2$, *and* $\gamma = 1.091$. *With increasing redshift, the normalization of the main sequence increases, and the slope at the high-mass end becomes steeper. This figure is taken from Tomczak et al. (2016).*

valuable because due to the limited observational capabilities at (sub-)mm wavelengths the available direct molecular gas studies at high$-z$ are few compared to efforts targeting ionized gas, including only a number of individual sources and few representative samples (see e.g. Carilli & Walter, 2013, for a review).

These studies established (i) that gas fraction $f_{\rm gas} = M_{\rm gas}/(M_{\rm gas} + M_*)$ increases rapidly with redshift for SFGs, such that $z \sim 2$ galaxies have typically $f_{\rm gas} \gtrsim 0.5$, while local SFGs have typically $f_{\rm gas} \leq 0.1$; and (ii) that the gas depletion time $t_{\rm depl} = M_{\rm molgas}/{\rm SFR}$ only modestly increases from a few 100 Myr at $z \sim 4$ to ~ 1 Gyr at $z = 0$, but is a strong function of offset from the main sequence (see Figure 1.7).

The galactic mass budget Taking into account the large gas mass fractions at high redshift, it has further been shown that massive ($M_* \gtrsim 10^9 M_\odot$) SFGs are increasingly baryon-dominated on galactic scales, such that $z \sim 1$ galaxies have typically $M_{\rm bar}/M_{\rm dyn} \approx 0.4 - 0.5$, while galaxies at $z \gtrsim 2$ can reach $M_{\rm bar}/M_{\rm dyn} \gtrsim 0.9$ (Förster Schreiber et al., 2009; van Dokkum et al., 2015; Alcorn et al., 2016;

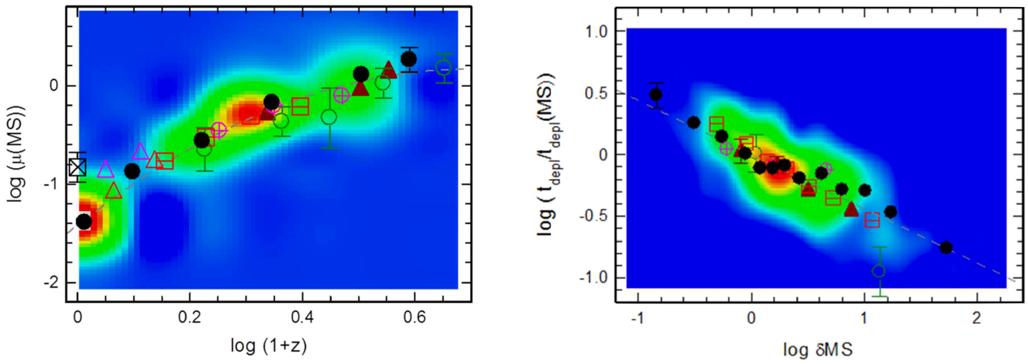

Figure 1.7: *Molecular gas-to-stellar mass ratio* $M_{\mathrm{gas,mol}}/M_* = \mu$ *as a function of redshift (left), and depletion time* t_{depl} *relative to the main sequence as a function of offset from the main sequence, after zero-point corrections to account for different measurement techniques (right). The offset from the main sequence,* $\log \delta\mathrm{MS} = \log(\mathrm{SFR}/\mathrm{SFR}_{\mathrm{MS(z,M*)}})$*, is derived based on the main sequence parametrization by Speagle et al. (2014). Symbols denote binned averages from the literature, and the color scale shows the overall distribution. Gas masses are higher at higher redshift, and depletion times are shorter for galaxies above the main sequence. These figures are taken from Tacconi et al. (2018).*

Stott et al., 2016; Wuyts et al., 2016b; Price et al., 2016; Genzel et al., 2017; Lang et al., 2017). In contrast, normal SFGs in the local Universe have $M_{\mathrm{bar}}/M_{\mathrm{dyn}} \approx 0.1-0.5$ (e.g. Martinsson et al., 2013a,b; Courteau et al., 2014). The high baryonic surface densities at high redshift are likely a result of gas dissipation processes and rapid conversion of gas into stars.

Structural properties One of the first realizations about high$-z$ SFGs was their different appearance compared to local disk galaxies: they often show a clumpy structure, unlike the regular patterns seen in local SFGs (Elmegreen, Elmegreen, & Sheets, 2004; Elmegreen, Elmegreen, & Hirst, 2004; Elmegreen et al., 2005; Elmegreen & Elmegreen, 2006). These features first observed in rest-frame UV imaging are also seen in rest-frame optical observations of ionized gas, revealing giant star-forming clumps (e.g. Förster Schreiber et al., 2009, 2011b; Genzel et al., 2011; Wisnioski et al., 2012).

However, these clump neither trace prominent accumulations of mass, nor deviate from, or disturb, the kinematic patterns of their host galaxies (Genzel et al., 2011; Wuyts et al., 2012). Instead, the mass distribution is observed to be fairly smooth, in accordance with the regular rotation patterns observed for the majority of massive, high$-z$ SFGs (see below). The work by Wuyts et al. (2011a) showed that most main sequence galaxies out to $z \sim 2.5$ are characterized by exponential disk-like profiles (median one-component Sérsic indices $n_S < 1.5$; see Figure 1.8).

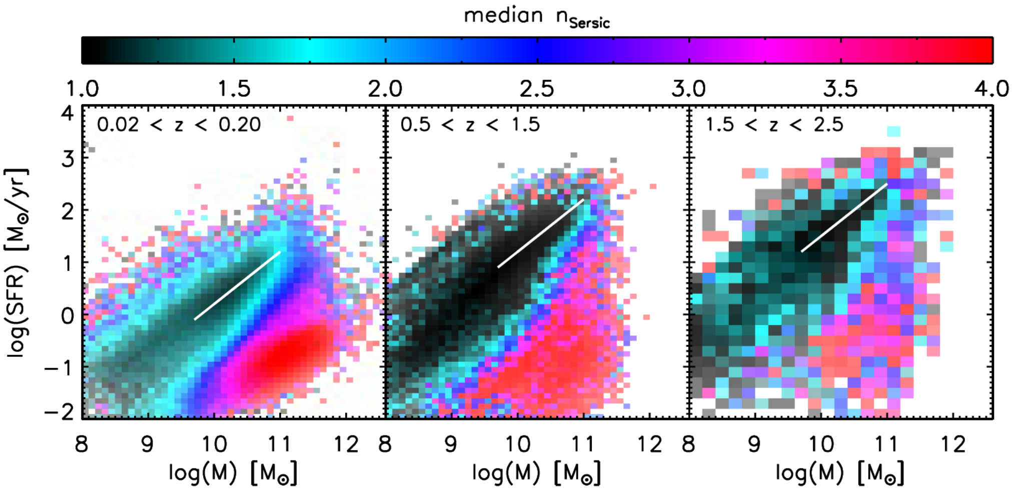

Figure 1.8: *Surface brightness profile shape in the M_*−SFR plane. Out to* $z = 2.5$ *galaxies on the main sequence are characterized by exponential profiles with a median Sérsic index* $n_{\rm Sersic} < 1.5$. *This figure is taken from Wuyts et al. (2011a).*

At the same time an increase in the bulge-to-total stellar mass fraction (B/T) with increasing mass has been found for both SFGs and quiescent galaxies through two-component bulge+disk profile fitting by Lang et al. (2014). The average B/T is lower for SFGs, but still reaches typical values of $B/T \approx 0.5$ for SFGs with $M_* \approx 10^{11.5} M_\odot$. These most massive SFGs above the Schechter mass ($M_* \gtrsim 10^{11} M_\odot$) were likely soon quenched and subsequently evolved into massive, quiescent early type galaxies by $z = 0$ (see Peng et al., 2010).

Kinematic properties The systematic study of the ionized gas kinematics of high−z SFGs has resulted in two main findings regarding their kinematic properties: (i) up to $z \sim 2.5$, the majority of massive SFGs show ordered rotation, and (ii) their velocity dispersions are higher by factors of 2-5 compared to local SFGs (Förster Schreiber et al., 2006, 2009, 2018; Genzel et al., 2006, 2008, 2014b; Kassin et al., 2007, 2012; Shapiro et al., 2008; Stark et al., 2008; Cresci et al., 2009; Epinat et al., 2009, 2012; Law et al., 2009; Wright et al., 2009; Jones et al., 2010; Wisnioski et al., 2011, 2015, 2019; Mancini et al., 2011; Miller et al., 2012; Swinbank et al., 2012a; Stott et al., 2016; Price et al., 2016; Simons et al., 2016, 2017; Johnson et al., 2018; Übler et al., 2019).

The rotation patterns are in good agreement with the smooth mass distributions mentioned above. The fraction of rotation-dominated systems, commonly defined by the ratio of rotation velocity to turbulent velocity, $v_{\rm rot}/\sigma > 1$, depends on mass and changes with redshift: at fixed redshift, more massive systems have larger rotational support, and the fraction of rotation-dominated SFGs at any given mass increases with decreasing redshift (Kassin et al., 2012; Simons et al.,

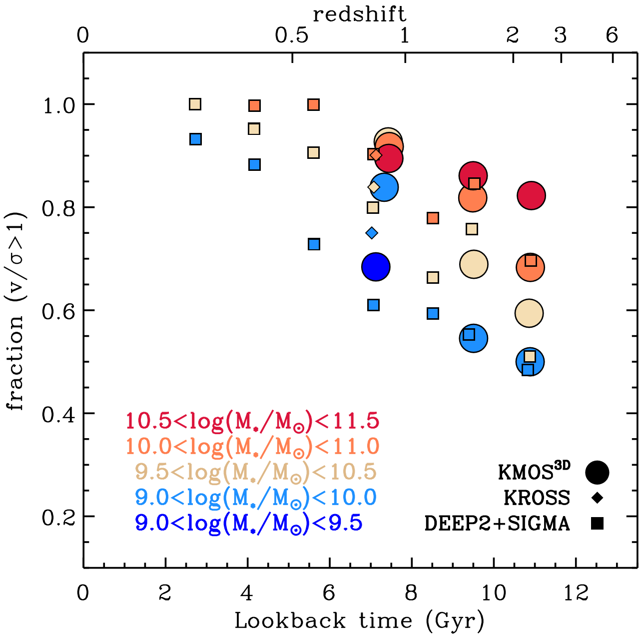

Figure 1.9: *Fraction of rotation-dominated ($v/\sigma > 1$) SFGs in different mass bins (colors) as a function of lookback time. With decreasing redshift, more SFGs are rotation-dominated, and earlier for more massive systems. This figure is taken from Wisnioski et al. (2019).*

2016, 2017; Turner et al., 2017; Wisnioski et al., 2019, see Figure 1.9). Above $z \sim 2.5$, the fraction of rotation-dominated systems drops below 50% (Gnerucci et al., 2011; Turner et al., 2017).

This decrease of rotational support goes together with a systematic increase of the intrinsic velocity dispersion with redshift. The velocity dispersion captures non-circular motions and unresolved velocity gradients in the disk. In hydrostatic equilibrium, turbulent motions create a pressure term that counter-acts part of the gravitational potential. To recover the circular velocity tracing the gravitational potential in which the galaxy is embedded, one has to consequently account for this pressure term (Burkert et al., 2010, 2016; Wuyts et al., 2016b). Other second-order motions, however, such as radial or vertical flows, can further complicate the picture (e.g. Genzel et al., 2008, 2017; Förster Schreiber et al., 2018).

1.3 Instruments used for this work

The work presented in this thesis is based on data collected at various ground-based observing facilities in the Southern and Northern hemispheres. In the following, the instruments most relevant for this work are introduced briefly.

KMOS at the VLT The K-band Multi-Object Spectrograph (KMOS; Sharples et al., 2004, 2013; Davies et al., 2013) is a second-generation instrument in the Nasmyth focus of Unit Telescope 1 (UT1) of the *Very Large Telescope* (VLT) on the Chilean Cérro Paranal observing site of the European Southern Observatory (ESO). It consists of 24 arms deployable over a $7.2'$ diameter patrol field, each equipped with an integral field unit (IFU) with an $2.8'' \times 2.8''$ field of view. The individual IFUs have a spatial sampling of $0.2'' \times 0.2''$. Observations can be performed in the IZ, YJ, H, K, and combined $H + K$ spectral bands, roughly covering a wavelength range $0.8 - 2.5\mu$m. The corresponding spectral resolutions are $R = \lambda/\Delta\lambda \approx 3400; 3600; 4000; 4200; 2000$, where $\Delta\lambda$ is the full-width-half-maximum (FWHM) resolution element.[4]

Most data used in this thesis have been taken with KMOS, as part of the KMOS^{3D} 75-night Guaranteed Time Observations (GTO) survey (Wisnioski et al., 2015, 2019; P.I.s Natascha M. Förster Schreiber and David Wilman) in the spectral bands YJ, H, and K. Results based on KMOS data are presented in Chapters 2, 3, and 4.1 of this thesis.

SINFONI at the VLT The Spectrograph for INtegral Field Observations in the Near Infrared (SINFONI; Eisenhauer et al., 2003; Bonnet et al., 2004) is a first-generation instrument mounted at the Cassegrain focus of UT4 at the VLT. SINFONI is an integral field spectrograph coupled to an adaptive optics module enabling higher resolution observations by correcting for atmospheric turbulence using a reference Natural or Laser Guide Star. The field of view can be chosen between $8'' \times 8''$, $3'' \times 3''$, and $0.8'' \times 0.8''$, with corresponding spatial samplings of $0.125'' \times 0.25''$, $0.05'' \times 0.1''$, and $0.0125'' \times 0.025''$. Observations can be performed in the J, H, K, and combined $H + K$ spectral bands, roughly covering the wavelength range $1.1 - 2.35\mu$m. The corresponding spectral resolutions are $R \approx 2000; 3000; 4000; 1500$.[5]

The SINFONI data used in this thesis was taken as part of the SINS/zC-SINF survey carried out over several GTO and open-time programs over about 100 nights (Förster Schreiber et al., 2009, 2018; Mancini et al., 2011). This work used a SINFONI field of view of $8'' \times 8''$, with a pixel scale of $0.125'' \times 0.25''$ for seeing-limited observations, and $0.05'' \times 0.1''$ for adaptive optics-assisted observations. Results based on SINFONI data are presented in Chapters 3 and 4.1 of this thesis.

LUCI at the LBT At the *Large Binocular Telescope* (LBT) the LBT near-infrared spectroscopic Utility with Camera 1, and Camera 2 (LUCI1 and LUCI2; Buschkamp et al., 2012) are mounted at the Bent Gregorian focus of the two

---

[4] Further information on the instrument can be found on the ESO KMOS webpage.

[5] Further information on the instrument can be found on the ESO SINFONI webpage.

mirrors of the LBT on Mount Graham in Arizona, USA. In spectroscopic mode (relevant for this work), observations can be performed either in longslit or in multi-object-slitmask (MOS) mode. Observations can be performed in a multi-purpose grating covering the z, J, H, and K bands, and in the H, K, Ks, and combined $H + K$ spectral bands, with varying spectral resolutions as described in detail by Buschkamp et al. (2012).

For the work presented in this thesis (Chapter 4.2), LUCI1 and LUCI2 were used in binocular mode, with a pixel scale of $0.25''$ in $H-$band and a MOS slit width of $1''$, corresponding to a spectral resolution of $R \sim 3000$.

NOEMA The NOrthern Extended Millimeter Array (NOEMA) on the Plateau de Bure operated by the Institut de RadioAstronomie Millimétrique (IRAM) is a millimeter radio interferometer currently consisting of ten 15 m antennas.[6] The NOEMA antennas can be positioned along two almost perpendicular tracks with a maximum separation of 760 m in East-West direction and 386 m in North-South direction. Observations can be performed in configurations from ‘compact’ to ‘extended’, leading to varying spatial resolutions. The currently best resolution achievable is $0.2''$. Observations can be taken in three frequency bands, at 3 mm, 2 mm, and 1.3 mm, roughly covering 70-280 GHz.

For the work presented in this thesis (Chapter 4.2), NOEMA was used in D (compact) and A (extended) configuration with a resolution of $0.6'' - 1.0''$, with seven or eight antennas, observing in the 2 mm band.

Ancillary data The galaxies discussed in this work benefit from multi-wavelength observations supporting the interpretation of the near-IR spectroscopic and millimeter interferometric data, either from publicly available surveys or obtained by our team in dedicated follow-up programs. The larger part of our targets are located in the extragalactic ‘deep fields’, particularly in the well-studied COSMOS (Cosmic Evolution Survey), GOODS-S (Great Observatories Origins Deep Survey field centered on the Chandra Deep Field South), UDS (Ultra Deep Survey), and EGS (Extended Groth Strip) fields.

Importantly, these deep fields are covered by the 3D-HST survey, a *Hubble Space Telescope* Treasury Program (Brammer et al., 2012; Skelton et al., 2014; Momcheva et al., 2016) providing $R \approx 130$ near-infrared grism spectra, optical-to-8μm photometric catalogues, and spectroscopic, grism, and/or photometric redshifts for sources in the EGS, COSMOS, GOODS-S, GOODS-N (centered on the Chandra Deep Field North), and UDS fields, and by the Cosmic Assembly Near-infrared Deep Extragalactic Legacy Survey (CANDELS; Grogin et al., 2011;

---

[6] Information up-to-date on the NOEMA interferometer can be found on the IRAM webpage.

Koekemoer et al., 2011; van der Wel et al., 2012), providing high-resolution near-infrared and optical imaging in the same five fields using the Wide Field Camera 3 (WFC3) and the Advanced Camera for Surveys (ACS) on the HST.

Further multi-wavelength $X-$ray to radio coverage is provided through imaging and spectroscopy, for instance from the European Photon Imaging Camera (EPIC) on board *XMM-Newton*, from the Advanced CCD Imaging Spectrometer imaging array (ACIS-I) on the *Chandra X-ray Observatory*, from the Multiband Imaging Photometer on the *Spitzer Space Telescope* (MIPS), from the Photoconductor Array Camera and Spectrometer (PACS) on the *Herschel Space Observatory*, from the Very Large Array (VLA), and from the Very Long Baseline Array (VLBA) (e.g. Ueda et al., 2008; Lutz et al., 2011; Middelberg et al., 2011; Xue et al., 2011; Civano et al., 2012; Magnelli et al., 2013; Miller et al., 2013; Whitaker et al., 2014).

1.4 Important scientific questions related to this work

This thesis sheds light on the dynamical evolution of $z \sim 1-2$ SFGs with the highest-quality data currently available from the ground. On the basis of this excellent data set, important questions addressed in this work are:

- *Do kinematic galaxy scaling relations known from the local Universe exist at $z \sim 1-2$? If so, how do they compare, and what drives their evolution?*
- *What dominates the dynamical support of SFGs over cosmic time, and why?*
- *What is the interplay of baryonic and dark matter on galaxy scales, and can our theoretical understanding of the structure evolution of dark matter be reconciled with observations?*

From the observational side, we are at the verge of being able to constrain in detail the dynamical support attributed to gas, stars, and dark matter in representative galaxy samples during the peak epoch of cosmic star formation rate density, and the pioneering work on individual objects is presented in this thesis. Increasingly large and representative samples of spatially-resolved observations of high$-z$ SFGs have been collected over the past years, benefitting in particular from multiplexing as afforded by KMOS, now enabling more complete censuses of the kinematic properties of distant galaxies.

From the theoretical perspective, we are in a better situation than ever before to interpret and connect observations to insights from simulations. The steady refinement and development of sub-grid models, and the progress in numerical implementations, lead to ever more detailed cosmological simulations of galaxy formation, as well as to smaller-scale, high-resolution simulations of physical processes and phenomena. Still there is tension between simulation results and particularly high$-z$ observations. In this thesis, we identify some of these issues.

1.5 Outline of this thesis

This thesis is structured as follows: in the first two chapters, we start with kinematic scaling relations that describe the evolution of the star-forming galaxy population as a whole. These studies are based primarily on data from the KMOS^{3D} survey which provides a homogeneous coverage of SFGs with stellar masses $10^9 M_\odot < M_* < 10^{11.5} M_\odot$ between redshifts $0.6 < z < 2.6$. In the third chapter we investigate in great detail the kinematics of a few individual galaxies through deep observations and dynamical modelling, and compare them to simulations.

In Chapter 2, we investigate the redshift evolution of the stellar and baryonic mass Tully-Fisher relations (Tully & Fisher, 1977; McGaugh et al., 2000) which describe the observed scaling between baryonic mass (stars, gas) and rotation velocity. They offer a unique tool to relate an observable, namely the stellar light or the gas emission, to something we cannot directly detect, namely the total dynamical mass, assumed to be partly composed by dark matter. Using this tool, we discuss a toy model of disk galaxy evolution to explain the observed changes in the galaxy mass budget over cosmic time.

In Chapter 3, we study the redshift evolution of the intrinsic ionized gas velocity dispersion. In context with literature observations, we quantify the evolution of different gas phases. Using observational evidence and theoretical results we argue that the majority of the turbulence seen in high$-z$ SFGs is driven by gravitational instabilities, caused by accretion, radial transport, clump formation and migration.

In Chapter 4 we zoom in on the detailed, high-resolution kinematic properties of individual galaxies. In Section 4.1, we perform detailed modelling of the ionized gas kinematics of six galaxies observed with SINFONI, partly in adaptive-optics mode, and KMOS. This study reveals unexpectedly low central dark matter fractions that create a tension with current cosmological models of galaxy evolution. In Section 4.2, we compare the kinematics traced through ionized and molecular gas in one galaxy. We find comparable dynamics, suggesting that both gas phases are subject to the same gravitational potential tracing the disk dynamics.

In Section 4.3, we compare simulated galaxies from the IllustrisTNG50 volume to the observed objects presented in Section 4.1. We identify a number of differences between the observed and simulated galaxies, suggesting that the observed objects do not have a counterpart in the simulation. Through comparison to the intrinsic properties of the simulated galaxies, we also validate the reliability of our observational pipeline to extract and model galaxy kinematics.

Chapter 2

The Evolution of the Tully-Fisher Relation between $z \sim 2.3$ and $z \sim 0.9$ with KMOS^{3D}

This Chapter, with exception of Section 2.12, is a reprint of the ApJ publication *The evolution of the Tully-Fisher relation between $z \sim 2.3$ and $z \sim 0.9$ with KMOS^{3D}* by Übler et al. (2017); DOI:10.3847/1538-4357/aa7558; ©AAS. Reproduced with permission.

This work is based on observations collected at the Very Large Telescope (VLT) of the European Southern Observatory (ESO), Paranal, Chile, under ESO program IDs 092.A-0091, 093.A-0079, 094.A-0217, 095.A-0047, and 096.A-0025.

Abstract – We investigate the stellar mass and baryonic mass Tully-Fisher relations (TFRs) of massive star-forming disk galaxies at redshift $z \sim 2.3$ and $z \sim 0.9$ as part of the KMOS^{3D} integral field spectroscopy survey. Our spatially resolved data allow reliable modelling of individual galaxies, including the effect of pressure support on the inferred gravitational potential. At fixed circular velocity, we find higher baryonic masses and similar stellar masses at $z \sim 2.3$ as compared to $z \sim 0.9$. Together with the decreasing gas-to-stellar mass ratios with decreasing redshift, this implies that the contribution of dark matter to the dynamical mass on the galaxy scale increases towards lower redshift. A comparison to local relations reveals a negative evolution of the stellar and baryonic TFR zero-points from $z = 0$ to $z \sim 0.9$, no evolution of the stellar TFR zero-point from $z \sim 0.9$ to $z \sim 2.3$, but a positive evolution of the baryonic TFR zero-point from $z \sim 0.9$ to $z \sim 2.3$. We discuss a toy model of disk galaxy evolution to explain the observed, non-monotonic TFR evolution, taking into account the empirically motivated redshift dependencies of galactic gas fractions, and of the relative amount of baryons to dark matter on the galaxy and halo scales.

2.1 Introduction

State-of-the-art cosmological simulations in a ΛCDM framework indicate that three main mechanisms regulate the growth of galaxies, namely the accretion of baryons, the conversion of gas into stars, and feedback. While gas settles down at the centers of growing dark matter (DM) haloes, cools and forms stars, it keeps in its angular momentum an imprint of the dark halo. Conservation of the net specific angular momentum, as suggested by analytical models of disk galaxy formation (e.g. Fall & Efstathiou, 1980; Dalcanton, Spergel, & Summers, 1997; Mo, Mao, & White, 1998; Dutton et al., 2007; Somerville et al., 2008), should result in a significant fraction of disk-like systems. In fact, they make up a substantial fraction of the observed galaxy population at high redshift ($1 \lesssim z \lesssim 3$; Labbé et al., 2003; Förster Schreiber et al., 2006, 2009; Genzel et al., 2006, 2014b; Law et al., 2009; Epinat et al., 2009, 2012; Jones et al., 2010; Miller et al., 2012; Wisnioski et al., 2015; Stott et al., 2016) and in the local Universe (e.g. Blanton & Moustakas, 2009, and references therein). The detailed physical processes during baryon accretion from the halo scales to the galactic scales are, however, complex, and angular momentum conservation might not be straightforward to achieve (e.g. Danovich et al., 2015). To produce disk-like systems in numerical simulations, feedback from massive stars and/or active galactic nuclei is needed to prevent excessive star formation and to balance the angular momentum distribution of the star-forming gas phase (e.g. Governato et al., 2007; Scannapieco et al., 2009, 2012; Agertz, Teyssier, & Moore, 2011; Brook et al., 2012a; Aumer et al., 2013; Hopkins et al., 2014; Marinacci, Pakmor, & Springel, 2014; Übler et al., 2014; Genel et al., 2015). Despite the physical complexity and the diverse formation histories of individual galaxies, local disk galaxies exhibit on average a tight relationship between their rotation velocity V and their luminosity L or mass M, namely the Tully-Fisher relation (TFR; Tully & Fisher, 1977). In its mass-based form, the TFR is commonly expressed as $M \propto V^a$, or $\log(M) = a \cdot \log(V) + b$, where a is the slope, and b is the zero-point offset.

In the local Universe, rotation curves of disk galaxies are apparently generally dominated by DM already at a few times the disc scale length, and continue to be flat or rising out to several tens of kpc (see e.g. reviews by Faber & Gallagher, 1979; Sofue & Rubin, 2001; and Catinella, Giovanelli, & Haynes, 2006). Therefore, the local TFR enables a unique approach to relate the baryonic galaxy mass, which is an observable once a mass-to-light conversion is assumed, to the potential of the dark halo. Although the luminosity-based TFR is more directly accessible, relations based on mass constitute a physically more fundamental approach since the amount of light measured from the underlying stellar population is a function of passband, systematically affecting the slope of the TFR (e.g. Verheijen, 1997, 2001; Bell & de Jong, 2001; Pizagno et al., 2007; Courteau et al., 2007; McGaugh & Schombert, 2015). The most fundamental relation is given by the baryonic mass TFR (bTFR). It places galaxies over several decades in mass onto a single relation, whereas there appears to be a break in the slope of the stellar mass TFR (sTFR) for low-mass galaxies (McGaugh et al., 2000; McGaugh, 2005).

Observed slopes vary mostly between $3 \lesssim a \lesssim 4.5$ for the local sTFR (e.g. Bell & de Jong, 2001; Pizagno et al., 2005; Avila-Reese et al., 2008; Williams, Bureau, & Cappellari, 2010; Gurovich et al., 2010; Torres-Flores et al., 2011; Reyes et al., 2011) and between $3 \lesssim a \lesssim 4$ for the local bTFR (e.g. McGaugh et al., 2000; McGaugh, 2005; Trachternach et al., 2009; Stark, McGaugh, & Swaters, 2009; Zaritsky et al., 2014; McGaugh & Schombert, 2015; Lelli, McGaugh, & Schombert, 2016b; Bradford, Geha, & van den Bosch, 2016; Papastergis, Adams, & van der Hulst, 2016). It should be noted that the small scatter of local TFRs can be partly associated to the very efficient selection of undisturbed spiral galaxies (e.g. Kannappan, Fabricant, & Franx, 2002; see also Courteau et al., 2007; Lelli, McGaugh, & Schombert, 2016b, for discussions of local TFR scatter). Variations in the observational results of low-z studies can be attributed to different sample sizes, selection bias, varying data quality, statistical methods, conversions from L to M, or to the adopted measure of V (Courteau et al., 2014; for a detailed discussion regarding the bTFR see Bradford, Geha, & van den Bosch, 2016).

Any such discrepancy becomes more substantial when going to higher redshift where measurements are more challenging and the observed scatter of the TFR increases with respect to local relations (e.g. Conselice et al., 2005; Miller et al., 2012). The latter is partly attributed to ongoing kinematic and morphological transitions (Flores et al., 2006; Kassin et al., 2007, 2012; Puech et al., 2008, 2010; Covington et al., 2010; Miller, Sullivan, & Ellis, 2013; Simons et al., 2016), possibly indicating non-equilibrium states. Another complication for comparing high-z studies to local TFRs arises from the inherently different nature of the so-called disk galaxies at high redshift: although of disk-like structure and rotationally supported, they are significantly more “turbulent”, geometrically thicker, and clumpier than local disk galaxies (Förster Schreiber et al., 2006, 2009, 2011a,b; Genzel et al., 2006, 2011; Elmegreen & Elmegreen, 2006; Elmegreen et al., 2007; Kassin et al., 2007, 2012; Epinat et al., 2009, 2012; Law et al., 2009, 2012; Jones et al., 2010; Nelson et al., 2012; Newman et al., 2013; Wisnioski et al., 2015; Tacchella et al., 2015b,a).

Despite the advent of novel instrumentation and multiplexing capabilities, there is considerable tension in the literature regarding the empirical evolution of the TFR zero-points with cosmic time. Several authors find no or only weak zero-point evolution of the sTFR up to redshifts of $z \sim 1.7$ (Conselice et al., 2005; Kassin et al., 2007; Miller et al., 2011, 2012; Contini et al., 2016; Di Teodoro, Fraternali, & Miller, 2016; Molina et al., 2017; Pelliccia et al., 2017), while others find a negative zero-point evolution up to redshifts of $z \sim 3$ (Puech et al., 2008, 2010; Cresci et al., 2009; Gnerucci et al., 2011; Swinbank et al., 2012b; Price et al., 2016; Tiley et al., 2016; Straatman et al., 2017). Similarly for the less-studied high$-z$ bTFR, Puech et al. (2010) find no indication of zero-point evolution since $z \sim 0.6$, while Price et al. (2016) find a positive evolution between lower-z galaxies and their $z \sim 2$ sample. There are indications that varying strictness in morphological or kinematic selections can explain these conflicting results (Miller, Sullivan, & Ellis, 2013; Tiley et al., 2016). The work by Vergani et al. (2012) demonstrates that also the assumed slope of the relation, which is usually adopted from a local TFR in high-z studies, can become relevant for the debate of zero-point evolution (see also Straatman et al., 2017).

A common derivation of the measured quantities as well as similar statistical methods and sample selection are crucial to any study which aims at comparing different results and studying the TFR evolution with cosmic time (e.g. Courteau et al., 2014; Bradford, Geha, & van den Bosch, 2016). Ideally, spatially well resolved rotation curves should be used which display a peak or flattening. Such a sample would provide an important reference frame for studying the effects of baryonic mass assembly on the morphology and rotational support of disk-like systems, for investigating the evolution of rotationally supported galaxies as a response to the structural growth of the parent DM halo, and for comparisons with cosmological models of galaxy evolution.

In this paper, we exploit spatially resolved integral field spectroscopic (IFS) observations of 240 rotation-dominated disk galaxies from the KMOS$^{\rm 3D}$ survey (Wisnioski et al., 2015, hereafter W15) to study the evolution of the sTFR and bTFR between redshifts $z = 2.6$ and $z = 0.6$. The wide redshift coverage of the survey, together with its high quality data, allow for a unique investigation of the evolution of the TFR during the peak epoch of cosmic star formation rate density, where coherent data processing and analysis are ensured. In Section 2.2 we describe our data and sample selection. We present the KMOS$^{\rm 3D}$ TFR in Section 2.3, together with a discussion of other selected high$-z$ TFRs. In Section 2.4 we discuss the observed TFR evolution, we set it in the context to local observations, and we discuss possible sources of uncertainties. In Section 2.5 we constrain a theoretical toy model to place our observations in a cosmological context. Section 2.6 summarizes our work.

Throughout, we adopt a Chabrier (2003) initial mass function (IMF) and a flat ΛCDM cosmology with $H_0 = 70\,{\rm km\,s^{-1}\,Mpc^{-1}}$, $\Omega_\Lambda = 0.7$, and $\Omega_m = 0.3$.

2.2 Data and sample selection

The contradictory findings about the evolution of the mass-based TFR in the literature motivate a careful sample selection at high redshift. In this work we concentrate on the evolution of the TFR for undisturbed disk galaxies. Galaxies are eligible for such a study if the observed kinematics trace the central potential of the parent halo. To ensure a suitable sample we perform several selection steps which are described in the following sections.

2.2.1 The KMOS^{3D} survey

This work is based on the first three years of observations of KMOS^{3D}, a multi-year near-infrared (near-IR) IFS survey of more than 600 mass-selected star-forming galaxies (SFGs) at $0.6 \lesssim z \lesssim 2.6$ with the $K-$band Multi Object Spectrograph (KMOS; Sharples et al., 2013) on the *Very Large Telescope.* The 24 integral field units of KMOS allow for efficient spatially resolved observations in the near-IR passbands YJ, H, and K, facilitating high-z rest-frame emission line surveys of unprecedented sample size. The KMOS^{3D} survey and data reduction are described in detail by Wisnioski et al. (2015), and we here summarize the key features. The KMOS^{3D} galaxies are selected from the 3D-HST survey, a *Hubble Space Telescope* Treasury Program (Brammer et al., 2012; Skelton et al., 2014; Momcheva et al., 2016). 3D-HST provides $R \sim 100$ near-IR grism spectra, optical to 8 μm photometric catalogues, and spectroscopic, grism, and/or photometric redshifts for all sources. The redshift information is complemented by high-resolution Wide Field Camera 3 (WFC3) near-IR imaging from the CANDELS survey (Grogin et al., 2011; Koekemoer et al., 2011; van der Wel et al., 2012), as well as by further multi-wavelength coverage of our target fields GOODS-S, COSMOS, and UDS, through *Spitzer*/MIPS and *Herschel*/PACS photometry (e.g. Lutz et al., 2011; Magnelli et al., 2013; Whitaker et al., 2014, and references therein). Since we do not apply selection cuts other than a magnitude cut of $Ks \lesssim 23$ and a stellar mass cut of $\log(M_* \ [M_\odot]) \gtrsim 9.2$, together with OH-avoidance around the survey's main target emission lines Hα+[Nii], the KMOS^{3D} sample will provide a reference for galaxy kinematics and Hα properties of high$-z$ SFGs over a wide range in stellar mass and star formation rate (SFR). The emphasis of the first observing periods has been on the more massive galaxies, as well as on $YJ-$ and $K-$band targets, i.e. galaxies at $z \sim 0.9$ and $z \sim 2.3$, respectively. Deep average integration times of $5.5, 7.0, 10.5$ h in YJ, H, K, respectively, ensure a detection rate of more than 75 per cent, including also quiescent galaxies.

The results presented in the remainder of this paper build on the KMOS^{3D} sample as of January 2016, with 536 observed galaxies. Of these, 316 are detected in, and have spatially resolved, Hα emission free from skyline contamination, from which two-dimensional velocity and dispersion maps are produced. Examples of those are shown in the work by Wisnioski et al. (2015) and Wuyts et al. (2016b, hereafter W16).

2.2.2 Masses and star-formation rates

The derivation of stellar masses M_* uses stellar population synthesis models by Bruzual & Charlot (2003) to model the spectral energy distribution of each galaxy. Extinction, star formation histories (SFHs), and a fixed solar metallicity are incorporated into the models as described by Wuyts et al. (2011b).

SFRs are obtained from the ladder of SFR indicators introduced by Wuyts et al. (2011b): if *Herschel*/PACS $60-160\mu$m and/or *Spitzer*/MIPS 24μm observations were available, the SFRs were computed from the observed UV and IR luminosities. Otherwise, SFRs were derived from stellar population synthesis modelling of the observed broadband optical to IR spectral energy distributions.

Gas masses are obtained from the scaling relations by Tacconi et al. (2018), which use the combined data of molecular gas ($M_{\mathrm{gas,mol}}$) and dust-inferred gas masses of SFGs between $0<z<4$ to derive a relation for the depletion time $t_{\mathrm{depl}} \equiv M_{\mathrm{gas,mol}}/\mathrm{SFR}$. It is expressed as a function of redshift, main sequence offset, stellar mass, and size. Although the contribution of atomic gas to the baryonic mass within $1-3\,R_e$ is assumed to be negligible at $z\sim1-3$, the inferred gas masses correspond to lower limits (Genzel et al., 2015).

Following Burkert et al. (2016), we adopt uncertainties of 0.15 dex for stellar masses, and 0.20 dex for gas masses. This translates into an average uncertainty of ~ 0.15 dex for baryonic masses (see Section 2.4.3.1 for a discussion).

2.2.3 Dynamical modelling

Wuyts et al. (2016b) use the two-dimensional velocity and velocity dispersion fields as observed in Hα to construct dynamical models for selected galaxies. The modelling procedure is described in detail by Wuyts et al. (2016b), where examples of velocity fields, velocity and dispersion profiles, and 1D fits can also be found (see also Figure 2.1). In brief, radial velocity and dispersion profiles are constructed from $0''8$ diameter circular apertures every other $0''2$ along the kinematic major axis using LINEFIT (Davies et al., 2009), where spectral resolution is taken into account. On average, the outermost apertures reach 2.5 times the effective H-band radius, corresponding to $\sim$15 and $\sim$12 extracted data points for galaxies at $z\sim0.9$ and $z\sim2.3$, respectively. A dynamical mass modelling is performed by fitting the extracted kinematic profiles simultaneously in observed space using an updated version of DYSMAL (Cresci et al., 2009; Davies et al., 2011).

The free model parameters are the dynamical mass M_{dyn} and the intrinsic velocity dispersion σ_0. The inclination i and effective radius R_e are independently constrained from GALFIT (Peng et al., 2010) models to the CANDELS H-band imaging by *HST* presented by van der Wel et al. (2012). The inclination is computed as $\cos(i)=[(q^2-q_0^2)/(1-q_0^2)]^{1/2}$. Here, $q=b/a$ is the axial ratio, and $q_0=0.25$ is the assumed ratio of scale height to scale length, representing

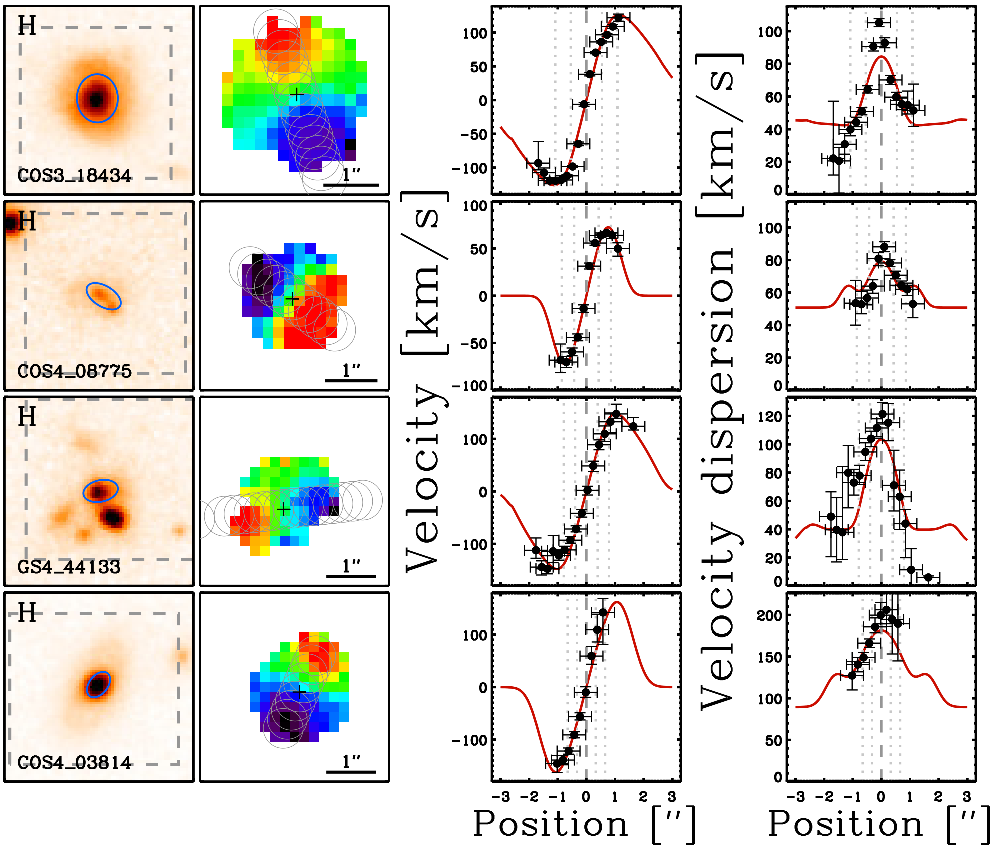

Figure 2.1: *Examples of galaxies from the sample modelled by Wuyts et al. (2016b) which do, or do not, pass our TFR selection criteria (Section 2.2.4). From left to right: surface brightness distribution in the WFC3 H−band, with blue ellipses indicating the* GALFIT *effective radius, and grey dashed lines marking the field of view of the KMOS observations; Hα velocity field, with circles marking the extracted pseudo slit; the observed (black data points with errors) and modelled (red lines) 1D velocity and velocity dispersion profiles along the kinematic major axis, with vertical dotted grey lines marking one and two effective radii. More examples can be found in Figure 3 by Wuyts et al. (2016b). The upper two rows show galaxies which pass our selection criteria for the TFR sample. The third row shows a galaxy which is rejected from the TFR sample because it is likely influenced by a neighboring object, based on projected distance, redshifts, and stellar mass ratio. The bottom row shows a galaxy which is rejected from the TFR sample because it is unclear if the maximum velocity is covered by the observations.*

the intrinsic thickness of the disk. The width of the point spread function (PSF) is determined from the average PSF during observations for each galaxy. The mass model used in the fitting procedure is a thick exponential disk, following Noordermeer (2008), with a Sérsic index of $n_{\rm S} = 1$. We note that the peak rotation velocity of a thick exponential disk is about 3 to 8 per cent lower than that of a Freeman disk (Freeman, 1970). For a general comparison of observed and modelled rotation velocities and dispersions, we refer the reader to Wuyts et al. (2016b). Another key product of the modelling is the baryonic (or DM) mass fraction on galactic scales, as presented in Wuyts et al. (2016b).

The merit of the Wuyts et al. (2016b) modelling procedure includes the coupled treatment of velocity and velocity dispersion in terms of beam-smearing effects and pressure support. The latter is of particular importance for our study since high-z galaxies have a non-negligible contribution to their dynamical support from turbulent motions (Förster Schreiber et al., 2006, 2009; Genzel et al., 2006, 2008, 2014a; Kassin et al., 2007, 2012; Cresci et al., 2009; Law et al., 2009; Gnerucci et al., 2011; Epinat et al., 2012; Swinbank et al., 2012b; Wisnioski et al., 2012, 2015; Jones et al., 2013; Newman et al., 2013). The resulting pressure compensates part of the gravitational force, leading to a circular velocity which is larger than the rotation velocity $v_{\rm rot}$ alone:

$$v_{\rm circ}(r)^2 = v_{\rm rot}(r)^2 + 2\,\sigma_0^2\,\frac{r}{R_d}, \tag{2.1}$$

where R_d is the disk scale length (Burkert et al., 2010; see also Burkert et al., 2016; Wuyts et al., 2016b; Genzel et al., 2017; Lang et al., 2017).

If not stated otherwise, we adopt the maximum of the modelled circular velocity, $v_{\rm circ,max} \equiv v_{\rm circ}$, as the rotation velocity measure for our Tully-Fisher analysis. For associated uncertainties, see Section 2.4.3.2. We use an expression for the peak velocity because there is strong evidence that high-z rotation curves of massive star forming disk galaxies exhibit on average an outer fall-off, i.e. do not posses a 'flat' part (van Dokkum et al., 2015; Genzel et al., 2017; Lang et al., 2017).[1] This is partly due to the contribution from turbulent motions to the dynamical support of the disk, and partly due to baryons dominating the mass budget on the galaxy scale at high redshift (see also van Dokkum et al., 2015; Stott et al., 2016; Wuyts et al., 2016b; Price et al., 2016; Alcorn et al., 2016; Pelliccia et al., 2017). A disk model with a flattening or rising rotation curve as the 'arctan model', which is known to be an adequate model for local disk

---

[1] *Note post publication:* We emphasize that this statement holds for the average rotation curve of massive SFGs particularly at $z > 1.5$, while a variety of outer rotation curve shapes is observed for SFGs with different physical properties. Particularly lower$-z$ systems with lower baryonic mass surface densities, or galaxies with smaller bulges, can show flat or even rising outer rotation curves, as typical for local SFGs.

galaxies (e.g. Courteau, 1997), might therefore be a less appropriate choice for high-z galaxies.

2.2.4 Sample selection

We start our investigation with a parent sample of 240 KMOS^{3D} galaxies selected and modelled by Wuyts et al. (2016b). The sample definition is described in detail by Wuyts et al. (2016b), and we briefly summarize the main selection criteria here: (i) galaxies exhibit a continuous velocity gradient along a single axis, the 'kinematic major axis'; (ii) their photometric major axis as determined from the CANDELS WFC3 H-band imaging and kinematic major axis are in agreement within 40 degrees; (iii) they have a signal-to-noise ratio within each $0''8$ diameter aperture along the kinematic major axis of $S/N \gtrsim 5$, with up to $S/N \sim 10 - 100$ within the central apertures. The galaxies sample a parameter space along the main sequence of star forming galaxies (MS) with stellar masses of $M_* \gtrsim 6.3 \times 10^9\ M_\odot$, specific star formation rates of sSFR $\gtrsim 0.7/t_{\rm Hubble}$, and effective radii of $R_e \gtrsim 2$ kpc. The Wuyts et al. (2016b) sample further excludes galaxies with signs of major merger activity based on their morphology and/or kinematics.

For our Tully-Fisher analysis we undertake a further detailed examination of the Wuyts et al. (2016b) parent sample. The primary selection step is based on the position-velocity diagrams and on the observed and modelled one-dimensional kinematic profiles of the galaxies. Through inspection of the diagrams and profiles we ensure that the peak rotation velocity is well constrained, based on the observed flattening or turnover in the rotation curve and the coincidence of the dispersion peak within $\lesssim 2$ pixels ($\lesssim 0''4$) with the position of the steepest velocity gradient. The requirement of detecting the maximum velocity is the selection step with the largest effect on sample size, leaving us with 149 targets. The galaxy shown in the fourth row of Figure 2.1 is excluded from the TFR sample based on this latter requirement.

To single out rotation-dominated systems for our purpose, we next perform a cut of $v_{\rm rot,max}/\sigma_0 > \sqrt{4.4}$, based on the properties of the modelled galaxy (see also e.g. Tiley et al., 2016). Our cut removes ten more galaxies where the contribution of turbulent motions at the radius of maximum rotation velocity, which is approximately at $r = 2.2\,R_d$, to the dynamical support is higher than the contribution from ordered rotation (cf. Equation (2.1)).

We exclude four more galaxies with close neighbours because their kinematics might be influenced by the neighbouring objects. These objects have projected distances of < 20 kpc, spectroscopic redshift separations of < 300 km/s, and mass ratios of $> 1 : 5$, based on the 3D-HST catalogue. One of the dismissed galaxies is shown in the third row of Figure 2.1.

After applying the above cuts, our refined TFR sample contains 135 galax-

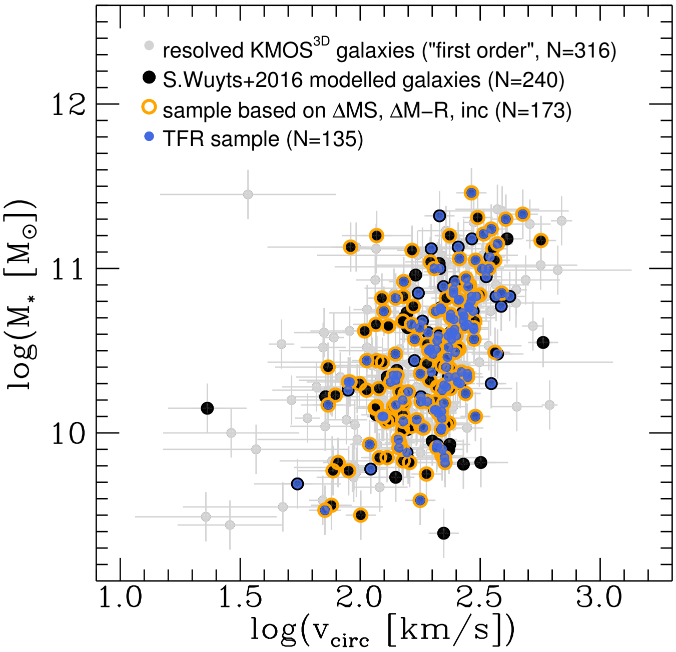

Figure 2.2: *A 'first order' sTFR of all detected and resolved KMOS^{3D} galaxies without skyline contamination at the position of Hα, where $v_{\rm circ}$ is computed from the observed maximal velocity difference and from the intrinsic velocity dispersion as measured from the outer disk region, after corrections for beam-smearing and inclination (see Wisnioski et al., 2015). The sample of galaxies which have been dynamically modelled by Wuyts et al. (2016b) is shown in black. In orange, we indicate a subsample of this latter sample based only on cuts in MS offset (±0.6 dex), mass-radius relation offset (±0.3 dex), and inclination ($0.5 \leq \sin(i) \leq 0.98$). In blue we show our final TFR sample as obtained from the selection steps outlined in Section 2.2.4.*

ies, with 65, 24, 46 targets in the YJ, H, K passbands with mean redshifts of $z \sim 0.9, 1.5, 2.3$, respectively. The median and central 68th percentile ranges of offsets between the morphological and kinematic position angle (PA) are 6.4° [0.1°; 18.4°]. This should minimize the possible impact of non-axisymmetric morphological features on the fixed model parameters (R_e, $\sin(i)$, PA) that are based on single-component Sérsic model fits to the observed H-band images (see Rodrigues et al., 2017, and also the discussion by Wuyts et al. (2016b)). The median physical properties of redshift subsamples are listed in Table 2.1. Individual properties of galaxies in the TFR sample in terms of z, M_*, $M_{\rm bar}$, $v_{\rm circ,max}$, and σ_0, are listed in Table 2.3.

To visualize the impact of our sample selection we show in Figure 2.2 a 'first order' sTFR of all detected and resolved KMOS^{3D} galaxies. Here, $v_{\rm circ}$ is computed from the observed maximal velocity difference and from the intrinsic velocity dispersion as measured from the outer disk region, after corrections for beam-smearing and inclination, as detailed in Appendix A.2 of Burkert et al. (2016). For simplicity, we assume in computing $v_{\rm circ}$ for this figure that the observed maximal velocity difference is measured at $r = 2.2R_d$, but we emphasize that, in contrast to the modelled circular velocity, this is not necessarily the case. We indicate our parent sample of modelled galaxies by Wuyts et al. (2016b) in black, and our final TFR sample in blue. For reference, we also show in orange a subsample of the selection by Wuyts et al. (2016b) which is only based on cuts in MS offset (±0.6 dex), mass-radius relation offset (±0.3 dex), and inclination ($0.5 \leq \sin(i) \leq 0.98$). We emphasize that the assessment of recovering the true maximum rotation velocity is not taken into account for such an objectively selected sample. We discuss in Appendix 2.7 in more detail the effects of sample selection, and contrast them to the impact of correcting for e.g. beam-smearing.

Table 2.1: *Median physical properties of our TFR subsamples at $z \sim 0.9$ (YJ), $z \sim 1.5$ (H), and $z \sim 2.3$ (K), together with the associated central 68th percentile ranges in brackets.*

	$z \sim 0.9$ (65 galaxies)	$z \sim 1.5$ (24 galaxies)	$z \sim 2.3$ (46 galaxies)
$\log(\mathrm{M}_* \ [\mathrm{M}_\odot])$	10.49 [10.03; 10.83]	10.72 [10.08; 11.07]	10.51 [10.18; 11.00]
$\log(\mathrm{M}_{\rm bar} \ [\mathrm{M}_\odot])$	10.62 [10.29; 10.98]	10.97 [10.42; 11.31]	10.89 [10.59; 11.33]
SFR $[\mathrm{M}_\odot/\mathrm{yr}]$	21.1 [7.1; 39.6]	53.4 [15.5; 134.5]	72.9 [38.9; 179.1]
log(Δ MS)[a]	0.20 [-0.21; 0.42]	0.10 [-0.21; 0.45]	-0.01 [-0.29; 0.13]
R_e^{5000} [kpc]	4.8 [3.0; 7.6]	4.9 [3.0; 7.0]	4.0 [2.5; 5.2]
log(Δ M-R)[b]	-0.02 [-0.17; 0.16]	0.08 [-0.10; 0.17]	0.06 [-0.14; 0.17]
$n_{\rm S}$	1.3 [0.8; 3.1]	0.9 [0.4; 2.2]	1.0 [0.4; 1.6]
B/T[c]	0.11 [0.00; 0.39]	0.00 [0.00; 0.23]	0.10 [0.00; 0.25]
$v_{\rm rot,max}$ [km/s]	233 [141; 302]	245 [164; 337]	239 [160; 284]
σ_0 [km/s]	30 [9; 52]	47 [29; 59]	49 [32; 68]
$v_{\rm rot,max}/\sigma_0$	6.7 [3.2; 25.3]	5.5 [3.4; 65.6]	4.3 [3.4; 9.1]
$v_{\rm circ,max}$ [km/s]	239 [167; 314]	263 [181; 348]	260 [175; 315]

[a] MS offset with respect to the broken power law relations derived by Whitaker et al. (2014), using the redshift-interpolated parametrization by Wisnioski et al. (2015), Δ MS=SFR $-$ $\mathrm{SFR}_{\mathrm{MS(z,M_*)[W14]}}$.

[b] Offset from the mass-size relation of SFGs with respect to the relation derived by van der Wel et al. (2014a), Δ M-R=$R_e^{5000} - R^{5000}_{\mathrm{e,M-R(z,M_*)[vdW14]}}$, after correcting the $H-$band R_e to the rest-frame 5000 .

[c] Bulge-to-total mass ratio if available, namely for 78, 92, and 89 per cent of our galaxies in $YJ-$, $H-$, and $K-$band, respectively. Values of $B/T = 0$ usually occur when the galaxy's Sérsic index $n_{\rm S}$ is smaller than 1 (cf. Lang et al., 2014).

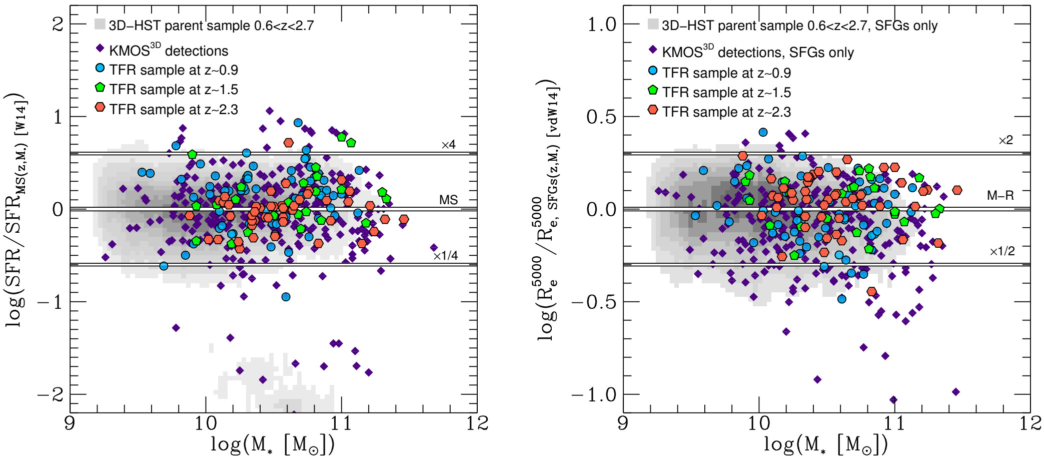

Figure 2.3: *Location of our TFR galaxies in the M_*-SFR (left) and in the M_*-R_e plane (right) as compared to all detected KMOS^{3D} galaxies (purple diamonds) and the underlying galaxy population at $0.6 < z < 2.7$ taken from the 3D-HST source catalogue (grey scale) with log($M_*\,[M_\odot]$) > 9.2, $K_{AB} < 23$ mag, and for the M_*-R_e relation sSFR $> 0.7/t_{\rm Hubble}$ ('SFGs only'). In the left panel, the SFR is normalized to the MS as derived by Whitaker et al. (2014) at the redshift and stellar mass of each galaxy, using the redshift-interpolated parametrization by Wisnioski et al. (2015). In the right panel, the effective radii as measured from $H-$band are corrected to the rest-frame 5000 and normalized to the M-R relation of SFGs as derived by van der Wel et al. (2014a) at the redshift and stellar mass of each galaxy. At $z\sim0.9$ the TFR galaxies lie on average a factor of ~1.6 above the MS, but on average on the M-R relation. At $z\sim2.3$, the TFR galaxies lie on average on the MS and the M-R relation, but their scatter with respect to higher SFRs and to smaller radii is not as pronounced as for the star-forming 3D-HST sample. For the 3D-HST 'SFGs only' population the median and 68th percentile ranges are log(Δ MS)=$0.00^{+0.33}_{-0.37}$, and log(Δ M-R)=$-0.04^{+0.17}_{-0.28}$. See Table 2.1 for the corresponding ranges of the TFR sample.*

The distribution of the TFR sample with respect to the full KMOS^{3D} sample (as of January 2016) and to the corresponding 3D-HST sample in terms of star formation rate and effective radius as a function of stellar mass is shown in Figure 2.3 (for a detailed comparison of the Wuyts et al. (2016b) sample, we refer the reader to Wuyts et al. (2016b)). We select 3D-HST galaxies with $0.6 < z < 2.7$, $\log(M_*\ [M_\odot]) > 9.2$, $Ks < 23$, and for the 'SFGs only' subset we apply sSFR $> 0.7/t_{\rm Hubble}$, for a total of 9193 and 7185 galaxies, respectively. Focussing on the 'SFGs only' subset, the median and corresponding 68th percentiles with respect to the MS relations for the $z\sim0.9$ and the $z\sim2.3$ populations are log(Δ MS)=$0.00^{+0.34}_{-0.39}$ and log(Δ MS)=$-0.05^{+0.26}_{-0.35}$, and with respect to the mass-size (M-R) relation log(Δ M-R)=$-0.04^{+0.16}_{-0.28}$ and log(Δ M-R)=$-0.02^{+0.17}_{-0.31}$, respectively. At $z\sim0.9$, the TFR galaxies lie on average a factor of ~1.6 above the MS, with log(Δ MS)=$0.20^{+0.42}_{-0.21}$, and have sizes corresponding to log(Δ M-R)=$-0.02^{+0.16}_{-0.17}$. At $z \sim 2.3$, the TFR galaxies lie on average on the MS and M-R relations (log(Δ MS)=$-0.01^{+0.13}_{-0.29}$, log(Δ M-R)=$0.06^{+0.17}_{-0.14}$), but their scatter with respect to higher SFRs and to smaller radii is not as pronounced as for the star-forming 3D-HST sample.

In summary, our analysis accounts for the following effects: (i) beam-smearing, through a full forward modelling of the observed velocity and velocity dispersion profiles with the known instrumental PSF; (ii) the intrinsic thickness of high$-z$ disks, following Noordermeer (2008); (iii) pressure support through turbulent gas motions, following Burkert et al. (2010), under the assumption of a disk of constant velocity dispersion and scale height. The former steps are all included in the dynamical modelling by Wuyts et al. (2016b). On top of that, we retain in our TFR sample only non-interacting SFGs which are rotationally supported based on the $v_{\rm rot,max}/\sigma_0 > \sqrt{4.4}$ criterion, and for which the data have sufficient S/N and spatial coverage to robustly map, and model, the observed rotation curve to or beyond the peak rotation velocity.

2.3 The TFR with KMOS^{3D}

2.3.1 Fitting

In general, there are two free parameters for TFR fits in log-log space: the slope a and the zero-point offset b. It is standard procedure to adopt a local slope for high$-z$ TFR fits[2]. This is due to the typically limited dynamical range probed by the samples at high redshift which makes it challenging to robustly constrain a. The TFR evolution is then measured as the relative difference in zero-point offsets (e.g. Puech et al., 2008; Cresci et al., 2009; Gnerucci et al., 2011; Miller et al., 2011, 2012; Tiley et al., 2016). In Appendix 2.8 we briefly investigate a method to measure TFR evolution which is independent of the slope. For clarity and consistency with TFR investigations in the literature, however, we present our main results based on the functional form of the TFR as given in Equation (2.2) below. For our fiducial fits, we adopt the local slopes by Reyes et al. (2011) and Lelli, McGaugh, & Schombert (2016b) for the sTFR and the bTFR, respectively.[3]

To fit the TFR we adopt an inverse linear regression model of the form

$$\log(M\ [M_\odot]) = a \cdot \log(v_{\rm circ}/v_{\rm ref}) + b. \tag{2.2}$$

---

[2] While the slope might in principle vary with cosmic time, a redshift evolution is not expected from the toy model discussed in Section 2.5.

[3] The sTFR zero-point by Reyes et al. (2011) is corrected by -0.034 dex to convert their Kroupa (2001) IMF to the Chabrier IMF which is used in this work, following the conversions given in Madau & Dickinson (2014).

Here, M is the stellar or baryonic mass, and a reference value of $v_{\mathrm{ref}} = \overline{v_{\mathrm{circ}}}$ is chosen to minimize the uncertainty in the determination of the zero-point b (Tremaine et al., 2002). If we refer in the remainder of the paper to b as the zero-point offset, this is for our sample in reference to $v_{\mathrm{circ}} = v_{\mathrm{ref}}$, and not to $\log(v_{\mathrm{circ}}$ [km/s]$)=0$. When comparing to other data sets in Sections 2.3.4 and 2.4.2 we convert their zero-points accordingly.

For the fitting we use a Bayesian approach to linear regression, as well as a least-squares approximation. The Bayesian approach to linear regression takes uncertainties in ordinate and abscissa into account.[4] The least-squares approximation also takes uncertainties in ordinate and abscissa into account, and allows for an adjustment of the intrinsic scatter to ensure for a goodness of fit of $\chi^2_{\mathrm{reduced}} \approx 1$.[5] To evaluate the uncertainties of the zero-point offset b of the fixed-slope fits, a bootstrap analysis is performed for the fits using the least-squares approximation. The resulting errors agree with the error estimates from the Bayesian approach within 0.005 dex of mass. We find that the intrinsic scatter obtained from the Bayesian technique is similar or larger by up to 0.03 dex of mass as compared to the least-squares method. Both methods give the same results for the zero-point b (see also the recent comparison by Bradford, Geha, & van den Bosch, 2016).

We perform fits to our full TFR sample, as well as to the subsets at $z \sim 0.9$ and $z \sim 2.3$. The latter allows us to probe the maximum separation in redshift possible within the KMOS$^{\mathrm{3D}}$ survey. Due to the low number of TFR galaxies in our $H-$band bin we do not attempt to fit a zero-point at $z \sim 1.5$.

2.3.2 The TFR at $0.6 < z < 2.6$

In this section, we investigate the Tully-Fisher properties of our full TFR sample at $0.6 < z < 2.6$. The sTFR as well as the bTFR are clearly in place and well defined at $0.6 < z < 2.6$, confirming previous studies (e.g. Cresci et al., 2009; Miller et al., 2011, 2012; Tiley et al., 2016, and other high$-z$ work cited in Section 2.1). In Figure 2.4 we show the best fits for the sTFR and the bTFR using the local slopes by Reyes et al. (2011) ($a = 1/0.278 = 3.60$) and Lelli, McGaugh, & Schombert (2016b) ($a = 3.75$), respectively. The best-fit parameters are given in Table 2.2. section

The intrinsic scatter as determined from the fits is with $\zeta_{\mathrm{int,sTFR}} \approx 0.22$ and $\zeta_{\mathrm{int,bTFR}} \approx 0.23$ larger by up to a factor of two in dex of mass than in the local

---

[4] We use the IDL routine LINMIX_ERR which is described and provided by Kelly (2007). A modified version of this code which allows for fixing of the slope was kindly provided to us by Brandon Kelly and Marianne Vestergaard.

[5] We use the IDL routine MPFITEXY which is described and provided by Williams, Bureau, & Cappellari (2010). It depends on the MPFIT package (Markwardt, 2009).

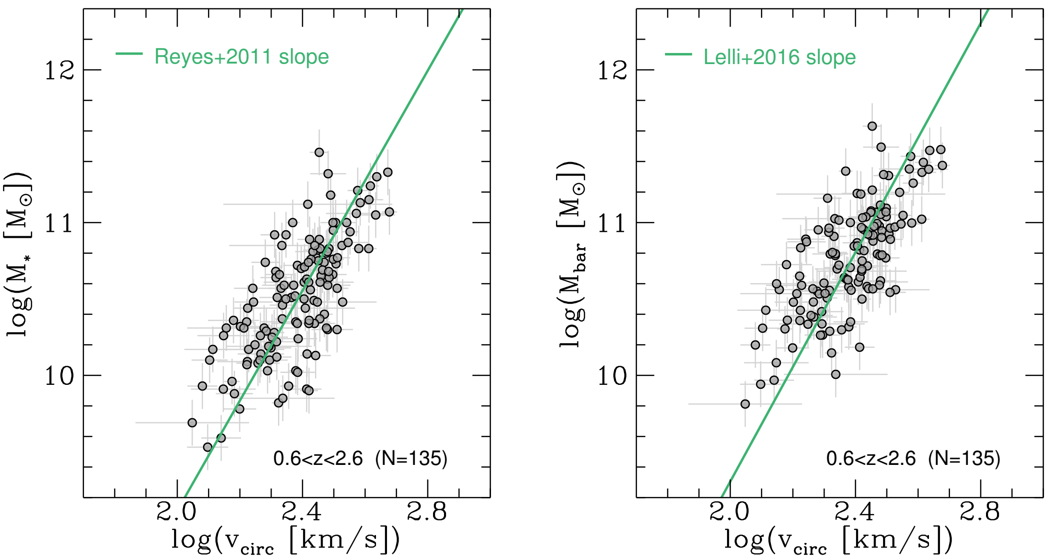

Figure 2.4: *The sTFR (left) and the bTFR (right) for our sample of 135 SFGs, with error bars in grey. The green lines show the fixed-slope fits to the inverse linear regression model as given in Equation* (2.2)*, using the corresponding local slopes by Reyes et al. (2011) and Lelli, McGaugh, & Schombert (2016b). The fit parameters are given in Table 2.2. A correlation between* $v_{\rm circ}$ *and the different mass tracers is evident.*

Universe (typical values for the observed intrinsic scatter of the local relations used in this study are $\zeta_{\rm int} = 0.1 - 0.13$ in dex of mass; see Reyes et al., 2011; Lelli, McGaugh, & Schombert, 2016b). A larger scatter in the high$-z$ TFR is expected simply due to the larger measurement uncertainties. It might further be due to disk galaxies being less "settled" (Kassin et al., 2007, 2012; Simons et al., 2016; see also Flores et al., 2006; Puech et al., 2008, 2010; Covington et al., 2010; Miller, Sullivan, & Ellis, 2013). This can become manifest through actual displacement of galaxies from the TFR due to a non-equilibrium state (see e.g. simulations by Covington et al., 2010).

Miller, Sullivan, & Ellis (2013) studied the connection between TFR scatter and bulge-to-total ratio, and found that above $z \approx 1$ the TFR scatter is increased due to an offset of bulge-less galaxies from the $B/T > 0.1$ galaxy population. B/T measurements for our galaxies come from bulge-disk decompositions based on two-component fits to the two-dimensional CANDELS H-band light distribution (Lang et al., 2014). If we select only galaxies with $B/T > 0.1$ (57 galaxies), we do not find a decrease in scatter for our sample ($\zeta_{\rm int,sTFR,\mathit{B/T}>0.1} = 0.22$ and $\zeta_{\rm int,bTFR,\mathit{B/T}>0.1} = 0.24$). The same is true if we select for galaxies with $B/T < 0.1$ (78 galaxies), leading to $\zeta_{\rm int,sTFR,\mathit{B/T}<0.1} = 0.23$ and $\zeta_{\rm int,bTFR,\mathit{B/T}<0.1} = 0.22$.

However, the scatter is affected by the sample selection: if we create 'first order' TFRs (Section 2.2.4, Figure 2.2), i.e. using all detected and resolved KMOS^{3D} galaxies without skyline contamination (316 SFGs), but also without selecting against dispersion-dominated systems, low S/N galaxies, or mergers, we find an intrinsic scatter of $\zeta_{\mathrm{int,sTFR}} = 0.60$ and $\zeta_{\mathrm{int,bTFR}} = 0.64$ for these 'first order' TFRs (for the parent Wuyts et al. (2016b) sample we find $\zeta_{\mathrm{int,sTFR}} = 0.27$ and $\zeta_{\mathrm{int,bTFR}} = 0.29$). We caution that this test sample includes galaxies where the maximum rotation velocity is not reached, thus introducing artificial scatter in these 'first order' TFRs. In contrast to the properties of our TFR sample, this scatter is asymmetric around the best fit, with larger scatter towards lower velocities, but also towards lower masses where more of the dispersion-dominated galaxies reside (cf. Figures 2.2 and 2.8). This underlines the importance of a careful sample selection.

Also the zero-points are affected by the sample selection (see also Figure 2.8). For our TFR sample, we find $b_{\mathrm{sTFR}} = 10.50 \pm 0.03$ and $b_{\mathrm{bTFR}} = 10.75 \pm 0.03$. If we consider the 'first order' samples we find an increase of the zero-points of $\Delta b_{\mathrm{sTFR}} = 0.37$ dex and $\Delta b_{\mathrm{bTFR}} = 0.39$ dex (for the parent Wuyts et al. (2016b) sample we find $\Delta b_{\mathrm{sTFR}} = 0.03$ dex and $\Delta b_{\mathrm{bTFR}} = 0.04$ dex).

It is common, and motivated by the scatter of the TFR, to investigate the existence of hidden parameters in the relation. For example, a measure of the galactic radius (effective, or exponential scale length) has been investigated by some authors to test for correlations with TFR residuals (e.g. McGaugh, 2005; Pizagno et al., 2005; Gnedin et al., 2007; Zaritsky et al., 2014; Lelli, McGaugh, & Schombert, 2016b). The radius, together with mass, determines the rotation curve (e.g. Equation (2.10)). Adopting the local slopes, we do not find significant correlations (based on Spearman tests) of the TFR residuals with R_e, B/T, n_{S}, stellar or baryonic mass surface density, offset from the main sequence or the mass-radius relation, SFR surface density Σ_{SFR}, or inclination. In Appendix 2.9 we investigate how the uncertainties in stellar and baryonic mass affect second-order parameter dependencies for TFR fits with free slopes, by example of R_e and Σ_{SFR}.

In summary, we find well defined mass-based TFRs at $0.6 < z < 2.6$ for our sample. If galaxies with underestimated peak velocity, dispersion-dominated and disturbed galaxies are included, the TFR zero-points are increasing, and also the scatter increases, especially towards lower velocities and masses. Adopting the local slopes, we find no correlation of TFR residuals with independent galaxy properties.

2.3.3 TFR evolution from $z \sim 2.3$ to $z \sim 0.9$

We now turn to the TFR subsamples at $z \sim 0.9$ and $z \sim 2.3$. We adopt the local slopes by Reyes et al. (2011) and Lelli, McGaugh, & Schombert (2016b) to investigate the zero-point evolution. Our redshift subsamples are shown in

Figure 2.5 for the sTFR (left) and bTFR (right), together with the corresponding local relations and the respective fixed-slope fits. The parameters of each fit are given in Table 2.2.

For the sTFR we find no indication for a significant change in zero-point between $z \sim 0.9$ and $z \sim 2.3$ within the best fit uncertainties. Using the local slope of $a = 3.60$ and the reference value $v_{\rm ref} = 242$ km/s, we find a zero-point of $b = 10.49 \pm 0.04$ for the subsample at $z \sim 0.9$, and of $b = 10.51 \pm 0.05$ for the subsample at $z \sim 2.3$, translating into a zero-point evolution of $\Delta b = 0.02$ dex between $z \sim 0.9$ and $z \sim 2.3$.

For the bTFR, however, using the local slope of $a = 3.75$, and again the reference value $v_{\rm ref} = 242$ km/s, we find a positive zero-point evolution between $z \sim 0.9$ and $z \sim 2.3$, with $b = 10.68 \pm 0.04$ and $b = 10.85 \pm 0.05$, respectively, translating into a zero-point evolution of $\Delta b = 0.17$ dex between $z \sim 0.9$ and $z \sim 2.3$.

If we consider the 'first order' TFR subsamples at $z \sim 0.9$ and $z \sim 2.3$, we find significantly different zero-point evolutions of $\Delta b_{\rm sTFR} = 0.23$ dex and $\Delta b_{\rm bTFR} = 0.28$ dex between $z \sim 0.9$ and $z \sim 2.3$. Again, this highlights the importance of a careful sample selection for TFR studies. Figure 2.9 shows that if instead we extend our data set to the sample from Wuyts et al. (2016b), we find qualitatively the same trends as for the adopted TFR sample, namely an evolution of $\Delta b_{\rm sTFR} = 0.05$ dex and $\Delta b_{\rm bTFR} = 0.20$ dex for the zero-point between $z \sim 0.9$ and $z \sim 2.3$ (see Appendix 2.7). Also, if we consider only TFR galaxies with $B/T > 0.1 (< 0.1)$, our qualitative results remain the same.

In summary, we find no evolution for the sTFR, but a positive evolution of the bTFR between $z \sim 0.9$ and $z \sim 2.3$. If galaxies with underestimated peak velocity, dispersion-dominated and disturbed galaxies are included, we find positive evolution of both the sTFR and the bTFR.

Table 2.2: *Results from the inverse linear regression fits to Equation* (2.2) *using the least-squares method, including bootstrapped errors of the zero-point. The reference velocity is* $v_{\text{ref}} = 242$ *km/s.*

TFR	redshift range	number of galaxies	slope a (local relation) $\left[\frac{\log(M\ [M_\odot])}{\log(v_{\text{circ}}\ [\text{km/s}])}\right]$	zero-point b (error) $[\log(M\ [M_\odot])]$	intrinsic scatter ζ_{int} [dex of $M_\odot$]
sTFR	$0.6 < z < 2.6$	135	3.60 (Reyes et al., 2011)	10.50 (±0.03)	0.22
	$z \sim 0.9$	65	3.60 (Reyes et al., 2011)	10.49 (±0.04)	0.21
	$z \sim 2.3$	46	3.60 (Reyes et al., 2011)	10.51 (±0.05)	0.26
bTFR	$0.6 < z < 2.6$	135	3.75 (Lelli, McGaugh, & Schombert, 2016b)	10.75 (±0.03)	0.23
	$z \sim 0.9$	65	3.75 (Lelli, McGaugh, & Schombert, 2016b)	10.68 (±0.04)	0.22
	$z \sim 2.3$	46	3.75 (Lelli, McGaugh, & Schombert, 2016b)	10.85 (±0.05)	0.26

2.3.4 Comparison to other high$-z$ studies

At $z \sim 0.9$ we compare our sTFR (65 KMOS^{3D} galaxies) to the work by Tiley et al. (2016) and Miller et al. (2011). Tiley et al. (2016) have investigated the sTFR at $z \sim 0.9$ using 56 galaxies from the KROSS survey with KMOS (Stott et al., 2016). Miller et al. (2011, 2012) have presented an extensive slit-based sTFR study at $0.2 < z < 1.7$ with 37 galaxies at $z \sim 1$. From Tiley et al. (2016), we use their best fixed-slope fit to their disky subsample ($a = 3.68$). From Miller et al. (2011), we use the $z \sim 1$ fit corresponding to total stellar mass and $v_{\mathrm{rot},3.2}$ ($a = 3.78$). For a sTFR comparison at $z \sim 2.3$ (46 KMOS^{3D} galaxies), we consider the work by Cresci et al. (2009). The authors have studied the sTFR at $z \sim 2.2$ for 14 galaxies from the SINS survey ($a = 4.5$). Despite the small sample size, the high-quality data based on the 2D modelling of velocity and velocity dispersion maps qualify the sample for comparison with our findings in the highest redshift bin.

In the following, we use $v_{\mathrm{rot,max}}$ to ensure a consistent comparison with the measurements presented in these studies. For a comparison with the literature data, we make the simplifying assumption that $v_{\mathrm{rot,max}}$ is comparable to $v_{\mathrm{rot},80}$ and $v_{\mathrm{rot},3.2}$ (see Section 2.4.3.3 for a discussion). We adopt the slopes reported in the selected studies to guarantee consistency in the determination of zero-point offsets. The results are shown in Figure 2.6 as dashed lines, while the original relations from the literature are shown as solid lines. The difference in zero-points, Δb, is then computed as the zero-point from the KMOS^{3D} fixed-slope fit minus the zero-point from the literature. Given the typical zero-point uncertainty of our fits of $\delta b \approx 0.05$ dex, our results are in agreement with Tiley et al. (2016) ($\Delta b = 0.06$) and Cresci et al. (2009) ($\Delta b = 0.07$), but in disagreement with Miller et al. (2011) at $z \sim 1$ ($\Delta b = -0.31$). We further note that our findings are in disagreement with the recent study by Di Teodoro, Fraternali, & Miller (2016) who employed a tilted ring model on a small subset of galaxies from the KMOS^{3D} and KROSS surveys at $z \sim 1$ ($\Delta b = -0.34$; see also Tiley et al., 2016).

A number of complications might give rise to conflicting results of different TFR studies, such as the use of various kinematic models, velocity tracers, mass estimates, or statistical methods. Tiley et al. (2016), who present an extensive comparison of several sTFR studies from the literature, argue that conflicting results regarding the zero-point evolution with redshift depend on the ability of the studies to select for rotationally supported systems. The two-dimensional information on the velocity and velocity dispersion fields is a major advantage of IFS observations as it allows for the robust determination of the kinematic center and major axis.

We test the case of selecting against dispersion-dominated or disturbed systems for our TFR samples. For the full sample of 240 SFGs by Wuyts et al. (2016b), which includes some dispersion-dominated systems and cases where the peak rotation velocity might be underestimated by the model, we indeed find that

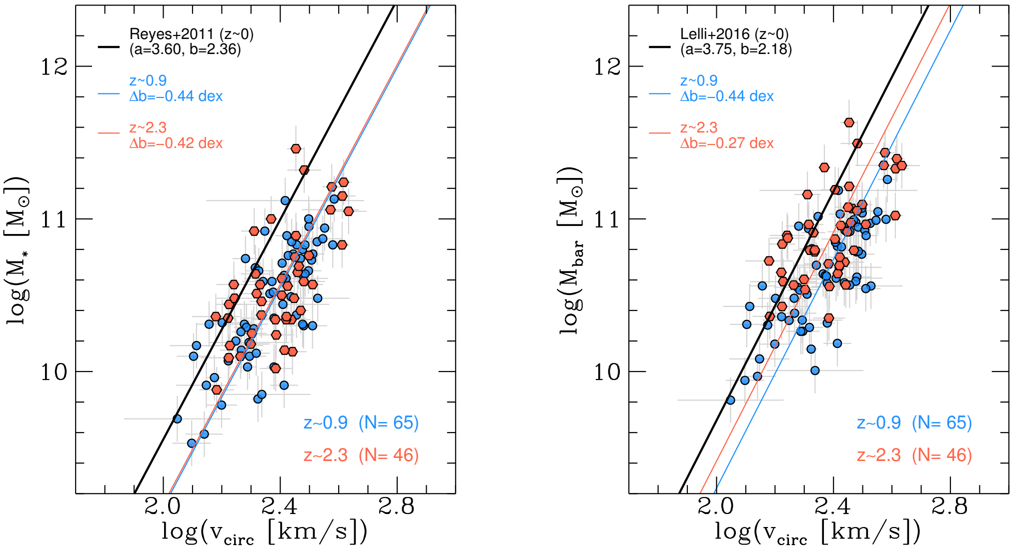

Figure 2.5: *Fixed-slope fits for the sTFR (left) and the bTFR (right) using local (black) slopes to our KMOS^{3D} subsamples at $z \sim 0.9$ (blue) and $z \sim 2.3$ (red). For the local relations, we give a and b corresponding to our adopted functional form of the TFR give in Equation (2.2), with log($v_{\rm ref}$ [km/s])=0. For the sTFR, we find no (or only marginal) evolution of the sTFR zero-point in the studied redshift range. Comparing to the local relation by Reyes et al. (2011) we find $\Delta b = -0.44$ and -0.42 dex at $z \sim 0.9$ and $z \sim 2.3$, respectively. For the bTFR, we find a positive evolution of the zero-point between $z \sim 0.9$ and $z \sim 2.3$. Comparing to the local relation by Lelli, McGaugh, & Schombert (2016b) we find $\Delta b = -0.44$ and -0.27 dex at $z \sim 0.9$ and $z \sim 2.3$, respectively.*

the difference in zero-point, Δb, with Miller et al. (2011) shrinks by ~ 30 per cent. If we now even turn to the purely observational ‘first order sTFR’, this time using only the $z < 1.3$ galaxies (122 SFGs) and the $v_{\rm rot,max}$ tracer, we find agreement to Miller et al. (2011) ($\Delta b = 0.02$). Again, we caution that this ‘first order’ sample contains not only dispersion-dominated and merging galaxies, but also galaxies for which the maximum velocity is underestimated. This exercise supports the interpretation that the disagreement with Miller et al. (2011) is partly due to our selection of rotation-dominated systems. Beam-smearing corrections could lead to effects of comparable order, as is discussed in more detail in Appendix 2.7 and explicitly shown in Figure 2.8.

The high$-z$ evolution of the bTFR has received less attention in the literature. At intermediate redshift ($z \sim 1.2$), Vergani et al. (2012) found no evolution of the bTFR when comparing to the local relation by McGaugh (2005). We compare our results to the slit-based relation at $z \sim 2$ by Price et al. (2016) using galaxies from the MOSDEF survey (Kriek et al., 2015). Price et al. (2016) use the $S_{0.5} =$

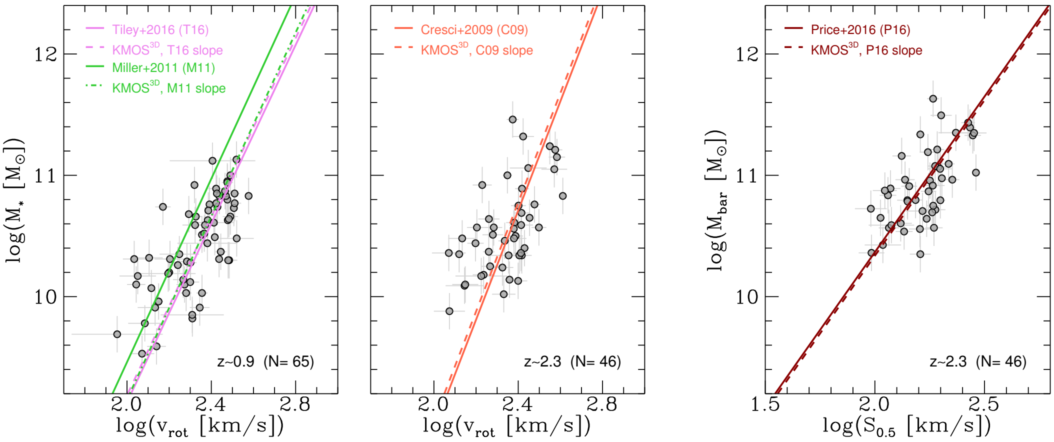

Figure 2.6: Left and middle panel: *the* $v_{\rm rot}$*-sTFRs at* $z \sim 0.9$ *(left panel) and* $z \sim 2.3$ *(middle panel). We show fits from Tiley et al. (2016) (*$z \sim 0.9$*; magenta), Miller et al. (2011) (*$z \sim 1$*; green) and Cresci et al. (2009) (*$z \sim 2.2$*; orange) as solid lines, together with corresponding fixed-slope fits to our samples as dashed lines. From Tiley et al. (2016), we use their best fixed-slope fit to their disky subsample. From Miller et al. (2011), we use the* $z \sim 1$ *fit corresponding to total stellar mass and* $v_{\rm rot,3.2}$*. Our findings regarding the zero-point offset are in agreement with Tiley et al. (2016) and Cresci et al. (2009), but in disagreement with Miller et al. (2011).* **Right panel:** *the* $S_{0.5}$*-bTFR at* $z \sim 2.3$*. We show the fit from Price et al. (2016) (*$z \sim 2$*; red) as a solid line, together with the corresponding fixed-slope fit to our sample as a dashed line. Our findings regarding the zero-point offset are in agreement.*

$(0.5 \cdot v_{\rm rot}^2 + \sigma_g^2)^{1/2}$ velocity tracer, which also incorporates dynamical support from disordered motions based on the assumption of isotropic (or constant) gas velocity dispersion σ_g (Weiner et al., 2006; Kassin et al., 2007). Price et al. (2016) show a plot of the $S_{0.5}-$bTFR of 178 SFGs, of which 35 (15) have detected (resolved) rotation measurements. For resolved galaxies, $S_{0.5}$ is obtained through combining a constant intrinsic velocity dispersion, and $v_{\rm rot,2.2}$. For unresolved galaxies, Price et al. (2016) estimate $S_{0.5}$ through an rms velocity (see their Appendix B for details). We use their fixed-slope fit ($a = 1/0.39$) to compare their results to our 46 KMOS^{3D} galaxies at $z \sim 2.3$ in the right panel of Figure 2.6. Our fixed-slope fit is in agreement with the result by Price et al. (2016) ($\Delta b = -0.03$). This is surprising at first, given the above discussion of IFS vs. slit-based rotation curve measurements, and the fact that the Price et al. (2016) sample contains a large fraction of objects without detected rotation. However, Price et al. (2016) state that their findings regarding the S$_{0.5}$-bTFR do not change if they consider only the galaxies with detected rotation measurements. This is likely due to the detailed modelling and well-calibrated translation of line width to rotation velocity by the authors. In general, any combination of velocity dispersion and velocity into a joined measure is expected to bring turbulent and even dispersion-dominated galaxies closer together in TFR space, which might further serve as an explanation for this good agreement (see also Covington et al., 2010).[6]

In summary, our inferred $v_{\rm rot}$-sTFR zero-points (i.e., not corrected for pressure support) agree with the work by Cresci et al. (2009) and Tiley et al. (2016), but disagree with the work by Miller et al. (2011). Our $S_{0.5}$-bTFR zero-point agrees with the result by Price et al. (2016). We emphasize that the negligence of turbulent motions in the balance of forces leads to a relation which has lost its virtue to directly connect the baryonic kinematics to the central potential of the halo.

2.4 TFR evolution in context

2.4.1 Dynamical support of SFGs from $z \sim 2.3$ to $z \sim 0.9$

At fixed $v_{\rm circ}$, our sample shows higher $M_{\rm bar}$ and similar M_* at $z \sim 2.3$ as compared to $z \sim 0.9$ (Figure 2.5). Galactic gas fractions are strongly increasing with redshift, as it has become clear in the last few years (Tacconi et al., 2010; Daddi et al., 2010; Combes et al., 2011; Genzel et al., 2015; Tacconi et al., 2018). In our TFR sample, the baryonic mass of the $z \sim 2.3$ galaxies is on average a factor of two larger as compared to $z \sim 0.9$, while stellar masses are comparable. The relative offset at fixed $v_{\rm circ}$ of our redshift subsamples in the bTFR plane, which is not visible in the sTFR plane, confirms the relevance of gas at high redshift.

Building on the recent work by Wuyts et al. (2016b) on the mass budgets of high$-z$ SFGs, we can identify through our Tully-Fisher analysis another redshift-dependent ingredient to the dynamical support of high$-z$ SFGs. The sTFR zero-point does not evolve significantly between $z \sim 2.3$ and $z \sim 0.9$. Since we know that there is less gas in the lower$-z$ SFGs, the 'missing' baryonic contribution to the dynamical support of these galaxies as compared to $z \sim 2.3$ has to be compensated by DM. We therefore confirm with our study the increasing importance of DM to the dynamical support of SFGs (within $\sim 1.3\,R_e$) through cosmic time. This might be partly due to the redshift dependence of the halo concentration parameters, which decrease with increasing redshift. In the context of the toy model mentioned in Section 2.1, it is indeed the case that a decrease of the DM fraction as probed by the central galaxy with increasing redshift can flatten out or even reverse the naively expected, negative evolution of the TFR offset with increasing redshift. This will be discussed in more detail in Section 2.5.

---

[6] Partly, this is also the case for the measurements by Miller et al. (2011, 2012), if a correction for turbulent pressure support is performed. Since their velocity dispersions are not available to us, however, only an approximative comparison is feasible. From this, we found agreement of their highest redshift bin ($z \sim 1.5$) with our $0.6 < z < 2.6$ data in the $v_{\rm circ}$-sTFR plane, but still a significant offset at $z \sim 1$.

The increase of baryon fractions with redshift is supported by other recent work: Wuyts et al. (2016b) find that the baryon fractions of SFGs within R_e increase from $z \sim 1$ to $z \gtrsim 2$, with galaxies at higher redshift being clearly baryon-dominated (see also Förster Schreiber et al., 2009; Alcorn et al., 2016; Price et al., 2016; Burkert et al., 2016; Stott et al., 2016; Contini et al., 2016). Wuyts et al. (2016b) also find that the baryonic mass fractions are correlated with the baryonic surface density within R_e, suggesting that the lower surface density systems at lower redshift are more diffuse and therefore probe further into the halo (consequently increasing their DM fraction). Most recently, Genzel et al. (2017) find in a detailed study based on the outer rotation curves of six massive SFGs at $z = 0.9 - 2.4$ that the three $z > 2$ galaxies are most strongly baryon-dominated. On a statistical basis, this is confirmed through stacked rotation curves of more than 100 high$-z$ SFGs by Lang et al. (2017).

Given the average masses of our galaxies in the YJ and K subsamples, we emphasize that we are generally not tracing a progenitor-descendant population in our sample, since the average stellar and baryonic masses of the $z \sim 2.3$ galaxies are already higher than for those at $z \sim 0.9$ (Table 2.1). It is very likely that a large fraction of the massive star-forming disk galaxies we observe at $z \gtrsim 1$ have evolved into early-type galaxies (ETGs) by $z = 0$, as discussed in the recent work by Genzel et al. (2017). Locally, there is evidence that ETGs have high SFRs at early times, with the most massive ETGs forming most of their stars at $z \gtrsim 2$ (e.g. Thomas, 2010; McDermid et al., 2015). This view is supported by co-moving number density studies (e.g. Brammer et al., 2011), which also highlight that the mass growth of today's ETGs after their early and intense SF activity is mainly by the integration of (stellar) satellites into the outer galactic regions (van Dokkum et al., 2010). The observed low DM fractions of the massive, highest$-z$ SFGs seem to be consistent with the early assembly of local ETGs, with rapid incorporation of their baryon content. In future work, we will compare our observations to semi-analytical models and cosmological zoom-in simulations to investigate in greater detail the possible evolutionary scenarios of our observed galaxies in the context of TFR evolution.

2.4.2 Comparison to the local Universe

In Figure 2.5 we show the TFR zero-point evolution in context with the recent local studies by Reyes et al. (2011) for the sTFR, and by Lelli, McGaugh, & Schombert (2016b) for the bTFR. Reyes et al. (2011) study the sTFR for a large sample of 189 disk galaxies, using resolved Hα rotation curves. Lelli, McGaugh, & Schombert (2016b) use resolved HI rotation curves and derive a bTFR for 118 disk galaxies. To compare these local measurements to our high$-z$ KMOS^{3D} data, we assume that at $z \approx 0$ the contribution from turbulent motions to the dynamical support of the galaxy is negligible, and therefore $v_{\rm circ} \equiv v_{\rm rot}$. We make the simplifying assumption that $v_{\rm circ}$ is comparable to v_{80} and $v_{\rm flat}$ used by Reyes et al. (2011) and Lelli, McGaugh, & Schombert (2016b), respectively (see Section 2.4.3.3 for a discussion). From Lelli, McGaugh, & Schombert (2016b), we use the fit to their subsample of 58 galaxies with the most accurate distances (see their classification).

For the sTFR as well as the bTFR we find significant offsets of the high$-z$ relations as compared to the local ones, namely $\Delta b_{\rm sTFR,z\sim0.9} = -0.44$, $\Delta b_{\rm sTFR,z\sim2.3} = -0.42$, $\Delta b_{\rm bTFR,z\sim0.9} = -0.44$ and $\Delta b_{\rm bTFR,z\sim2.3} = -0.27$. We have discussed in SectionSection 2.3.2 and 2.3.3 the zero-points of the 'first order' TFRs as compared to our fiducial TFRs: while there is significant offset for both the 'first order' sTFR and bTFR when comparing the $z \sim 0.9$ and the $z \sim 2.3$ subsamples, the overall offset to the local relations is reduced. The difference between the local relations and the full 'first order' samples is only $\Delta b_{\rm sTFR} = -0.06$ and $\Delta b_{\rm bTFR} = 0.02$, which would be consistent with no or only marginal evolution of the TFRs between $z = 0$ and $0.6 < z < 2.3$.

For the interpretation of the offsets to the local relations, it is important to keep in mind that we measure the TFR evolution at the typical fixed circular velocity of galaxies in our high$-z$ sample. This traces the evolution of the TFR itself through cosmic time, not the evolution of individual galaxies. Our subsamples at $z \sim 0.9$ and $z \sim 2.3$ are representative of the population of massive MS galaxies observed at those epochs, with the limitations as discussed in Section 2.2.4. Locally, however, the *typical* disk galaxy has lower circular velocity than our adopted reference velocity, and consequently lower mass (cf. e.g. Figure 1 by Courteau & Dutton, 2015). Figure 2.5 does therefore not indicate how our galaxies will evolve on the TFR from $z \sim 2$ to $z \sim 0$, but rather shows how the relation itself evolves, as defined through the population of disk galaxies at the explored redshifts and mass ranges. This is also apparent if actual data points of low- and high-redshift disk galaxies are shown together. We show a corresponding plot for the bTFR in Appendix 2.8.

In summary, our results suggest an evolution of the TFR with redshift, with zero-point offsets as compared to the local relations of $\Delta b_{\rm sTFR,z\sim0.9} = -0.44$, $\Delta b_{\rm sTFR,z\sim2.3} = -0.42$, $\Delta b_{\rm bTFR,z\sim0.9} = -0.44$ and $\Delta b_{\rm bTFR,z\sim2.3} = -0.27$. If galaxies with underestimated peak velocity, dispersion-dominated and disturbed galaxies are included, the overall evolution between the $z = 0$ and $0.6 < z < 2.6$ samples is insignificant.

2.4.3 The impact of uncertainties and model assumptions on the observed TFR evolution

Before we interpret our observed TFR evolution in a cosmological context in Section 2.5, we discuss in the following uncertainties and modelling effects related to our data and methods. We find that uncertainties of mass estimates and velocities cannot explain the observed TFR evolution. Neglecting the impact of turbulent motions, however, could explain some of the tension with other work.

2.4.3.1 Uncertainties of stellar and baryonic masses

A number of approximations go into the determination of stellar and baryonic masses at high redshift. Simplifying assumptions like a uniform metallicity, a single IMF, or an exponentially declining SFH introduce significant uncertainties to the stellar age, stellar mass, and SFR estimates of high$-z$ galaxies. While the stellar mass estimates appear to be more robust against variations in the model assumptions, the SFRs, which are used for the molecular gas mass calculation, are affected more strongly (see e.g. Förster Schreiber et al., 2004; Shapley et al., 2005; Wuyts et al., 2007, 2009, 2016b; Maraston et al., 2010; Mancini et al., 2011, for detailed discussions about uncertainties and their dependencies). Most systematic uncertainties affecting stellar masses tend to lead to underestimates; if this were the case for our high$-z$ samples, the zero-point evolution with respect to local samples would be overestimated. However, the dynamical analysis by Wuyts et al. (2016b) suggests that this should only be a minor effect, given the already high baryonic mass fractions at high redshift.

An uncertainty in the assessment of gas masses at high redshift is the unknown contribution of atomic gas. In the local Universe, the gas mass of massive galaxies is dominated by atomic gas: for stellar masses of $\log(M_* \; [M_\odot]) \approx 10.5$, the ratio of atomic to molecular hydrogen is roughly $M_{\text{HI}}/M_{\text{H}_2} \sim 3$ (e.g. Saintonge et al., 2011). While there are currently no direct galactic HI measurements available at high redshift,[7] a saturation threshold of the HI column density of only $\lesssim 10\,M_\odot/\text{pc}^2$ has been determined empirically for the local Universe (Bigiel & Blitz, 2012). The much higher gas surface densities of our high$-z$ SFGs therefore suggest a negligible contribution from atomic gas within $r \lesssim R_e$ (see also Wuyts et al., 2016b). Consequently, the contribution of atomic gas to the maximum rotation velocity and to the mass budget within this radius should be negligible. However, there is evidence that locally HI disks are much more extended than optical disks (e.g. Broeils & Rhee, 1997). If this is also true at high redshift, the total galactic HI mass fractions could still be significant at $z \sim 1$, as is predicted by theoretical models (e.g. Lagos et al., 2011; Fu et al., 2012; Popping et al., 2015). Due to the lack of empirical confirmation, however, these models yet remain uncertain, especially given that they under-predict the observed high$-z$

---

[7] But see e.g. Wolfe, Gawiser, & Prochaska (2005); Werk et al. (2014) for measurements of HI column densities of the circum- and intergalactic medium using quasar absorption lines. From these techniques, a more or less constant *cosmological* mass density of neutral gas since at least $z \sim 3$ is inferred (e.g. Péroux et al., 2005; Noterdaeme et al., 2009). Recently, the need for a significant amount of non-molecular gas in the haloes of high$-z$ galaxies has also been invoked by the environmental study of the 3D-HST fields by Fossati et al. (2017).

molecular gas masses by factors of $2-5$. Within these limitations, we perform a correction for missing atomic gas mass at high$-z$ in our toy model discussion in Section 2.5.

Following Burkert et al. (2016), we have adopted uncertainties of 0.15 dex for stellar masses, and 0.20 dex for gas masses. This translates into an average uncertainty of ~ 0.15 dex for baryonic masses. These choices likely underestimate the systematic uncertainties in the error budget which can have a substantial impact on some of our results, because the slope as well as the scatter of the TFR are sensitive to the uncertainties. For the presentation of our main results, we adopt local TFR slopes, thus mitigating these effects. In Appendix 2.9, we explore the effect of varying mass uncertainties on free-slope fits of the TFR, together with implications on TFR residuals and evolution. We find that measurements of the zero-point are little affected by the uncertainties on mass, to an extent much smaller than the observed bTFR evolution between $z \sim 2.3$ and $z \sim 0.9$.

2.4.3.2 Uncertainties of circular velocities

We compute the uncertainties of the maximum circular velocity as the propagated errors on the *observed* velocity and σ_0, including an uncertainty on q of $\sim$ 20 per cent. The latter is a conservative choice in the light of the current KMOS$^{\rm 3D}$ magnitude cut of $Ks < 23$ (cf. van der Wel et al., 2012). For details about the observed quantities, see Wisnioski et al. (2015), and Wuyts et al. (2016b) for a comparison between observed and modelled velocities and velocity dispersions. The resulting median of the propagated circular velocity uncertainty is 20 km/s.

Maximum circular velocities can be systematically underestimated: although the effective radius enters the modelling procedure as an independent constraint, the correction for pressure support can lead to an underestimated turn-over radius if the true turn-over radius is not covered by observations. For our TFR sample we selected only galaxies where modelled and observed velocity and dispersion profiles are in good agreement, and where the maximum or flattening of the rotation curve is covered by observations. It is therefore unlikely that our results based on the TFR sample are affected by systematic uncertainties of the maximum circular velocity.

2.4.3.3 Effects related to different velocity measures and models

The different rotation velocity models and measures used in the literature might affect comparisons between different studies. Some TFR studies adopt the rotation velocity at 2.2 times R_d, $v_{2.2}$, as their fiducial velocity to measure the TFR. We verified that for the dynamical modelling as described above, $v_{\rm circ,2.2}$ equals $v_{\rm circ,max}$, and $v_{\rm rot,2.2}$ equals $v_{\rm rot,max}$ with an average accuracy of $\lesssim 1$ km/s. Other commonly used velocity measures are $v_{\rm flat}$, $v_{3.2}$, and v_{80}, the rotation velocity at the radius which contains 80 per cent of the stellar light. For a pure exponential disk, this corresponds to roughly $v_{3.0}$ (Reyes et al., 2011). It has been shown by Hammer et al. (2007) that v_{flat} and v_{80} are comparable in local galaxies. For the exponential disk model including pressure support which we use in our analysis, $v_{\mathrm{rot(circ),max}}$ is on average $\lesssim 15(10)$ km/s larger than $v_{\mathrm{rot(circ)},3.2}$. Since $v_{3.2}$ and v_{80} are, however, usually measured from an 'arctan model' with an asymptotic maximum velocity (Courteau, 1997), reported values in the literature generally do *not* correspond to the respective values at these radii from the thick exponential disk model with pressure support. Miller et al. (2011) show that for their sample of SFGs at $0.2 < z < 1.3$, the typical difference between $v_{2.2}$ and $v_{3.2}$, as computed from the arctan model, is on the order of a few per cent (see also Reyes et al., 2011). This can also be assessed from Figure 6 by Epinat et al. (2010), who show examples of velocity fields and rotation curves for different disk models (exponential disk, isothermal sphere, 'flat', arctan). By construction, the peak velocity of the exponential disk is higher than the arctan model rotation velocity at the corresponding radius.

We conclude that our TFR 'velocity' values derived from the peak rotation velocity of a thick exponential disk model are comparable to v_{flat}, and close to $v_{3.2}$ and v_{80} from an arctan model, with the limitations outlined above. The possible systematic differences of < 20 km/s between the various velocity models and measures cannot explain the observed evolution between $z = 0$ and $0.6 < z < 2.6$.

Another effect on the shape of the velocity and velocity dispersion profiles is expected if contributions by central bulges are taken into account. We have tested for a sample of more than 70 galaxies that the effect of including a bulge on our adopted velocity tracer, $v_{\mathrm{circ,max}}$ is on average no larger than 5 per cent. From our tests, we do not expect the qualitative results regarding the TFR evolution between $z \sim 2.3$ and $z \sim 0.9$ presented in this paper to change if we include bulges into the modelling of the mass distribution.

2.4.3.4 The impact of turbulent motions

The dynamical support of star-forming disk galaxies can be quantified through the relative contributions from ordered rotation and turbulent motions (see also e.g. Tiley et al., 2016). We consider only rotation-dominated systems in our TFR analysis, namely galaxies with $v_{\mathrm{rot,max}}/\sigma_0 > \sqrt{4.4}$. Because of this selection, the effect of σ_0 on the velocity measure is already limited, with median values of $v_{\mathrm{rot,max}} = 233$ km/s at $z \sim 0.9$, and 239 km/s at $z \sim 2.3$, *vs.* median values of $v_{\mathrm{circ,max}} = 239$ and $v_{\mathrm{circ,max}} = 260$ km/s at $z \sim 0.9$ and $z \sim 2.3$, respectively (Table 2.1).

However, this difference translates into changes regarding e.g. the TFR scatter: for the $v_{\mathrm{rot,max}}$-TFR, we find a scatter of $\zeta_{\mathrm{int,sTFR}} = 0.28$ and $\zeta_{\mathrm{int,bTFR}} = 0.31$ at $z \sim 0.9$, and at $z \sim 2.3$ we find $\zeta_{\mathrm{int,sTFR}} = 0.33$ and $\zeta_{\mathrm{int,bTFR}} = 0.33$, with those values being consistently higher than the values reported for the $v_{\rm circ,max}$-TFR sample in Table 2.2. More significantly, neglecting the contributions from turbulent motions affects the zero-point evolution: without correcting $v_{\rm rot,max}$ for the effect of pressure support, we would find $\Delta b_{\rm sTFR,z\sim0.9} = -0.34$, $\Delta b_{\rm sTFR,z\sim2.3} = -0.26$, $\Delta b_{\rm bTFR,z\sim0.9} = -0.33$ and $\Delta b_{\rm bTFR,z\sim2.3} = -0.09$. The inferred zero-points at higher redshift are affected more strongly by the necessary correction for pressure support (cf. Figure 2.5).

These results emphasize the increasing role of pressure support with increasing redshift, confirming previous findings by e.g. Förster Schreiber et al. (2009); Epinat et al. (2009); Kassin et al. (2012); Wisnioski et al. (2015). It is therefore clear that turbulent motions must not be neglected in kinematic analyses of high$-z$ galaxies. If the contribution from pressure support to the galaxy dynamics is dismissed, this will lead to misleading conclusions about TFR evolution in the context of high$-z$ and local measurements.

2.5 A toy model interpretation

The relative comparison of our $z \sim 2.3$ and $z \sim 0.9$ data and local relations indicates a non-monotonic evolution of the bTFR zero-point with cosmic time (Figure 2.5). In this section, we present a toy model interpretation of our results, aiming to explain the redshift evolution of both the sTFR and the bTFR, in particular the relative zero-point offsets at $z \sim 2.3$, $z \sim 0.9$, and $z \sim 0$.

The basic premise is that galaxies form at the centers of DM haloes. A simple model for a DM halo in approximate equilibrium is a truncated isothermal sphere, limited by the radius R_h where the mean density equals 200 times the critical density of the Universe. The corresponding redshift-dependent relations between halo radius, mass M_h, and circular velocity V_h are

$$M_h = \frac{V_h^3}{10G \cdot H(z)} \quad ; \quad R_h = \frac{V_h}{10H(z)} \tag{2.3}$$

(Mo, Mao, & White, 1998), where $H(z)$ is the Hubble parameter, and G is the gravitational constant. The first equation shows that the relation between M_h and V_h is a smooth function of redshift.

In theory, the relation between these halo properties and corresponding galactic properties can be complex due to the response of the halo to the formation of the central galaxy (see e.g. the discussions on halo contraction *vs.* expansion by Duffy et al., 2010; Dutton et al., 2016; Velliscig et al., 2014). However, recent studies and modelling of high$-z$ SFGs now provide a number of empirical constraints that implicitly contain information on the DM halo profile on galactic scales.

Relations corresponding to Equations (2.3) for the central baryonic galaxy can then be derived by assuming a direct mapping between the halo and galaxy mass and radius. Information on the inner halo profile is contained in parameters such as the disk mass fraction $m_d = M_{\rm bar}/M_h$, or the central DM fraction $f_{\rm DM}(r) = v^2_{\rm DM}(r)/v^2_{\rm circ}(r)$. For our galaxies, we know their stellar mass M_* and effective radius R_e, their baryonic mass $M_{\rm bar}$ and gas mass fraction $f_{\rm gas} = M_{\rm gas}/M_{\rm bar}$ from empirical scaling relations, and their circular velocity $v_{\rm circ}(r)$ and related central DM fraction $f_{\rm DM}(r)$ from dynamical modelling, as detailed in Sections 2.2.2 and 2.2.3 and in the references given there. We further have an estimate of their average baryonic disk mass fraction m_d (Burkert et al., 2016). We can combine this information to construct a toy model of the TFR zero-point evolution, where we take the redshift dependencies of these various parameters into account (see Appendix 2.10.1 for a detailed derivation):

$$M_{\rm bar} = \frac{v^3_{\rm circ}(R_e)}{H(z)} \cdot \frac{[1 - f_{\rm DM}(R_e,z)]^{3/2}}{m_d^{1/2}(z)} \cdot C \tag{2.4}$$

$$M_* = \frac{v^3_{\rm circ}(R_e)}{H(z)} \cdot \frac{[1 - f_{\rm DM}(R_e,z)]^{3/2}\,[1 - f_{\rm gas}(z)]}{m_d^{1/2}(z)} \cdot C', \tag{2.5}$$

where C and C' are constants. Here, we have assumed that, in contrast to the disk mass fraction, the proportionality factor between DM halo radius and galactic radius is independent of redshift (see e.g. Burkert et al., 2016).

Equations (2.4) and (2.5) reveal that the TFR evolution can be strongly affected by changes of $f_{\rm DM}(R_e)$, m_d, or $f_{\rm gas}$ with redshift, and does not necessarily follow the smooth evolution of the halo parameters given in Equation (2.3). There have been indications for deviations from a simple smooth TFR evolution scenario in the theoretical work by Somerville et al. (2008). Also the recent observational compilation by Swinbank et al. (2012b) showed a deviating evolution (although qualified as consistent with the smooth evolution scenario).

Evaluating Equations (2.4) and (2.5) at fixed $v_{\rm circ}(R_e)$, we learn the following: (i) if $f_{\rm DM}(R_e)$ decreases with increasing redshift, the baryonic and stellar mass will increase and consequently the TFR zero-point will increase; (ii) if m_d increases with increasing redshift, the baryonic and stellar mass will decrease and consequently the TFR zero-point will decrease; (iii) if $f_{\rm gas}$ increases with increasing redshift, the stellar mass will decrease and consequently the sTFR zero-point will decrease. These effects are illustrated individually in Figure 2.14 in Appendix 2.10.

We constrain our toy model at redshifts $z = 0$, $z \sim 0.9$, and $z \sim 2.3$ as follows: the redshift evolution of $f_{\rm gas}$ is obtained through the empirical atomic and molecular gas mass scaling relations by Saintonge et al. (2011) and Tacconi et al. (2018). At fixed circular velocity, $f_{\rm gas}$ evolves significantly with redshift, where

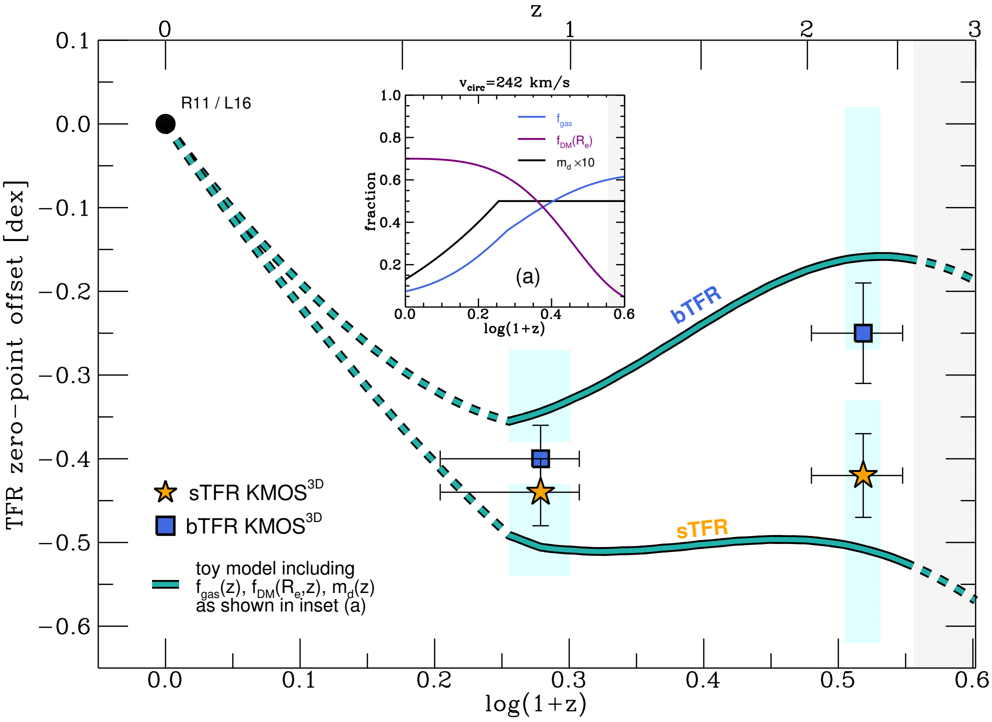

Figure 2.7: *TFR zero-point offsets of the stellar and baryonic mass TFRs as a function of cosmic time. The KMOS*^{3D} *data is shown as yellow stars (sTFR) and blue squares (bTFR), in relation to the corresponding local normalizations by Reyes et al. (2011; R11) and Lelli, McGaugh, & Schombert (2016b; L16). The horizontal error bars of the KMOS*^{3D} *data points indicate the spanned range in redshift, while the vertical error bars show fit uncertainties. The bTFR data points are corrected for neglected atomic gas at* $z \sim 0.9$ *and* $z \sim 2.3$*, as detailed in the main text. The green dashed and solid lines show predictions for the bTFR and sTFR evolution from our toy model (Equations* (2.4) *and* (2.5)*). This model takes into account the empirically motivated redshift dependencies of* $f_{\rm gas}$, $f_{\rm DM}(R_e)$*, and* m_d*, in particular as they are shown in inset (a). Regions in redshift space where the model is not well constrained due to a lack of observational constraints in particular on* m_d *are indicated as dashed lines. Observational constraints come from Saintonge et al. (2011) and Tacconi et al. (2018) for* $f_{\rm gas}(z)$*, from Martinsson et al. (2013a,b) and Wuyts et al. (2016b) for* $f_{\rm DM}(R_e, z)$*, and from Moster, Naab, & White (2013) and Burkert et al. (2016) for* $m_d(z)$*, as detailed in Appendix 2.10.2. Our proposed parametrizations are valid only up to* $z \approx 2.6$*, as indicated by the grey shading in the main figure and inset (a). As cyan shaded areas we indicate by way of example how the model TFR evolution would change if DM fractions would be higher/lower by 0.1 at* $z = 0$, $z = 0.9$*, and* $z = 2.3$ *(horizontal ranges are* $\pm 0.1z$*). The observed TFR evolution is reasonably matched by a model where the disk scale length is proportional to the halo radius, and where* $f_{\rm gas}$ *and* m_d *increase with redshift, while* $f_{\rm DM}(R_e)$ *decreases with redshift.*

$z \sim 2$ galaxies have gas fractions which are about a factor of eight higher than in the local Universe. The redshift evolution of $f_{\rm DM}(R_e)$ is constrained through the observational results by Martinsson et al. (2013a,b) in the local Universe, and by Wuyts et al. (2016b) at $z \sim 0.9$ and $z \sim 2.3$. We tune the redshift evolution of $f_{\rm DM}(R_e)$ within the ranges allowed by these observations to optimize the match between the toy model and the observed TFR evolution presented in this paper. $f_{\rm DM}(R_e)$ evolves significantly with redshift, with $z \sim 2$ DM fractions which are about a factor of five lower than at $z = 0$. m_d is constrained by the abundance matching results by Moster, Naab, & White (2013) in the local Universe, whereas at $0.8 < z < 2.6$ we adopt the value deduced by Burkert et al. (2016). Details on the parametrization of the above parameters are given in Appendix 2.10.2.

In Figure 2.7 we show how these empirically motivated, redshift-dependent DM fractions, disk mass fractions, and gas fractions interplay in our toy model framework to approximately explain our observed TFR evolution, specifically the TFR zero-point offsets at fixed circular velocity as a function of cosmic time. In particular, this is valid at $z = 0$, $z = 0.9$, and $z = 2.3$, while we have partially interpolated in between. Our observed KMOS$^{\rm 3D}$ TFR zero-points of the bTFR (blue squares) and the sTFR (yellow stars) at $z \sim 0.9$ and $z \sim 2.3$ are shown in relation to the local TFRs by Lelli, McGaugh, & Schombert (2016b) and Reyes et al. (2011). The horizontal error bars of the KMOS$^{\rm 3D}$ data points indicate the spanned range in redshift, while the vertical error bars show fit uncertainties. For this plot, we also perform a correction for atomic gas at high redshift:[8] we follow the theoretical prediction that, at fixed M_*, the ratio of atomic gas mass to stellar mass does not change significantly with redshift (e.g. Fu et al., 2012). We use the fitting functions by Saintonge et al. (2011) to determine the atomic gas mass for galaxies with $\log(M_*\ [M_\odot]) = 10.50$, which corresponds to the average stellar mass of our TFR galaxies at $v_{\rm ref} = 242$ km/s in both redshift bins. We find an increase of the zero-point of $+0.04$ dex at $z \sim 0.9$ and $+0.02$ dex at $z \sim 2.3$. This is included in the figure.

We show as green lines our empirically constrained toy model governed by Equations (2.4) and (2.5). This model assumes a redshift evolution of $f_{\rm gas}$, $f_{\rm DM}(R_e)$, and m_d as shown by the blue, purple, and black lines, respectively, in inset (a) in Figure 2.7 (details are given in Appendix 2.10.2). In this model, the increase in $f_{\rm gas}$ is responsible for the deviating (and stronger) evolution of the sTFR as compared to the bTFR. The decrease of $f_{\rm DM}(R_e)$ is responsible for the upturn/flattening of the bTFR/sTFR evolution. The increase of m_d leads to a TFR evolution which is steeper than what would be expected from a model governed only by $H(z)$ (see also Fig. 2.14). Our toy model evolution is particularly sensitive to changes of $f_{\rm DM}(R_e)$ with redshift. We illustrate this by showing as

---

[8] Lelli, McGaugh, & Schombert (2016b) neglect molecular gas for their bTFR, but state that it has generally a minor dynamical contribution.

cyan shaded areas in Figure 2.7 how the toy model evolution would vary if we would change only $f_{\rm DM}(R_e)$ by ± 0.1 at $z = 0$, $z = 0.9$, and $z = 2.3$.

We note that the toy model zero-point offset at R_e as derived from Equations (2.4) and (2.5), and based on a thin exponential baryon distribution, is comparable to our empirical TFR offset for a thick exponential disk and using $v_{\rm circ,max}$, since the correction factors for the circular velocity measure from thin to thick exponential disk, and from $v_{\rm circ}(R_e)$ to $v_{\rm circ,max} \approx v_{\rm circ}(r_{2.2})$, are both of the order of ~ 5 per cent and approximately compensate one another. The toy model slope ($a = 3$) is shallower than our adopted local slopes. In Appendix 2.9 we show that the usage of a reference velocity leads to negligible zero-point differences of TFR fits with different slopes.

Although our toy model is not a perfect match to the observed TFR evolution, it reproduces the observed trends reasonably well: for the sTFR, the zero-point decreases from $z = 0$ to $z \sim 1$, but there is no or only marginal evolution between $z \sim 1$ and $z \sim 2$. In contrast, there is a significantly non-monotonic evolution of the bTFR zero-point, such that the zero-point first decreases from $z = 0$ to $z \sim 1$, and then increases again up to $z \sim 2$. We note that although we show the TFR evolution up to $z = 3$, the constraints on $f_{\rm DM}(R_e)$ and m_d are valid only up to $z \approx 2.6$, as indicated in the figure by the grey shading. Also in the redshift range $0 \lesssim z \lesssim 0.8$ the model is poorly constrained because we assume a simplistic evolution of m_d (cf. Appendix 2.10.2).

A more complete interpretation of our findings also at intermediate redshift has to await further progress in observational work. With the extension of the KMOS$^{\rm 3D}$ survey towards lower mass galaxies and towards a more complete redshift coverage in the upcoming observing periods, we might already be able to add in precision and redshift range to our model interpretation. Our current data and models, however, already show the potential of state-of-the-art high$-z$ studies of galaxies to constrain parameters which are important also for theoretical work.

We would like to caution that our proposed model certainly draws a simplified picture. For instance, the assumption of a common scale length of the atomic gas as well as the molecular gas plus stars, as we did for this exercise, can only be taken as approximate, given the high central surface mass densities of our typical high$-z$ galaxies (see Section 2.4.3.1, and Wuyts et al. (2016b)). Also, the effective radii predicted by our "best fit" toy model are 10-30 per cent larger than what is observed. Other factors not addressed in our approach might also come into play: we did not explore in detail the possible effects of varying halo spin parameter λ or of the ratio between baryonic and DM specific angular momenta $j_{\rm bar}/j_{\rm DM}$, which commonly relate R_h to R_d. We also note that possible conclusions on the NFW halo concentration parameter c are in tension with current models (cf. Appendix 2.10.2). We therefore caution that our proposed toy model perspective can only reflect general trends, in particular the relative TFR zero-point offsets at $z = 0$, $z = 0.9$, and $z = 2.3$, and likely misses other relevant ingredients.

Having in mind the limitations outlined above, we conclude that the observed evolution of the mass-based TFRs can be explained in the framework of virialized haloes in an expanding ΛCDM universe, with galactic DM fractions, disk mass fractions, and gas fractions that are evolving with cosmic time. Adopting the proposed evolution of the model parameters in Equations (2.4) and (2.5) as described above and shown in inset (a) in Figure 2.7, namely at fixed $v_{\rm circ}$ increasing $f_{\rm gas}$ and m_d, and decreasing $f_{\rm DM}(R_e)$ with redshift, leads to a redshift evolution of the TFR which is non-monotonic, in particular for the bTFR.

2.6 Summary

We have investigated the mass-based Tully-Fisher relations (TFRs) of massive star-forming disk galaxies between redshift $z \sim 2.3$ and $z \sim 0.9$ as part of the KMOS$^{\rm 3D}$ survey. All our data are reduced and analyzed in a self-consistent way. The spatially resolved nature of our observations enables reliable modelling of individual galaxies, and allows for a careful selection of objects based on kinematic properties and data quality. We have taken into account inclination, beam-smearing, and instrumental broadening, and we have incorporated the significant effects of pressure support to the gravitational potential at these redshifts in our derivation of the circular velocities.

We find that the TFR is clearly in place already at $0.6 < z < 2.6$ (Section 2.3.2). Its scatter increases with redshift, but we did not find any second-order parameter dependencies when adopting a local slope. At fixed $v_{\rm circ,max}$, we find higher $M_{\rm bar}$ but similar M_* at $z \sim 2.3$ as compared to $z \sim 0.9$ (Section 2.3.3). This highlights the important effects of the evolution of $f_{\rm gas}$, where, at the same stellar mass, high$-z$ star-forming galaxies (SFGs) have significantly higher gas fractions than lower$-z$ SFGs. This strengthens earlier conclusions by Cresci et al. (2009) in the context of the interpretation of TFR evolution. Since we do not find a significant evolution of the sTFR between $z \sim 2.3$ and $z \sim 0.9$, our observed TFR evolution together with the decrease of $f_{\rm gas}$ with decreasing redshift, implies that the contribution of dark matter (DM) to the dynamical mass on the galaxy scale has to increase with decreasing redshift to maintain the dynamical support of the galaxy as measured through $v_{\rm circ,max}$. Our results complement the findings in other recent work that higher$-z$ SFGs are more baryon-dominated (Section 2.4.1).

Comparing to other selected high$-z$ TFR studies, we find agreement with the work by Cresci et al. (2009); Price et al. (2016); Tiley et al. (2016), but disagreement with the work by Miller et al. (2011) (Section 2.3.4). The significant differences in zero-point offsets of our high$-z$ TFRs as compared to the local relations by Reyes et al. (2011) and Lelli, McGaugh, & Schombert (2016b) indicate an evolution of the TFR with cosmic time (Section 2.4.2). From the local Universe to $z \sim 0.9$ and further to $z \sim 2.3$, we find a non-monotonic TFR zero-point evolution which is particularly pronounced for the bTFR.

To explain our observed TFR evolution, we present a toy model interpretation guided by an analytic model of disk galaxy evolution (Section 2.5). This model takes into account empirically motivated gas fractions, disk mass fractions, and central DM fractions with redshift. We find that the increasing gas fractions with redshift are responsible for the increasingly deviating evolution between the sTFR and the bTFR with redshift. The decreasing central DM fractions with redshift result in the flattening/upturn of the sTFR/bTFR zero-point evolution at $0.9 < z < 2.3$. This simple model matches our observed TFR evolution reasonably well.

It will be interesting to make more detailed comparisons between the growing amount of observations that can constrain the TFR at high redshift, and the newest generation of simulations and semi-analytical models. Further investigations of galaxies at lower ($z \lesssim 0.7$) and higher ($z \gtrsim 2.5$) redshifts using consistent reduction and analysis techniques will help to unveil the detailed evolution of the mass-based TFR, and to reconcile current tensions in observational work. Another important quest is to provide data which cover wider ranges in velocity and mass at these high redshifts to minimize uncertainties in the fitting of the data, and to investigate if the TFR slope changes with redshift.

Acknowledgements

We are grateful to the anonymous referee for a constructive report which helped to improve the manuscript. We thank the ESO Paranal staff for their helpful support with the KMOS observations for this work. We are grateful to Jonathan Freundlich, Susan Kassin, Federico Lelli, Raymond Simons, Jakob Walcher, and in particular to Amiel Sternberg and Simon White, for fruitful discussions, and to Rachel Somerville, Mike Williams, and Dennis Zaritsky for valuable insight into various aspects of this work. We thank Sedona Price for providing us with details on the fits by Price et al. (2016), and we are grateful to Brandon Kelly and Marianne Vestergaard for providing us with a modified version of the Bayesian approach to linear regression code (Kelly, 2007) which allows for fixing the slope. JC acknowledges the support of the Deutsche Zentrum für Luft- und Raumfahrt (DLR) via Project ID 50OR1513. MF and DJW acknowledge the support of the Deutsche Forschungsgemeinschaft (DFG) via Projects WI 3871/1-1, and WI 3871/1-2.

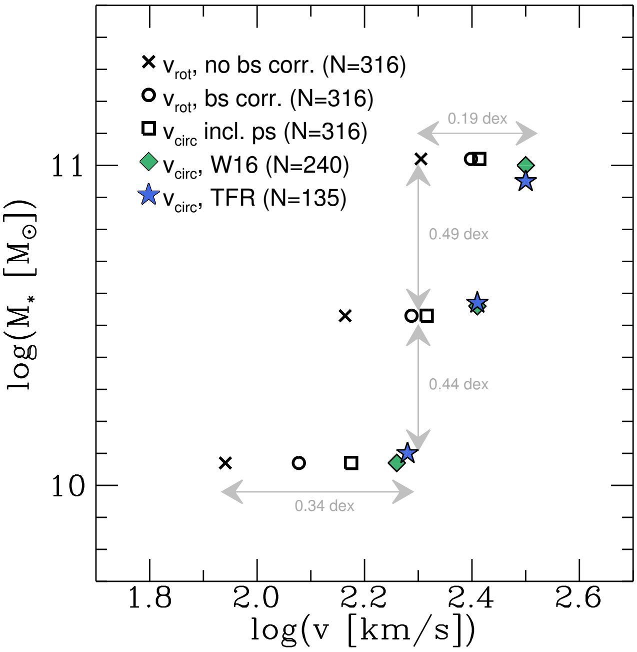

Figure 2.8: *Illustration of different correction (black symbols) and selection (colored symbols) effects on the mean maximum rotation, or circular, velocity for three stellar mass bins, log(M_* [$M_\odot$])<10.3, 10.3<log(M_* [$M_\odot$])<10.8, and 10.8<log(M_* [$M_\odot$]). Black crosses show the observed maximum velocity corrected for inclination but not beam-smearing. Black circles include the beam-smearing correction. Black squares include the correction for pressure support, leading to the maximum circular velocity as defined in Equation* (2.1)*. These data points consider all resolved KMOS^{3D} galaxies. The corresponding mean circular velocities for the Wuyts et al. (2016b) sample are shown as green diamonds, and the final TFR sample is shown as blue stars. The final selection steps for our TFR sample detailed in Section 2.2.4 have a much smaller effect than the beam-smearing and pressure support correction, and than the selection of galaxies suited for a kinematic disk modelling.*

2.7 Appendix A – The effects of sample selection

For the discussion of the TFR at high redshift it is important to be aware not only of the location of the subsample of 'TFR galaxies' within a larger parent sample, but also of the effect of the necessary corrections to the observed velocity which ultimately lead to the high-z TFR. Figure 2.8 illustrates for three stellar mass bins (log(M_* [$M_\odot$])<10.3; 10.3<log(M_* [$M_\odot$])<10.8; 10.8<log(M_* [$M_\odot$])) how the mean maximum rotation velocity changes through corrections for beam-smearing

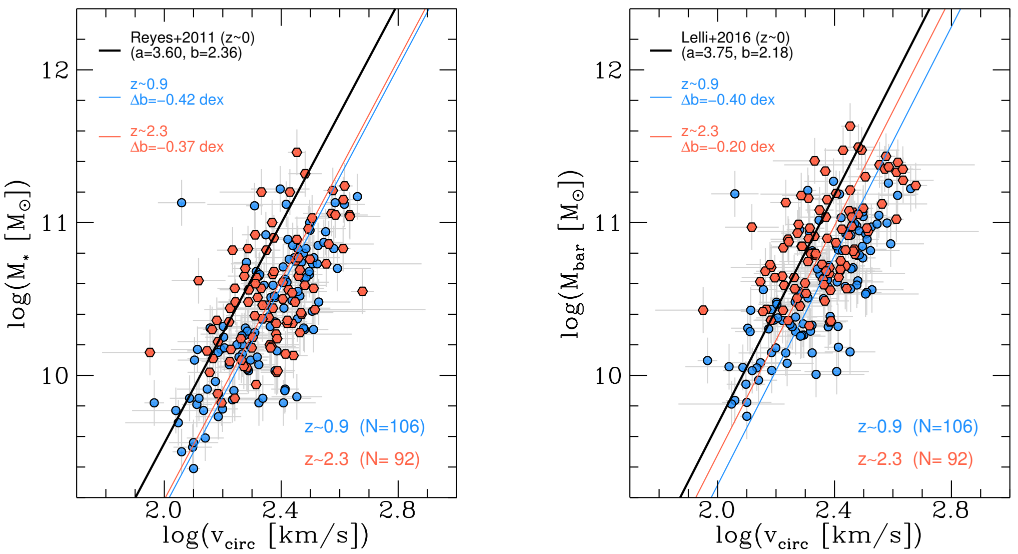

Figure 2.9: *Fixed-slope fits for the sTFR (left) and the bTFR (right) using local (black) slopes to the Wuyts et al. (2016b) subsamples at* $z \sim 0.9$ *(blue) and* $z \sim 2.3$ *(red). We find no (or only marginal) evolution of the sTFR zero-point in the studied redshift range, but significant evolution of the bTFR given the typical fit uncertainties of* $\delta b = 0.05$ *dex. While there are changes of up to* $+0.07$ *dex when comparing to the TFR sample evolution (Figure 2.5), mostly due to underestimated velocities when the maximum of the rotation curve is not covered by data, we see the same general trends as for the refined TFR sample.*

and pressure support, when selecting for rotating disks, and when eventually selecting for 'TFR galaxies' following the steps outlined in Section 2.2.4.

The effect of beam-smearing on the rotation velocity is with differences of $\gtrsim 0.1$ dex significant for our galaxies, translating into an offset in stellar mass of $\gtrsim 0.4$ dex. Considering next the impact of turbulent motions, one can clearly see how this is larger for lower-mass (and lower-velocity) galaxies.[9] This reflects the larger proportion of dispersion-dominated systems at masses of $\log(M_* \ [M_\odot]) \lesssim 10$. Correcting the observed rotation velocity for these two effects does not involve a reduction of the galaxy sample, and the corresponding data points in Figure 2.8 include all 316 resolved KMOS^{3D} galaxies. The procedure of selecting galaxies suitable for a kinematic disk modelling (Wuyts et al. (2016b); Section 2.2.4) has a noticeable effect in the full mass range explored here. It becomes clear that the further, careful selection of galaxies best eligible for a Tully-Fisher study has an

---

[9] Taking turbulent motions into account also has a larger effect at higher redshift due to the increase of intrinsic velocity dispersion with redshift. This is not explicitly shown in Figure 2.8.

appreciable effect on the mean velocity of about 0.02 − 0.03 dex, but is minor as compared to the other effects discussed.

While we consider the selection of the 'TFR sample' important due to the $v_{\rm rot,max}/\sigma_0$ cut and the reliable recovery of the true maximum rotation velocity, we note that it only leads to a small change in TFR parameters as compared to the Wuyts et al. (2016b) sample (Figure 2.9).

2.8 Appendix B – An alternative method to investigate TFR evolution

It is standard procedure in investigations of the TFR to adopt a local slope for galaxy subsamples in different redshift bins, and to quantify its evolution in terms of zero-point variations, since high−z samples often span too limited a range in mass and velocity to reliably constrain a slope. This method has two shortcomings: first, potential changes in slope with cosmic time are not taken into account. Second, every investigation of TFR evolution is tied to the adopted slope which sometimes complicates comparative studies.

We consider an alternative, non-parametric approach. In Figure 2.10 we show our TFR galaxies at $z \sim 2.3$ (red) and $z \sim 0.9$ (blue) together with the local sample by Lelli, McGaugh, & Schombert (2016b) (black) in the bTFR plane. In the mass bins labeled 'A', 'B', and 'C', we compute the weighted mean velocity of each redshift and mass subsample. We then compare the weighted mean velocities at different redshifts, as indicated in the figure, and determine an average velocity difference from combining the results from individual mass bins.

Although this approach is strongly limited by the number of galaxies per mass bin, and by the common mass range which is spanned by low- as well as high−z galaxies, its advantage becomes clear: not only is the resulting offset in velocity independent of any functional form usually given by a TFR, but the method would also be sensitive to changes of the TFR slope with redshift if the covered mass range would be large enough.

For our TFR samples, we find an average difference in velocity as measured from the average local velocity minus the average high-redshift velocity, $\Delta\overline{\log(v_{\rm circ}\ [{\rm km/s}])}$, of −0.119 between $z = 0$ and $z \sim 0.9$, and of −0.083 between $z = 0$ and $z \sim 2.3$. This confirms our result presented in Section 2.4.2, that the bTFR evolution is not a monotonic function of redshift.

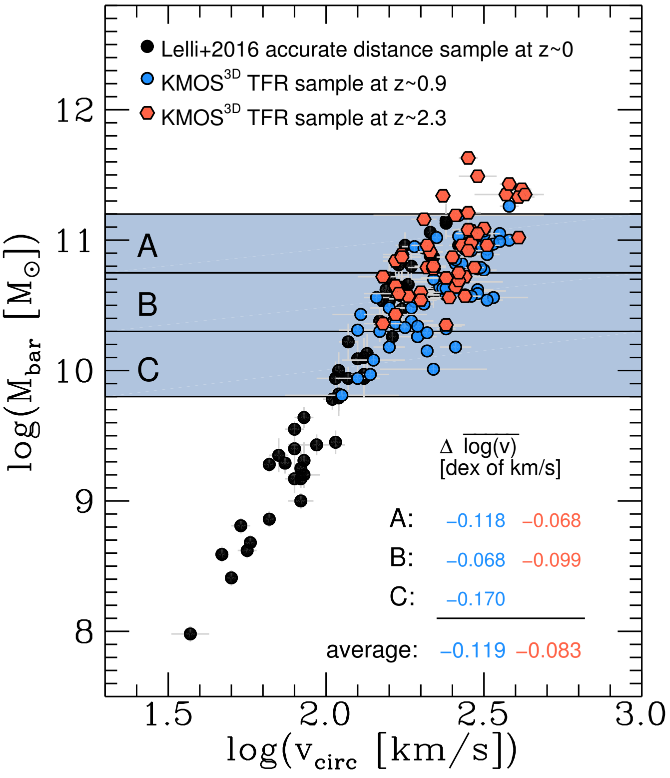

Figure 2.10: *Our TFR galaxies at $z \sim 2.3$ (red) and $z \sim 0.9$ (blue) together with the local sample by Lelli, McGaugh, & Schombert (2016b) (black) in the bTFR plane. We calculate weighted mean velocities of the redshift subsamples in the three mass bins labelled 'A', 'B', and 'C', in order to investigate the TFR evolution in a way independent of the usual functional form of the TFR. The velocity differences averaged over the mass bins of* $\Delta\overline{\log(v_{\rm circ}\ [{\rm km/s}])} = -0.119$ *between* $z \sim 0.9$ *and* $z = 0$*, and of* $\Delta\overline{\log(v_{\rm circ}\ [{\rm km/s}])} = -0.083$ *between* $z \sim 2.3$ *and* $z = 0$ *are in agreement with our results presented in Section 2.4.2, that the redshift evolution of the bTFR is non-monotonic.*

2.9 Appendix C – The impact of mass uncertainties on slope and residuals of the TFR

The slope and scatter of the TFR are affected by the adopted uncertainties in mass. In Figure 2.11 we show fit examples to the bTFR of the full sample with varying assumptions for the mass uncertainties, namely $0.05 \leq \delta\log(M_{\rm bar}\ [M_\odot]) \leq 0.4$. The corresponding changes in slope (from $a = 2.11$ to $a = 3.74$) are well beyond the already large fit uncertainties on the individual slopes, confirming that a proper assessment of the mass uncertainties is essential. For simple linear regression, the effect of finding progressively flatter slopes for samples with larger uncertainties is known as 'loss of power', or 'attenuation to the null' (e.g. Carroll et al., 2006). The relevant quantity for our study, however, is the change in zero-point offset, which is for the explored range only 0.02 dex. This is due to the use of $v_{\rm ref}$ in Equation (2.2) which ensures only little dependence of the zero-point b on the slope a.

Variations of the TFR slope naturally affect the TFR residuals to the best-fit relation (see also Zaritsky et al., 2014). We define the TFR residuals as follows:

$$\Delta\log(v_{\rm circ}) = \log(v_{\rm circ}) - \left[\frac{-b}{a} + \frac{\log(M/M_\odot)}{a} + \log(v_{\rm ref})\right]. \tag{2.6}$$

To demonstrate the effect of changing the slope, we show in Figure 2.12 the bTFR residuals as a function of R_e. In the upper panel, we show the residuals to a fit with baryonic mass uncertainties of 0.05 dex, leading to a slope which approximately corresponds to the local slope by Lelli, McGaugh, & Schombert (2016b). In the lower panel, we show the same for a fit adopting 0.4 dex uncertainties for $M_{\rm bar}$. While there is no correlation found for the former case (Spearman correlation coefficient $\rho = 0.02$ with a significance of $\sigma = 0.8059$), we find a weak correlation when adopting $\delta M_{\rm bar} = 0.4$ dex ($\rho = -0.19$, $\sigma = 0.0295$).

We find a similar behaviour for baryonic (and stellar) mass surface density, with no significant correlation between TFR offset and mass surface density for the $\delta M_{\rm bar} = 0.05$ dex fit, but a strong correlation for the $\delta M_{\rm bar} = 0.4$ dex fit (not shown). No correlation for the $\delta M_{\rm bar} = 0.05$ dex fit residuals is found for SFR surface density ($\rho = -0.08$, $\sigma = 0.3557$), but a significant correlation with $\rho = -0.37$ and $\sigma = 1.1 \times 10^{-5}$ for the $\delta M_{\rm bar} = 0.4$ dex fit (Figure 2.13).

From this exercise it becomes clear that the high$-z$ slope, and with it the TFR residuals, are strongly dependent on the accuracy of the mass and SFR measurements.

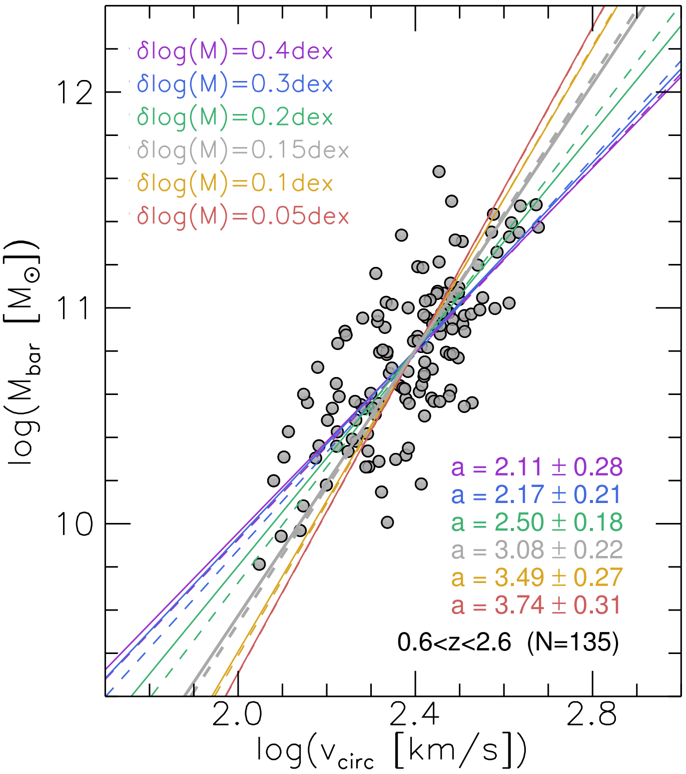

Figure 2.11: *Effect of varying uncertainties for the baryonic mass estimates on the slope of the bTFR for our full TFR sample, as indicated in the legend (solid lines, least-squares fits). The resulting best-fit slopes a vary by a factor of ~ 2 for the explored range of mass uncertainties. As dashed lines, we show the corresponding fits using the Bayesian approach by Kelly (2007) which show a similar behaviour.*

2.10 Appendix D – Derivation of the toy model for TFR evolution

2.10.1 The theoretical framework

In the following, we give details on the theoretical toy model derivation of the TFR and its evolution. The relationship between the DM halo mass, radius, and circular velocity are given by Equations (2.3), describing a truncated isothermal sphere. A plausible model for a SFG which has formed inside the dark halo is a self-gravitating thin baryonic disk with an exponential surface density profile

$$\Sigma(r) = \Sigma_0\, e^{-r/R_d}, \tag{2.7}$$

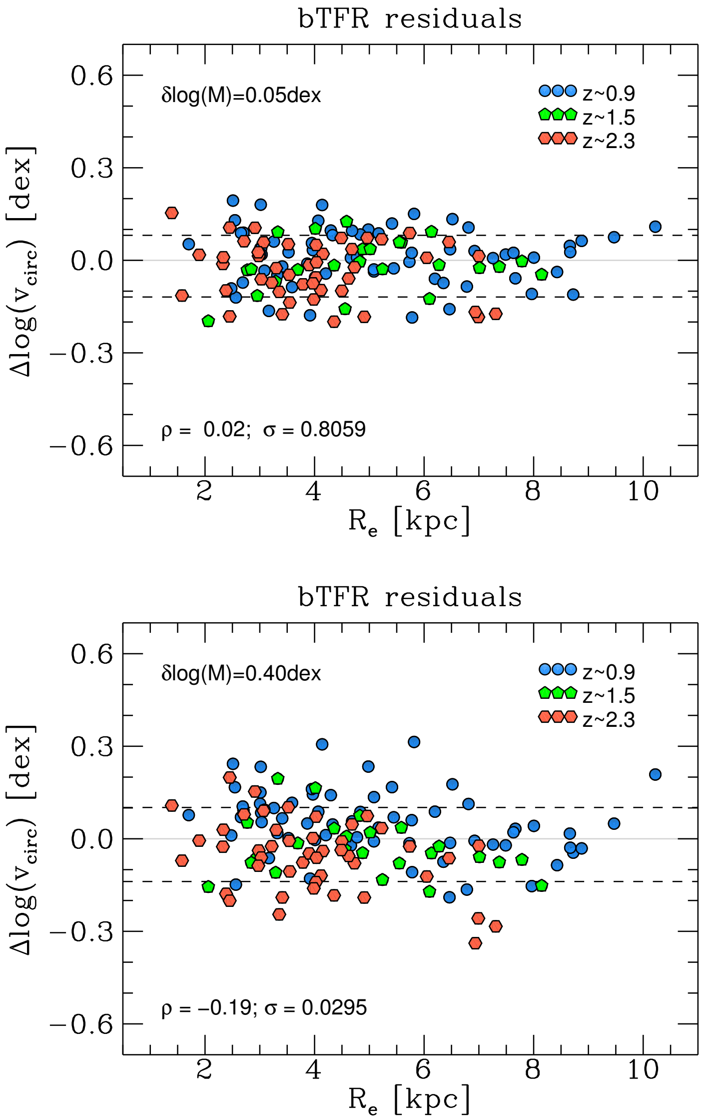

Figure 2.12: Top panel: *residuals of the bTFR as a function of effective radius, using* $\delta M_{\rm bar} = 0.05$ *dex. The dashed lines show the sample standard deviation. While we find no significant correlation for our full sample (*$\rho = 0.02$*,* $\sigma = 0.8059$*), a slightly stronger correlation for the highest redshift bin (red) is visible.* **Bottom panel:** *same as above, but using* $\delta M_{\rm bar} = 0.4$ *dex. We find a weak correlation for our full sample (*$\rho = -0.19$*,* $\sigma = 0.0295$*), and again a slightly stronger correlation for the highest redshift bin.*

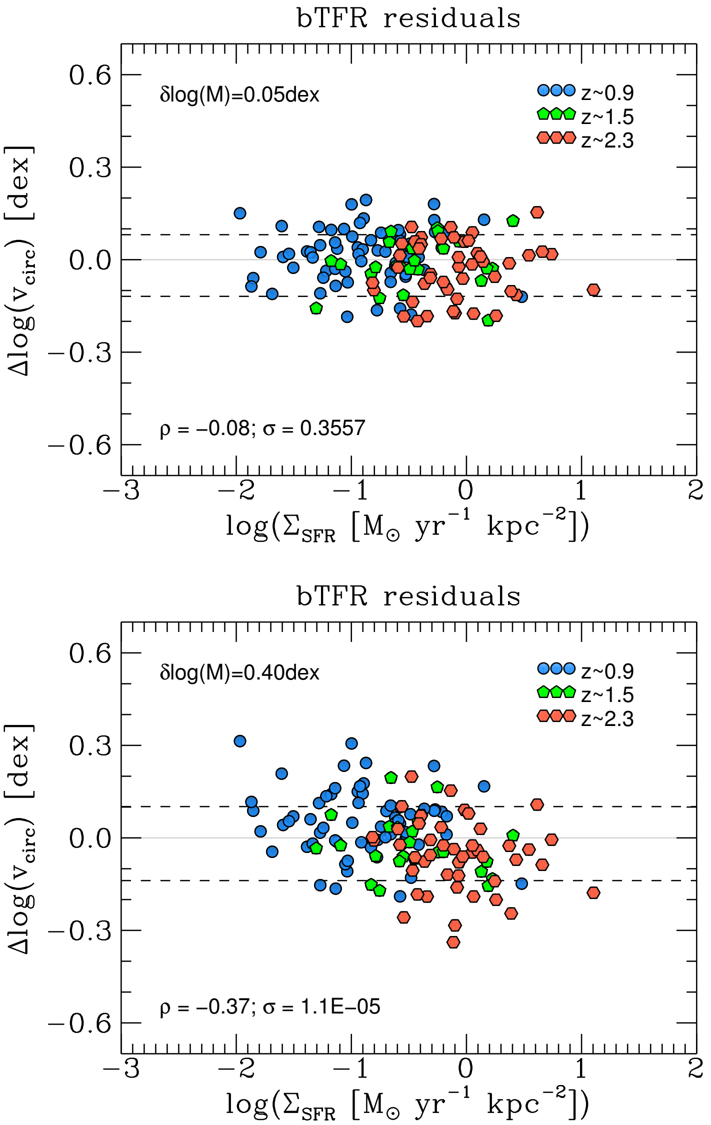

Figure 2.13: Top panel: *residuals of the bTFR as a function of SFR surface density* $\Sigma_{\rm SFR}$*, using* $\delta M_{\rm bar} = 0.05$ *dex. The dashed lines show the sample standard deviation. We find no correlation for our fiducial fit (*$\rho = -0.08$*,* $\sigma = 0.3557$*).* **Bottom panel:** *same as above, but using* $\delta M_{\rm bar} = 0.4$ *dex. We find a significant correlation (*$\rho = -0.37$*,* $\sigma = 1.1 \times 10^{-5}$*).*

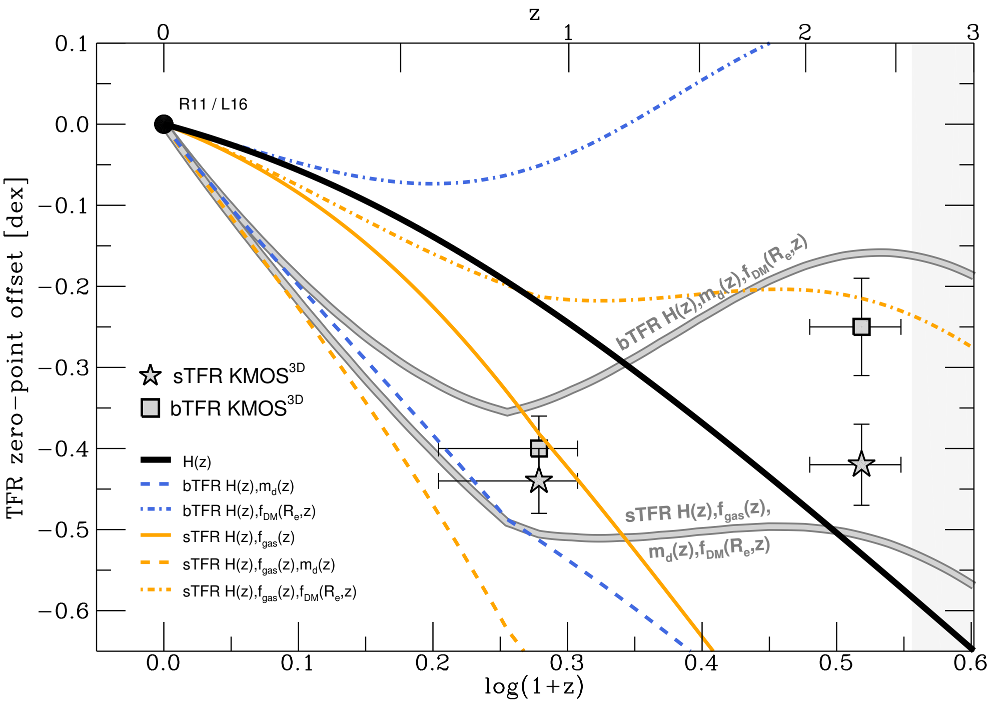

Figure 2.14: *TFR zero-point offsets of the stellar and baryonic mass TFRs as a function of cosmic time. The symbols show the KMOS^{3D} data in relation to the corresponding local normalizations by Reyes et al. (2011; R11) and Lelli, McGaugh, & Schombert (2016b; L16), as shown in Figure 2.7. The black line shows the TFR evolution for a model governed solely by $H(z)$. The colored lines show toy models for the bTFR (blue) and the sTFR (orange) evolution for different combinations of additional redshift dependencies of $f_{\rm gas}$, $f_{\rm DM}(R_e)$, or m_d, as detailed in Appendix 2.10, and as indicated in the legend. The grey lines show our final toy model following Equations* (2.4) *and* (2.5) *and including $f_{\rm gas}(z)$, $f_{\rm DM}(R_e, z)$, and $m_d(z)$ as shown in inset (a) in Figure 2.7.*

where Σ_0 is the central surface density, related to the baryonic disk mass as $M_{\rm bar} \propto \Sigma_0\, R_d^2$. In reality, disk galaxies feature a finite thickness. This does not affect the scalings presented here (see e.g. Courteau & Rix, 1999; Binney & Tremaine, 2008, and references therein). To associate the baryonic disk to the dark halo, one can assume a simple model where the corresponding masses and radii are related through a proportionality factor:

$$M_{\rm bar} = m_d \cdot M_h \quad ; \quad R_{\rm bar} = r_f \cdot R_h. \tag{2.8}$$

$R_{\rm bar}$ can be expressed through the disk scale length R_d, or the effective radius R_e, which for rotation-dominated disks are related through $R_e \approx R_d \cdot 1.68$. As noted in Section 2.5, we take r_f to be independent of redshift. In standard models of disk galaxy evolution, r_f combines information on the halo spin parameter, on the halo concentration parameter, and on the ratios of the angular momenta and masses of baryons and DM (cf. Equation (28) of Mo, Mao, & White (1998), accounting for adiabatic contraction). It has however been shown that the ratio between R_h and R_d is approximately constant for massive SFGs in the redshift range $0.8 < z < 2.6$ (Burkert et al., 2016). This does also hold for our TFR sample and the average values at $z \sim 0.9$ and $z \sim 2.3$, even though there is substantial scatter for individual objects.

To quantify the contributions of baryons and DM to the circular velocity at a given radius we write

$$v_{\rm circ}(r) = \sqrt{v^2_{\rm bar}(r) + v^2_{\rm DM}(r)}. \tag{2.9}$$

The baryonic contribution can be computed, for instance, using the expression for an infinitely thin exponential disk (Freeman, 1970),

$$v^2_{\rm bar}(r) = 4\pi G\,\Sigma_0 R_d y^2 [I_0(y)K_0(y) - I_1(y)K_1(y)], \tag{2.10}$$

where $y = r/(2R_d)$, and $I_i(y)$ and $K_i(y)$ are the modified Bessel functions of the first and second kind. At $r = R_e$, this equation becomes

$$v^2_{\rm bar}(R_e) = \frac{M_{\rm bar}}{R_d} \cdot C'', \tag{2.11}$$

where C'' is a constant. The DM component can be derived simply through a DM fraction at the radius of interest, $f_{\rm DM}(r) = v^2_{\rm DM}(r)/v^2_{\rm circ}(r)$, or via adopting a full mass profile (e.g. NFW or Einasto, Navarro, Frenk, & White, 1996; Einasto, 1965).

Equations (2.3) can be combined to

$$M_h = R_h^3 H(z)^2\; 10^2\; G^{-1}. \tag{2.12}$$

By inserting Equations (2.8) into Equation (2.12), and by substituting R_d through a re-arranged Equation (2.11), one arrives at Equation (2.4) given in Section 2.5. After introducing the gas fraction $f_{\rm gas} = M_{\rm gas}/M_{\rm bar}$, one arrives at Equation (2.5). These equations predict a TFR evolution with a constant slope, but evolving zero-point with cosmic time, depending not only on $H(z)$, but also on changes in m_d, $f_{\rm DM}(R_e)$, and $f_{\rm gas}$ with cosmic time.

We note that deviations from the proposed slope ($a = 3$) can be related to additional dependencies on $v_{\rm bar}$, e.g. of the surface density Σ (Courteau et al., 2007).

2.10.2 Observational constraints on the redshift evolution of $f_{\rm gas}$, m_d, and $f_{\rm DM}(R_e)$

In the following sections, we discuss the motivation for the adopted redshift evolution of $f_{\rm gas}$, m_d, and $f_{\rm DM}(R_e)$ in the toy model context. Figure 2.14 summarizes the individual and combined effects of adopting the respective redshift evolutions of $f_{\rm gas}$, m_d, and $f_{\rm DM}(R_e)$ for the bTFR and sTFR evolution.

2.10.2.1 The redshift evolution of $f_{\rm gas}$

For our toy model approach, we consider the gas fraction $f_{\rm gas}$ to be the sum of molecular and atomic gas mass divided by the total baryonic mass, $f_{\rm gas} = (M_{\rm gas,mol} + M_{\rm gas,at})/(M_{\rm gas,mol} + M_{\rm gas,at} + M_*)$. The evolution of the molecular gas mass-to-stellar mass ratio is given through the scaling relation by Tacconi et al. (2018):

$$\begin{aligned}\log\left(\frac{M_{\rm gas,mol}}{M_*}\right) \approx\, & 0.12 - 3.62\cdot[\log(1+z) - 0.66]^2 \\ & - 0.33\cdot[\log(M_*\ [M_\odot]) - 10.7]\,.\end{aligned} \tag{2.13}$$

Here, we do not take into account the additional dependencies given in the full parametrization by Tacconi et al. (2018) on MS offset, and offset from the M-R relation, but assume that the model galaxies lie on these relations.

Locally, the galactic gas mass is dominated by atomic gas. To account for atomic gas mass at $z = 0$, we use the fitting functions presented by Saintonge et al. (2011). We use a local reference stellar mass of $\log(M_*\ [M_\odot]) = 10.94$, i.e. the stellar mass corresponding to our reference velocity $v_{\rm ref} = 242$ km/s in the context of the sTFR fit by Reyes et al. (2011).

To account for atomic gas masses at $z > 0$, we follow the theoretical prediction that, at fixed M_*, the ratio of atomic gas mass to stellar mass does not change significantly with redshift (e.g. Fu et al., 2012). We use again the fitting functions by Saintonge et al. (2011) to now determine the atomic gas mass for galaxies with $\log(M_*\ [M_\odot]) = 10.50$, which corresponds to the average stellar mass of our TFR galaxies at $v_{\rm ref} = 242$ km/s in both redshift bins.

Between $z = 0$ and $z = 0.9$, we assume a smooth TFR evolution, meaning that at fixed circular velocity, galaxies have decreasing M_* with increasing redshift, in order to compute the gas fractions. Although we cannot quantify this assumption with our observations, we note that in comparing to our data, only the relative offset in $f_{\rm gas}$ (or any other parameter discussed below) between $z = 0$, $z = 0.9$, and $z = 2.3$ is relevant. Our assumption therefore serves mainly to avoid sudden (unphysical) offsets in the redshift evolution of $f_{\rm gas}$.

Corresponding values of the gas mass fraction at $z = \{0.0; 0.9; 2.3\}$ are $f_{\rm gas} \approx \{0.07; 0.36; 0.58\}$.

2.10.2.2 The redshift evolution of m_d

The baryonic disk mass fraction, $m_d = M_{\rm bar}/M_h$, is not a direct observable, since it depends on the usually unknown DM halo mass. For the local Universe, we use the fitting function by Moster, Naab, & White (2013) from abundance matching to determine a stellar disk mass fraction, $m_{d,*} = M_*/M_h$. For a stellar mass of $\log(M_*\ [M_\odot]) = 10.94$, this gives $m_{d,*} \approx 0.012$. Again, we use the fitting functions by Saintonge et al. (2011) to determine the corresponding gas mass, taking into account contributions from helium via $M_{\rm He} \approx 0.33\ M_{\rm HI}$. This results in a baryonic disk mass fraction at $z = 0$ of $m_d \approx 0.013$.

The recent study by Burkert et al. (2016) finds a typical value of $m_d = 0.05$ for SFGs at $0.8 < z < 2.6$ based on a Monte-Carlo NFW modelling of data from the KMOS$^{\rm 3D}$ and SINS/zC-SINF (Förster Schreiber et al., 2009; Mancini et al., 2011) surveys. These galaxies have masses similar to the galaxies in our TFR sample. We adopt their value of $m_d = 0.05$ for $0.8 < z < 2.6$.

Between $z = 0$ and $z = 0.8$ we assume a linear increase of m_d. Clearly, this is a simplifying conjecture. As for the atomic gas masses, we emphasize that this assumption has primarily cosmetic effects, while the crucial quantity is the relative difference in m_d between $z = 0$, $z \sim 0.9$, and $z \sim 2.3$.

2.10.2.3 The redshift evolution of $f_{\rm DM}(R_e)$

For the DM fraction of local disk galaxies, we follow Figure 1 by Courteau & Dutton (2015) which, among others, shows galaxies from the DiskMass survey (Martinsson et al., 2013a,b). At $v_{\rm circ} = 242$ km/s, DM fractions of local disk galaxies lie roughly between $f_{\rm DM}(r_{2.2}) = 0.55$ and $f_{\rm DM}(r_{2.2}) = 0.75$, with large scatter and uncertainties.

At higher redshift, Wuyts et al. (2016b) derived DM fractions from the difference between dynamical and baryonic masses of the KMOS$^{\rm 3D}$ subsample of 240 SFGs, which represents our parent sample. Corresponding values, also corrected for mass completeness, are given in their Table 1.

For convenience, we parametrize the evolution of the DM fraction with redshift as follows: $f_{\rm DM}(R_e) = 0.7 \cdot \exp[-(0.5 \cdot z)^{2.5}]$. This gives an evolution which is somewhat stronger than what is suggested by just taking the average values provided by Courteau & Dutton (2015) and Wuyts et al. (2016b), but easily within the uncertainties presented in both papers. We adopt this marginally stronger evolution to better match our observed TFR offsets with the toy model.

Corresponding values of the DM fraction at $z = \{0.0; 0.9; 2.3\}$ are $f_{\rm DM}(R_e) \approx \{0.70; 0.61; 0.17\}$.

We note that our toy model evolution is particularly sensitive to the parametrization of $f_{\rm DM}(R_e, z)$ which is in our implementation with the simplistic description for $m_d(z)$ responsible for the flattening/upturn of the sTFR/bTFR (see Figure 2.14). The high value for the local DM fraction (which would at $r = R_e$ rather be lower than at $r = r_{2.2}$) as well as the comparably strong evolution at $z > 1$ can certainly be challenged.

2.10.2.4 Comments on the evolution of the halo concentration parameter

The predicted evolution of the halo concentration parameter c between $z = 2$ and $z = 0$ for haloes of masses that are relevant to this study (i.e. central stellar masses of $\log(M_* \; [M_\odot]) \approx 10.5$ at $z \sim 2$, and $\log(M_* \; [M_\odot]) \approx 10.9$ at $z \sim 0$) goes from $c \approx 4$ at $z = 2$ to $c \approx 6$ at $z = 1$ and to $c \approx 7$ at $z = 0$ (Dutton & Macciò, 2014). This alone would increase the DM fraction at R_e by roughly 0.1.

Starting from the central DM fractions as determined by Wuyts et al. (2016b), abundance-matched haloes (Moster, Naab, & White, 2013) would require concentrations of $c \approx 3$ and $c \approx 12$ at $z \sim 2.3$ and $z \sim 0.9$, respectively (cf. Eq. 19 by Mo, Mao, & White, 1998). Extending this to $z = 0$ is not straight-forward since local late-type galaxies have typically lower circular velocity as required for the extrapolation of the local TFR to our $v_{\mathrm{ref}} = 242$ km/s (see discussion in Section 2.4.2). However, using the stellar mass-radius relation presented by van der Wel et al. (2014a), inferred concentrations of these hypothetical haloes would have to be $c \approx 13$.

This points towards a potential issue in the observational constraints to our toy model because the m_d values inferred by Burkert et al. (2016) are based on Monte-Carlo modelling involving standard NFW haloes. One could consider fitting m_d to better match the observed TFR zero-point evolution.

In general, the possible effects of adiabatic contraction or expansion of the halo as a response to baryonic disk formation make theoretical predictions of the central DM fractions uncertain (see e.g. the discussions by Duffy et al., 2010; Velliscig et al., 2014; Dutton et al., 2016; and also Dutton & Macciò, 2014 for an overview of predictions of concentration-mass relations from analytical models).

2.11 Appendix E – Physical properties of galaxies in the TFR sample

In Table 2.3 we list redshift z, stellar mass M_*, baryonic mass M_{bar}, maximum modelled circular velocity $v_{\mathrm{circ,max}}$, and modelled intrinsic velocity dispersion σ_0 of our TFR galaxies. The full table is available in machine readable form in the online version of this paper.

Table 2.3: *Physical properties of galaxies in our TFR sample in terms of redshift z, stellar mass M_*, baryonic mass M_{bar}, maximum modelled circular velocity $v_{\mathrm{circ,max}}$, and modelled intrinsic velocity dispersion σ_0.*

#	z	$\log(M_* \; [M_\odot])$	$\log(M_{\mathrm{bar}} \; [M_\odot])$	$v_{\mathrm{circ,max}}$ [km/s]	σ_0 [km/s]
1	0.602	10.85	10.93	274.9	30.9
2	0.626	11.00	11.07	314.3	25.8
3	0.669	10.76	10.82	267.5	49.8
4	0.678	10.49	10.58	273.4	38.5
5	0.758	10.66	10.77	313.8	24.3
6	0.777	10.35	10.58	239.1	81.4
7	0.785	10.52	10.63	237.8	23.0

Table 2.3: *(continued)*

#	z	$\log(M_* \ [M_\odot])$	$\log(M_{\rm bar} \ [M_\odot])$	$v_{\rm circ,max}$ [km/s]	σ_0 [km/s]
8	0.787	10.77	10.89	324.7	8.5
9	0.788	9.78	10.18	158.2	51.0
10	0.798	10.68	10.94	206.4	29.9
11	0.799	10.63	10.78	300.7	1.0
12	0.800	9.69	9.81	111.6	32.9
13	0.803	10.59	10.70	219.4	29.4
14	0.803	10.48	10.56	337.4	29.3
15	0.809	10.20	10.33	177.1	38.0
16	0.820	11.12	11.19	261.2	27.4
17	0.823	10.03	10.26	194.2	16.8
18	0.824	10.59	10.63	235.4	9.3
19	0.828	10.87	10.99	351.2	96.4
20	0.831	10.37	10.57	285.3	28.9
21	0.832	10.07	10.36	166.9	52.1
22	0.852	10.83	10.95	305.2	37.1
23	0.854	10.73	10.93	321.4	1.8
24	0.868	10.31	10.55	189.4	49.8
25	0.889	10.63	10.82	259.0	44.3
26	0.892	10.03	10.32	239.1	35.7
27	0.892	9.82	10.15	210.7	24.4
28	0.893	9.59	9.97	138.1	1.0
29	0.895	10.12	10.29	207.9	27.5
30	0.896	10.26	10.48	184.3	28.5
31	0.896	10.28	10.51	203.9	18.2
32	0.900	10.30	10.54	323.9	51.3
33	0.900	10.31	10.56	143.4	47.5
34	0.901	10.10	10.26	197.2	28.8
35	0.905	10.14	10.38	184.9	1.0
36	0.906	10.92	11.02	222.5	36.2
37	0.907	10.85	10.97	335.7	41.4
38	0.907	10.77	10.94	278.3	40.0
39	0.912	9.96	10.30	149.6	23.3
40	0.912	10.83	10.92	285.9	38.3
41	0.913	11.13	11.26	384.0	95.2
42	0.914	10.71	10.85	255.0	36.3
43	0.914	10.32	10.48	159.1	47.4
44	0.919	10.94	11.05	356.4	94.9
45	0.921	10.61	10.68	262.8	22.8
46	0.922	10.19	10.34	196.3	58.8

Table 2.3: *(continued)*

#	z	$\log(M_* \ [M_\odot])$	$\log(M_{\rm bar} \ [M_\odot])$	$v_{\rm circ,max}$ [km/s]	σ_0 [km/s]
47	0.927	10.66	10.80	212.1	1.0
48	0.939	10.30	10.62	301.9	1.9
49	0.949	10.17	10.43	129.8	31.6
50	0.950	10.74	10.95	191.0	60.6
51	0.952	10.10	10.31	126.9	30.2
52	0.953	9.91	10.18	259.0	65.8
53	0.953	9.85	10.01	217.2	35.5
54	0.953	9.91	10.08	140.3	16.3
55	0.954	10.95	11.04	315.0	46.8
56	1.002	10.83	11.00	380.0	19.9
57	1.004	10.29	10.53	192.5	1.0
58	1.010	9.53	9.94	125.0	19.7
59	1.017	10.44	10.61	256.5	42.2
60	1.018	10.31	10.59	299.6	58.7
61	1.019	10.51	10.64	231.5	21.7
62	1.024	10.64	10.79	305.6	12.1
63	1.026	10.89	11.03	264.7	1.0
64	1.031	10.74	10.99	294.5	57.9
65	1.032	10.80	10.98	299.4	1.7
66	1.306	10.70	10.85	248.8	21.4
67	1.382	11.00	11.31	320.5	82.4
68	1.382	10.08	10.39	181.1	18.4
69	1.382	10.82	11.07	281.1	29.3
70	1.418	10.50	10.72	222.3	44.6
71	1.427	10.26	10.60	140.6	40.1
72	1.493	10.22	10.56	207.4	29.7
73	1.498	10.31	10.53	163.2	52.0
74	1.510	11.00	11.20	347.6	39.4
75	1.518	11.07	11.37	476.1	158.9
76	1.525	10.81	11.11	301.7	25.4
77	1.526	11.33	11.48	470.6	32.4
78	1.534	10.19	10.42	195.9	52.3
79	1.548	10.81	11.04	271.3	49.5
80	1.551	9.93	10.30	226.8	59.4
81	1.551	9.93	10.20	120.3	40.5
82	1.588	10.72	11.00	241.9	34.4
83	1.599	10.85	11.03	215.8	46.8
84	1.612	10.68	10.90	304.4	39.5
85	1.613	11.18	11.31	309.0	50.5

Table 2.3: *(continued)*

#	z	$\log(M_* \ [M_\odot])$	$\log(M_\mathrm{bar} \ [M_\odot])$	$v_\mathrm{circ,max}$ [km/s]	σ_0 [km/s]
86	1.614	10.61	10.88	285.8	48.2
87	1.615	11.30	11.47	433.7	59.7
88	1.656	9.90	10.50	263.5	52.3
89	1.665	10.74	10.97	262.4	52.4
90	2.028	10.34	10.69	263.2	32.1
91	2.036	10.65	10.98	288.0	21.2
92	2.037	11.24	11.39	413.8	104.1
93	2.042	10.75	11.08	281.9	61.0
94	2.063	10.76	11.09	315.0	45.2
95	2.113	10.13	10.57	276.6	55.9
96	2.152	10.46	10.80	216.8	1.2
97	2.163	10.35	10.65	166.6	50.8
98	2.167	10.64	10.96	206.7	47.1
99	2.171	10.02	10.35	242.3	54.5
100	2.171	10.40	10.79	295.0	58.0
101	2.180	11.21	11.43	377.0	11.1
102	2.182	11.32	11.49	303.3	71.6
103	2.186	10.36	10.75	263.8	23.9
104	2.187	11.00	11.34	233.8	32.9
105	2.191	11.46	11.63	284.1	77.6
106	2.193	10.92	11.16	204.6	56.5
107	2.197	10.17	10.59	169.0	9.8
108	2.219	10.09	10.43	167.5	45.4
109	2.225	10.25	10.54	200.8	37.6
110	2.226	10.10	10.57	183.6	59.2
111	2.227	10.50	10.87	254.1	33.6
112	2.227	10.36	10.72	151.2	47.6
113	2.228	10.51	10.79	208.6	40.9
114	2.229	10.61	11.19	254.4	39.0
115	2.246	10.37	10.78	216.5	57.6
116	2.298	10.24	10.56	243.3	58.5
117	2.301	10.83	11.02	408.9	1.9
118	2.307	10.48	10.87	175.2	55.3
119	2.308	10.57	10.91	214.5	45.8
120	2.313	10.48	10.92	280.2	70.7
121	2.320	11.06	11.35	373.3	124.6
122	2.359	10.57	10.89	174.3	33.1
123	2.391	10.34	10.72	274.2	39.6
124	2.408	10.69	11.07	291.0	62.7

Table 2.3: *(continued)*

#	z	$\log(M_* \ [M_\odot])$	$\log(M_\mathrm{bar} \ [M_\odot])$	$v_\mathrm{circ,max}$ [km/s]	σ_0 [km/s]
125	2.416	10.18	10.60	199.2	48.9
126	2.432	10.14	10.64	259.8	60.0
127	2.433	10.59	11.05	302.3	75.8
128	2.437	10.56	10.96	266.2	56.1
129	2.439	10.89	11.21	284.2	52.7
130	2.441	10.57	10.96	324.2	36.1
131	2.452	10.34	10.71	241.7	40.5
132	2.454	9.88	10.36	152.2	47.9
133	2.464	10.44	10.84	167.8	27.5
134	2.519	11.05	11.35	430.4	104.9
135	2.529	11.15	11.33	409.7	68.4

2.12 Appendix F – Comments on related work post publication

After the publication of our work reprinted in this Chapter (Übler et al., 2017), Tiley et al. (2019) published a Tully-Fisher study comparing $z = 0$ and $z \sim 0.9$ data, finding no evolution for the stellar mass TFR (sTFR). The authors use data from the SAMI Galaxy Survey (Bryant et al., 2015), degrade it to the quality of their $z \sim 0.9$ KMOS observations from the KROSS survey (Stott et al., 2016), and compare it to their KROSS data. In this Section, be briefly discuss the results by Tiley et al. (2019) and comment on their relevance regarding our work. We concentrate on results regarding their 'disky' subsample, which is in selection closest to our data presented above (good fit quality, and $v_{2.2}/\sigma + \Delta(v_{2.2}/\sigma) > 3$).

The main results by Tiley et al. (2019) relevant to our work are the following:

- Through matching the original SAMI data quality to $z \sim 0.9$ KMOS observations, including adjustments of the spectral and spatial resolution, sampling, S/N, and restriction of the photometric bands used to derive stellar masses, the physical parameters relevant to the rotation velocity based sTFR, namely stellar mass and beam-smearing corrected, modelled rotation velocity (the authors use $v_{2.2}$), are to first order unchanged.

- Primarily through selection effects, the slopes of the original and matched SAMI sTFR deviate, however for the 'disky' subsample the relation is basically unchanged.

- Fixing the TFR slope of the $z \sim 0.9$ data to that of the matched $z = 0$ data, the authors find no significant zero-point offset for the 'disky' subsample: the $z \sim 0.9$ zero-point is lower by $\Delta b = -0.09 \pm 0.06$ dex of $M_\odot$ (their Table 5; a free slope gives a steeper $z \sim 0.9$ relation, cf. their Table 4).

- The authors interpret their results such that SFGs evolve along the sTFR relation, with matching amounts of stellar mass accreted or created, and dark matter mass accreted, between $z \sim 1$ and the present day.

Tiley et al. (2019) specifically discuss differences between their results and their own earlier work (Tiley et al., 2016), and our results. As discussed in detail in Section 2.3.4, the sTFR results by Tiley et al. (2016) and Übler et al. (2017) are in agreement, with our zero-point being only 0.06 ± 0.05 dex lower when adopting their slope. Regarding their own earlier work, Tiley et al. (2019) explain the difference to their new results through three factors: (i) different $z = 0$ relations are used to compare to the high$-z$ data; (ii) a different velocity measure is used ($v_{2.2}$ *vs.* v_{80}); (iii) different selection criteria are used. Accounting for the latter two effects, Tiley et al. (2019) find a reduced difference in zero-point offsets within twice the standard error, which they deem statistically insignificant. On the basis of the good agreement between the results by Tiley et al. (2016) and our work, the authors invoke equivalent explanations for the discrepant findings.

As suggested by Tiley et al. (2019), and as discussed in Section 2.7, selection effects can have a substantial impact on TFR parameters (up to $\sim \Delta b = 0.45$ dex in the study by Übler et al. (2017)). Different selection cuts might therefore explain to some extent the difference in the results by Übler et al. (2017) and Tiley et al. (2019). With respect to the velocity measure, we did not find an appreciable difference in measurements for the maximum velocity used by Übler et al. (2017) and $v_{2.2}$ (see Section 2.4.3.3). Regarding the different slopes used, Vergani et al. (2012) and Straatman et al. (2017) have shown that the choice of the TFR slope can have a substantial effect on the derived zero-point offset (up to $\sim \Delta b = 0.3$ dex in the study by Vergani et al. (2012)). Generally, these more practical considerations may explain the different results of the work by Tiley et al. (2019) and our work.

It is however important to also consider the theoretical framework. Tiley et al. (2019) interpret their findings such that the accretion or creation of stellar mass is matched by the accretion of dark matter mass onto the galaxies from $z \sim 0.9$ to $z = 0$ in a way that galaxies evolve along the TFR and the stellar disk mass fraction $m_{d,*} = M_*/M_{\rm halo}$ is constant with redshift.[10] Their small zero-point offset at $z \sim 0.9$ is in agreement with the prediction from the semi-analytical model by Dutton et al. (2011), who find a zero-point evolution that is weaker than the evolution for the corresponding dark matter halo properties. As Dutton et al. (2011) point out, this model relies on the assumption that the disk mass fraction m_d does not evolve with redshift.

Burkert et al. (2016), however, find a *baryonic* disk mass fraction at $0.8 < z < 2.6$ that is higher compared to typical $z = 0$ estimates. In our model for TFR zero-point evolution, we have incorporated the evolution of the disk mass fraction with redshift in a simplistic manner. Indeed, as can be appreciated from Figure 14 by Übler et al. (2017), assuming a constant $m_d(z)$ would result in a much shallower evolution of the sTFR (dash-dotted orange line in Figure 14).[11] Tiley et al.

---

[10] The distinction between galaxy-scale stellar mass-to-dark mass ratio and halo-scale stellar mass-to-dark mass ratio is not clearly drawn by Tiley et al. (2019). It appears their argument is primarily concerned with the corresponding ratio on galaxy scales, but they state their interpretation is in agreement with other studies that find no evolution of the stellar-to-halo mass ratio. A clear distinction between the galaxy and halo scales would be very useful here, since their theoretically predicted evolutions differ as quantified through the halo concentration parameter. In our work we demonstrate that the separation of these scales has a large impact on the predicted TFR evolution. This can be easily understood because important baryonic processes particularly at higher redshift such as rapid gas dissipation efficiently concentrating baryonic matter primarily act on galaxy scales, while the dark matter haloes extending to regions ~ 10 times larger and will not be affected by this in a similar way as the galaxy-scale dark matter distribution.

[11] Note that, unlike Tiley et al. (2019), we show a prediction for the circular velocity TFRs,

(2019) acknowledge the existence of higher gas masses in SFGs at higher redshift, and conclude that the conversion of gas into stars should be balanced by corresponding amounts of dark matter accretion to the central region. Of course, the presence of large amounts of gaseous mass must also affect the measured rotation velocities, clearly implying that not only the stellar mass-to-total halo mass ratios are relevant, but importantly also the gas and stellar mass ratios on the galaxy scale, where rotation velocities are measured. Furthermore, theoretically constrained changes of the halo concentration parameter with redshift must also have an impact.

In our analytical toy model we have to our best ability incorporated the observationally constrained, important redshift dependencies of the central gas and dark matter fraction, and the baryonic-to-total halo mass fraction, and the cosmological evolution of dark matter haloes. This model predicts a strong evolution of the TFR zero-points between $z \sim 0.8$ and $z = 0$. If the disk mass fractions at high redshift would be lower than measured by Burkert et al. (2016), this would alleviate the tension between the results by Tiley et al. (2019) and our work. However, given the convincing evidence from several studies of efficient baryon assembly, rapid gas dissipation processes, and high baryonic surface densities of main sequence $1 < z < 2.6$ SFGs (e.g. Förster Schreiber et al., 2009; van Dokkum et al., 2015; Alcorn et al., 2016; Burkert et al., 2016; Contini et al., 2016; Price et al., 2016; Stott et al., 2016; Wuyts et al., 2016b; Genzel et al., 2017; Lang et al., 2017) the assumption of a constant baryonic disk mass fraction seems questionable.

This is also supported by the recent abundance matching model by Moster, Naab, & White (2018): at $z = 2$, the predicted stellar disk mass fraction $m_{d,*}$ for main sequence SFGs of stellar mass $\log(M_*/M_\odot)$=9–11 is approximately constant with redshift (but close to the Schechter mass, above $\log(M_*/M_\odot)$=10.5, higher redshift galaxies have increasingly higher stellar disk mass fractions by $\Delta m_{d,*} \approx 0.01 - 0.02$). However, with gas-to-baryonic mass fractions of ~ 50 % at $z \sim 2$, ~ 35 % at $z \sim 1$, and $\sim 5 - 15$ % at $z = 0$, the high$-z$ baryonic disk mass fractions must be higher compared to local values. A higher disk mass fraction at earlier times will inevitably lead to a more pronounced negative zero-point evolution of the sTFR.

It is clear that many factors have to be accounted for in measuring the TFR redshift evolution. Tiley et al. (2019) have undertaken an important step in matching data quality over a wide range in cosmic time. It is generally difficult to

---

i.e. stellar and baryonic mass *vs.* circular velocity $v_{\rm circ}$, which incorporates the effects of pressure support. The predicted evolution for $v_{\rm rot}$ would be less pronounced. At the high mass end, accounting for pressure support increases the TFR offset by $\Delta b \approx -0.1$ dex, while towards lower masses, where galaxies are increasingly more dispersion-supported, this difference increases. As a consequence, the TFR slope is steeper when circular velocities are considered.

compare TFR evolution results between independent studies with different ways of measuring kinematic parameters, different adopted TFR slopes, and different sample selections. Apart from these practical difficulties, however, a theoretical assessment of TFR evolution based on the cosmological evolution of dark matter haloes predicts a redshift dependence of the TFR. Furthermore, for a complete picture, the redshift dependencies of the central gas, stellar, and dark matter mass fractions have to be considered, leading to a complex evolution of the TFR, as we demonstrate in Übler et al. (2017). The fine-tuning of this prediction depends crucially on analytically and observationally constrained mass fractions. Through future observations and improved model predictions it will be possible to more precisely constrain TFR evolution.

Chapter 3

The Evolution and Origin of Ionized Gas Velocity Dispersion from $z \sim 2.6$ to $z \sim 0.6$ with KMOS$^{\mathrm{3D}}$

This Chapter is a reprint of the ApJ publication *The Evolution and Origin of Ionized Gas Velocity Dispersion from* $z \sim 2.6$ *to* $z \sim 0.6$ *with KMOS*^{3D} by Übler et al. (2019); DOI:10.3847/1538-4357/ab27cc; ©AAS. Reproduced with permission.

This work is based on observations collected at the Very Large Telescope (VLT) of the European Southern Observatory (ESO), Paranal, Chile, under ESO program IDs 092.A-0091, 093.A-0079, 094.A-0217, 095.A-0047, 096.A-0025, 097.A-0028, 098.A-0045, 099.A-0013, 0100.A-0039, and 0101.A-0022.

Abstract – We present the $0.6 < z < 2.6$ evolution of the ionized gas velocity dispersion in 175 star-forming disk galaxies based on data from the full KMOS$^{\mathrm{3D}}$ integral field spectroscopic survey. In a forward-modelling Bayesian framework including instrumental effects and beam-smearing, we fit simultaneously the observed galaxy velocity and velocity dispersion along the kinematic major axis to derive the intrinsic velocity dispersion σ_0. We find a reduction of the average intrinsic velocity dispersion of disk galaxies as a function of cosmic time, from $\sigma_0 \sim 45$ km s^{-1} at $z \sim 2.3$ to $\sigma_0 \sim 30$ km s^{-1} at $z \sim 0.9$. There is substantial intrinsic scatter ($\sigma_{\sigma_0,\mathrm{int}} \approx 10$ km s^{-1}) around the best-fit $\sigma_0 - z$-relation beyond what can be accounted for from the typical measurement uncertainties ($\delta\sigma_0 \approx 12$ km s^{-1}), independent of other identifiable galaxy parameters. This potentially suggests a dynamic mechanism such as minor mergers or variation in accretion being responsible for the scatter. Putting our data into the broader lit-

erature context, we find that ionized and atomic+molecular velocity dispersions evolve similarly with redshift, with the ionized gas dispersion being $\sim 10-15$ km s^{-1} higher on average. We investigate the physical driver of the on average elevated velocity dispersions at higher redshift, and find that our galaxies are at most marginally Toomre-stable, suggesting that their turbulent velocities are powered by gravitational instabilities, while stellar feedback as a driver alone is insufficient. This picture is supported through comparison with a state-of-the-art analytical model of galaxy evolution.

3.1 Introduction

Extragalactic surveys over the last decades have produced thousands of spectrally and spatially resolved observations of galaxies from the present day out to $z \sim 4$. For massive galaxies on the star-forming main sequence, these efforts resulted in two main findings regarding their kinematic evolution: (i) already by $z \sim 2$, the majority of star-forming galaxies (SFGs) show ordered rotation, and (ii) their velocity dispersions are higher by factors of 2-5 compared to local SFGs (Labbé et al., 2003; Förster Schreiber et al., 2006, 2009, 2018; Genzel et al., 2006, 2008, 2014b; Cresci et al., 2009; Epinat et al., 2009, 2012; Law et al., 2009; Jones et al., 2010; Gnerucci et al., 2011; Wisnioski et al., 2011, 2015, in prep.; Miller et al., 2012; Swinbank et al., 2012b; Stott et al., 2016; Simons et al., 2017). The redshift evolution of the ionized gas velocity dispersion has captured a lot of attention through its potential to constrain feedback and star formation models (Förster Schreiber et al., 2006; Genzel et al., 2006, 2008, 2011; Weiner et al., 2006; Kassin et al., 2007, 2012; Epinat et al., 2009, 2012; Law et al., 2009; Lehnert et al., 2009, 2013; Gnerucci et al., 2011; Wisnioski et al., 2012, 2015; Swinbank et al., 2012a; Newman et al., 2013; Simons et al., 2016, 2017; Turner et al., 2017; Mason et al., 2017; Zhou et al., 2017; Johnson et al., 2018; Girard et al., 2018).

Starting from small scales in the Milky Way, the velocity dispersion in molecular clouds is proportional to cloud size and mass, in a way that suggests molecular clouds are turbulent, with kinetic and gravitational energy being in near equipartition (Larson, 1981; McKee & Ostriker, 2007; Heyer & Dame, 2015, and references therein). However, the lack of dependence of the turbulence level on factors such as environment or local star formation activity points towards larger scale drivers (Heyer & Brunt, 2004; Brunt, Heyer, & Mac Low, 2009; but see Heyer & Dame, 2015 for extreme environments).

In nearby galaxies, velocity dispersions of atomic gas are $\sigma_{\mathrm{HI}} \approx 10-12$ km s^{-1} on scales of ~ 100 pc (Dib, Bell, & Burkert, 2006; Tamburro et al., 2009; Ianjamasimanana et al., 2012; Fukui et al., 2009; Caldú-Primo et al., 2013; Mogotsi et al., 2016; Koch et al., 2019). Molecular gas velocity dispersions are typically lower, with reported ratios in the range $\sigma_{\mathrm{CO}}/\sigma_{\mathrm{HI}} \approx 0.3-1$ (Tamburro et al., 2009; Ianjamasimanana et al., 2012; Fukui et al., 2009; Wong et al., 2009; Caldú-

Primo et al., 2013; Druard et al., 2014; Mogotsi et al., 2016; Levy et al., 2018; Koch et al., 2019). Ionized gas velocity dispersions are substantially higher, with $\sigma_{\mathrm{H}\alpha} \approx 24$ km s^{-1} (Epinat et al., 2010).

At high redshift, most measurements of gas velocity dispersion are based on ionized gas, which is accessible from the ground in the near-infrared through strong rest-frame optical lines. Typical values are $\sigma = 25 - 100$ km s^{-1} for disk galaxies. It is more challenging to measure accurate velocity dispersions at high redshift because of the combined effects of beam-smearing and limited instrumental spectral resolution (see Davies et al., 2011). The former can be corrected for instance by using the velocity field and the spatial resolution of the observations to create a beam-smearing map (e.g. Green et al., 2010; Gnerucci et al., 2011; Epinat et al., 2012), through model-based look-up tables (e.g. Burkert et al., 2016; Johnson et al., 2018), or through forward-modelling (e.g. Cresci et al., 2009; Genzel et al., 2011; Di Teodoro, Fraternali, & Miller, 2016; Wuyts et al., 2016b; Varidel et al., 2019). Typical spectral resolutions of near-infrared spectroscopic observations at $z \sim 1 - 3$ correspond to velocity dispersions of $\sigma_{\mathrm{instrumental}} \approx 30 - 40$ km s^{-1}. However, depending on the signal-to-noise ratio (S/N), it is possible to recover velocity dispersions through forward-modelling down to 1/3 of the instrumental resolution.

It is well established that the galactic gas velocity dispersion is correlated with redshift (e.g. review by Glazebrook, 2013), but the physical processes responsible for driving and maintaining the dispersions are still debated. It has been shown theoretically that constant energy input is necessary to maintain turbulence in the interstellar medium (ISM) because it will otherwise decay within a few Myr (e.g. Mac Low et al., 1998; Stone, Ostriker, & Gammie, 1998). A number of potential drivers has been identified, with two main classes: (i) the conversion of kinetic energy through stellar feedback in the form of winds, expanding HII regions, and supernovae, and (ii) the release of gravitational energy through clump formation, radial flows within the disk, and accretion from the cosmic web. Other possible sources include effects of galactic rotation, fluid instabilities, and galaxy interactions (see Elmegreen & Scalo, 2004, for a review). Generally, the different scales on which the proposed mechanisms operate present a challenge to simulations (see Naab & Ostriker, 2017, for a review).

In this paper, we investigate the intrinsic velocity dispersion of the ionized gas phase in rotation-dimonated, star-forming galaxies from our KMOS$^{3\mathrm{D}}$ survey at $0.6 < z < 2.6$. In Section 3.2 we briefly present the KMOS$^{3\mathrm{D}}$ data set. Our modelling and sample selection is discussed in Section 3.3. In Section 3.4 we investigate the evolution of the intrinsic velocity dispersion with redshift and put it into the broader context of multi-phase literature values from $z = 4$ to $z = 0$. In Section 3.5 we discuss possible drivers of turbulence, particularly gravitational instabilities and stellar feedback, and compare our data to a state-of-the-art analytical model by Krumholz et al. (2018). We conclude our study in Section 3.6.

Throughout, we adopt a Chabrier (2003) initial mass function and a flat ΛCDM cosmology with $H_0 = 70\,\mathrm{km\,s^{-1}\,Mpc^{-1}}$, $\Omega_\Lambda = 0.7$, and $\Omega_m = 0.3$.

3.2 The KMOS$^{\rm 3D}$ survey

Our study is based on data from the KMOS$^{\rm 3D}$ survey, targeting the Hα line emission of primarily main sequence galaxies in three redshift bins centered at $z \sim 0.9$, $z \sim 1.5$, and $z \sim 2.3$. The survey is presented by Wisnioski et al. (2015) and Wisnioski et al., in prep., to which we refer the reader for details. Below, we summarize its main characteristics.

The KMOS$^{\rm 3D}$ galaxies were selected from the 3D-HST survey (Brammer et al., 2012; Skelton et al., 2014; Momcheva et al., 2016), providing optical-to-8μm photometry and, importantly, secure spectroscopic or grism redshifts, so that bright OH skylines at the location of the Hα line emission could be avoided. In addition, high-resolution imaging for all galaxies is available through CANDELS (Grogin et al., 2011; Koekemoer et al., 2011; van der Wel et al., 2012), and further multi-wavelength coverage through photometry from *Spitzer*/MIPS and *Herschel*/PACS (Lutz et al., 2011; Magnelli et al., 2013; Whitaker et al., 2014, and references therein).

For the KMOS$^{\rm 3D}$ survey, we selected galaxies with stellar masses $\log(M_*/M_\odot) > 9$ and $K_{\rm AB} \lesssim 23$. The selection aimed to provide a homogeneous coverage of the star formation main sequence across stellar mass in the three redshift slices, thus ensuring near equal statistical coverage up to the highest masses. In addition, KMOS$^{\rm 3D}$ also extends below the main sequence regime where galaxies are 'quiescent', and it contains starburst outliers above the main sequence.

Stellar masses were derived following Wuyts et al. (2011b), by fitting the broad- and medium-band optical-to-mid-infrared spectral energy distribution with Bruzual & Charlot (2003) stellar population synthesis models, adopting a Calzetti et al. (2000) extinction law, solar metallicity, and a range of star formation histories. Gas mass measurements are not available for most of our galaxies. We exploit the scaling relation by Tacconi et al. (2018) which depends on redshift, offset from the main sequence, and stellar mass, with the main sequence prescription by Whitaker et al. (2014), to estimate the molecular gas masses ($M_{\rm gas}$) of our galaxies. We don't account for atomic gas in this study. The derivation of star-formation rates (SFRs) followed the ladder of SFR indicators as described by Wuyts et al. (2011b).

Structural properties such as the axis ratio $q = b/a$, the disk effective radius R_e, and the bulge-to-total stellar mass fraction B/T are based on two-dimensional Sérsic models to the stellar light distribution high-resolution $H-$band images from

HST observations (van der Wel et al., 2012; Lang et al., 2014). For the effective radius we apply a color correction following van der Wel et al. (2014a).

The survey was conducted during the years 2013 to 2018 with the multiplexing near-infrared integral field spectrograph KMOS (Sharples et al., 2004, 2013) at the *Very Large Telescope*. The full KMOS^{3D} sample consists of 740 targeted galaxies (Wisnioski et al., in prep.).

3.3 Dynamical modelling and sample selection

We constrain the intrinsic velocity dispersions by forward-modelling the observed one-dimensional velocity and velocity dispersion profiles extracted from the data cubes. For this work, we use the two-dimensional kinematic information to determine the kinematic major axis, and to distinguish rotation-dominated, dispersion-dominated, and disturbed systems. The full kinematic information on the motions of stars or gas in the plane of a rotating disk can be extracted along its kinematic major axis. Modelling the one-dimensional kinematics instead of the two- or three-dimensional data increases the S/N of our measurements, and thus allows us to study a larger sample of galaxies with reliable modelling. We have verified that this has only a minor impact on the derived dynamical parameters, with an average, non-systematic difference of one-dimensional *vs.* two-dimensional intrinsic velocity dispersion of $\sim 5-10\%$.

3.3.1 One-dimensional kinematic profiles

We derive two-dimensional projected Hα velocity and velocity dispersion fields for all KMOS^{3D} galaxies using LINEFIT (Davies et al., 2009, 2011; Förster Schreiber et al., 2009), a code that takes into account the instrument line spread function and fits a Gaussian model for each spaxel of the reduced data cube after continuum subtraction. From these maps we exclude spaxels with $S/N \leq 2$, uncertainties on the velocity or velocity dispersion of ≥ 100 km s^{-1}, as well as off-source fits to noise features. We determine the maximum and minimum of the velocity map through a weighted average of either the 5 % of spaxels of both the highest and lowest velocity values for galaxies with ≥ 50 suitable spaxels, or otherwise of the five spaxels with highest and lowest velocities. The kinematic major axis is defined as the line going through the maximum and minimum of the velocity map. The kinematic center is defined as the midpoint on the kinematics major axis connecting the maximum and minimum of the velocity map. This method follows the procedures outlined by Wisnioski et al. (2015), and in the KMOS^{3D} data release and final survey paper by Wisnioski et al., in prep.

Along the kinematic major axis, we then extract spectra in circular apertures of diameter 2×FWHM of the model-independent point spread function (PSF) associated with each individual galaxy. Here, the flux from all spaxels within an aperture is integrated to create a single spectrum. For the dynamical modelling of our galaxies (see Section 3.3.2), we repeat this same procedure for each iteration of the model fitting to properly account for any effects related to this integration process. We consider a galaxy to be spatially resolved if we can measure its kinematics over a total of at least $3\times\mathrm{PSF}_{\mathrm{FWHM}}$ along the kinematic major axis. We fit the Hα velocity and velocity dispersion from the resulting spectra, providing us with the one-dimensional rotation curve $v_{\mathrm{rot}}(r) \cdot \sin(i)$ and dispersion profile $\sigma(r)$, uncorrected for beam-smearing. Uncertainties for each data point are derived using Monte Carlo analysis and have typical values of 6 km s^{-1} and 10 km s^{-1} for the velocity and dispersion values, respectively.

With this methodology we have successfully extracted kinematic profiles for all 535 KMOS$^{\mathrm{3D}}$ Hα−detected galaxies with secure redshifts.

3.3.2 Dynamical modelling with DYSMAL

As a next step, we consider all galaxies with kinematic profile extractions that are resolved, a total of 456 SFGs. We further exclude targets for which we detect multiple systems within the IFU, and we eliminate merging or potentially interacting systems with larger separations based on projected distances, redshift separations, and mass ratios, as informed through the 3D-HST catalog (Mendel et al., in prep.). Galaxies that are strongly contaminated by sky features, have prominent broad line regions, or have very strong outflows affecting the recovery of the galaxies' velocity and dispersion, are also excluded. This results in 356 galaxies.

We exploit the dynamical fitting code DYSMAL (Cresci et al., 2009; Davies et al., 2011; Wuyts et al., 2016b; Übler et al., 2018) to model our galaxies. DYSMAL is a forward-modeling code that allows for a flexible number of components (disk, bulge, halo, etc.) and free parameters. It accounts consistently for finite scale heights and flattened spheroidal potentials (Noordermeer, 2008), and it includes the effects of pressure support on the rotation velocity. It also accounts for the instrument line spread function, and for beam-smearing effects by convolving with the two-dimensional PSF of each galaxy.

For our modelling, we assume a velocity dispersion that is isotropic and constant throughout the disk, motivated by deep adaptive optics imaging spectroscopy on kpc scales of 35 $z = 1 - 2.6$ SFGs in the SINS/zC-SINF sample (Genzel et al., 2006, 2008, 2011, 2017; Cresci et al., 2009; Förster Schreiber et al., 2018, see also Section 3.5.2). We note that for nearby galaxies radially declining velocity dispersions have been observed for atomic and molecular gas (van der

Kruit & Freeman, 1984; Dickey, Hanson, & Helou, 1990; Boulanger & Viallefond, 1992; Kamphuis & Sancisi, 1993; Meurer et al., 1996; Petric & Rupen, 2007; Tamburro et al., 2009; Wilson et al., 2011; Caldú-Primo et al., 2013; Mogotsi et al., 2016; Sun et al., 2018; Koch et al., 2019), where the velocity dispersion usually reaches a constant level only in the disk outskirts. The observed radial changes in velocity dispersion are however rarely larger than $10-20$ km s^{-1}, and such variations on small scales are likely washed out through the coarser spatial resolution of typical high$-z$ observations (but see Section 3.5.2 for a high-resolution example).

We create a three-dimensional mass model of each galaxy consisting of an exponential disk with the effective radius R_e adopted from the $H-$band measurements, with ratio of scale height to scale length $q_0 = 0.25$, and with a central bulge ($R_{e,\mathrm{bulge}} = 1$ kpc, Sérsic index $n_{\mathrm{S,bulge}} = 4$, e.g. Lang et al., 2014; Tacchella et al., 2015b). The value of $q_0 = 0.25$ is motivated by the fall-off in the $q = b/a$ distribution of SFGs at the mass and redshift of our sample (van der Wel et al., 2014b). For galaxies without an $H-$band based measurement of the bulge mass (see Section 3.2; ca. 30%) we use average values of $B/T = [0.25; 0.35; 0.45; 0.5]$ for total stellar masses of $\log(M_\star/M_\odot) = [< 10.8; 10.8-11; 11-11.4; > 11.4]$, following Lang et al. (2014). We fix the physical size of the bulge because individual measurements of $R_{e,\mathrm{bulge}}$ are very uncertain, in contrast to measurements of B/T (see Tacchella et al., 2015b). In a population-averaged sense, however, $R_{e,\mathrm{bulge}} = 1$ kpc is a robust choice (see Lang et al., 2014). We calculate the galaxy inclination i as $\cos(i) = [(q^2 - q_0^2)/(1 - q_0^2)]^{1/2}$. The mass model is then rotated to match the galaxy's observed orientation in space, convolved with the line spread function and the PSF of the observation to take into account beam-smearing, and subsequently pixelated to resemble the spatial sampling of the observation. We approximate the PSF as a two-dimensional Moffat function that has been fitted to the standard star observations associated with each KMOS detector and pointing. For our modelling, we assume that light traces mass.

Using DYSMAL, we simultaneously fit the one-dimensional velocity and velocity dispersion profiles of our galaxies in observed space. The best-fitting intrinsic rotation velocity, v_{rot}, is constrained both through the mass model and the intrinsic velocity dispersion via pressure support. We apply Markov chain Monte Carlo (MCMC) sampling to determine the model likelihood based on comparison to the observed one-dimensional kinematic profiles, and assuming Gaussian measurement noise. To ensure convergence of the MCMC chains, we model each galaxy with 400 walkers, a burn-in phase of 50-100 steps, followed by a running phase of another 50-100 steps (>10 times the maximum autocorrelation time of the individual parameters). For each free parameter, we adopt the median of all model realizations as our best fit value, with asymmetric uncertainties corresponding to the 1σ confidence ranges of the one-dimensional marginalized posterior distributions.

In order to recover the intrinsic velocity dispersion as best as possible, we consider a total of three setups with varying free parameters and treatment of the kinematic profiles:

1. In our first setup, we feed the kinematic profiles obtained as described in Section 3.3.1, with free parameters being the total dynamical mass in the range $\log(M_{\rm tot}/M_{\odot}) = [9; 13]$, and the intrinsic velocity dispersion in the range $\sigma_0 = [5; 300]$ km s^{-1}. $M_{\rm tot}$ is the total mass distributed in the three-dimensional disk plus bulge structure necessary to reproduce the observed kinematics. Other parameters are fixed, specifically i, R_e, and B/T.

2. Due to extinction, skyline contamination, and noise limitations, some galaxies display asymmetric kinematic profiles. Therefore, we employ a symmetrization technique in a second setup, where the one-dimensional profiles are folded (for the dispersion profile) or rotated (for the rotation curve) around the kinematic centre, interpolated onto a common grid, and averaged by calculating the mean at each radial grid point to obtain symmetric profiles, with uncertainties added in quadrature. Again, free parameters are $M_{\rm tot}$ and σ_0, allowed to vary within the same ranges as for setup 1.

3. As noted in Section 3.2, R_e and B/T of our galaxies are derived from $H-$band imaging. It is known that the mass distribution derived from the $H-$band light might differ from the corresponding Hα flux profiles (e.g. Wuyts et al., 2012; Tacchella et al., 2015a; Nelson et al., 2016b; Wilman et al., in prep.). In particular the dispersion profiles can be sensitive to the central mass concentration. In the third setup we therefore proceed as in setup 2, but additionally leave the disk effective radius R_e and the bulge-to-total fraction B/T as free parameters. For R_e we use an effectively flat prior centered on the fiducial value and truncated at ±2.5 kpc, with hard bounds of $R_e = [0.1; 20]$ kpc. For B/T we use an effectively flat prior with hard bounds of $B/T = [0; 1]$.

Comparing results from the three setups, we generally find good agreement for both the derived intrinsic dispersions and the dynamical masses, as listed in Table 3.1. For setup 3, the model-derived (mass/Hα) effective radii are systematically higher compared to the $H-$band measurements by ~ 0.6 kpc. For the range of $R_e \approx 2 - 10$ kpc and $\log(M_*/M_{\odot}) \approx 9.2 - 11.5$ in our kinematic sample, this is agreement with the results by Nelson et al. (2016b) and Wilman et al., in prep., who find $R_{e,{\rm H}\alpha}/R_{e,H} \approx 1.1 - 1.2$ from high-resolution *HST* observations and from our full KMOS$^{\rm 3D}$ sample, respectively. The average agreement between the $H-$band-derived B/T and the model-derived B/T is better, however the model-derived value is likely more realistic for cases with only a grid-based B/T.

Table 3.1: *Comparison of modelling results from the three setups (S1, S2, S3) described in Section 3.3.2.*

comparison	quantity	mean	std. dev.
S1 – S2	$\Delta\sigma_0$ [km s^{-1}]	0.9	6.0
	$\Delta\log(M_{\rm tot})$ [dex of $M_\odot$]	-0.01	0.03
S1 – S3	$\Delta\sigma_0$ [km s^{-1}]	0.5	7.4
	$\Delta\log(M_{\rm tot})$ [dex of $M_\odot$]	-0.06	0.11
S2 – S3	$\Delta\sigma_0$ [km s^{-1}]	-1.4	5.3
	$\Delta\log(M_{\rm tot})$ [dex of $M_\odot$]	-0.04	0.10
S3: $H-$band – Hα[a]	ΔR_e [kpc]	-0.6	1.0
	$\Delta B/T$	0.03	0.14

[a] Comparison of the fiducial R_e and B/T as derived from the stellar light $H-$band images (see Section 3.2) to the modelling results from setup 3, where we fit for R_e and B/T as detailed in Section 3.3.2.

We tested a fourth setup for a subset of our sample, including not only the bulge and disk components but in addition an NFW halo (Navarro, Frenk, & White, 1996), with a prior on the expected dark matter halo mass (Moster, Naab, & White, 2018) and the concentration parameter fixed to the theoretically expected value (Dutton & Macciò, 2014). The resulting best-fit velocity dispersions are robust in that they agree within the uncertainties with the results from the other three setups with a standard deviation of 5.9 km s^{-1}, and there are no systematic effects. However, the limited field-of-view of KMOS (compared to e.g. SINFONI) together with our typical integration times of $5-9$ h per target constrain our ability to map the faint outskirts of galaxies where the kinematics are most sensitive to additional dynamical components with a different mass distribution. Therefore, we do not include fits from this fourth setup in our final sample.

3.3.3 The kinematic sample

We inspect the fits from all three model setups to create our best-fit sample. By default, we choose the fit to setup 1, but if it is bad or poorly constrained, we consider setups 2 and 3 in this order. Galaxies with poor fits in all setups are excluded. With this strategy we stay as closely as possible to the original data, but at the same time do not need to disregard galaxies with one-sided extinction or skyline contamination that otherwise show good data quality, and we can choose fits from setup 3 with a more appropriate mass distribution, if necessary.

Finally, we impose a $v_{\rm rot}/\sigma_0 \geq 1$ cut to focus on rotation-dominated systems. Here, $v_{\rm rot}$ is the model intrinsic rotation velocity at 1.38 R_e, which is the location of the peak of the rotation curve for a Noordermeer disk with $n_{\rm S} = 1$. Our final sample consists of 175 galaxies, with 80, 47, and 48 galaxies in the redshift slices $z = 0.6 - 1.1$, $z = 1.2 - 1.7$, and $z = 1.9 - 2.6$. Of those galaxies, 56 % are from setup 1, 31 % from setup 2, and 13 % from setup 3. We show examples of galaxies and their fits from different setup in Appendix 3.7. The averaged uncertainties on our derived σ_0 values cover the range $\delta\sigma_0 = 2 - 29$ km s^{-1}, with 68$^{\rm th}$ percentiles of $\delta\sigma_0 = 5 - 15$ km s^{-1}, and mean values in the three redshift slices $z \sim 0.9; 1.5; 2.3$ of $\delta\sigma_0 = 8; 10; 13$ km s^{-1}. Asymmetric uncertainties can be as high as $\delta\sigma_0 = 37$ km s^{-1}.

In Figure 3.1, we compare physical properties of our final sample (blue shading) to the underlying representative population of star-forming galaxies from the 3D-HST survey (grey shading) and to the full KMOS$^{\rm 3D}$ sample (pink lines). Compared to our full KMOS$^{\rm 3D}$ sample, we have not selected preferentially in redshift. In terms of stellar mass, both our full KMOS$^{\rm 3D}$ sample and our kinematic sample include fewer lower mass systems compared to the 3D-HST galaxies, such that our sample is not mass-complete. This is mainly a consequence of the $K_{\rm AB} \lesssim 23$ cut. With respect to the main sequence of star-forming galaxies, however, our kinematic sample follows the distribution of both the full KMOS$^{\rm 3D}$ and the 3D-HST sample. The fraction of systems with effective radii below the population average is smaller for our kinematic sample compared to the 3D-HST and KMOS$^{\rm 3D}$ samples. This is due to our conservative definition of resolved kinematics, where we request measurements over at least $3 \times {\rm PSF}_{\rm FWHM}$, with the primary effect of reducing the number of galaxies with $R_e < 2$ kpc. Generally, for very small systems it is more challenging to recover the intrinsic velocity dispersion, because the kinematics are often unresolved (but see Wisnioski et al., 2018, for a detailed study of the kinematics of compact galaxies in the KMOS$^{\rm 3D}$ survey). Axis ratios of our galaxies are homogeneously distributed, following the KMOS$^{\rm 3D}$ and 3D-HST parent samples (see also Section 3.3.6).

In Figure 3.2, we show SFR (top) and size (bottom) both as a function of stellar mass for the 3D-HST parent sample (grey density histogram), the full KMOS$^{\rm 3D}$ sample (purple diamonds), and our final kinematic sample at redshifts $z \sim 0.9$ (blue circles), $z \sim 1.5$ (green pentagons), and $z \sim 2.3$ (red hexagons). The figure illustrates the homogeneous coverage of the KMOS$^{\rm 3D}$ survey of typical main sequence galaxies over more than two orders of magnitude in stellar mass. Similarly, the galaxies from our final sample are distributed along the main sequence and have typical sizes for their redshifts, with a tendency towards higher-than-average sizes particularly at $z \sim 2.3$. This bias at the highest redshifts is introduced through our conservative definition of resolved galaxies, and ensures robust σ_0 measurements even at these high redshifts.

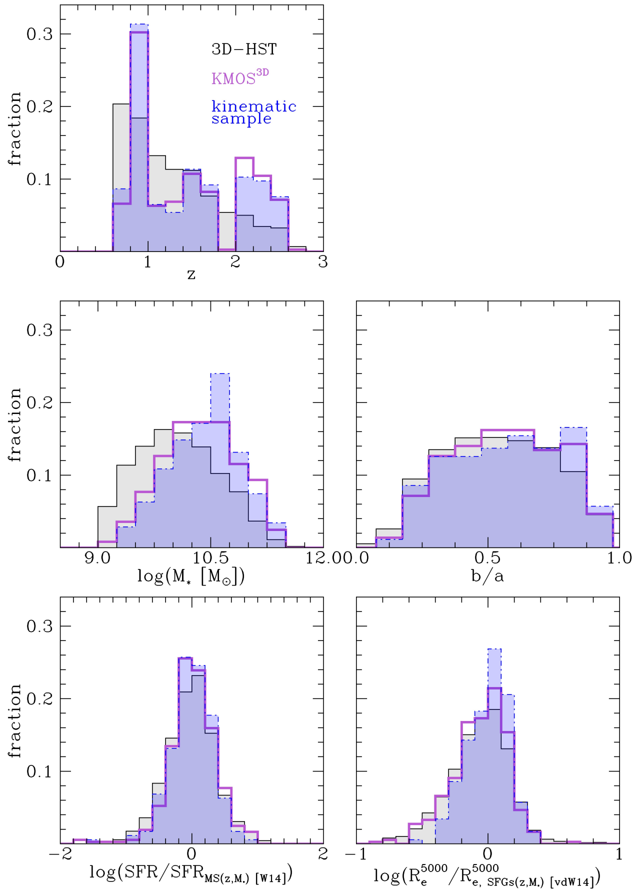

Figure 3.1: *Distribution of physical properties of our kinematic sample (blue shading) compared to the full KMOS*$^{\mathrm{3D}}$ *survey (pink lines) and the underlying star-forming galaxy population at* $0.6 < z < 2.7$ *taken from the 3D-HST source catalog (grey shading) with log*$(M_*/M_\odot) \geq 9$, $K_{\mathrm{AB}} < 23$ *mag, and* $\mathrm{SFR}/M_* > 0.7/t_{\mathrm{Hubble}}$. *We show redshift z (top left), stellar mass (middle left), axis ratio b/a (middle right), offset from the main sequence (bottom left), and offset from the mass-size relation (bottom right). The SFR is normalized to the main sequence as derived by Whitaker et al. (2014) at the redshift and stellar mass of each galaxy, using the redshift-interpolated parametrization by Wisnioski et al. (2015). The effective radii as measured from the H−band are corrected to the rest-frame 5000 Å and normalized to the mass-size relation of SFGs as derived by van der Wel et al. (2014a) at the redshift and stellar mass of each galaxy. For our kinematic sample, there is no selection bias in redshift z, axis ratio b/a, or offset from the main sequence. Due to the* $K_{\mathrm{AB}} < 23$ *mag cut for our KMOS*$^{\mathrm{3D}}$ *survey, KMOS*$^{\mathrm{3D}}$ *galaxies have higher stellar masses compared to the 3D-HST sample. Galaxies in our kinematic sample have on average larger sizes compared to all KMOS*$^{\mathrm{3D}}$ *galaxies as well as the 3D-HST sample. This is due to our conservative definition of resolved kinematics (see Section 3.3.1).*

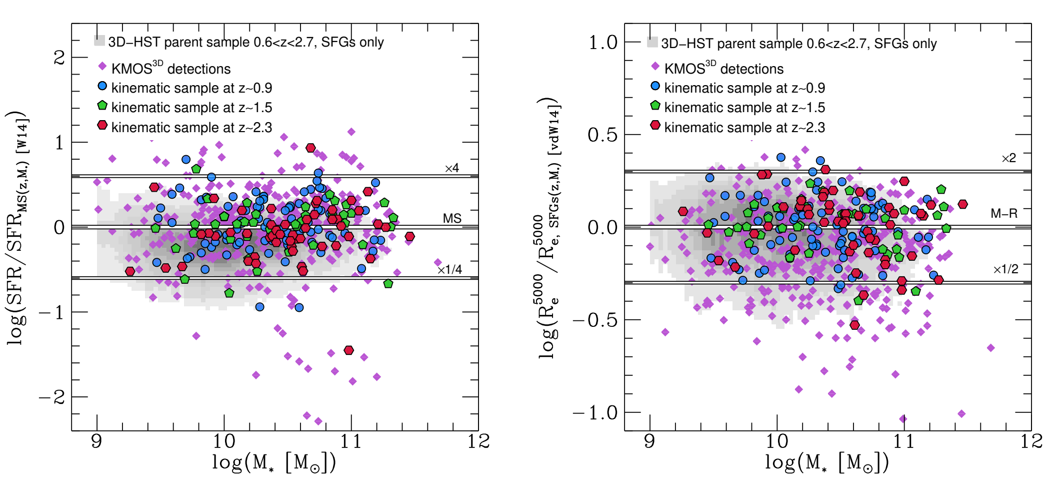

Figure 3.2: *Location of our kinematic sample in the M_*−SFR (left) and $M_* - R_e$ (right) planes as compared to all detected KMOS*^{3D} *galaxies (pink diamonds) and the underlying star-forming galaxy population at* $0.6 < z < 2.7$ *taken from the 3D-HST source catalog (greyscale) with log($M_*/M_\odot$) $\geq$ 9, $K_{\mathrm{AB}} < 23$ mag, and* $\mathrm{SFR}/M_* > 0.7/t_{\mathrm{Hubble}}$. *In the left panel, the SFR is normalized to the main sequence as derived by Whitaker et al. (2014) at the redshift and stellar mass of each galaxy, using the redshift-interpolated parametrization by Wisnioski et al. (2015). In the right panel, the effective radii as measured from the H−band are corrected to the rest-frame 5000 Å and normalized to the mass-size relation of SFGs as derived by van der Wel et al. (2014a) at the redshift and stellar mass of each galaxy. The galaxies in our kinematic sample are distributed along the main sequence, and have typical sizes for their redshifts. However, the size distribution of our targets is biased towards higher-than-average sizes, also compared to our KMOS*^{3D} *parent sample. This is introduced through our selecting only galaxies with resolved kinematics (see Section 3.3.1).*

3.3.4 Upper limit cases

Our final sample contains 28 galaxies for which the best-fit σ_0 value within the 1σ uncertainties is lower than 10 km s^{-1}. In using the Hα line we are supposedly tracing emission originating from ionized HII regions. Due to thermal broadening ($\sigma_{\mathrm{th}} \approx 10$ km s^{-1}) as well as the expansion of HII regions ($v_{\mathrm{ex}} \gtrsim 10$ km s^{-1}), we expect some minimum velocity dispersion for the average galaxy of $\sigma_0 \approx 10 - 15$ km s^{-1} (Shields, 1990).

This minimum value is lower than the typical spectral resolution of KMOS: the effective FWHM spectral resolution at the Hα line measured from the reduced data of galaxies in our KMOS^{3D} survey is $\Delta R = \lambda/\Delta\lambda \sim 3515; 3975; 3860$ in the YJ, H, and K bands, respectively (Wisnioski et al., in prep.). For our kinematic sample, the corresponding mean spectral resolutions are $\sigma_{\mathrm{instrumental}} \sim 37; 32; 34$ km s^{-1}. However, as discussed in more detail in Wisnioski et al., in prep., within the bands there are variations of the spectral resolution of up to $\Delta R = 1000$ for individual IFUs. It is therefore crucial to measure the associated spectral resolution at Hα for each individual galaxy from sky or arc lines in order to reliably recover the velocity dispersion, as it is done for KMOS$^{\rm 3D}$.

Our line fitting procedure can recover intrinsic velocity dispersions that are a fraction of the instrumental resolution. However, these measurements get increasingly uncertain for decreasing intrinsic velocity dispersions. For galaxies for which the best-fit σ_0 value within the 1σ uncertainties is lower than 10 km s^{-1}, we adopt as a conservative upper limit the upper 2σ boundary of the marginalized posterior distribution derived from the MCMC chain. The resulting upper limits lie between 18 and 53 km s^{-1}.

3.3.5 Validation of point spread function and line spread function corrections

Before we investigate in detail the redshift evolution of σ_0 and its potential drivers, we want to exclude any residual effects of beam-smearing. Therefore we consider σ_0 as a function of the effective radius, R_e, and of the ratio of the outermost measured data point to the effective radius, $R_{\rm max}/R_e$.

We do not find significant correlations with R_e or $R_{\rm max}/R_e$, as listed in Table 3.2 (for R_e see also Figure 3.17). We would expect correlations with these parameters if unresolved rotation enters our measure of velocity dispersion. As mentioned in Sections 3.3.1 and 3.3.3, we only consider galaxies for our final sample for which we can extract kinematics over a distance of at least $3 \times \rm PSF_{FWHM}$, with a mean value of $4 \times \rm PSF_{FWHM}$. However, the extracted kinematics can still be affected by beam-smearing even in the outer parts of the galaxies. The fact that we do not find correlations with size implies that our forward-modelling procedure properly accounts for beam-smearing even for the smaller systems we include.

Similarly, we test for correlations of σ_0 with instrumental resolution and again we do not find a significant correlation, indicating that both our kinematic fitting code and forward-modelling procedure properly account for the instrumental line-spread function (see Table 3.2).

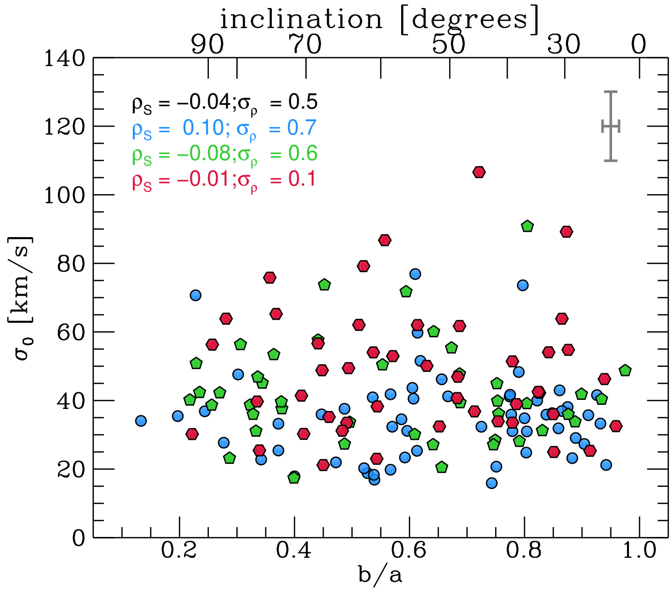

Figure 3.3: *Intrinsic velocity dispersion* σ_0 *as a function of axis ratio* b/a *as measured from the* $H-$*band. Spearman rank correlation coefficients* ρ_S *and their significance* σ_ρ *are given in the panel for the full sample (black) and the redshift slices at* $z \sim 0.9$ *(blue),* $z \sim 1.5$ *(green), and* $z \sim 2.3$ *(red). A typical error bar is shown in the top right corner. We do not find significant correlations between* σ_0 *and* b/a *for the full sample nor the individual redshift bins.*

Table 3.2: *Spearman rank correlation coefficients,* ρ_S*, and their significance* σ_ρ*, between* σ_0 *and respectively* R_e*,* $R_{\max}/R_e$*,* $\sigma_{\text{instrumental}}$*, and* b/a*.*

quantity	ρ_S	σ_ρ
R_e	0.01	1.2
$R_{\max}/R_e$	-0.05	0.7
$\sigma_{\text{instrumental}}$	-0.07	0.9
b/a	-0.04	0.5

3.3.6 Vertical *vs.* radial velocity dispersion

For local galaxies there exists a correlation between galaxy inclination and line-of-sight velocity dispersion. This is due to the transition from measuring predominantly vertical velocity dispersion in face-on systems to measuring predominantly radial velocity dispersion in edge-on systems, with a typical ratio of $\sigma_z/\sigma_r \sim 0.6$ (van der Kruit & Freeman, 2011; Glazebrook, 2013). For instance, Leroy et al. (2008) find for the THINGS sample that the HI line-of-sight velocity dispersion increases for galaxies with $i > 60°$ ($b/a < 0.5$), as does the variation of velocity dispersion in individual galaxies. Intriguingly, evidence for higher velocity dispersions in more edge-on systems has been found in the higher resolution $z \sim 1-2$ data from the SINS survey (Genzel et al., 2011). For our KMOS^{3D} kinematic sample, and in agreement with the earlier results by Wisnioski et al. (2015), we do not find a correlation between σ_0 and b/a, as shown in Figure 3.3 and Table 3.2, possibly due to the coarser spatial resolution of our data.

3.4 Velocity dispersion increases with redshift

Previous studies have shown that the velocity dispersion of star-forming galaxies increases with redshift (Förster Schreiber et al., 2006; Genzel et al., 2006, 2011; Weiner et al., 2006; Kassin et al., 2007, 2012; Wisnioski et al., 2012, 2015; Newman et al., 2013; Simons et al., 2016, 2017; Mason et al., 2017; Turner et al., 2017; Johnson et al., 2018), albeit with large uncertainties and scatter. In the following, we confirm and increase the robustness of this conclusion with the highest quality IFU data now available with KMOS^{3D} on sub-galactic scales, over a wider redshift and mass range than previously, and using a sample purely selected on the basis of disk galaxies near the main sequence at each redshift. We further put our results into the broader literature context, including multi-phase gas velocity dispersion and expanding the redshift range to $0 < z < 4$.

3.4.1 The KMOS^{3D} velocity dispersions from $z = 2.6$ to $z = 0.6$

In Figure 3.4 we show the intrinsic velocity dispersion of our KMOS^{3D} galaxies in the kinematic sample as a function of redshift, where upper limits are indicated as arrows (Section 3.3.4). Our data reflect the known trend of increasing average velocity dispersions with increasing redshift.

To quantify the evolution, we fit a linear relation in $\sigma_0 - z$ space to our best-fit data.[1] We use the Bayesian approach to linear regression by Kelly (2007) which allows for the inclusion of censored data (i.e., upper limits). The routine requires symmetric uncertainties, which we calculate as the mean of the asymmetric uncertainties on σ_0 from our MCMC modelling.[2] Figure 3.4 shows the derived fit as

---

[1] Our results do not depend on this particular functional form, and we list fits in $\sigma_0 - \log(1+z)$ and $\log(\sigma_0) - \log(1+z)$ space in Appendix 3.8.

[2] We assume an uncertainty on z of five times the spectral resolution in each redshift bin, translating into (negligible) uncertainties of $\delta z \sim 0.001 - 0.002$.

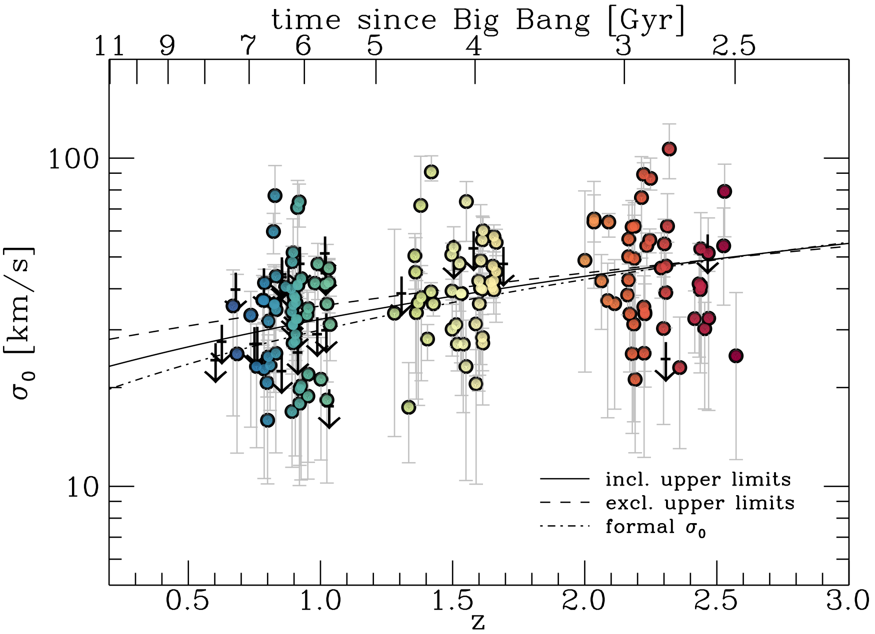

Figure 3.4: *Intrinsic velocity dispersion σ_0 as a function of redshift and cosmic time for our kinematic sample, color-coded by redshift. Upper limits are shown as black arrows. On average, σ_0 increases with redshift, but the scatter at fixed redshift is large. The solid line shows our fiducial linear regression including the upper limits. The dashed line shows a corresponding fit for which the upper limit cases have been entirely excluded, resulting in a slightly shallower evolution. Taking the formal fit results for all galaxies at face value, we find a slightly steeper evolution (dash-dotted line).*

a solid line, with average values of $\sigma_0 \sim 31.1; 38.3; 46.7$ km s^{-1} at $z \sim 0.9; 1.5; 2.3$. The corresponding fit is described by the equation

$$\sigma_0\,[\mathrm{kms}^{-1}] = (21.1 \pm 3.0) + (11.3 \pm 2.0) \cdot z. \tag{3.1}$$

We also perform a ‘robust’ fit where the upper limit cases are not included, but entirely left out. We find a slightly shallower evolution indicated by the dashed line. If, instead, for these galaxies we do not assign upper limits but take the formal median of the posterior distribution at face value, we find a slightly steeper evolution indicated by the dash-dotted line. In Table 3.3 we list our fit parameters and uncertainties.

The σ_0−evolution we derive between $z \sim 0.9$ and $z \sim 2.3$ is slightly shallower than what has been reported for the first year of data from the KMOS^{3D} survey by Wisnioski et al. (2015). In particular, the authors cite $\sigma_0 \sim 24.9$ km s^{-1} at $z \sim 0.9$ and $\sigma_0 \sim 47.5$ km s^{-1} at $z \sim 2.3$, i.e. a difference of $6 - 7$ km s^{-1} for the lowest redshift bin. We partly attribute this difference to our treatment of upper limits. Indeed, if we take the formal best-fit values of the upper limit cases at face value, we find through linear regression a value of $\sigma_0 \sim 28.4$ km s^{-1} at $z \sim 0.9$ (see Table 3.3), reducing the difference to ~ 4 km s^{-1}. This difference is smaller than the uncertainty on the average σ_0 value we derive through our fitting based on the standard deviation of the posterior distribution of the zero-point and slope, which is $\delta\sigma_0 = 4.8$ km s^{-1} for the $z \sim 0.9$ bin.

3.4.2 Quantification of observational uncertainties and the scatter in σ_0

Figure 3.4 shows substantial scatter in σ_0 at fixed redshift with values from $\sigma_0 \approx 20$ km s^{-1} to $\sigma_0 \approx 100$ km s^{-1}. The question is whether this scatter is physical, or purely driven by observational uncertainties.

As listed in Table 3.3, our robust best-fit relation has an intrinsic scatter around the regression with a standard deviation of 10.4 km s^{-1}, suggesting that part of the scatter is indeed due to real variations of the intrinsic dispersion values, and not just due to measurement uncertainties. To quantify the intrinsic variance in each redshift slice, we first calculate the observed variance around the robust best-fit relation, i.e. the variance of the redshift-normalized dispersion values excluding upper limits. The redshift-normalized values are defined as

$$\sigma_{0,\mathrm{norm}} = \sigma_0 - (a + b \cdot z), \tag{3.2}$$

with coefficients a and b as listed in Table 3.3. Then, we perform a Monte Carlo analysis of the scatter due to uncertainties: for each measurement i, we draw 1000 times from a normal distribution $\mathcal{N}(0, \delta\sigma_{0,i})$, where $\delta\sigma_{0,i}$ is the symmetric uncertainty of $\sigma_{0,i}$ derived from our DYSMAL MCMC modelling, and calculate the corresponding sample variance per redshift slice.
We calculate this intrinsic variance as

$$\mathrm{VAR}_{\mathrm{int}}(z) = \mathrm{VAR}_{\mathrm{obs}}(z) - \mathrm{VAR}_{\delta\sigma_0}(z), \tag{3.3}$$

and list the corresponding values in Table 3.4. From this analysis we conclude that at least ∼40–50% of the observed variance, i.e. ∼60–70% of the observed scatter, is due to real variations of the intrinsic dispersion values, mostly independent of redshift. We also show a histogram of the redshift-normalized dispersion values in Figure 3.5, $\sigma_{0,\mathrm{norm}}$, in black, together with a histogram of the Monte Carlo draws from the uncertainty distribution in red. Again, this clearly shows that, even though the uncertainties are substantial, there is residual scatter in our σ_0 distribution beyond what can be accounted for by uncertainties. Further, if we focus on the absolute values listed in Table 3.4, the intrinsic variance increases above $z \sim 1.5$ such that at $z \sim 2.3$ it has doubled compare to $z \sim 0.9$ and $z \sim 1.5$. This suggests that the population of galaxies in our highest redshift bin is more diverse in ISM conditions compared to the lower-redshift samples.

Table 3.3: *Results from the linear regression fits of the form* $\sigma_0/\mathrm{km\,s} = a + b \cdot z + c$ *for our kinematic sample, where* a *and* b *are the regression coefficients, and* c *is the intrinsic random scatter about the regression (see Kelly, 2007). For each parameter* a, b, *the standard deviation of* c, *and the derived linear correlation coefficient* l_{corr} *between* σ_0 *and* z, *we list the median together with the standard deviation of the posterior distribution. For each redshift slice we list the best-fit* σ_0 *value corresponding to these medians.*

sample	N	a [km s^{-1}]	b [km s^{-1}]	σ_c [km s^{-1}]	l_{corr}	σ_0 at $z \sim 0.9$ [km s^{-1}]	σ_0 at $z \sim 1.5$ [km s^{-1}]	σ_0 at $z \sim 2.3$ [km s^{-1}]
including upper limits	175	21.1 ± 3.0	11.3 ± 2.0	11.3 ± 1.1	0.50 ± 0.08	31.1	38.3	46.7
excluding upper limits (robust)	147	26.2 ± 3.1	9.2 ± 2.1	10.4 ± 1.1	0.46 ± 0.09	34.3	40.3	47.1
using formal best-fit σ_0	175	17.2 ± 3.2	12.7 ± 2.2	13.2 ± 1.1	0.49 ± 0.07	28.4	36.7	46.1

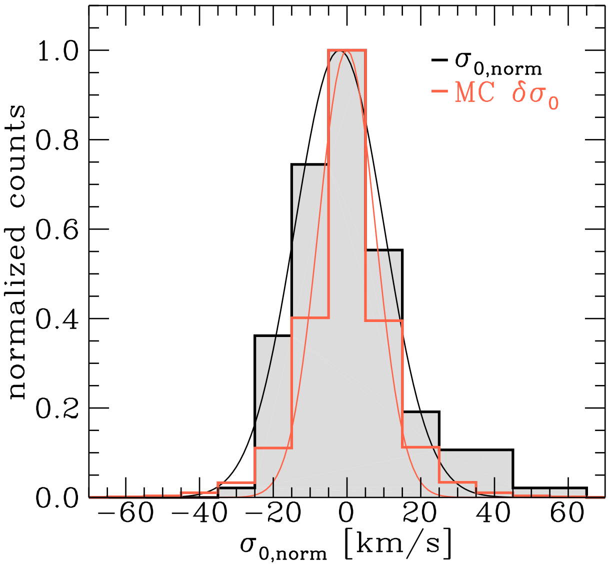

Figure 3.5: *Histogram of redshift-normalized intrinsic dispersion values, $\sigma_{0,\mathrm{norm}}$, in black, and histogram of the contribution to the scatter from uncertainties based on a Monte Carlo analysis in red (see Section 3.4.2 for details). To guide the eye we show simple Gaussian fits to the two distributions as thin curves. There is excess scatter beyond what can be accounted for by uncertainties in the distribution of $\sigma_{0,\mathrm{norm}}$, indicating that we observe real physical variations of σ_0 at fixed redshift (see also Table 3.4).*

Table 3.4: *Variances of σ_0 around the robust best-fit relation: observed variance VAR_{obs}, variance due to measurement uncertainties $VAR_{\delta\sigma_0}$, and intrinsic variance, VAR_{int}.*

measure	$z \sim 0.9$	$z \sim 1.5$	$z \sim 2.3$	$0.6 < z < 2.6$
$\mathrm{VAR_{obs}}$ [km^2 s^{-2}]	171	208	357	237
$\mathrm{VAR}_{\delta\sigma_0}$ [km^2 s^{-2}]	87	130	194	133
$\mathrm{VAR_{int}}$ [km^2 s^{-2}]	85	78	163	104
$\mathrm{VAR_{int}/VAR_{obs}}$	0.50	0.38	0.46	0.44

However, no significant residual trends with $\sigma_{0,\mathrm{norm}}$ and physical properties related to SFR, mass, size, or rotation velocity remain, as we show in detail in Figure 3.16 in Appendix 3.9. That means that we cannot identify a physical source for the scatter in σ_0 at fixed redshift. This might be due to the limited dynamical range of our data, or it could imply that the intrinsic scatter is driven through the interplay of more than one parameter. Alternatively, the scatter could be due to real variations of the velocity dispersion on short timescales, for instance caused by a dynamic driver such as minor mergers or variations in gas accretion from the cosmic web. This has recently been proposed by Hung et al. (2019) based on results from the FIRE simulations, where variations of intrinsic dispersion are connected to variations of the gas inflow rate on time scales $\lesssim 100$ Myr.

3.4.3 Comment on the effect of sample selection

The results presented above and in the remainder of the paper are based on our kinematic sample as defined in Section 3.3.3, i.e. 175 resolved and rotation-dominated disk galaxies that are well-fit by our dynamical model, without strong contamination from OH lines or outflows, and without close neighbours. If we instead consider all modelled galaxies from setup 1, about twice as many compared to the kinematic sample (see Section 3.3.2), we find a similar *median* evolution of $\sigma_0 \approx 31; 40; 49$ km s^{-1} at $z \sim 0.9; 1.5; 2.3$, however the *mean* values in the three redshift slices are systematically higher with $\sigma_0 \approx 34; 45; 58$ km s^{-1}. While at all redshifts the scatter is substantially increased due to galaxies with higher observational uncertainties or poor fits ($\mathrm{VAR_{obs}} \approx 730; 850; 1560$ km^2 s^{-2}), the systematic increase of the mean values is mostly due to the inclusion of dispersion-dominated systems (see e.g. Newman et al., 2013, for a discussion of such galaxies).

3.4.4 Multi-phase gas velocity dispersions from $z = 4$ to $z = 0$

To put the evolution of velocity dispersion from $z = 2.6$ to $z = 0.6$ based on our KMOS^{3D} sample into a broader context, we collect measurements reported in the literature from $z \sim 4$ to $z = 0$, covering 12 Gyr of cosmic history (Table 3.5).

In Figure 3.6 we show again our KMOS^{3D} kinematic sample as clouds of grey circles, including upper limits as arrows, in the $\sigma_0 - z$ space. The median values at $z \sim 0.9; 1.5; 2.3$, shown as large circles in blue, green, and red, are based on the best fit plotted in Figure 3.4 and its uncertainties (see Table 3.3). We include other individual intrinsic dispersion measurements or averages from ionized gas as colored symbols, and atomic and molecular data as black symbols, which are listed in Table 3.5. Error bars show the mean uncertainty of individual systems in those samples. In our comparison, we do not apply any corrections or normalizations in mass (cf. Wisnioski et al., 2015) which are expected to be small for main sequence galaxies (Simons et al., 2017).

In Table 3.5 we also list the different techniques used to correct for beam-smearing effects. As explained in Section 3.3.2 and in the references listed there, we account for beam-smearing effects through a full forward-modelling of both the velocity and velocity dispersion fields with a unique PSF model for each galaxy. Techniques based on only the velocity information, or on grid-based models or look-up tables, might perform less well in their beam-smearing corrections generally resulting in overestimated intrinsic velocity dispersions. For slit surveys, systematic offsets towards higher values might be expected due to the sometimes uncertain galaxy position angle and the resulting difficulties in disentangling rotational and turbulent motions (see Price et al., 2016, 2019, for a discussion and solution approach). Similarly, the methods chosen to calculate or model the intrinsic velocity dispersion might further introduce systematic differences. We note that recent work by Varidel et al. (2019) on a sample of 20 local SFGs suggests that complex structure in the gas distribution may further impact the derived dispersion values.

Figure 3.6 shows generally good agreement of the various σ_0 measurements reported in the literature. Comparing slit *vs.* IFU techniques, the slit measurements shown here, i.e. data from DEEP2, SIGMA, and MOSDEF, have a tendency towards higher values as compared to the averages derived from our KMOS$^{\rm 3D}$ and SINS/zC-SINF surveys, likely for the reasons discussed above, but agree within their uncertainty with the IFU data where available. Interestingly, the deep measurements obtained for individual targets by Genzel et al. (2017), and particularly for the lensed systems by Livermore et al. (2015); Jones et al. (2010) at $1.5 < z < 3$ also tend towards higher σ_0 values, but have moderate values at $z > 3$ in agreement with the averages obtained from seeing-limited IFU and slit spectroscopy by Gnerucci et al. (2011); Turner et al. (2017); Price et al. (2019). Generally, the statistical power of these time-intensive and challenging individual measurements is still very limited. Systematic differences in σ_0 may arise through selection effects: for instance, the nearby galaxies from the DYNAMO sample are selected to be $z \sim 2$ analogues and have many physical properties, including dispersions, similar to high$-z$ SFGs (see Green et al., 2014; White et al., 2017; Fisher et al., 2019).

In contrast, the molecular and atomic data indicated by black points suggest somewhat lower values on average, particularly at $z \approx 0$. Levy et al. (2018) study 17 nearby, rotation-dominated SFGs in CO and ionized gas. They find consistently higher rotation velocities ($<v_{\rm CO} - v_{\rm H\alpha}> \approx 14$ km s^{-1}) and lower velocity dispersions ($<\sigma_{\rm CO} - \sigma_{\rm H\gamma}> \approx -17$ km s^{-1}) for the molecular gas as compared to the ionized gas (see also Cortese, Catinella, & Janowiecki, 2017, for a comparison at $z \sim 0.2$). At high redshift, there exist only few multi-phase measurements of the intrinsic gas velocity dispersion. Detailed observations reveal comparable values for ionized and molecular gas (Genzel et al., 2013; Übler et al., 2018), however the uncertainties are larger such that differences like those found locally could be washed out.

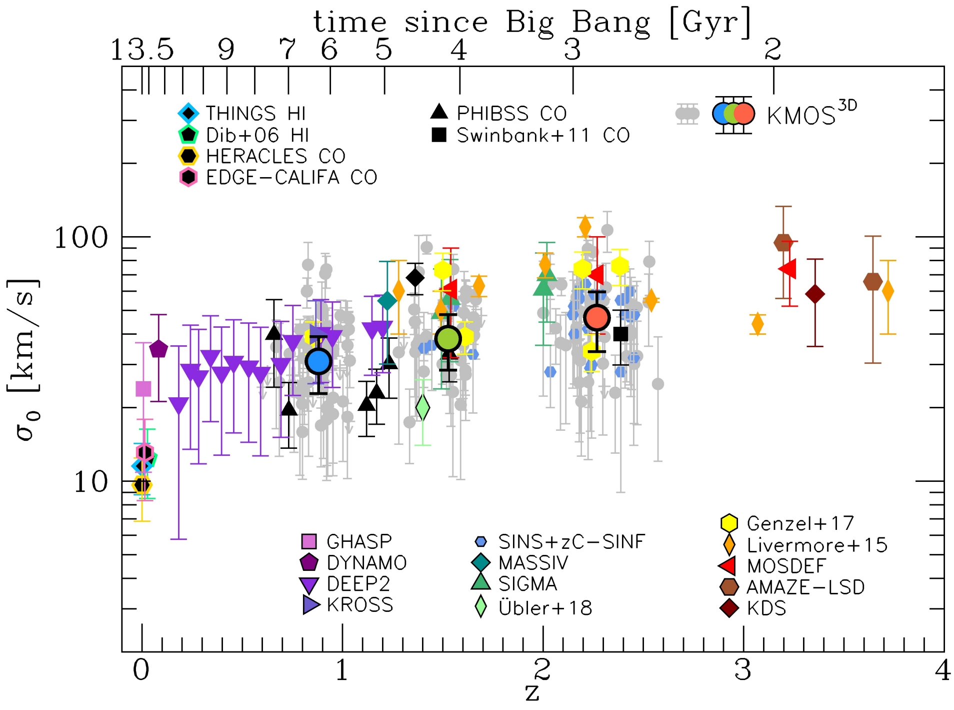

Figure 3.6: *Intrinsic velocity dispersion σ_0 as a function of redshift and cosmic time for measurements from the literature at $0 < z < 4$ (see Table 3.5). Our kinematic sample is shown in grey, with colored averages. Other individual and average ionized gas measurements are shown in color, as indicated in the legend. Molecular and atomic gas measurements are shown in black. For averages, the error bar shows the typical uncertainty of individual measurements in the sample.*

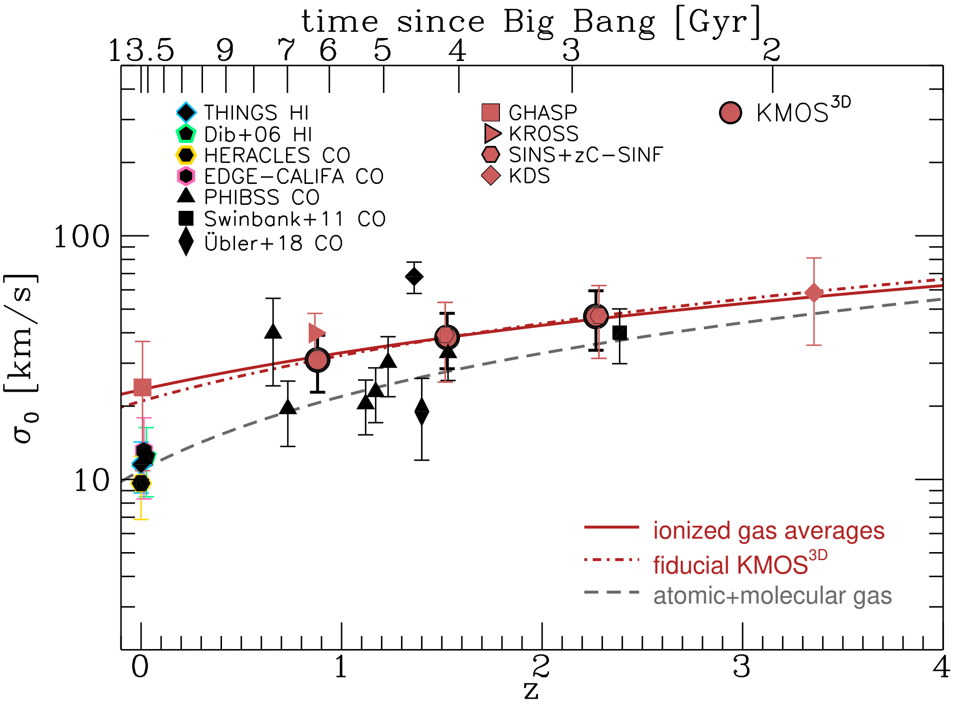

Figure 3.7: *Intrinsic velocity dispersion σ_0 as a function of redshift and cosmic time for measurements from the literature at $0 < z < 4$ (see Table 3.5). Averages from selected ionized gas measurements are shown in red. Local atomic and molecular averages and individual high−z molecular gas measurements are shown in black. Based on these data, we show best-fit relations (see Table 3.6) for molecular gas (grey dashed) and ionized gas (red solid), as well as the best fit derived solely on our KMOS$^{3\mathrm{D}}$ data (red dash-dotted, see Section 3.4.1 and Table 3.3). Confirming the trend seen in our kinematic sample for the redshift range $0.6 < z < 2.6$, σ_0 increases with redshift over a time span of almost 12 Gyr. In the local Universe, velocity dispersions measured from molecular or atomic gas are lower than corresponding measurements from ionized gas, by ca. 10–15 km s^{-1}. The slopes derived from the molecular data and from our KMOS$^{3\mathrm{D}}$ sample are almost identical, suggesting an analogous redshift evolution of the different gas phase velocity dispersions.*

Table 3.5: *Literature data of the* $0 < z < 4$ *velocity dispersion measurements shown in Figure 3.6.*

Sample/References	z	Primary Target Line	N included	Instrument/Method	BS correction	Comment on Selection
KDS	3.8 − 3.1	[OIII]	14	KMOS/IFU	(1)	their 'RD'
MOSDEF	3.8 − 1.4	Hα, Hβ, [OIII]	108	MOSFIRE/slit	(2)	their 'resolved/aligned'
AMAZE-LSD	3.7 − 3.1	[OIII]	11	SINFONI/IFU	(1)	their 'rotating'
Livermore et al. (2015)	3.7 − 1.3	Hα, Hβ	8	SINFONI+NIFS+OSIRIS/IFU+lensing	(3)	their 'Disk' with $v_{\rm rot}/\sigma_0 > 1$
KMOS^{3D}	2.6 − 0.6	Hα	175	KMOS/IFU	(2)	see Section 3.3.3
SINS/zC-SINF	2.5 − 1.4	Hα	25	SINFONI/IFU+AO	(2)	see Section 3.3.3
SIGMA	2.5 − 1.3	Hα, [OIII]	49	MOSFIRE/slit	(4)	
Genzel et al. (2017)	2.4 − 0.9	Hα	6	KMOS+SINFONI/IFU+AO	(2)	see Section 3.3.3
MASSIV	1.6 − 0.9	Hα, [OIII]	53	SINFONI/IFU	(1)	
DEEP2	1.2 − 0.1	Hα, Hβ, [OII], [OIII]	544	DEIMOS/slit	(4)	
KROSS	1.0 − 0.8	Hα	171	KMOS/IFU	(4)	their 'sigma0_flag=O' with $v_{2.2}/\sigma_0 > 1$
DYNAMO	∼ 0.1	Hα	25	SPIRAL+WiFeS/IFU	(1)	their 'RD'
GHASP	local	Hα	153	scanning Fabry-Perot	(1)	
Übler et al. (2018)	1.4	Hα, CO(3–2)	1	LUCI/slit+NOEMA/interferometry	(2)	see Section 3.3.3
Swinbank et al. (2011)	2.4	CO(6–5), CO(1–0)	1	IRAM+EVLA/interferometry	(3)	
PHIBSS	1.5 − 0.7	CO(3–2)	7	IRAM+NOEMA/interferometry	(4)	see Section 3.3.3
HERACLES	local	CO(2–1)	13	IRAM/single dish	(5)	
EDGE-CALIFA	local	CO(1–0)	17	CARMA/interferometry	(1)	
THINGS	local	HI	35	VLA/interferometry	(5)	
Dib, Bell, & Burkert (2006)	local	HI	13	literature compilation		

Note: Beam-smearing (BS) correction methods: (1) correction map derived from the model velocity field including two-dimensional PSF; (2) simultaneous forward-modelling of both the velocity and dispersion including two-dimensional PSF, cf. Section 3.3.2; (3) subtraction in quadrature of the velocity gradient across each spaxel; (4) model-based look-up grid; (5) exclusion of regions most strongly affected based on a model grid. References: KDS Turner et al. (2017), MOSDEF Kriek et al. (2015); Price et al. (2019), AMAZE-LSD Gnerucci et al. (2011), KMOS^{3D} Wisnioski et al. (2015); Wisnioski et al. (in prep.), SINS/zC-SINF Förster Schreiber et al. (2006, 2009, 2018), SIGMA Simons et al. (2016, 2017), MASSIV Contini et al. (2012); Epinat et al. (2012), DEEP2 Davis et al. (2003); Kassin et al. (2007, 2012), KROSS Stott et al. (2016); Johnson et al. (2018), DYNAMO Green et al. (2014), GHASP Epinat, Amram, & Marcelin (2008); Epinat et al. (2010), PHIBSS Tacconi et al. (2013); Freundlich et al. (2019), HERACLES Leroy et al. (2009); Tamburro et al. (2009); Caldú-Primo et al. (2013); Mogotsi et al. (2016), EDGE-CALIFA Bolatto et al. (2017); Levy et al. (2018), THINGS Walter et al. (2008); Tamburro et al. (2009); Ianjamasimanana et al. (2012); Caldú-Primo et al. (2013); Mogotsi et al. (2016).

3.4.5 Multi-phase gas velocity dispersions evolve similarly with redshift

We quantify the difference between the atomic+molecular and the ionized gas velocity dispersions over cosmic time in Figure 3.7. Fitting a robust linear relation[3] to the average local and individual high$-z$ measurements of atomic+molecular gas, we find a zero point of $a = 10.9 \pm 0.6$ km s^{-1} and a slope of $b = 11.0 \pm 2.0$ km s^{-1} (grey dashed line). For the ionized velocity dispersion, we choose in addition to our own averages from the KMOS^{3D} and SINS/zC-SINF surveys the other large KMOS surveys, KROSS and KDS, and the local average from the GHASP survey. This choice maximizes the redshift range and avoids systematic effects at $z > 0$ through different instrumentation. We find a higher zero-point offset of $a = 23.3 \pm 4.9$ and a somewhat shallower slope of $b = 9.8 \pm 3.5$, while the extrapolation of our best fit to the KMOS^{3D} data only gives $a = 21.1 \pm 3.0$ and $b = 11.3 \pm 2.0$ (Table 3.3). Fixing the slope to that of the atomic+molecular fit, the zero point shifts in between these measurements, with $a = 22.8$. In Table 3.6 we list our fit parameters and uncertainties.

Table 3.6: *Results and standard deviations from the robust least-squares linear regression fits of the form* $\sigma_0/\mathrm{km\,s} = a + b \cdot z$ *to the data sets shown in Figure 3.7.*

sample	a [km s^{-1}]	b [km s^{-1}]
ionized gas (best averages)	23.3±4.9	9.8±3.5
... fixing slope to atomic+molecular	22.8	11.0 (fixed)
KMOS^{3D} incl. upper limits (Table 3.3)	21.1±3.0	11.3±2.0
atomic+molecular gas	10.9±0.6	11.0±2.0

This suggests that the redshift evolution of the intrinsic velocity dispersion in all gas phases is quite comparable, but their normalization differs. Typical thermal broadening of the atomic/molecular and the ionized gas due to their characteristic temperatures are ~ 5 km s^{-1} and ~ 10 km s^{-1}, respectively, meaning the measured velocity dispersions are super-thermal even in the local Universe. Part of the difference between atomic+molecular and ionized gas velocity dispersions can be explained through the expansion of HII regions from which the ionized emission originates, with typical values of $10 - 25$ km s^{-1} (Shields, 1990), accounting for another $\sim 5 - 15$ km s^{-1} when added in quadrature. In combination, these effects can explain the difference in the local normalizations of the gas phase velocity dispersions, as well as their average offset of $\sim 10 - 15$ km s^{-1} at fixed redshift.

Clearly, more studies of high$-z$ molecular kinematics are warranted to corroborate our result, which potentially has important implications for work on

---

[3] We use the least trimmed squares method by Cappellari et al. (2013).

ionized gas kinematics.

3.4.6 Comments on thin *vs.* thick disk evolution

Figure 3.7 shows a smooth evolution of velocity dispersion with redshift over the past ~ 12 Gyr, likely connected to decreasing accretion rates and gas fractions with cosmic time (see Sections 3.5.3 and 3.5.4). This evolution suggests that also the typical thickness of the *young, star-forming gas disk* is lower for lower redshift SFGs, as has also been found in state-of-the-art cosmological simulations (Pillepich et al., 2019).

This is potentially interesting in the context of Galactic archeology: early research of the vertical structure of our Milky Way found evidence for two main, distinct exponential disks with scale heights of ~ 300 pc and ~ 1450 pc (Gilmore & Reid, 1983). This was confirmed through later work on the Milky Way as well as nearby edge-on galaxies (e.g. Dalcanton & Bernstein, 2002; Yoachim & Dalcanton, 2006; Jurić et al., 2008). The thick disk components have been found to be generally older (> 6 Gyr) than the thin disks, raising the question of distinct formation periods. Naturally, observations of the typically thick high$-z$ disks also prompted the question of the connection between these early thick disks and modern disk structure (e.g. Elmegreen & Elmegreen, 2006).

To explicitly address the question of distinct formation periods of thin *vs.* thick disks, we make the simple assumption of a step function describing σ_0 of the ionized gas below and above $z = 1$. Unsurprisingly, the resulting fit with $\sigma_0 = 28$ km s^{-1} at $z < 1$ and $\sigma_0 = 42$ km s^{-1} at $z > 1$ is not a good description of the compiled data, with a goodness of fit that is a factor ~ 20 worse compared to the linear fit shown in Figure 3.7.

Our results suggest that in the absence of recent major mergers it should depend primarily on the star-formation history (connected to gas accretion) if present-day galaxies have distinct disks of different age and scale height, or if there is rather one component with a vertical age gradient (see also Leaman et al., 2017). This interpretation is in agreement with the recent work by Bovy et al. (2012, 2016); Rix & Bovy (2013) who argue based on elemental abundances that the Milky Way has a continuous range of different scale heights, with no sign of a thin-thick disk bimodality. Simulations by e.g. Burkert, Truran, & Hensler (1992); Aumer, Binney, & Schönrich (2016); Aumer & Binney (2017); Grand et al. (2016) support this picture.

However, in this context it is important to remember that based on stellar and gas masses of our galaxies and results from co-moving number density studies (e.g. Brammer et al., 2011), only the lower mass, lower redshift systems in our sample may evolve into present-day disk galaxies, while the galaxies that have high baryonic masses already at high redshift will most likely evolve into present-day's early-type galaxies. With our data, we do therefore not necessarily track the change in star-forming scale height over time for progenitor-descendant populations, but rather the change in average star-forming scale height of main sequence galaxies at different epochs.

3.5 What drives the gas velocity dispersion?

3.5.1 Galaxy-scale velocity dispersion correlates with gas mass and SFR properties

The redshift dependence of σ_0 suggests that one or more physical galaxy properties that are themselves redshift-dependent drive velocity dispersion. Consistent with previous findings in the literature (e.g. Johnson et al., 2018), we find several properties positively correlating with σ_0, particularly, SFR, SFR surface density $\Sigma_{\rm SFR}$, gas and stellar mass, and their surface densities. We list direct and residual (after correcting for redshift dependence) Spearman rank correlations in Table 3.7 and show plots for several quantities in Figure 3.17 in Appendix 3.9. In Table 3.7, we also list $\rm SFR_{H\alpha}$ and $\Sigma_{\rm SFR,H\alpha}$ derived from the Hα fluxes (see Wisnioski et al., in prep.), tracing the more recent star formation history, but find no appreciable difference in correlations compared to our fiducial SFR properties (see Section 3.2).

We emphasize that due to the limited dynamical range covered by the individual redshift slices, we do not find significant correlations of σ_0 within one redshift slice with any of the above properties, such that we cannot readily connect the scatter in σ_0 at fixed redshift to a physical driving source. Similarly, if we remove the redshift dependence of σ_0 by normalizing with our best-fit relation, we do not find any significant correlations of the normalized σ_0 with physical properties (see Section 3.4.2 and Figure 3.16).

Over the full redshift range covered by our KMOS$^{\rm 3D}$ survey, SFR and gas mass correlate most strongly and significantly with intrinsic velocity dispersion. In order to identify which of these two physical quantities is most directly tied to the elevated velocity dispersions at high redshift, we discuss in the following sections the physical mechanisms through which quantities such as SFR and gas mass may affect velocity dispersion, namely stellar feedback and gravitational instabilities, and we comment on the tentative connection to AGN feedback for individual galaxies.

Table 3.7: *Spearman rank correlation coefficients ρ_{S}, and their significance σ_ρ, between σ_0 and different galaxy properties for our robust sample before and after accounting for the redshift dependence of σ_0 .*

	$\sigma_0(z)$		$\sigma_{0,\mathrm{norm}}$	
quantity	ρ_{S}	σ_ρ	ρ_{S}	σ_ρ
z	0.33	4.0	–	–
SFR	0.38	4.6	0.18	2.1
Σ_{SFR}	0.32	3.9	0.06	1.0
M_{gas}	0.38	4.6	0.19	2.3
Σ_{gas}	0.31	3.8	0.07	0.9
M_*	0.26	3.1	0.20	2.4
Σ_*	0.26	3.1	0.14	1.6
M_{bar}	0.32	3.9	0.20	2.4
Σ_{bar}	0.30	3.6	0.12	1.5
ΔMS	–	–	0.15	1.8
ΔMR	–	–	-0.05	0.6

3.5.2 Stellar feedback

Turbulence-driving can be provided through thermal and momentum feedback from massive stars. Correlations between intrinsic velocity dispersion and SFR properties have previously been reported in the literature (e.g. Dib, Bell, & Burkert, 2006; Lehnert et al., 2009, 2013; Green et al., 2010, 2014; Moiseev, Tikhonov, & Klypin, 2015; Johnson et al., 2018), and often invoked the argument for stellar feedback-driven turbulence.

From a theoretical point of view, feedback-driven turbulence is mainly generated through momentum injection from supernovae into the ISM (contributions to the momentum injection from e.g. expanding HII regions or stellar winds are minor, see Mac Low & Klessen, 2004; Ostriker & Shetty, 2011). Feedback-driven turbulence should therefore primarily depend on the decay rate of turbulence, the momentum injected per supernova, and the supernova rate, where the latter is the quantity connecting turbulence to SFR and Σ_{SFR}. Ostriker & Shetty (2011) and Shetty & Ostriker (2012) derive a weak dependence of σ_0 on star formation rate surface density. Even considering the case where stellar feedback maximally vertically stabilizes the disk, the resulting velocity dispersions are low (Equation (22) by Ostriker & Shetty, 2011):

$$\sigma_z = 5.5\ \mathrm{kms}^{-1} \cdot \frac{f_p}{(1+\chi)^{1/2}} \left(\frac{\epsilon_{\mathrm{ff}}(\rho_0)}{0.005}\right) \left(\frac{p_*/m_*}{3000\ \mathrm{kms}^{-1}}\right). \tag{3.4}$$

Here, f_p is a factor characterizing the evolution of turbulence, with $f_p = 1$ for strong dissipation, and $f_p = 2$ for weak dissipation. χ is a measure of the importance of the gas disk's self-gravitational weight, and is below 0.5 for marginally

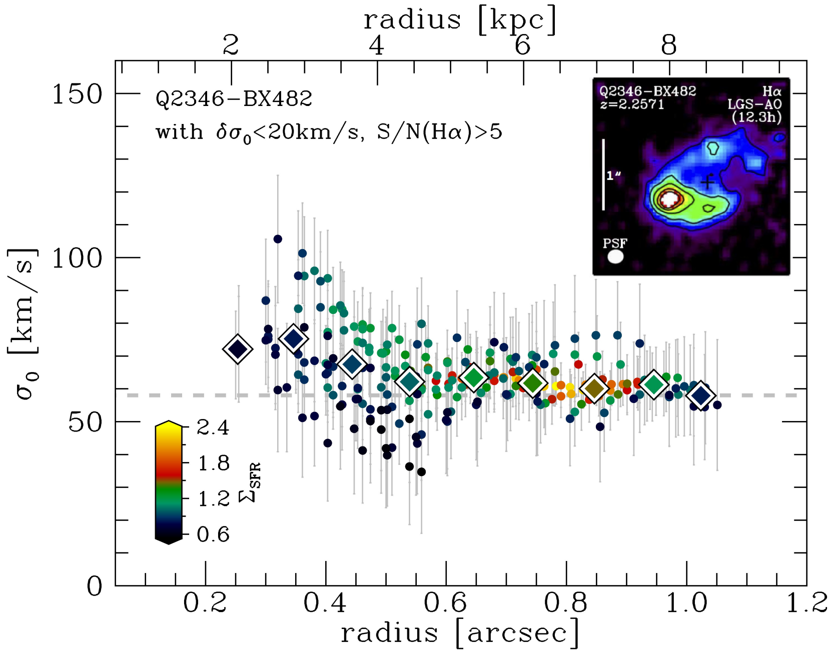

Figure 3.8: *Intrinsic local velocity dispersion σ_0 as a function of radius for galaxy Q2346-BX482, measured from individual spaxels (circles) and color-coded by local Σ_{SFR} (adopted from Figure A1 by Genzel et al., 2011). Larger diamonds show the running median. The grey dashed line shows the best-fit intrinsic velocity dispersion from kinematic modelling where σ_0 is assumed to be constant. The inset in the top right corner shows the projected map of Hα flux, featuring the bright star-forming clump to the South-East, adopted from Figure 16 by Förster Schreiber et al. (2018). There is no correlation between local Σ_{SFR} and local velocity dispersion.*

stable disks, such that the first factor is in the range $\sim 0.8-2$. The mean star formation efficiency $\epsilon_{\mathrm{ff}}(\rho_0)$ is assumed to be approximately constant with a fiducial value of $\epsilon_{\mathrm{ff}}(\rho_0) = 0.005$. $p_*/m_* = 3000$ km s^{-1} is the fiducial value of momentum injection per supernova (but see e.g. Fisher et al., 2019, for arguments for a z-dependent p_*/m_*). As a result, the gas velocity dispersion is expected to vary only mildly due to supernova explosions.

Similar results are obtained by other theoretical models investigating stellar feedback as the sole driver of the turbulence in the ISM, for instance the models discussed by Dib, Bell, & Burkert (2006); Joung, Mac Low, & Bryan (2009); Kim, Ostriker, & Kim (2013). In fact, the resulting velocity dispersions in the ISM do not even seem to depend much on the supernova rate. Rather, very high supernova rates might create super-bubble structures that, instead of stirring the ambient medium, will eventually blow out of the galactic disk, thus transferring energy and metals into the circum-galactic medium (Mac Low, McCray, & Norman, 1989; Joung, Mac Low, & Bryan, 2009; Baumgartner & Breitschwerdt, 2013;

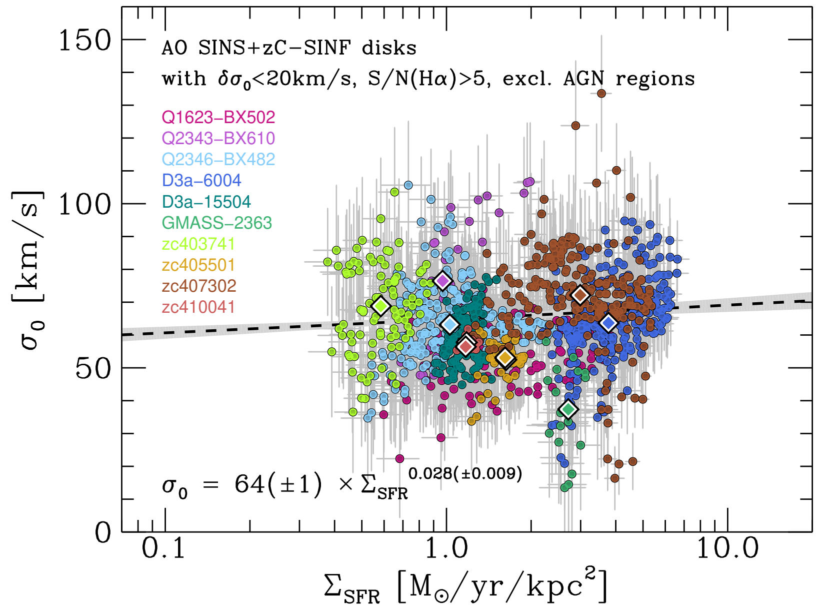

Figure 3.9: *Intrinsic local velocity dispersion* σ_0 *as a function of star formation rate surface density* $\Sigma_{\rm SFR}$*, measured from individual spaxels in ten galaxies from the SINS/zC-SINF survey adaptive optics follow-up. We select spaxels with* $\delta\sigma_0 < 20$ *km* s^{-1}*, S/N(Hα)>5, and exclude the regions of three galaxies that are affected by AGN feedback. Colored circles correspond to data from the different galaxies as listed in the legend, and larger diamonds show the median values. The black dashed line shows the linear regression to the individual spaxel data, with fit uncertainties shown as grey shading, as given in the bottom of the figure*

Kim & Ostriker, 2018). This is an important result because at higher redshift also the supernova rate is higher. However, other work indicates that not only the rate but also the *location* of supernovae is crucial for the efficiency of stellar feedback turbulence driving: considering peak driving, where supernovae go off in the densest ISM regions (e.g. their birth clouds), Gatto et al. (2015) find local Hα velocity dispersions of up to 60 km s^{-1} for gas mass surface densities of $\Sigma_{\rm gas} \sim 100\ M_\odot$ pc^{-2}. This is similar to high$-z$ conditions and therefore suggests that stellar feedback can more easily maintain elevated velocity dispersions at higher redshift. Also, some idealized simulations of isolated galaxies are able to produce velocity dispersion of ~ 50 km s^{-1} from strong stellar feedback (Hopkins, Quataert, & Murray, 2011).

If stellar feedback is an important factor in powering turbulence, then not only would the (observed) global scaling of velocity dispersion with SFR or $\Sigma_{\rm SFR}$ be expected, but particularly locally elevated velocity dispersion in regions of high star formation rate density (cf. Gatto et al., 2015). We exploit the high-resolution data from the SINS-zC/SINF AO survey (Förster Schreiber et al., 2018) to study local correlations between $\Sigma_{\rm SFR}$ and σ_0. In Figure 3.8 we show the local intrinsic velocity dispersion per spaxel of galaxy Q2346-BX482 as a function of radius, color-coded by $\Sigma_{\rm SFR}$ (adopted from Figure A1 by Genzel et al., 2011). The local intrinsic velocity dispersion is derived from the observed dispersion map, after correcting all instrumental and beam-smearing effects through modelling. In the vicinity of the giant star-forming clump ~ 6.5 kpc South-East from the center (inset), no elevated velocity dispersion can be registered.

In Figure 3.9 we show the local intrinsic velocity dispersion per spaxel as a function of local $\Sigma_{\rm SFR}$ for ten SINS/zC-SINF galaxies. The velocity dispersions of these galaxies with a mean redshift of $z \sim 2.2$ have somewhat higher values compared to our KMOS$^{\rm 3D}$ sample, consistent with their higher average SFR and $\Sigma_{\rm SFR}$. Only two of these galaxies show an intrinsic scaling of σ_0 with $\Sigma_{\rm SFR}$. The best-fit power-law relation derived from this sub-galactic, high-quality data shows a very weak dependence of local σ_0 on $\Sigma_{\rm SFR}$,[4] confirming the earlier findings by (Genzel et al., 2011, see also Patrício et al., 2018; Tadaki et al., 2018; but Swinbank et al., 2012a). Similar results are found for both ionized gas (Varidel et al., 2016; Zhou et al., 2017) and molecular gas (Caldú-Primo & Schruba, 2016) in local galaxies. For atomic gas, several studies of local galaxies find correlations with SFR or $\Sigma_{\rm SFR}$ that are too weak to explain the turbulent velocities in the galaxy outskirts (e.g. Tamburro et al., 2009; Ianjamasimanana et al., 2015; Utomo, Blitz, & Falgarone, 2019).

In summary, while global σ_0 correlates with SFR properties, we do not find a direct connection between high, *local* star-formation activity and elevated σ_0, as suggested by some simulations. Generally, however, simulations and models agree that stellar feedback is able to maintain galaxy-wide turbulence on scales of 10-20 km s^{-1}.

3.5.3 Marginally Toomre-stable disks

Turning to gravity-driven turbulence, an empirical model to describe the redshift evolution of velocity dispersion is that of marginally stable disks, where (non-interacting) galaxies are subject to gas replenishment from the halo or the cosmic web, and to gas loss through either outflows or star formation (Noguchi, 1999; Silk, 2001; Immeli et al., 2004a,b; Förster Schreiber et al., 2006; Elmegreen et al.,

---

[4] This finding does not extend to nuclear regions, since more complex circum-nuclear kinematic structure caused by a combination of nuclear outflows, radial inflow and bulge induced rotation in a number of cases generates unresolved velocity fields that appear as an increased velocity dispersion. To explore its true nature will require $< 0.1''$ IFU spectroscopy on 30 m class telescopes.

2007; Genzel et al., 2008; Dekel et al., 2009; Dekel & Burkert, 2014; Bouché et al., 2010; Krumholz & Burkert, 2010; Krumholz & Burkhart, 2016; Cacciato, Dekel, & Genel, 2012; Davé, Finlator, & Oppenheimer, 2012; Lilly et al., 2013; Saintonge et al., 2013; Rathaus & Sternberg, 2016; Leaman et al., 2017). In this framework, the (in)stability of the disk directly corresponds to the level of turbulence in the interstellar medium, where turbulence is fed through external (accretion) and internal (radial flows, clump formation) events via the release of gravitational energy, creating a self-regulation cycle to maintain marginal stability (Dekel et al., 2009; Genel, Dekel, & Cacciato, 2012; but see Elmegreen & Burkert, 2010).

For a snapshot in time that represents the observation of a high$-z$ galaxy, this equilibrium situation is captured through the Toomre Q parameter (Toomre, 1964), where generally $Q < Q_{\rm crit} \approx 1$ indicates gravitational instability. Considering the one-component approximation for a gas disk, we can write (Binney & Tremaine, 2008; Escala & Larson, 2008; Dekel, Sari, & Ceverino, 2009)

$$Q_{\rm gas} = \frac{\sigma_0 \kappa}{\pi G \Sigma_{\rm gas}} = \frac{\sigma_0}{\pi G \Sigma_{\rm gas}} \frac{a v_c(r)}{r}. \tag{3.5}$$

Here, κ is the epicyclic frequency, a is a constant taking values of 1 and $\sqrt{2}$ for Keplerian and constant rotation velocity, respectively, and v_c is the circular velocity tracing the dynamical mass.

The framework of Toomre-(in)stability generally refers to the linear regime, where perturbations are assumed to be axisymmetric. The galaxies studied here, however, are in the non-linear limit where the ISM is turbulent and many stars have formed (Mandelker et al., 2014). Inoue et al. (2016) investigated the stability of simulated high$-z$ disks, finding that large parts of the disks are in the non-linear regime with $Q > 1-3$. This result however depends on gas fraction, which is generally too low in the simulations. Indeed, for those simulated galaxies with the highest gas fractions ($f_{\rm gas} \sim 0.4$, still lower than for typical $z \sim 2$ SFGs), Inoue et al. (2016) find values more compatible with observational findings. Meng, Gnedin, & Li (2019) argue in recent work that the Toomre$-Q$ linear stability analysis is still applicable to simulated high$-z$ galaxies, with values of $Q \sim 0.5 - 1$ in gas-rich regions (see also Behrendt, Burkert, & Schartmann, 2015, for simulations of isolated gas-rich disks).

Generally, for a multi-component system an effective Q parameter has to be computed, $Q_{\rm eff}^{-1} = \sum_i Q_i^{-1}$, where i refers to e.g. stars or different gas phases (e.g. Wang & Silk, 1994; Escala & Larson, 2008; Genzel et al., 2011; Romeo & Falstad, 2013; Obreschkow et al., 2015, and references therein). Simulations of galaxy formation support a picture where $Q_{\rm eff} \sim 1$ for high$-z$ galaxies, and $Q_{\rm eff} \sim 2-3$ for low$-z$ galaxies where the increasing impact of a stellar disk increases $Q_{\rm crit}$ (Hohl, 1971; Athanassoula & Sellwood, 1986; Bottema, 2003; Immeli et al., 2004a; Kim & Ostriker, 2007; Agertz et al., 2009; Agertz, Teyssier, & Moore, 2009; Aumer

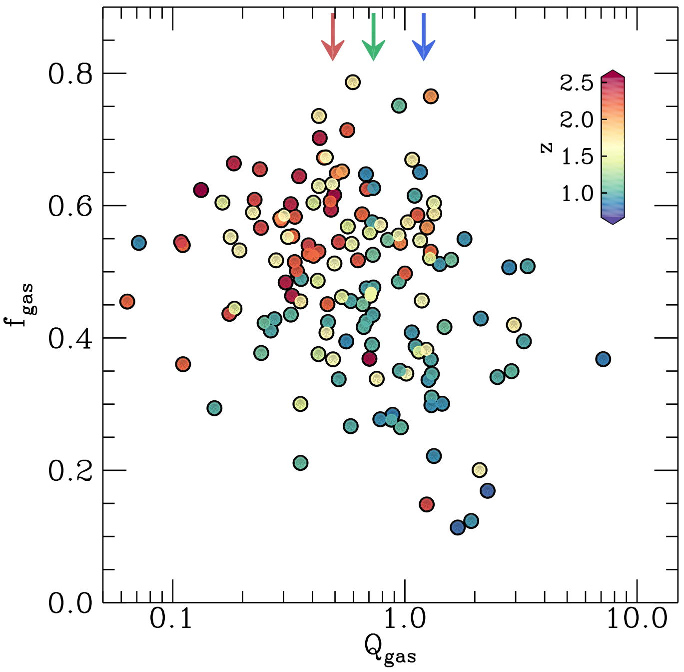

Figure 3.10: *Gas-to-baryonic mass fraction* $f_{\rm gas}$ *as a function of* $Q_{\rm gas}$*, color-coded by redshift. The arrows indicate the average value of* $Q_{\rm gas}$ *at* $z \sim 0.9$ *(blue),* $z \sim 1.5$ *(green), and* $z \sim 2.3$ *(red).* $f_{\rm gas}$ *and* $Q_{\rm gas}$ *are weakly anti-correlated with Spearman rank correlation coefficient* $\rho_S = -0.30$ *and significance* $\sigma_\rho = 3.6$*. Higher−z galaxies with higher gas fractions reach values below* $Q_{\rm gas} = 1$*.*

et al., 2010; Ceverino, Dekel, & Bournaud, 2010; Hopkins, Quataert, & Murray, 2011; Genel et al., 2012; Danovich et al., 2015). For gas-rich, thick disks instead $Q_{\rm crit}$ decreases, such that for $z \gtrsim 1$ galaxies values $Q_{\rm crit} \approx 0.7$ are expected (e.g. Goldreich & Lynden-Bell, 1965; Kim & Ostriker, 2007; Wang et al., 2010; Romeo & Agertz, 2014; Behrendt, Burkert, & Schartmann, 2015).

It has been shown that the gas-rich, star-forming disks observed at high redshift are at most marginally stable to gravitational fragmentation (Genzel et al., 2011; see also Swinbank et al., 2017; Johnson et al., 2018; Tadaki et al., 2018; and Fisher et al., 2017 for local high$-z$ analogues), and Wisnioski et al. (2015) have shown that the redshift evolution predicted by Equation (3.5) for $Q \sim 1$ gas disks is in remarkable agreement with observations (see also e.g. Green et al., 2014; Turner et al., 2017; White et al., 2017; Johnson et al., 2018). In addition, Genzel et al. (2011) have shown that on sub-kpc spatially resolved scales, values of $Q \sim 0.2$ can be reached in regions of star-forming clumps, possibly demonstrating gravitational fragmentation at work.

We calculate $Q_{\rm gas}$ for our galaxies following Eq. (3.5) by evaluating the circular velocity at $v_c(r = 1.38R_e)$. As mentioned in Section 3.3.3, this radius corresponds to the theoretical peak of a Noordermeer disk with $n_S = 1$, such that the local gradient of the rotation curve is flat, leading to $a = \sqrt{2}$. The circular velocity v_c is computed from the model rotation velocity corrected for pressure support from the turbulent motions (Burkert et al., 2010, 2016; Wuyts et al., 2016b). In Figure 3.10 we show $f_{\rm gas} = M_{\rm gas}/M_{\rm bar}$, with $M_{\rm bar} = M_* + M_{\rm gas}$, as a function of $Q_{\rm gas}$, color-coded by redshift as in Figure 3.4. Albeit large scatter, an anti-correlation between $f_{\rm gas}$ and $Q_{\rm gas}$ is evident, such that galaxies with higher gas fractions have lower Q (Spearman rank correlation coefficient $\rho_S = -0.30$ with significance $\sigma_\rho = 3.6$). This is in agreement with the theoretical prediction that SFGs that are more gas rich have lower Q values. The average $Q_{\rm gas}$ for our galaxies in the redshift bins $z \sim 0.9; 1.5; 2.3$ is $Q_{\rm gas} = 1.2; 0.7; 0.5$ (arrows in Figure 3.10). Our results on the average offset of ionized *vs.* atomic+molecular gas from Section 3.4.5 suggest that the cold gas tracing the bulk of the gas mass might have lower velocity dispersion by $10-15$ km $^{-1}$. This would lower the $Q_{\rm gas}$ values by a factor $\sim 1.2-2$. While our calculation of the Toomre$-Q$ parameter is simplified through the omission of the stellar component, this suggests that thick high$-z$ disks with high gas fractions of $\gtrsim 50$ % can be marginally stable even down to $Q_{\rm gas} < 0.7$.

3.5.4 Combining feedback and gravity

While gravitational instabilities are likely important drivers of the elevated velocity dispersions at $z > 1$, the contribution from stellar feedback-driven turbulence of the order of $10-20$ km s^{-1} could become comparable or even dominant for lower$-z$, low$-\sigma_0$ galaxies. Therefore, one must consider both processes to get a complete picture.

The combination of stellar feedback and gravitational processes for turbulence driving has recently been investigated through the analytic model for structure and evolution of gas in galactic disks by Krumholz et al. (2018), who combine prescriptions for star formation, stellar feedback, and gravitational instabilities into a unified 'transport+feedback' model to explain the range of observed dispersions from $z = 3$ to the present day. In their model, gas is in vertical hydrostatic equilibrium and energy equilibrium. This model assumes (isolated) rotating galactic disks built of gas and stars within a quasi-spherical dark matter halo over a wide redshift range. Disks are stable or marginally stable to gravitational collapse, regulated by mass transport through the disk. The gas is in vertical hydrostatic equilibrium, and in energy equilibrium such that losses through the decay of turbulence are balanced by energy input into the system via stellar feedback and the release of gravitational energy via mass transport through the disk.

Consistent with the discussion above, Krumholz et al. (2018) show in their model that stellar feedback may maintain velocity dispersions of ~ 10 km s^{-1}, creating a dispersion floor, while gravitational instabilities, for instance created through radial mass transport through the disk, are necessary to constantly drive velocity dispersions beyond $\sigma_0 \sim 20$ km s^{-1} for moderate star-formation rates (cf. also Figure 4 by Krumholz et al., 2018). They make a prediction for galactic gas velocity dispersion and its correlation with SFR. Particularly, they show that (see their Equation (60))

$$\mathrm{SFR} = \frac{0.42}{\pi G}\frac{1}{Q} \cdot f_{\mathrm{gas}} v_{\mathrm{circ}}^2 \sigma_0, \tag{3.6}$$

where we have substituted appropriate constants for high$-z$ galaxies following Krumholz et al. (2018). Specifically, we adopt a rotation curve slope of $\beta = 0$, an offset between resolved and unresolved star formation law normalizations of $\phi_a = 3$, a fraction of ISM in the star-forming phase $f_{\mathrm{sf}} = 1$, a ratio of total pressure to turbulent pressure at the midplane of $\phi_{\mathrm{mp}} = 1.4$, a star-formation efficiency per free-fall time of $\epsilon_{\mathrm{ff}} = 0.0015$, an orbital period of $t_{\mathrm{orb,out}} = 200$ Myr, and a maximum star-formation time-scale of $t_{\mathrm{sf,max}} = 2$ Gyr.

We make two adjustments to our data to properly compare to the model: here, and for all of Section 3.5.4, we subtracted 15 km s^{-1} in quadrature from our intrinsic dispersion values, denoted by $\sigma_{0,15}$, to ensure consistency with the theoretical model (see Krumholz & Burkhart, 2016 and Krumholz et al., 2018, Appendix B). These 15 km s^{-1} represent the average combination of thermal motions and expansion of HII regions that enter our ionized gas velocity dispersion measurement (see also Sections 3.3.4 and 3.4.5). We also modify our gas mass fractions: the corresponding parameter used by Krumholz et al. (2018) describes an effective gas fraction at the mid plane. This has typically higher values than our gas fraction f_{gas} because of the larger stellar scale heights compared to the gas scale heights. For the comparison here we adopt a scaling factor of 1.5 for our gas mass fractions, motivated by measurements in the Solar neighbourhood (McKee, Parravano, & Hollenbach, 2015; Krumholz et al., 2018; M. Krumholz, private communication).

To compare the model prediction from Equation (3.6) to our data, we group correlated quantities and separate the star formation properties SFR and f_{gas} from the kinematic tracers v_{circ} and σ_0. We show the result for our kinematic sample in Figure 3.11, specifically SFR divided by gas fraction as a function of circular velocity squared times intrinsic velocity dispersion. Figure 3.11 reveals a clear trend between the displayed quantities, with a Spearman rank correlation of $\rho_{\mathrm{S}} = 0.57$ with significance $\sigma_\rho = 6.8$. We also show model predictions from Krumholz et al. (2018) as quoted in Equation (3.6) for three values of Q. There is a tendency for higher$-z$ galaxies to have a predicted $Q \lesssim 1$, consistent with our results presented in Figure 3.10. Generally, however, our galaxies scatter around $Q = 1$ at all redshifts. This suggests that SFGs self-regulate at all times such that the population of SFGs evolves roughly along lines of constant Q. This result is largely independent from the specific choices of parameters such as ϕ_a or f, which will only affect the average Q value. Note that the above correlation between SFR and velocity dispersion is predicted for both the combined

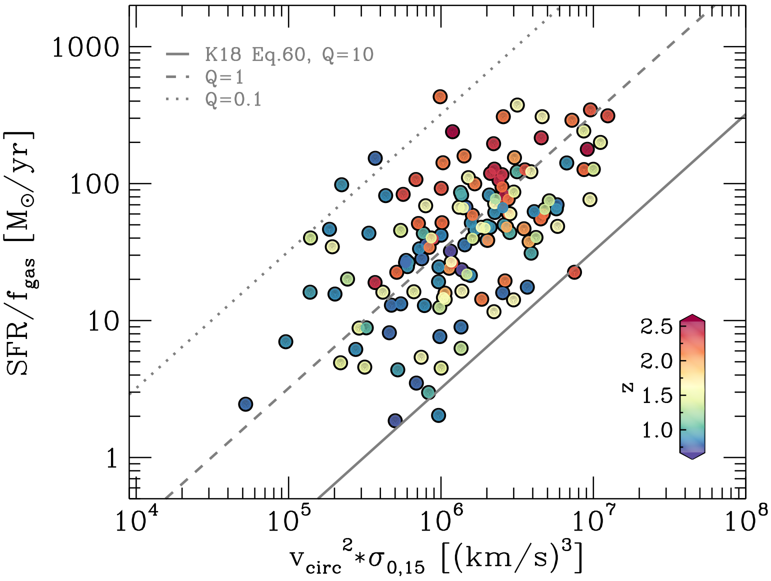

Figure 3.11: *SFR divided by gas fraction as a function of circular velocity squared times intrinsic velocity dispersion for our kinematic sample, color-coded by redshift. The lines show predictions from the 'transport+feedback' model by Krumholz et al. (2018) for different values of Q (Equation* (3.6)*). We find a strong correlation between the displayed quantities (*$\rho_S = 0.57$*;* $\sigma_\rho = 6.8$*), where galaxies scatter around constant Q, suggesting dominant self-regulation processes in our galaxies at all redshifts.*

'transport+feedback' model and a model without feedback, but not for models lacking the 'transport' component accounting for gravitational instabilities (see also Krumholz & Burkhart, 2016).

In the following, we now investigate separately changes of circular velocity and gas fraction in the σ_0−SFR parameter space. In Figure 3.12 we show for our kinematic sample the intrinsic velocity dispersion as a function of SFR, color-coded by rotation velocity. As expected from the main sequence and Tully Fisher relation (Tully & Fisher, 1977), which is in place for our data set at all redshifts (Übler et al., 2017), our data display a gradient such that rotation velocity on average increases with increasing SFR. As lines we plot the high−z model by Krumholz et al. (2018), but we modify it such that we vary the galaxy circular velocity from $v_{\rm circ} = 50$ km s^{-1} to $v_{\rm circ} = 450$ km s^{-1} in order to appropriately cover the range of observed rotation velocities in our kinematic sample. In the model framework, stellar feedback creates sustains a dispersion floor, represented through the horizontal regime of the model lines. The predicted rapid increase of velocity dispersion with SFR, the exact location here dependent on rotation velocity, requires the release of gravitational energy through radial transport through the disk (see Krumholz et al., 2018, for details). The agreement between the the-

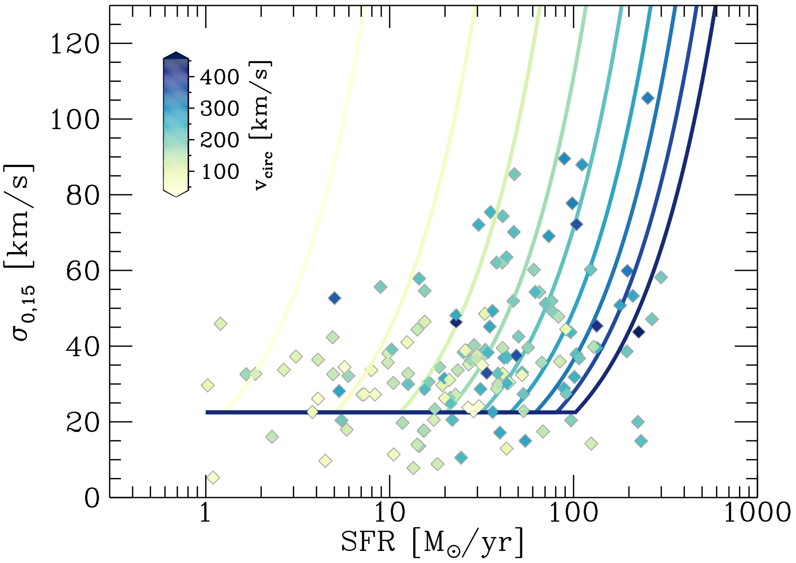

Figure 3.12: *Intrinsic velocity dispersion $\sigma_{0,15}$ as a function of star formation rate SFR, color coded by circular velocity. The data points show our kinematic sample. The lines are predictions from the 'transport+feedback high−z' model by Krumholz et al. (2018), where we additionally vary the galaxy circular velocity $v_{\rm circ}$ between 50 km s^{-1} and 450 km s^{-1} in steps of 50 km s^{-1}. For 60 % of our galaxies in the $\sigma_{0,15}$−SFR parameter space, the model predicts the correct rotation velocity, with all other parameters being fixed as specified in the main text.*

oretical model and our data is remarkably good: $\sim 60\%$ of our data are matched by the model for this simple variation of only the rotation velocity, with all other parameters being fixed to the fiducial 'transport+feedback high-z' parameters.

For the gas fraction we can make only an approximate comparison. As mentioned in Section 3.2, gas masses for our galaxies are calculated applying the scaling relation by Tacconi et al. (2018), since direct gas mass measurements are not available for most of our galaxies. With this, we get the total gas mass over the total baryonic mass per galaxy. Again, we use a scaling factor of 1.5 for our gas mass fractions. In Figure 3.13 we show the same parameter space as in Figure 3.12 but now color coded by gas fraction. While galaxies with SFR $\lesssim 10\ M_\odot$ yr^{-1} have on average lower gas fractions, no strong trend is apparent at higher SFRs. We show again lines based on the 'transport+feedback high−z' model by Krumholz et al. (2018), but now we vary the gas fraction (and with it $f_{g,P}$) from $f_{g,Q} = 0.2$ to $f_{g,Q} = 1.0$ in order to explore the range of scaled gas fractions of galaxies in our kinematic sample. With solid lines we show models with $v_\phi = 400$ km s^{-1}, and dashed lines show $v_\phi = 200$ km s^{-1}. It becomes clear that in the model framework galaxies at fixed SFR and σ_0 can have higher $f_{g,Q}$ and

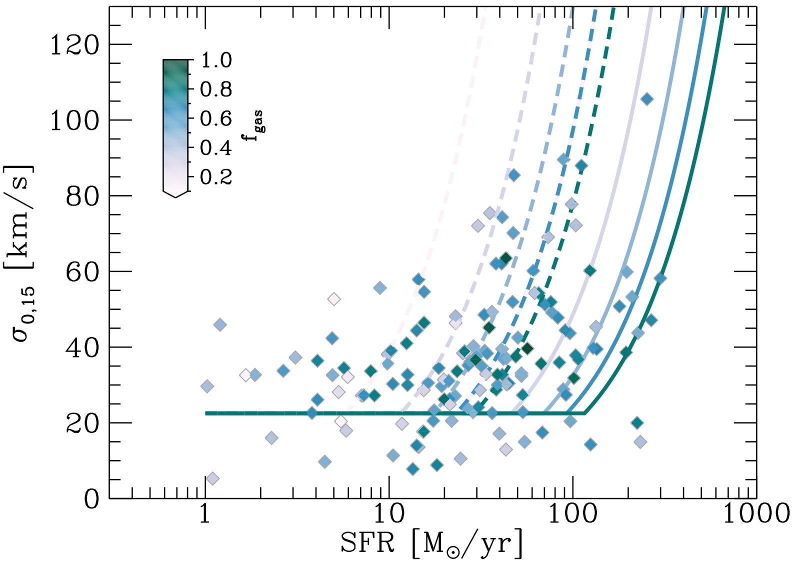

Figure 3.13: *Intrinsic velocity dispersion $\sigma_{0,15}$ as a function of star formation rate SFR, color coded by (scaled) gas fraction (see main text for details). The data points show our kinematic sample. The lines are predictions from the 'transport+feedback high–z' model by Krumholz et al. (2018), where we additionally vary $f_{g,Q}$ in lock-step with $f_{g,P}$ between 0.2 and 1 in steps of 0.2, and the galaxy rotation velocity v_ϕ from 200 km s^{-1} (dashed lines) to 400 km s^{-1} (solid lines). The location of the model predictions illustrate how the observed scatter in gas fractions at fixed SFR and σ_0 may be caused by different rotation velocities.*

lower v_ϕ, or lower $f_{g,Q}$ and higher v_ϕ, but rotation velocity has to be varied to cover the full range of SFRs in our observations.

Horizontal variations of the model predictions can be reached through changing the fraction of gas assumed to be in the star-forming ISM, and through changes in the outer rotation curve slope. For instance, assuming only 20% of the gas to be in the star-forming phase pushes the horizontal floor of the model below 10 km s^{-1}, and lowers the predicted SFR by almost an order of magnitude. Assuming a dropping rotation curve, on the other hand, lifts the horizontal floor and increases the predicted SFR. Assuming an outer rotation curve slope of $\beta = -0.5$ increases the horizontal saturation of the model to ~ 32 km s^{-1}, whilst increasing the star-formation rate only marginally. Lang et al. (2017) have shown that the typical outer rotation curve slope of galaxies in our sample is negative. This is more pronounced at higher redshift, possibly offering an additional reason for the elevated velocity dispersions at $z \gtrsim 2$ in this model framework.

Considering these analytic model prescriptions, and the typical uncertainty of the intrinsic dispersion measurements of $\delta\sigma_0 \sim 10$ km s^{-1} in our kinematic sample,

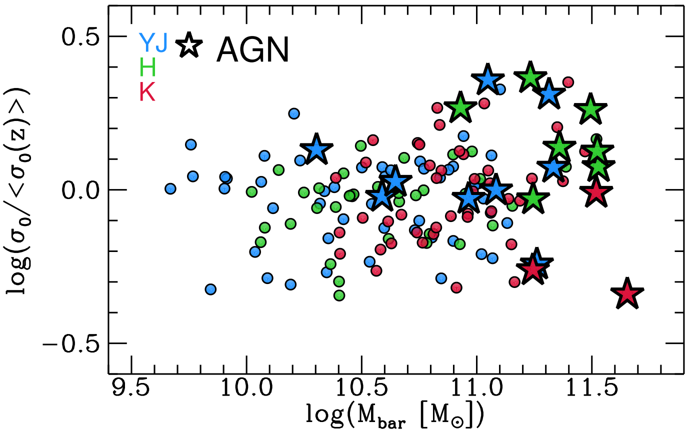

Figure 3.14: *Redshift-normalized intrinsic velocity dispersion as a function of baryonic mass. Blue, green, and red colors indicate $z \sim 0.9$, $z \sim 1.5$, and $z \sim 2.3$ SFGs, respectively. Galaxies that host an AGN are shown as stars. Most galaxies with log*($M_{\rm bar}/M_\odot$) $\gtrsim 11.3$ *have above-average velocity dispersions and about half of them host an identified AGN.*

we conclude that galaxies with $\sigma_0 \gtrsim 35$ km s^{-1} are dominated by gravitational instability-driven turbulence. This encompasses more than 60% of galaxies in our sample, underlining the importance of gravity-driven turbulence in star forming galaxies at $z \sim 1-3$.

3.5.5 AGN feedback

As a final remark, we briefly want to comment on AGN feedback as a potential additional source for elevated velocity dispersions in the SFGs in our kinematic sample. While we excluded galaxies, or regions of galaxies, that are so strongly affected by the AGN and associated outflows that the disk kinematics cannot be recovered, we do not entirely exclude AGN. This ensures that we can explore the full mass range covered by the KMOS$^{\rm 3D}$ survey, including the high-mass end where at $\log(M_*/M_\odot) > 11$, above the Schechter mass, the fraction of AGN increases rapidly (Förster Schreiber et al., 2014, 2018; Genzel et al., 2014b)

While we do not find significant correlations between $z-$normalized σ_0 and mass properties (Table 3.7), we do note a cloud of galaxies from *all redshifts* with dispersions above average for the highest stellar ($\log(M_*/M_\odot) > 11$) and baryonic masses ($\log(M_{\rm bar}/M_\odot) \gtrsim 11.3$) as shown in Figure 3.14. About half of the $\log(M_{\rm bar}/M_\odot) \gtrsim 11.3$ above-average dispersion galaxies are known to host an AGN (stars in Figure 3.14). We speculate that the energy deposited by strong AGN feedback in the form of nuclear outflows could induce turbulence in the disk via the re-accretion of material at larger radii.

It is important to keep in mind that outflow components with velocities similar to the galaxy rotation velocity can broaden the line width but may not be distinguishable from the star-forming regions due to S/N limitations. Comparing to the deep AO data from the SINS/zC-SINF survey that we show in Figure 3.9, one of the three identified, $\log(M_*/M_\odot) \gtrsim 11$ AGN (Q2343-BX610) shows above-average velocity dispersions (after excluding the regions clearly affected by the nuclear outflow), while the other two (D3a-6004, D3a-15504) have average dispersions.

3.6 Conclusions

We have investigated the evolution of the ionized gas intrinsic velocity dispersions, σ_0, between $0.6 < z < 2.6$ based on data from our full KMOS$^{\rm 3D}$ survey. We have selected a high-quality, rotation-dominated ($v_{\rm rot}/\sigma_0 \geq 1$) sample for which we forward-modelled in a Bayesian framework the one-dimensional galaxy kinematics extracted from the Hα velocity and velocity dispersion maps, taking into account instrumental effects, beam smearing, and pressure support. Our main conclusions are as follows:

- Assuming an isotropic and radially constant intrinsic velocity dispersion, we find an average decrease of the Hα intrinsic dispersion for our kinematic sample from $\sigma_0 \sim 46$ km s^{-1} at $z \sim 2.3$ to $\sigma_0 \sim 31$ km s^{-1} at $z \sim 0.9$, solidifying trends previously reported in the literature (Section 3.4.1). Putting our sample into the broader context of literature measurements from $z = 4$ to $z = 0$, tracing ionized, molecular, and atomic gas phases, confirms the general increase of intrinsic galaxy velocity dispersion with redshift (Section 3.4.4).

- Comparing the redshift evolution of ionized and molecular plus atomic gas velocity dispersion, we find that the ionized gas dispersion is on average higher by ~ 12 km s^{-1} (Section 3.4.5). This offset can in principle be accounted for through the different gas temperatures together with the line broadening through expansion of HII regions the ionized gas emission typically originates from.

- For our KMOS$^{\rm 3D}$ kinematic sample, we find that there is intrinsic scatter in the σ_0 distribution at fixed redshift after accounting for measurement and modelling uncertainties, and it increases for our highest redshift slice (Section 3.4.2). However, we cannot single out a physical mechanism behind this scatter. This could imply that the velocity dispersion is highly variable in time, due to a dynamic mechanism such as minor mergers or variation in accretion (see Hung et al., 2019, for evidence from simulations). Alternatively, the scatter could be caused by the interplay of different physical properties responsible to maintain marginal stability (see Section 3.5.4).

- Investigating the physical driver of the elevated velocity dispersions at higher redshift, we find that galaxies in our kinematic sample are at most marginally Toomre-stable, i.e. they are consistent with their turbulence being powered through gravitational instabilities in a self-regulated environment (Sections 3.5.3 and 3.5.4).
- We find no evidence from our high-resolution SINS/zC-SINF AO data that stellar feedback as traced through $\Sigma_{\rm SFR}$ typically increases the velocity dispersion on sub-galactic scales beyond the average level, or that the *local* velocity dispersion correlates strongly with $\Sigma_{\rm SFR}$, suggesting that contributions from stellar feedback to turbulence driving are minor for our $z > 1$ SFGs (Section 3.5.2).
- We find good agreement between data from our KMOS$^{\rm 3D}$ kinematic sample and predictions from the state-of-the-art analytical model of galaxy formation and evolution by Krumholz et al. (2018), further strengthening the evidence that the majority of our galaxies ($\gtrsim 60\%$) are dominated by gravity-driven turbulence (Section 3.5.4).

The measurement of intrinsic gas velocity dispersion at $z > 0$ is challenging. Next-generation instruments such as ERIS+AO at the VLT or HARMONI at the ELT will expand current samples on spatial scales that are currently only achievable for strongly lensed objects, and push spectral scales down to ~ 15 km s^{-1}. The statistics from these observations will facilitate further investigation of the scatter of the intrinsic velocity dispersion at fixed redshift, and tests of theoretical predictions such as the transition regime from gravity-driven turbulence to feedback-driven turbulence as a function of redshift and mass (Krumholz et al., 2018). Deep, high-S/N observations of particularly molecular gas reaching 1–2 kpc resolution at $z > 1$ with NOEMA or ALMA are necessary to test if the redshift evolution of molecular and ionized gas velocity dispersion is indeed comparable.

Acknowledgements

We are grateful to the anonymous referee for a very constructive report that helped to improve the quality of this manuscript. We thank the ESO Paranal staff for their helpful support with the KMOS observations for this work. We are grateful to Raymond Simons and Susan Kassin for providing us with data from the DEEP2 and SIGMA surveys. We thank Luca Cortese, Amiel Sternberg, Vadim Semenov, and Chia-Yu Hu for fruitful discussions, and we are particularly grateful to Blakesley Burkhart, Mark Krumholz, and Andreas Schruba for valuable comments on various aspects of this work. DW acknowledges the support of the Deutsche Forschungsgemeinschaft via projects WI 3871/1-1 and WI 3871/1-2. EW acknowledges support by the Australian Research Council Centre of Excellence for All Sky Astrophysics in 3 Dimensions (ASTRO 3D), through project number CE170100013. MF acknowledges the support from the European Research Council (ERC) under the European Union's Horizon 2020 research and innovation programme (grant agreement No. 757535). PL acknowledges funding from the ERC under the European Union's Horizon 2020 research and innovation programme (grant agreement No. 694343).

3.7 Appendix A – Example galaxies and fits

We show examples of galaxies in our kinematic sample together with their best-fit kinematic models in Figure 3.15. See the figure caption for details.

3.8 Appendix B – Alternative fits to our KMOS^{3D} velocity dispersions

We list fits to our KMOS^{3D} velocity dispersion data from $z = 2.6$ to $z = 0.6$ in $\sigma_0 - \log(1 + z)$ space and $\log(\sigma_0) - \log(1 + z)$ space in Tables 3.8 and 3.9, respectively. These results agree with our fiducial fits in $\sigma_0 - z$ space listed in Table 3.3, and do not change our conclusions.

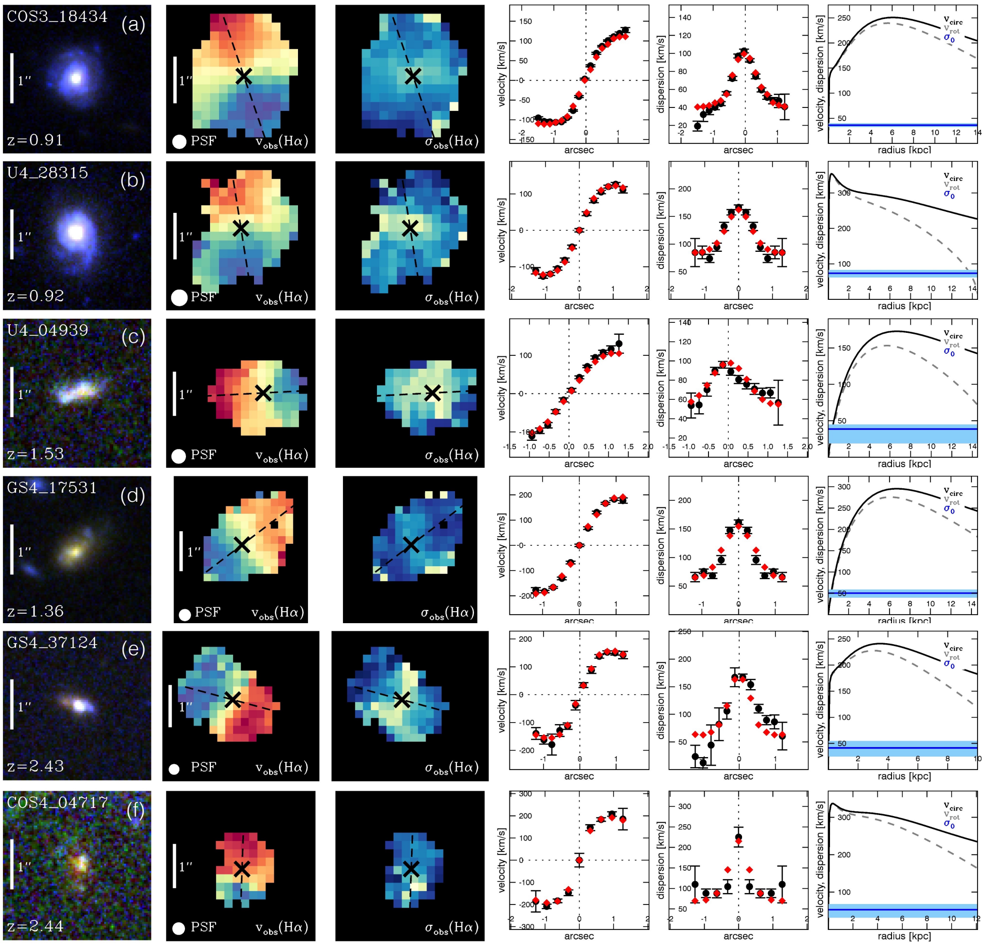

Figure 3.15: *Example cases of galaxies in our kinematic sample. From top to bottom, we show for each redshift slice a galaxy modelled with setup 1 and with setup 2 (see Section 3.3.2). From left to right, we show an IJH HST color-composite image; the projected Hα velocity map; the projected Hα velocity dispersion map; the observed velocity $v_{\rm rot}(r) \cdot \sin(i)$ along the kinematic major axis (black) and the best-fit model (red); the observed velocity dispersion $\sigma(r)$ correspondingly; and the intrinsic model circular velocity $v_{\rm circ}$ (black), rotation velocity $v_{\rm rot}$ (grey dashed), and intrinsic velocity dispersion (blue) together with its uncertainties derived from the MCMC posterior distribution (blue shading). The kinematic maps and profiles are corrected for the instrument line-spread function, but not for beam-smearing. The kinematic major axis is indicated by the black dashed line on top of the velocity and dispersion maps, and the black crosses indicate the midpoint between the observed minimum and maximum velocities (not necessarily the kinematic center). Note that the intrinsic rotation curves are falling by construction because we do not include a dark matter halo (but see Section 3.3.2). Rows (a), (c), and (e) show examples from setup 1, and rows (b), (d), and (f) show examples from setup 2.*

Table 3.8: *Results from the linear regression fits of the form* $\sigma_0/\mathrm{km\,s} = a + b \cdot \log(1+z) + c$ *for our kinematic sample, where* a *and* b *are the regression coefficients, and* c *is the intrinsic random scatter about the regression (see Kelly, 2007). For each parameter* a, b, *the standard deviation of* c, *and the derived linear correlation coefficient* l_{corr} *between* σ_0 *and* z, *we list the median together with the standard deviation of the posterior distribution. For each redshift slice we list the best-fit* σ_0 *value corresponding to these medians.*

sample	N	a [km s^{-1}]	b [km s^{-1}]	σ_c [km s^{-1}]	l_{corr}	σ_0 at $z \sim 0.9$ [km s^{-1}]	σ_0 at $z \sim 1.5$ [km s^{-1}]	σ_0 at $z \sim 2.3$ [km s^{-1}]
including upper limits	175	19.4 ± 3.8	52.6 ± 10.1	9.8 ± 1.1	0.48 ± 0.08	33.8	40.6	46.5
excluding upper limits (robust)	147	19.5 ± 4.5	53.1 ± 11.4	10.4 ± 1.1	0.46 ± 0.09	34.1	40.9	46.9
using formal best-fit σ_0	175	19.5 ± 4.5	53.1 ± 11.3	10.4 ± 1.1	0.46 ± 0.09	34.1	40.9	46.8

Table 3.9: *Results from the linear regression fits of the form* $\log(\sigma_0/\mathrm{km\,s}) = a + b \cdot \log(1+z) + c$ *for our kinematic sample, where* a *and* b *are the regression coefficients, and* c *is the intrinsic random scatter about the regression (see Kelly, 2007). For each parameter* a*,* b*, the standard deviation of* c*, and the derived linear correlation coefficient* l_{corr} *between* σ_0 *and* z*, we list the median together with the standard deviation of the posterior distribution. For each redshift slice we list the best-fit* σ_0 *value corresponding to these medians.*

sample	N	a [km s^{-1}]	b [km s^{-1}]	σ_c [km s^{-1}]	l_{corr}	σ_0 at $z \sim 0.9$ [km s^{-1}]	σ_0 at $z \sim 1.5$ [km s^{-1}]	σ_0 at $z \sim 2.3$ [km s^{-1}]
including upper limits	175	1.29 ± 0.05	0.77 ± 0.13	0.12 ± 0.01	0.54 ± 0.08	31.8	39.9	48.6
excluding upper limits (robust)	147	1.38 ± 0.05	0.61 ± 0.13	0.11 ± 0.01	0.49 ± 0.09	35.3	42.2	49.4
using formal best-fit σ_0	175	1.30 ± 0.05	0.75 ± 0.13	0.12 ± 0.01	0.53 ± 0.07	32.3	40.3	49.0

3.9 Appendix C – Correlations of physical properties with velocity dispersion and redshift-normalized velocity dispersion

We show correlations of various physical properties with velocity dispersion after (see Equation (3.2)) and before correcting for the redshift dependence of σ_0 in Figures 3.16 and 3.17 (see also Table 3.7). While several properties positively correlate with σ_0, particularly SFR and $M_{\rm gas}$, we do not find any significant correlation after correcting for the redshift-dependence of σ_0. This means that we cannot readily identify a single physical driving source behind the intrinsic scatter in σ_0 (see discussions in Sections 3.4.2 and 3.5).

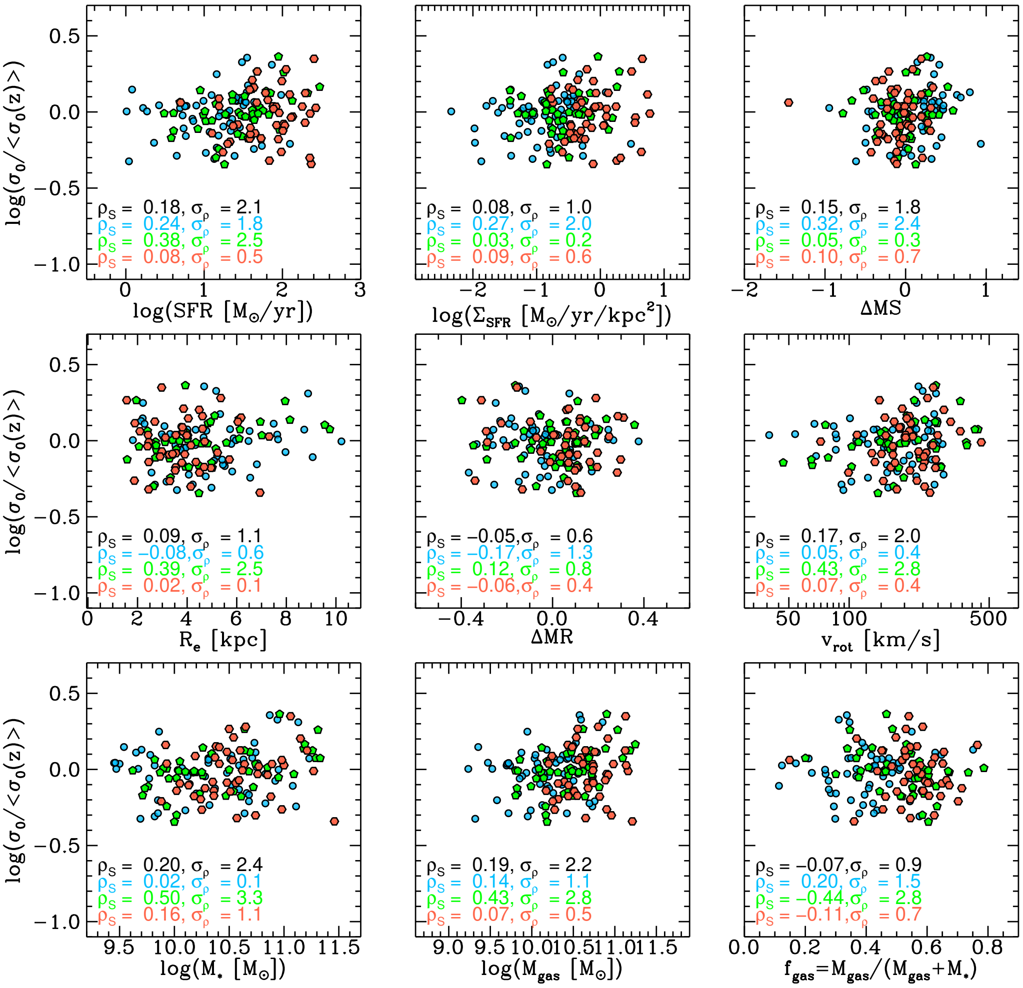

Figure 3.16: *Redshift-normalized velocity dispersion (see Equation (3.2)) as a function of several physical properties. Colors show our redshift subsamples at* $z \sim 0.9$ *(blue),* $z \sim 1.5$ *(green), and* $z \sim 2.3$ *(red). Spearman rank correlation coefficients* ρ_S *and their significance* σ_ρ *are listed in each panel for the full sample (black) and the individual redshift bins (colors). We do not find any significant correlations between redshift-normalized velocity dispersion and the considered physical properties (see Table 3.7 for additional quantities) for our kinematic KMOS*^{3D} *sample, meaning that we cannot identify a single physical driving source behind the intrinsic scatter in velocity dispersion.*

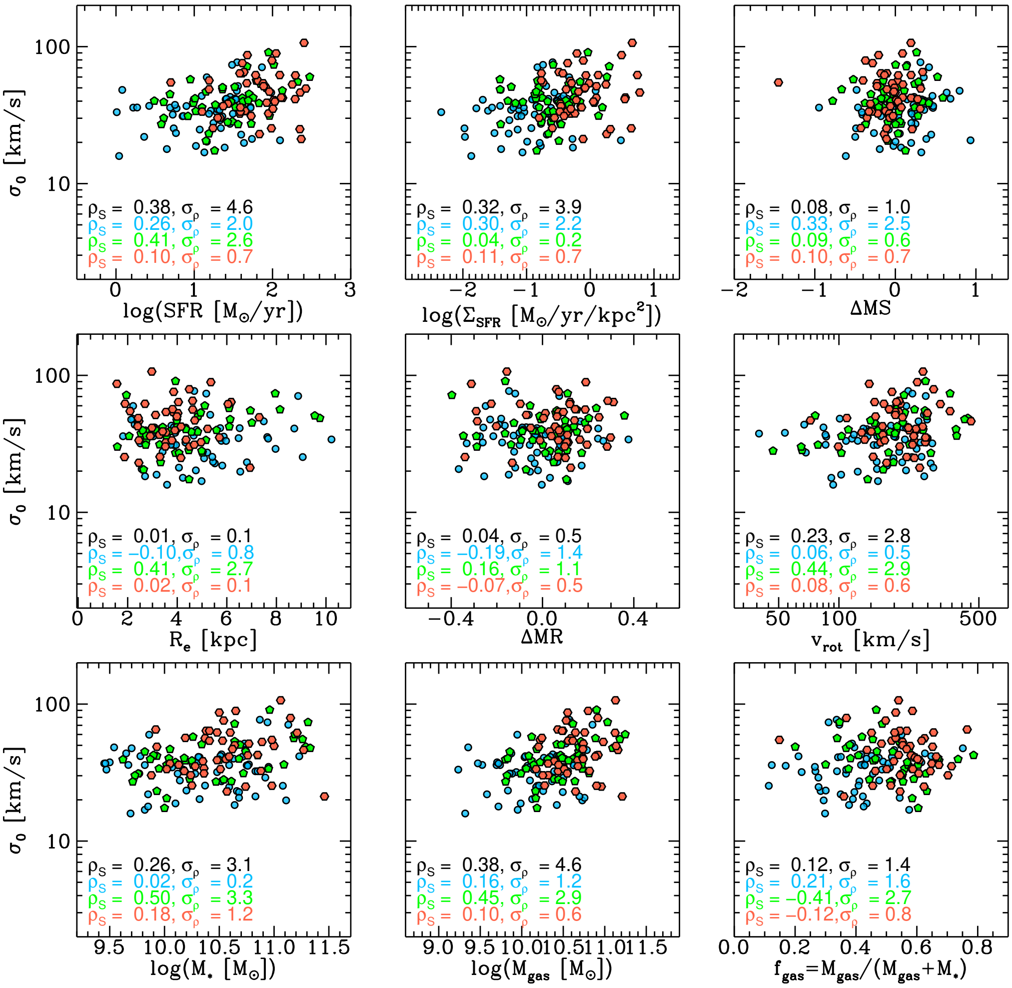

Figure 3.17: *Velocity dispersion as a function of several physical properties. Colors show our redshift subsamples at* $z \sim 0.9$ *(blue),* $z \sim 1.5$ *(green), and* $z \sim 2.3$ *(red). Spearman rank correlation coefficients* ρ_S *and their significance* σ_ρ *are listed in each panel for the full sample (black) and the individual redshift bins (colors). Velocity dispersion positively correlates with several physical properties, some of which correlate themselves with redshift. For our kinematic KMOS*^{3D} *sample, we find the strongest and most significant correlations between* σ_0 *and SFR, as well as* $M_{\rm gas}$*, which we further investigate in Section 3.5.*

Chapter 4

Detailed Kinematics of Individual Galaxies

In this Chapter we zoom in on the detailed, high-resolution kinematics of individual galaxies in three dedicated studies. In Section 4.1 we present the resolved outer rotation curves of a small set of galaxies based on ionized gas emission probing into a radial regime where the dark matter halo may start to leave a measurable imprint on the galaxy kinematics, therefore taking the first step in resolving the multi-component mass budget in normal (and unlensed) $z \sim 1-2.5$ main sequence galaxies. In Section 4.2 we analyse the resolved outer rotation curve of one galaxy from two independent tracers, namely ionized and molecular gas, to assess the reliability of the ionized gas in tracing the gravitational potential and dynamical support. In Section 4.3 we use mock observations of high-resolution cosmological simulations to validate the kinematic extraction and modeling methodology used for our observational work, and to highlight potential differences motivating future observational and theoretical work.

4.1 Strongly baryon-dominated disk galaxies at the peak of galaxy formation ten billion years ago

This Section is a reprint of the Nature publication *Strongly Baryon-dominated Disk Galaxies at the Peak of Galaxy Formation Ten Billion Years ago* by Genzel et al. (2017); DOI:10.1038/nature21685; ©Springer Nature. Reproduced with permission.

This work is based on observations obtained at the Very Large Telescope (VLT) of the European Southern Observatory (ESO), Paranal, Chile, under ESO program IDs 076.A-0527, 079.A-0341, 080.A-0330, 080.A-0635, 082.A-0396, 183.A0781, 091.A-0126, 092. A-0091, 093.A-0079, 094.A-0217, 095.A-0047, 096.A-0025, 097.B-0065, and 097.A-0353.

Abstract – In the cold dark matter cosmology, the baryonic components of galaxies – stars and gas – are thought to be mixed with and embedded in non-baryonic and non-relativistic dark matter, which dominates the total mass of the galaxy and its dark matter halo (White & Rees, 1978). In the local Universe, the mass of dark matter within a galactic disk increases with disk radius, becoming appreciable and then dominant in the outer, baryonic regions of the disks of star-forming galaxies. This results in rotation velocities of the visible matter within the disk that are constant or increasing with disk radius – a hallmark of the dark matter model (Sofue & Rubin, 2001). Comparison between the dynamical mass and the sum of stellar and cold-gas mass at the peak epoch of galaxy formation ten billion years ago, inferred from ancillary data, suggest high baryon factions in the inner, star-forming regions of the disks (Förster Schreiber et al., 2009; van Dokkum et al., 2015; Price et al., 2016; Wuyts et al., 2016b). Although this implied baryon fraction may be larger than in the local Universe, the systematic uncertainties (stellar initial mass function, calibration of gas masses) render such comparisons inconclusive in terms of the mass of dark matter (Courteau & Dutton, 2015). Here we report rotation curves for the outer disks of six massive star-forming galaxies, and find that the rotation velocities are not constant, but decrease with radius. We propose that this trend arises because of a combination of two main factors: first, a large fraction of the massive, high-redshift galaxy population was strongly baryon dominated, with dark matter playing a smaller part than in the local Universe; and second, the large velocity dispersion in high-redshift disks introduces a substantial pressure term that leads to a decrease in rotation velocity with increasing radius. The effect of both factors appears to increase with redshift. Qualitatively, the observations suggest that baryons in the early Universe efficiently condensed at the centres of dark matter halos when

gas fractions were high, and dark matter was less concentrated.

Over the last few years, there have been significant studies of ionised gas dynamics of redshift 0.6–2.6 star-forming galaxies. These were drawn from mass-selected parent samples in cosmological deep fields, and from imaging and grism surveys with the Hubble Space telescope (Förster Schreiber et al., 2009; Price et al., 2016; Wisnioski et al., 2015; Grogin et al., 2011; Koekemoer et al., 2011; Kong et al., 2006; Brammer et al., 2012; Momcheva et al., 2016), with well characterized properties (see Section 4.1.1). We obtained deep (5-22 h integration), imaging spectroscopy of the Hα emission line, with the near-infrared integral field spectrometers SINFONI and KMOS on the Very Large Telescope of the European Southern Observatory, as part of our “SINS/zC-SINF” and “KMOS^{3D}” surveys (henceforth ‘IFS-samples’; Förster Schreiber et al., 2009; Wisnioski et al., 2015). From the data we extract Hα rotation curves, rotation velocities as a function of galactic radius, for several hundred star-forming galaxies (see Section 4.1.1). Rotation curves give valuable constraints on the baryonic and dark matter mass distributions in massive star-forming disks at the peak of cosmic galaxy formation 10 billion years ago, largely independent of assumptions on star-formation histories and stellar mass functions.

Figure 4.1 shows the angular distributions of stellar mass/light, integrated Hα intensity, Hα velocity and dispersion, together with cuts of the latter two along the kinematic major axis, for six of our best star-forming galaxies. We selected galaxies for deep spectroscopy from the IFS-samples to have large stellar masses ($\log(M_*/M_\odot) \sim 10.6 - 11.1$), to not participate in a merger, to have rotationally dominated kinematics, and to have large half-light radii ($R_{1/2} \sim 4 - 9$ kpc), such that the disk penetrates far into the dark matter halo.

The extracted velocity and velocity dispersion fields in all cases demonstrate that the sources are rotationally supported (Wisnioski et al., 2015; see Section 4.1.1). The ratio of peak rotation velocity to the amplitude of random motions, as estimated from the velocity dispersion in the outer disks, is between 4 and 9, lower than in present-day disks ($v_{\rm rot}/\sigma_0 \sim 10 - 20$), and in excellent agreement with other observations (Förster Schreiber et al., 2009; Wisnioski et al., 2015). This means that “turbulent” motions contribute significantly to the energy balance (Burkert et al., 2010).

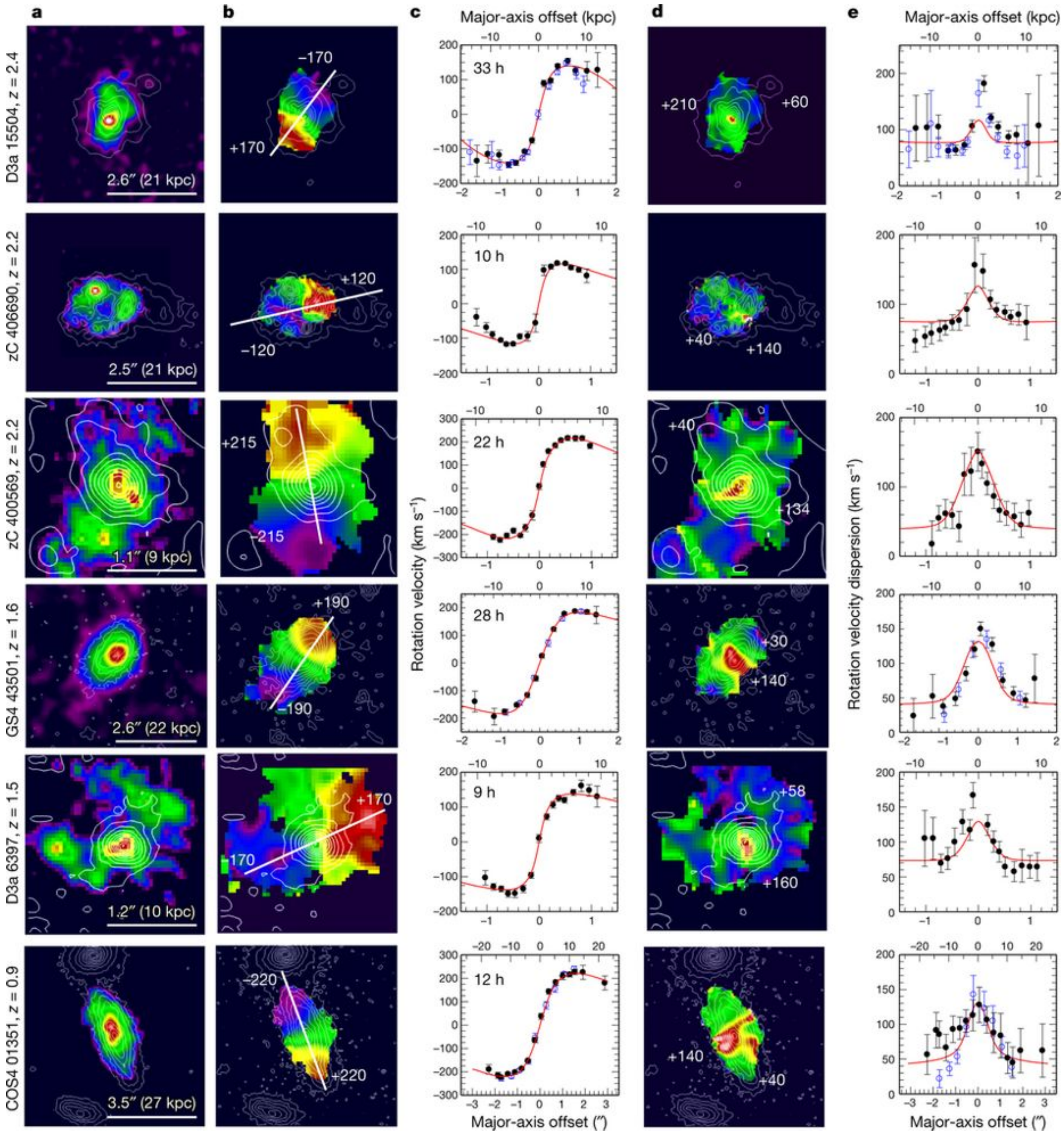

Figure 4.1 Hα gas dynamics from KMOS and SINFONI in six massive star-forming galaxies.

Figure 4.1 ***(Cont.)*****:** *The galaxies have redshifts between* $z = 0.9$ *and* $z = 2.4$*. KMOS provides seeing-limited data (full-width at half-maximum, FWHM*$\approx 0.6''$*); SINFONI allows both seeing-limited and adaptive-optics-assisted observations (FWHM*$\approx 0.2''$*).* **(a)** *For each galaxy, the distribution of the integrated H*α *line surface brightness is shown (colour scale; with a linear scaling), superposed on the stellar surface density (*Σ_**; top three panels) or the H−band continuum surface brightness (*Σ_{H}*; bottom three panels) (white contours; square-root scaling). The horizontal white bar denotes the physical size scale.* **(b)** *Velocity maps (colour scale; with extreme values indicated, in km s*$^{-1}$*) superposed on* Σ_* *or* Σ_{H} *contours (white lines; square-root scaling), derived from fitting a Gaussian line profile to the H*α *data in each pixel (*$0.05''$*). All galaxies have FWHM*$\approx 0.25''$ *(2 kpc) except GS4 43501 and COS4 01351, which have FWHM*$\approx 0.55'' - 0.67''$ *(5 kpc).* **(c)** *Extracted line centroids (and* ± 1 *r.m.s. uncertainties) along the kinematic major axis (white line in (b)). For COS4 01351 (bottom panel) and GS4 43501 (fourth panel), we show SINFONI (black filled circles) and KMOS (open blue circles) datasets; for D3a 15504 (top panel) we show SINFONI datasets at* $0.2''$ *(filled black circles) and* $0.5''$ *(open blue circles) resolution. Red continuous lines denote the best-fit dynamical model, constructed from a combination of a central compact bulge, an exponential disk and an NFW halo without adiabatic contraction, with a concentration of* $c = 4$ *at* $z \approx 2$ *and* $c = 6.5$ *at* $z \approx 1$*. For the modelling of the disk rotation, we also take into account the asymmetric drift correction inferred from the velocity dispersion curves ((d) and (e); Burkert et al., 2010). The times shown in each panel indicate the total on-source integration time.* **(d), (e)** *Two-dimensional ((d); colour scale) and major-axis ((e); with* ± 1*r.m.s. uncertainties) velocity dispersion distributions inferred from the Gaussian fits (after removal of the instrumental response:* $\sigma_{\mathrm{instr}} \approx 37$ *km s*$^{-1}$ *at* $z \approx 0.85$ *and* $z \approx 2.2$*;* $\sigma_{\mathrm{instr}} \approx 45$ *km s*$^{-1}$ *at* $z = 1.5$*), superposed on* Σ_* *or* Σ_{H} *contours ((d); white lines). The numbers in (d) indicate the minimum and maximum velocity dispersions. The colouring of the data and red lines in (e) are as in (c). All physical units are based on a concordance, flat cold dark matter cosmology, with cosmological constant* Λ*, matter density relative to the critical density of closing the Universe* $\Omega_{\mathrm{m}} = 0.3$ *and ratio of baryonic to total matter density* $\Omega_{\mathrm{baryon}}/\Omega_{\mathrm{m}} = 0.17$*, and for the* $z = 0$ *Hubble parameter* $H_0 = 70$ *km s*$^{-1}$ *Mpc*$^{-1}$*.*

The most surprising result is that the projected rotation velocities along the kinematic major axis (panels (c) in Figure 4.1) reach a maximum value |vmax| at $R_{\max}$ and decrease further out, symmetrically on either side of the galaxy centre. Averaging the two sides of the galaxy further improves the signal-to-noise ratio (Figure 4.2). The six rotation curves drop to $v(R_{\text{out}})/v_{\max} \sim 0.3-0.9$ to 0.9 at the outermost radius sampled. Falling rotation curves have previously been detected at low redshift in some compact, high surface density, or strongly bulged disks (such as Andromeda, Figure 4.2), although these are rare and drops are modest, to $v/v_{\max} \sim 0.8-0.95$ (Sofue & Rubin, 2001; Casertano & van Gorkom, 1991; Honma & Sofue, 1997; Carignan et al., 2006).

How common are the falling rotation curves at high redshift? We investigate the prevalence of falling rotation curves at high redshift. A a co-added rotation curve (Lang et al., 2017) of 97 rotationally supported $z \sim 0.6-2.6$ isolated disks from the same IFS samples that we use (but excluding the six above) provides a representative and fairly unbiased sample of the redshift-stellar mass-star formation rate, parameter space for $\log(M_*/M_\odot) > 9.7$ star-forming galaxies (see Section 4.1.1 and Figure 4.4). Star-forming galaxies over the entire mass range of the parent sample enter the stack (Figure 4.4). Within the uncertainties, the stack confirms the results presented here for individual sources, and implies that falling rotation curves at $z = 0.7-2.6$ are common. The uncertainties of individual velocity measurements in the faint outer disks are substantial, such that the significance of the velocity drops in each individual data point is ≤ 3.5 rms. When all data points at $> R_{\max}$ are considered together the statistical significance for a non-flat, falling rotation curve becomes compelling (6-10 rms).

We investigated the possibility that the falling rotation curves are artefacts, caused by warping of the disks, radial streaming along galactic bars, radial changes in the direction of the kinematic axis, tidal interactions with nearby satellites, non-equilibrium motions caused by variations in the amount and/or the direction of the baryonic accretion (Section 4.1.1). We find interacting low mass satellites in three of our six sources and evidence for some tidal stripping in one, but the rotation curve is symmetric, even near the satellite. We do see strong radial streaming confined to the nuclear region in one galaxy. Warps are expected because of the non-planar accretion of gas from the intergalactic web, but also less likely at high$-z$ than in the low$-z$ Universe to be stable, because of the large, isotropic velocity dispersions. The point-symmetric, falling rotation curves in Figure 4.1 argue against strong warping. We also find no evidence in the two dimensional residual maps (data minus model) for radial variations in the line of nodes, as a result of interactions and variations in the angular momentum of the incoming gas (Figure 4.9). Four galaxies have massive bulges (ratio of the mass of the bulge to that of the total galaxy, $B/T > 0.3$), which likely will accentuate centrally peaked rotation curves. Keeping in mind the important effects of non-equilibrium dynamics in the early phases of galaxy formation, the prevalence of point-symmetric, smooth rotation curves in all six cases suggests that these are intrinsic properties of the galaxies.

We compare the final average of all seven rotation curves with an average rotation curve of local massive disks (Catinella, Giovanelli, & Haynes, 2006), the curves of the Milky Way (Bland-Hawthorn & Gerhard, 2016) and M31 (Carignan et al., 2006), and the theoretical curve of a thin, purely baryonic, exponential 'Freeman' disk (Freeman, 1970) in panel (b) of Figure 4.2. All local rotation curves are above the Freeman model, and thus require additional (dark) matter in various amounts. This is not the case for the average high-redshift curve. It is consistent with a pure baryonic disk to $R \sim 1.8\ R_{1/2}$, and falls below it further out.

Since high-redshift disks exhibit large random motions, the equation of hydrostatic equilibrium of the disk contains a radial pressure gradient, which results in slowing down the rotation velocity ('asymmetric drift'; Burkert et al., 2010, Section 4.1.1). If we apply this correction and also allow for the resulting significant thickness of the disk, the rotation curve indeed drops rapidly with radius, as long as σ_0 stays approximately constant. Figure 4.2 shows a $v_{\mathrm{rot}}/\sigma_0 \sim 5$ galaxy, which provides an excellent match to the average observations.

Our analysis leaves little space for dark matter in the outer disks (and inner halos) of massive, high-redshift star-forming galaxies. This conclusion is consistent with the earlier, but less secure, analysis of the 'inner disk dynamics' (Förster Schreiber et al., 2009; van Dokkum et al., 2015; Price et al., 2016; Wuyts et al., 2016b; Section 4.1.1). We quantify our conclusion by fitting the major axis velocity and velocity dispersion data of each galaxy (Figure 4.1) with a three component mass model, consisting of the sum of a central compact (spheroidal) stellar bulge, an exponential gaseous and stellar disk ($n_{\mathrm{Sersic}} = 1$), and a Navarro-Frenk-White (NFW) dark matter halo (Navarro, Frenk, & White, 1996). The output of the fitting is the dark matter to total mass fraction at $R_{1/2}$, $f_{\mathrm{DM}}(R = R_{1/2})$ (Section 4.1.1). We list the fitting results (and ±2 rms uncertainties) in Table 4.1 and summarize in Figure 4.3, which compares the high-redshift data to previous low-redshift results (Courteau & Dutton, 2015), and to the results of Wuyts et al. (2016b). With these basic assumptions we find that the dark matter fractions near the half-light radius for all our galaxies are modest to negligible, even if the various parameter correlations and uncertainties are included (Figure 4.3 and Section 4.1.1). We note that spatially variable σ_0 and deviations from planarity and exponential disk distributions undoubtedly make reality more complex than can be captured in these simple models.

All six disks are 'maximal' (Courteau & Dutton, 2015). Their dark matter fractions are at the lower tail of local star-forming disks, and in the same region of v_c-f_{DM} parameter space as local massive, passive galaxies (Cappellari et al., 2013) and some strongly bulged, early-type disks (Courteau & Dutton, 2015).

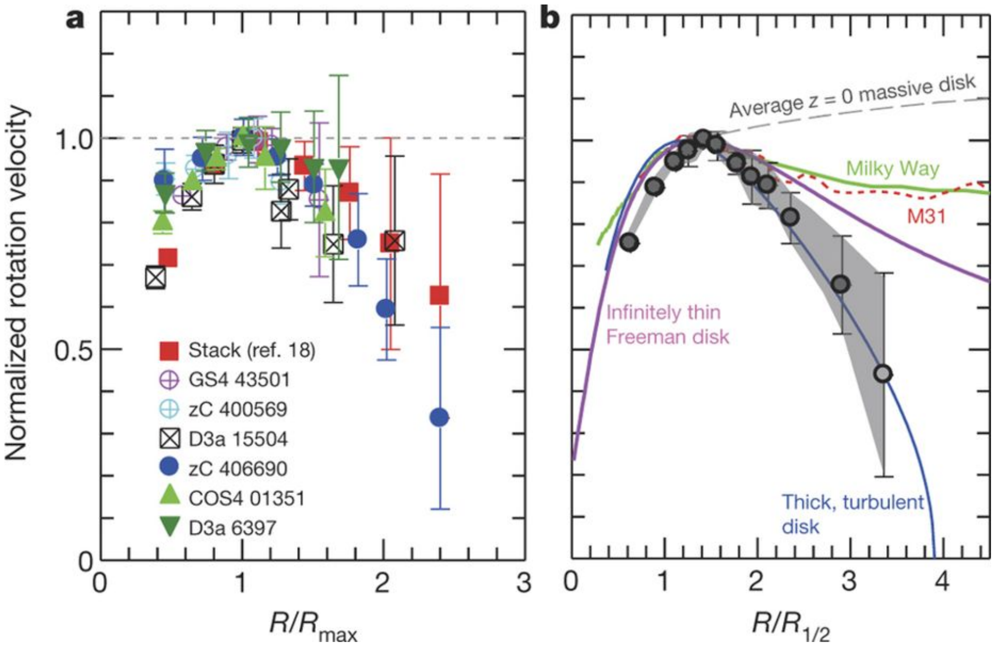

Figure 4.2: **(a)** *The various symbols denote the folded and binned rotation curve data for the six galaxies in Figure 4.1, combined with the stacked rotation curve of 97* z)$0.6-2.6$ *star-forming galaxies (Lang et al., 2017; see Section 4.1.1). For all rotation curves, we averaged data points located symmetrically on either side of the dynamical centres, and plot the rotation velocities normalized by the maximum rotation velocity against the radii* R *normalized by the radius at which the amplitude of the rotation velocity is maximum* ($|v_{\rm rot}| = v_{\rm max}$), $R_{\rm max}$. *Error bars are* ±1 *r.m.s.* **(b)** *The black data denote the binned averages of the six individual galaxies, as well as the stack shown in (a), with 1 r.m.s. uncertainties of the error-weighted means shown as grey shading (the outermost point has lighter shading to indicate that only two data points entered the average). In individual galaxies,* $R_{\rm max}$ *depends on the ratio of bulge to total baryonic mass of the galaxy, the size of the galaxy and the instrumental resolution, leading to varying amounts of beam smearing. We assume an average value of* $R_{\rm max} \approx (1.3-1.5)\ R_{1/2}$. *For comparison, the grey dashed line indicates the slope of a typical rotation curve for low-redshift* ($z = 0$), *massive* ($\log(M_*/M_\odot) \approx 11$), *star-forming disk galaxies (Catinella, Giovanelli, & Haynes, 2006), which are comparable to the six galaxies we studied; the dotted red and solid green curves are the rotation curves of M31 (the Andromeda galaxy; Carignan et al., 2006) and the Milky Way (Bland-Hawthorn & Gerhard, 2016). The thick magenta curve is the rotation curve of an infinitely thin, 'Freeman' exponential disk (Freeman, 1970) with Sérsic index* $n_{\rm Sersic} = 1$. *The blue curve is a turbulent, thick exponential disk, including 'asymmetric drift' corrections for an assumed radially constant velocity dispersion of* $\sigma_0 \approx 50$ *km* s^{-1} *(and a ratio of rotation velocity to dispersion of* $v_{rmrot}/\sigma_0 \approx 5$; *Carignan et al., 2006).*

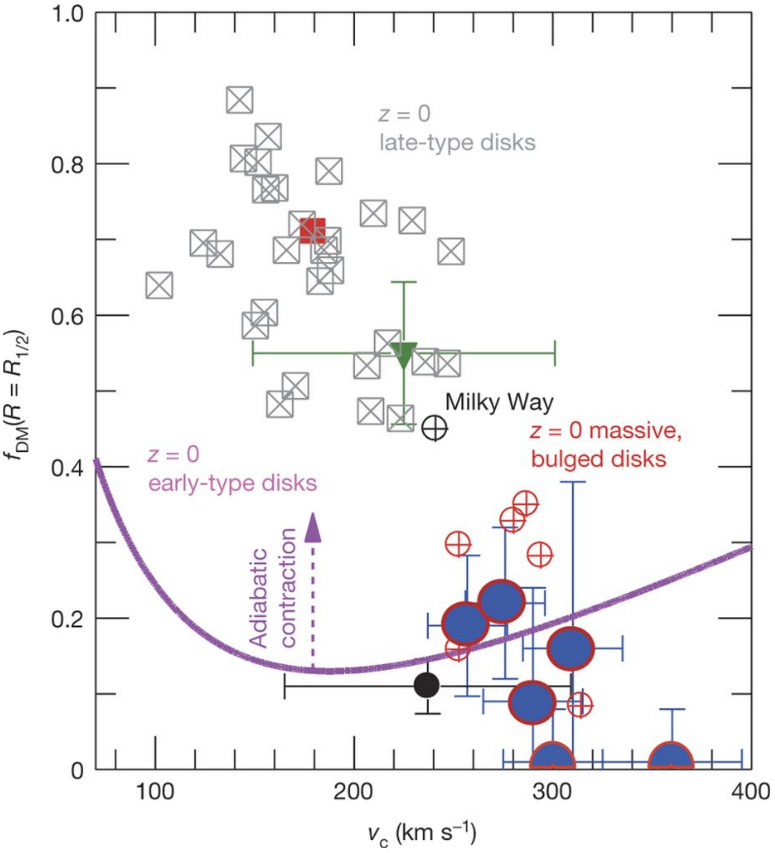

Figure 4.3: *Dark-matter fractions f_{DM} from different methods are listed as a function of the circular velocity of the disk v_c, at approximately the half-light radius of the disk $R_{1/2}$, for galaxies in the current Universe and about 10 Gyr ago. The large blue circles with red outlines indicate the dark-matter fractions derived from the outer-disk rotation curves for the six high-redshift disks presented here (Table 4.1), along with the ±2 r.m.s. uncertainties of the inferred dark-matter fractions and circular velocities. The average dark-matter fractions (and their ±1 r.m.s. errors/dispersions in the two coordinates) obtained from the comparison of inner rotation curves and the sum of stellar and gas masses for 92 $z = 2-2.6$ and 106 $z = 0.6-1.1$ star-forming galaxies are indicated by the filled black circle and green triangle, respectively (Wuyts et al., 2016b). We compare these high-redshift results to $z = 0$ estimates obtained using different independent techniques for late-type, star-forming disks (crossed grey squares, red filled square; Courteau & Dutton, 2015), for the Milky Way (crossed black circle; Bland-Hawthorn & Gerhard, 2016), for massive, bulged, lensed disks (crossed red circles; Courteau & Dutton, 2015), and for passive early-type disks (thick magenta line; Cappellari et al., 2013). The upward magenta arrow marks the typical change if the $z = 0$ data dark-matter haloes are maximally adiabatically contracted.*

Dark matter fractions drop with increasing redshift from $0.8 - 2.36$ (Table 4.1, Figure 4.3). The agreement of the dark matter fraction in the $z = 0.6 - 2.6$ star-forming galaxies and local passive galaxies is interesting. Passive galaxies are likely the descendants of the massive 'main-sequence' star-forming population we are observing in our IFS-samples. Their star formation was likely quenched rapidly at $z \leq 2$ once they had grown to $M_{*,\mathrm{Schechter}} \sim 10^{10.6-10.9}\ M_{\odot}$, after which they transited to the passive galaxy sequence (Peng et al., 2010). The low dark matter fractions in the high-redshift star-forming galaxies may thus be preserved in the 'archaeological' evidence of the local passive population.

Why should high$-z$ disks have been more baryon dominated than low-redshift disks? First, high-redshift disks are gas rich and compact. Star-forming galaxies at $z \approx 2.3$ have molecular gas-to-stellar mass ratios about 25 times larger than those of $z = 0$ galaxies (Genzel et al., 2015) ($M_{\mathrm{molgas}}/M_* \propto (1+z)^{2.7}$), are 2.4 times smaller in size (van der Wel et al., 2014a) ($R_{1/2} \propto (1+z)^{-0.75}$), and so have molecular gas surface densities that are more than two orders of magnitude greater than those of local galaxies. Large gas columns can easily dissipate angular momentum and drive gas inward. The strong redshift dependence of the gas fractions could explain the drop of f_{DM} between $z = 2.3$ and 1 (Figure 4.3). Massive galaxies at high redshift are thought to grow by rapid gas accretion, gas rich mergers and star formation triggered by this accretion (Guo & White, 2008; Oser et al., 2010). In this dissipation dominated peak phase of galaxy growth the centres of dark matter halos can become baryon-dominated in 'compaction events' triggered by mergers, disk instabilities or colliding streams in the inter-galactic web (Zolotov et al., 2015), or by gas 'pile-up' at early times when the gas accretion rates were larger than the star formation consumption rates. However, abundance matching results indicate that the average stellar-to-dark-matter ratio at the virial radius of the halo does not depend strongly on cosmic epoch and is well below the cosmic baryon fraction, $f_b \sim 0.17$, suggestive of very efficient removal of baryons due to galactic outflows (Moster, Naab, & White, 2013).

Could the baryon dominance be caused by a lack of dark matter in the inner disk? These dark matter haloes could deviate from the standard NFW profile, with low concentration parameter ($c < 5$), if they were still growing rapidly and not yet in equilibrium, or if they were perturbed by strong stellar and AGN feedback. We briefly discuss some of these alternatives, such as low concentration parameters, in Section 4.1.1, where we also give a first quantitative comparison between observations and simulations.

Acknowledgments

We thank our colleagues at ESO-Garching and ESO-Paranal, as well as those in the 3D-HST and SINFONI/zC-SINF and KMOS/KMOS^{3D} teams, for their support and high-quality work, which made these technically difficult observations possible. DW and MF acknowledge the support provided by DFG Projects WI 3871/1-1 and WI 3871/1-2. JC acknowledges the support of the Deutsche Zentrum für Luft- und Raumfahrt (DLR) via Project ID 50OR1513. TA and AS acknowledge support by the I-CORE Program of the PBC and Israel Science Foundation (Center No. 1829/12). We thank S. Lilly and A. Dekel for comments on the manuscript.

Author Contributions

Drafting text, figures and Methods: R.G., N.M.F.S., H.Ü., T.N., L.J.T., O.G., D.L., A.R., R.S. and A.S.; data analysis and modelling: R.G., H.Ü., P.L., S.W. and R.D.; data acquisition and reduction: R.G., N.M.F.S., H.Ü., P.L., L.J.T., E.W., S.W., A.Be., S.B., J.C., M.F., A.G., J.T.M. and K.T.; KMOS^{3D} and SINS/zC-SINF IFS survey design and management: N.M.F.S., R.B., E.W., C.M.C., A.R., R.S., S.T. and D.W.; 3D-HST survey analysis: N.M.F.S., S.W., G.B., I.M. and E.J.N.; theoretical interpretation: T.N., T.A., A.Bu., S.G. and O.G.

Table 4.1: *Physical parameters of observed star-forming galaxies*

	COS4 01351	D3a 6397	GS4 43501	zC 406690	zC 400569	D3a 15504
Redshift, z	0.854	1.500	1.613	2.196	2.242	2.383
Scale [kpc arcsec^{-1}]	7.68	8.46	8.47	8.26	8.23	8.14
Priors						
Stellar mass, M_* [$10^{11} M_\odot$]	0.54 ± 0.16	1.20 ± 0.37	0.41 ± 0.12	0.42 ± 0.12	1.20 ± 0.37	1.10 ± 0.34
Total (gas+stars) baryonic mass, $M_{\rm baryon}$ [$10^{11} M_\odot$]	0.9 ± 0.5	2.3 ± 1.1	0.75 ± 0.37	1.4 ± 0.7	2.5 ± 1.2	2.0 ± 1.0
$H-$band half-light radius, $R_{1/2}$ [kpc]	8.6 ± 1.3	5.9 ± 0.8	4.9 ± 0.7	5.5 ± 1.0	4 ± 2	6.3 ± 1.0
Inclination, i [°]	75 ± 5	30 ± 5	62 ± 5	25 ± 12	45 ± 10	34 ± 5
Dark-matter concentration parameter, c	6.8	5	5	4	4	4
Fit parameters						
$v_c(R = R_{1/2}{}^{\rm a}$[km s^{-1}]	276	310	257	301	364	299
$R_{1/2}(n = 1)$ [kpc]	7.3	7.4	4.9	5.5	3.3	6
Velocity dispersion, σ_0 [km s^{-1}]	39	73	39	74	24	76
Total (gas+stars, including bulge) baryonic mass, $M_{\rm baryon}$ [$10^{11} M_\odot$]	1.7	2.3	1.0	1.7	1.7	2.1
$M_{\rm bulge}/M_{\rm baryon}{}^{\rm b}$	0.2	0.35	0.4	0.6	0.37	0.15
$f_{\rm DM}(R = R_{1/2})^{\rm c}$	0.21 (0.1)	0.17 (<0.38)	0.19 (0.09)	0.0 (<0.08)	0.0 (<0.07)	0.12 (<0.26)

[a] Total circular velocity at the half-light radius (rest-frame optical) $R_{1/2}$, including bulge, exponential disk ($n = 1$) and dark matter, and corrected for asymmetric drift: $v_c(R)^2 = v_{\rm rot}(R)^2 + 3.36\sigma_0^2(R/R_{1/2})|_{n=1}$.

[b] $M_{\rm bulge}$ is the baryonic mass confined to the central 1 kpc of the galaxy, less the contribution from the exponential disk.

[c] Ratio of dark-matter mass to total mass at the best-fit half-light radius of the optical light, $f_{\rm DM}(R = R_{1/2}) = (v_{\rm DM}/v_c)^2|_{R=R_{1/2}}$; numbers in parentheses are the ±2 r.m.s. or upper limits (goodness of fit $\delta\chi^2 = 4$, about 95% probability) uncertainties. We use an NFW halo with concentration parameter c and no adiabatic contraction.

4.1.1 Methods

Galaxy Samples The galaxies discussed in this paper were taken from two near-IR integral field spectroscopic samples ('IFS-samples') of distant, massive ($\log(M_*/M_\odot) \gtrsim 9.6$) star-forming galaxies, targeting primarily rest-frame optical emission around the Hα line,

(1) The SINS/zC-SINF survey of $z \sim 1.5 - 2.5$ star-forming galaxies (Förster Schreiber et al., 2009; Mancini et al., 2011) observed with SINFONI on the ESO Very Large Telescope (Eisenhauer et al., 2003; Bonnet et al., 2004) (VLT) in both seeing-limited mode ($2R_{1/2,\mathrm{beam}}$ = FWHM $\sim 0.45'' - 0.6''$) and at higher resolution with adaptive optics (AO; FWHM$\sim 0.15'' - 0.25''$).

(2) The first 2.5-year sample from the ongoing five-year KMOS$^{\mathrm{3D}}$ survey of $0.6 < z < 2.6$ galaxies (Wisnioski et al., 2015), all observed in seeing-limited mode (FWHM$\sim 0.4'' - 0.7''$) with the KMOS multiplexed IFS instrument on the VLT (Sharples et al., 2013).

The IFS-sample galaxies are bench-marked to be representative in all important physical parameters of the high$-z$, 'field' star-forming population (stellar mass, star formation rate, size). We have not included galaxies in very dense ('cluster'-like) environments, and mergers or strongly interacting galaxies are relatively rare (Wisnioski et al., 2015). These galaxies are located on and around (± 0.6 dex) of the 'star-formation main sequence' at all redshifts included. Below, we summarize the selection criteria used for drawing the individual objects and the stacking sample from the SINS/zC-SINF and KMOS$^{\mathrm{3D}}$ surveys, and then discuss how their stellar, structural, and kinematic properties were derived. A comprehensive description of the surveys, target selections, and galaxy properties can be found in Grogin et al. (2011); Koekemoer et al. (2011); van Dokkum et al. (2011); Brammer et al. (2012); Skelton et al. (2014); Momcheva et al. (2016).

Outer Rotation Curve Samples The six individual galaxies studied here were selected for very sensitive follow-up observations primarily based on their having (i) high quality and high signal-to-noise data in the initial SINFONI and KMOS observations, (ii) rotation-dominated disk kinematics from Hα, with a ratio of rotation velocity to velocity dispersion of $v_{\mathrm{rot}}/\sigma_0 > 3$, (iii) no bright neighboring galaxy in line or continuum emission, and (iv) extended well-resolved star-forming disks. All six galaxies lie close to the main-sequence of star-forming galaxies at $\log(M_*/M_\odot) \geq 10.5$. By design, their half-light radii ($R_{1/2} \gtrsim 4$ kpc) place them in the upper half of the size distribution of massive star-forming galaxies, such that their disk emission probes further into the halo than for typical star-forming galaxies and their inferred baryonic angular momenta are comparable or larger than the population average (about 0.037, Burkert et al., 2016). Smaller galaxies would therefore place less stringent constraints on the dark matter fraction in the outer disk, while they are likely to be even more baryon dominated (van Dokkum et al., 2015). Although an optimum selection of rotation-curve candidates would favour high-inclination galaxies, the six galaxies exhibit a wide range of inclination ($i \approx 25^\circ - 75^\circ$), with the low inclination systems drawn from the AO SINS/zC-SINF sample (Förster Schreiber et al., 2018), which is high quality in terms of angular resolution and depth, but too small to allow an inclination cut.

For the stacking analysis (Lang et al., 2017), we selected star-forming galaxies based on their SINFONI or KMOS Hα kinematics and their Hubble Space Telescope (HST) rest-optical morphologies as follows: (i) rotation-dominated disk kinematics from Hα with $v_{\mathrm{rot}}/\sigma_0 > 1$, and (ii) detection of a significant change of slope in the extracted velocity curve. The latter criterion is the most stringent one: while roughly 3/4 of the parent KMOS$^{3\mathrm{D}}$ and SINS/zC-SINF samples are fairly unperturbed, rotation-dominated disks, only half of them show a flattening of the velocity curve at large radii. This large downsizing from the initial samples is driven by the limited field of view (FOV) of the IFS data not reaching the radius of velocity turnover for the more extended galaxies (about $3'' \times 3''$ for the KMOS IFSs with which the largest parent sample was observed and for the AO-assisted SINFONI data with a scale of $0.05''$ per pixel, and about $4'' \times 4''$ for the seeing-limited SINFONI data at $0.125''$ per pixel with the on-source dithering strategy used for most targets), or insufficient signal-to-noise at large radii to detect a change of slope. The resulting stacking sample consists of 103 near-main-sequence galaxies spanning $0.6 \leq z \leq 2.6$ and $9.3 \leq \log(M_*/M_\odot) \leq 11.5$. Their size and angular momentum distributions overlap well with those of the bulk of star-forming galaxies in similar redshift and mass ranges; there is only a mild bias toward larger $R_{1/2}$ for galaxies entering the stack especially for the $z > 1.3$ subset, caused primarily by the implicit signal-to-noise requirement at large radii imposed by the necessity of detecting a velocity curve flattening. We performed simulations to determine that the selection criteria and analysis methodology (see below) did not introduce a significant bias in the shape of the resulting stacked rotation curve. A more detailed discussion of the stacking methodology and so on is provided below.

In Figure 4.4, we compare the distributions in stellar mass, star formation rate, and size properties of the six individual galaxies, the stacking sample, and the parent SINS/zC-SINF and KMOS$^{3\mathrm{D}}$ samples to those of the underlying $\log(M_*/M_\odot) \geq 9.0$ galaxy population drawn from the 3D-HST survey source catalog at $JH_{\mathrm{AB}} < 26$ mag (for which the mass completeness is below $\log(M_*/M_\odot) = 9.0$ out to $z = 3$; Skelton et al., 2014; Momcheva et al., 2016) in the five CANDELS extragalactic fields (Grogin et al., 2011; Koekemoer et al., 2011). To account for the large evolution in star formation rate and size at fixed mass, Figure 4.4 shows the offsets in star formation rate relative to the main sequence at the same z and M_* (Whitaker et al., 2014), and the offsets in effective radius at rest-frame 5000Å

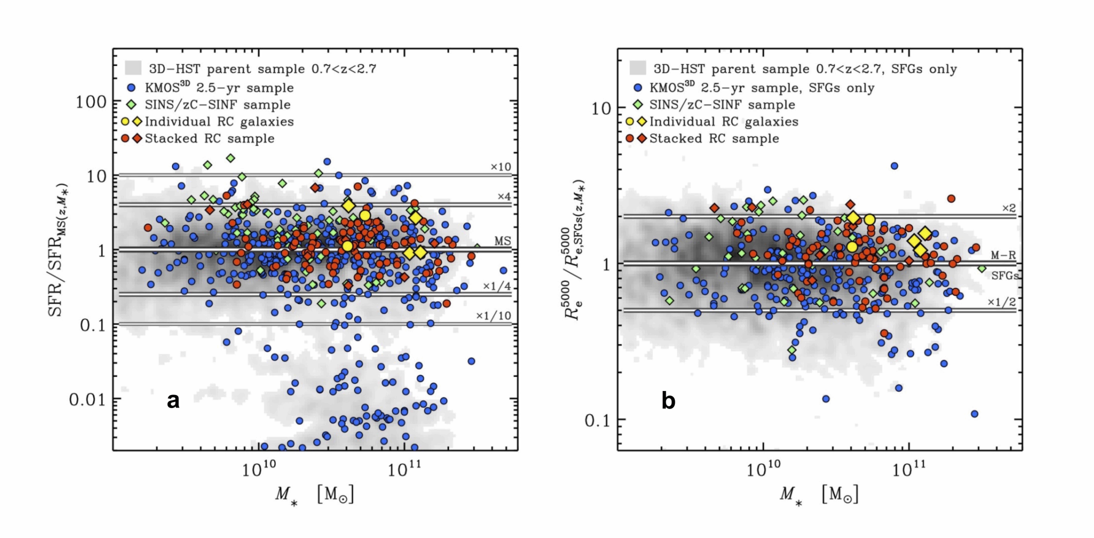

Figure 4.4: **(a)** *Location in stellar-mass – star-formation-rate space. The star-formation rate (SFR) is normalized to that of the 'main sequence' (Whitaker et al., 2014) at the redshift and stellar mass of each galaxy ($SFR_{\rm MS}(z, M_*)$).* **(b)** *Location in stellar-mass – size space. The size is the half-light radius measured in the observed H−band corrected to the rest-frame 5,000Å (R_e^{5000}) and normalized to that of the mass – size relation for star-forming galaxies (van der Wel et al., 2014a) at the redshift and stellar mass of each source ($R^{5000}_{e,\rm SFGs(z,M_*)}$). In (a) and (b), the greyscale image shows the distribution of the underlying galaxy population at $0.7 < z < 2.7$ taken from the 3D-HST source catalogue at $\log(M_*/M_\odot) > 9.0$ and $K_{\rm AB} < 23$ mag (the magnitude cut applied when selecting KMOS$^{\rm 3D}$ targets and corresponding roughly to the completeness limits of the parent samples for SINS/zC-SINF targets). The current 2.5-year KMOS$^{\rm 3D}$ sample is shown with blue circles, and the SINS/zC-SINF sample with green diamonds. The two KMOS$^{\rm 3D}$ and four SINS/zC-SINF galaxies with individual outer rotation curves (RCs) are plotted as yellow circles and diamonds, respectively. Similarly, the KMOS$^{\rm 3D}$ and SINS/zC-SINF galaxies included in the stacked rotation curve are plotted as red circles and diamonds. All 3D-HST and KMOS$^{\rm 3D}$ galaxies are included in (a), whereas only star-forming galaxies (SFGs) are shown in (b), defined as having a specific star-formation rate higher than the inverse of the Hubble time at their redshift. The galaxies with individual outer rotation curves lie on and up to a factor of four times the main-sequence (MS) in star-formation rate (with mean and median log(SFR/SFR$_{\rm MS}$)=0.24), and have sizes 1.2-2 times the $M_* - R_e^{5000}$ relation ('M-R SFGs'; mean and median offset in $\log(R_e^{5000}) \approx 0.2$ dex). In star-formation rate and R_e^{5000}, the distribution of the stacked rotation-curve sample is essentially the same as the reference 3D-HST population in mean/median offsets (approximately 0.06 dex above the main-sequence and 0.07 dex above the mass – size relation) and in their scatter about the relationships (approximately 0.3 dex in log(SFR) and 0.17 dex in $\log(R_e^{5000}$); (see van der Wel et al., 2014a; Whitaker et al., 2014).*

relative to the mass-size relation for star-forming galaxies (van der Wel et al., 2014a).

Parent kinematic samples The SINS/zC-SINF Hα sample was drawn from large optical spectroscopic surveys of high-redshift candidates photometrically pre-selected in multi-band imaging surveys based on various magnitude and/or color criteria at optical to mid-infrared wavelengths. As extensively described in two articles (Förster Schreiber et al., 2009; Mancini et al., 2011), the SINS/zC-SINF Hα sample collectively provides a reasonable representation of massive star-forming galaxies at $z \approx 1.5-2.5$, with some bias towards bluer systems stemming from the primary criterion of having a secure optical spectroscopic redshift. In addition, the objects chosen for the near-infrared SINFONI observations were also required to have Hα falling away from bright OH sky lines and within high atmospheric transmission windows, and to have an expected total Hα flux of about 5×10^{-17} erg s^{-1} cm^{-2} or, correspondingly, a star formation rate of about $10 M_{\odot}$yr^{-1} assuming a typical visual extinction of $A_V \approx 1$ mag. The latter flux criterion was applied last and did not significantly impact the final set of targets.

The KMOS$^{3\mathrm{D}}$ sample is taken from the '3D-HST' source catalog (Brammer et al., 2012; Skelton et al., 2014; Momcheva et al., 2016) in fields with deep HST imaging from the CANDELS Treasury program (Grogin et al., 2011; Koekemoer et al., 2011) and $R \approx 130\lambda = 1.1 - 1.7\mu$m slitless spectroscopy using the HST WFC3/G141 grism from the 3D-HST Treasury program (Wuyts et al., 2011b). Multi-band photometry and grism spectra are extracted for sources reaching $JH_{\mathrm{AB}} \approx 26$ mag, redshifts are determined from the grism spectra (probing Balmer/4000-Å continuum break and/or emission lines) combined with the full optical-to-mid-infrared photometry and supplemented with spectroscopic redshifts available from the literature (Skelton et al., 2014; Momcheva et al., 2016). The KMOS$^{3\mathrm{D}}$ targets are selected primarily to have a stellar mass $10^{9.5} M_{\odot}$ (derived from modeling the photometry; see below) and $K_{\mathrm{AB}} = 23$ mag, and a sufficiently accurate redshift (dominated by grism and spectroscopic redshifts) ensuring avoidance of sky lines and poor telluric transmission for Hα. No explicit cut in star formation rate, color, or size is applied. Both the 3D-HST and KMOS$^{3\mathrm{D}}$ near-infrared and mass selections result in a wide coverage of the full underlying galaxy population $0.7 < z < 2.7$, including the redder dust-obscured and/or more passive objects. In the first 2.5 years of our on-going KMOS$^{3\mathrm{D}}$ survey, we emphasized high-mass targets (but over a very wide range of three orders of magnitude in specific star formation rate relative to the 'main sequence' relationship). The resulting mass distribution is weighted towards high masses compared to a purely mass-selected sample; once accounting for this bias, the sample provides however a good representation of the underlying galaxy population in other properties (Wisnioski et al., 2015; Burkert et al., 2016; Wuyts et al., 2016b).

Global stellar and gas properties The global stellar properties were derived following the procedures outlined by Wuyts et al. (2011b). In brief, stellar masses were obtained from fitting the observed broadband optical to near-/mid-IR (rest-UV to optical/near-IR) spectral energy distributions (SEDs) with population synthesis models (Bruzual & Charlot, 2003), adopting a reddening law (Calzetti et al., 2000), a Chabrier (2003) initial mass function, a solar metallicity, and a range of star formation histories (constant star formation rate, exponentially declining or increasing star formation rates with varying e-folding timescales). Over the mass and redshift ranges of the galaxies, gas-phase O/H abundances inferred from rest-optical nebular emission lines suggest metallicities of about 1/4 to 1 times the metallicity of the Sun (Erb et al., 2006; Zahid, Kewley, & Bresolin, 2011; Zahid et al., 2014; Stott et al., 2013; Steidel et al., 2014; Wuyts et al., 2014, 2016a; Sanders et al., 2015). Varying the assumed metallicity in this range would change the stellar masses in our modeling by less than 0.1 dex (Förster Schreiber et al., 2009; Wuyts et al., 2007). Given this small impact and the uncertainties in metallicity determinations for high-z star-forming galaxies (Kewley et al., 2013), we chose to keep a fixed solar metallicity. We note that throughout the paper, we define stellar mass as the ‘observed’ mass (‘live’ stars plus remnants), after mass loss from stars.

The star formation rates were obtained from rest-frame ultraviolet + infrared luminosities through the Herschel-Spitzer-calibrated ladder of star formation rate indicators (Wuyts et al., 2011b) or, if infrared luminosities are not available (from lack of observations or the source was undetected), from the broadband SED modeling described above.

Individual determinations of molecular gas masses (from CO line or submillimeter/far-infrared dust continuum emission) are scarce for our galaxy samples, and atomic hydrogen masses are not known for any of our high$-z$ star-forming galaxies. We computed molecular gas masses from the general scaling relations between star formation rates, stellar masses, and molecular gas masses for main sequence galaxies (as a function of redshift; Genzel et al., 2015; Tacconi et al., 2018). We assumed, as argued previously (Genzel et al., 2015), that at $z \sim 1-3$ the cold gas content of star-forming galaxies is dominated by the molecular component such that the atomic fraction can be neglected. As such the gas masses estimated from these scaling relations may be lower limits.

Structural properties The stellar structural parameters used as priors in our detailed kinematic modeling were derived by fitting two-dimensional Sérsic models to the high-resolution $H-$band images from HST observations available for all KMOS^{3D} objects and most SINS/zC-SINF galaxies (Förster Schreiber et al., 2011a,b; Wuyts et al., 2012, 2016b; Lang et al., 2014; van der Wel et al., 2014a; Tacchella et al., 2016b,a). For the remainder of the SINS/zC-SINF galaxies (without HST imaging), structural parameters were estimated from the line integrated

Hα distributions and/or from the continuum images synthesized from the IFS data, depending on the galaxy. To first order this approach is justified as high-redshift star-forming galaxies are gas-rich with large star formation rates and young stellar populations although there are some small systematic differences on average because of the presence of substantial stellar bulges in the more massive star-forming galaxies and of possible bright clumps and asymmetric distributions in tracers of on-going star formation (Wuyts et al., 2013; Lang et al., 2014; Genzel et al., 2014b; Tacchella et al., 2015b,a; Nelson et al., 2016b). Of the individual galaxies and stacking sample of interest in the present study, only D3a 6397 lacks HST imaging.

For all but the most massive $z \approx 1-3$ star-forming galaxies, the stellar and Hα surface brightness distributions of main-sequence galaxies across the mass- and redshift range discussed in this paper are reasonably well fit by near-exponential (Sérsic index $n_{\rm Sersic} \approx 1-1.5$) profiles (Wuyts et al., 2011a; Bell et al., 2012; Bruce et al., 2014a,b; Lang et al., 2014; Genzel et al., 2014b; Tacchella et al., 2015b,a). Above $\log(M_*/M_\odot) \approx 11$, $z \approx 1-3$ star-forming galaxies feature a prominent stellar bulge component with characteristic $R_e \approx 1$ kpc and median bulge-to-total ratio in $H-$band light reaching about 20% – 30% (and higher, about 40% – 50% in terms of stellar mass ratio Lang et al., 2014; Tacchella et al., 2015b,a). While central drops in Hα equivalent width, and even flux, of individual galaxies appear to be more frequent at the high-mass end, there is nonetheless evidence that on average the profiles are near-exponential (Nelson et al., 2016a) and that otherwise large central gas and dust concentrations may be present and obscure the optical light from star-forming regions in the inner parts of massive star-forming galaxies (Tadaki et al., 2015, 2017; Nelson et al., 2016b; Barro et al., 2016). These findings motivate our modeling assumption that the baryonic component is distributed in a compact spheroidal bulge at the center of an exponential disk.

The half-light (effective) radii $R_{1/2}$ estimates used for the galaxies refer to the major axis radii. To determine the inclination from the best-fit axial ratios, we account for the fact that for the mass range $\log(M_*/M_\odot) > 10$ spanned by most galaxies of interest here, half or more of the high-redshift star-forming galaxies consist of symmetric, oblate thick disks (Elmegreen et al., 2005; Law et al., 2012; van der Wel et al., 2014b), linked to their large intrinsic gas velocity dispersion (Genzel et al., 2006; Förster Schreiber et al., 2009; Kassin et al., 2012; Newman et al., 2013; Tacconi et al., 2013; Wisnioski et al., 2015) and $v_{\rm rot}/\sigma_0 \lesssim 10$. We note that the H band probes a significant range of rest-frame wavelengths over the $0.6 < z < 2.6$ of the individual galaxies and stacked sample considered in this work. A 'k-correction' (van der Wel et al., 2014a) should ideally be applied to the structural parameters for consistency (and similarly, a statistical correction between Hα and rest-optical sizes could be applied; Nelson et al., 2016a). However, the uncertainties adopted for the size and inclination priors are significant and larger than these corrections would be, and our modeling procedure accounts for them.

Kinematic classification and properties The kinematic information was derived from the SINFONI and KMOS data cubes following our well-established methods (Förster Schreiber et al., 2009; Davies et al., 2011; Wisnioski et al., 2015; where all details of the data reduction and calibration procedures can also be found). In summary, for each galaxy we fitted Gaussian line profiles to each IFS spatial pixel in the final reduced data cube, in some cases after some prior smoothing to increase signal-to-noise ratios. The main kinematic parameters of interest are then derived from the resulting spatially-resolved maps of the velocity centroid and velocity dispersion: $v_{\rm rot}$, σ_0, and $\mathrm{PA}_{\rm kin}$. The quantity $v_{\rm rot}$ is the maximum rotational velocity corrected for beam smearing and inclination i ($v_{\rm rot} = c_{{\rm psf},v} v_{\rm obs} / \sin(i)$), where $v_{\rm obs}$ is half of the difference between the maximum positive and negative velocities on both sides of the galaxy, and $c_{{\rm psf},v}$ is the beam smearing correction for velocity. The quantity σ_0 is the intrinsic velocity dispersion, corrected for beam smearing ($\sigma_0 = c_{{\rm psf},\sigma} \sigma_{\rm obs}$), where $\sigma_{\rm obs}$ is the measured line width in the outer parts of the galaxy corrected for instrumental spectral resolution (i.e., subtracting in quadrature $\sigma_{\rm instr}$), and $c_{{\rm psf},\sigma}$ is the beam smearing correction for the velocity dispersion. $\mathrm{PA}_{\rm kin}$ is the position angle of the kinematic major axis passing through the extrema of the velocity field (the 'line of nodes'). The beam smearing corrections were derived based on model disks for a range of masses, inclinations, ratios of galaxy to beam size, and radii of measurement appropriate for the SINS/zC-SINF and KMOS$^{\rm 3D}$ data sets; all details are given in Appendix A of reference (Burkert et al., 2016)).

With these kinematic maps and properties, a galaxy is classified as a 'rotation dominated' disk if (Wisnioski et al., 2015)

1. the velocity map exhibits a continuous velocity gradient along a single axis; in larger systems with good signal to noise ratio this is synonymous with the detection of a 'spider' diagram in the two-dimensional, first moment velocity map (van der Kruit & Allen, 1978);
2. $v_{\rm rot}/\sigma_0 > 1$
3. the position of the steepest velocity gradient, as defined by the midpoint between the velocity extrema along the kinematic axis, is coincident within the uncertainties with the peak of the velocity dispersion map;
4. the morphological and kinematic major axes are in agreement ($\leq 30°$); and
5. the kinematic center of the galaxy coincides with the maximum/centroid of the stellar distribution.

For the seeing limited KMOS^{3D} survey, 83% of the resolved galaxies fulfill criteria (1) and (2) (92% at $z \approx 1$ and 74% at $z \approx 2$; Wisnioski et al., 2015). This fraction slowly drops if the stricter criteria (3), (4) and (5) are added, and amounts to 70% if all 5 criteria are used. Similar results are obtained in the other recent surveys (Genzel et al., 2014b; Tacchella et al., 2015a; Newman et al., 2013; Förster Schreiber et al., 2018).

The six individual galaxies discussed in this paper, and the stacking sample, satisfy all of the above disk criteria based on their SINFONI and KMOS data. With the higher signal-to-noise of the deeper follow-up observations of the individual galaxies, additional asymmetric features became apparent in the kinematic maps of three of them, associated with gas inflows towards the center (D3a 15504; Genzel et al., 2006), and gas outflows from the inner few kpc plausibly driven by an AGN and from bright off-center clumps driven by star formation (D3a 15504, zC 406690, zC 400569, D3a 6397; Genzel et al., 2011; Newman et al., 2012; Förster Schreiber et al., 2014).

Kinematic Analysis and Mass Modelling In our kinematic analysis we proceed as follows below. For details we refer the reader to published papers (Burkert et al., 2010, 2016; Bland-Hawthorn & Gerhard, 2016), which provide more details on the mathematical and fitting methodology. These papers also refer to the publicly available data analysis tools in the ESO KMOS analysis pipeline as well as the LINEFIT tool (Davies et al., 2011) and a generalized fitting tool, MPEFIT, as well as the general cube analysis tool QFitsView[1] to fit the kinematics by a combination of an exponential disk and dark-matter halos.

(1) We fit a Gaussian profile to each spaxel of the data cube, suitably smoothed to deliver sufficiently high SNR in the outer parts of the galaxy. We infer the systemic redshift (or velocity) of the galaxy by symmetrizing the red- and blue-shifted peak velocities. We determine the position angle of the kinematic axis $\mathrm{PA_{kin}}$ by determining the line of nodes along the maximum velocity gradient, as well as the morphological major axis of the galaxy $\mathrm{PA_{morph}}$ from the stellar surface density map or the $H-$band HST map, and take an average. These two angles typically agree to better than 5-7 degrees. Finally we determine the galaxy centre x_0, y_0 from an average of the zero-crossing of the line of nodes, the velocity dispersion peak and with the position of the central stellar bulge, which is prominent in all 6 of our galaxies. This allows the determination of x_0, y_0 to about 0.5-1 pixel, which is small compared to the size of the final extraction slitlet in the next step. We infer the disk's inclination from the minor to major axis ratio, $q = b/a$, of the stellar distribution or the HST $H-$band data, and $\cos^2(i) = (q^2 - q_0^2)/(1 - q_0^2)$, with $q_0 \approx 0.15 - 0.2$ appropriate for $z \approx 1 - 3$ (see

---

[1] `http://www.mpe.mpg.de/~ott/QFitsView/`

references above). We have found in KMOS^{3D} that this method works reasonably well for inclined disks (Wuyts et al., 2016b) but naturally becomes very uncertain for the three face-on disks in our sample, D3a 15504, zC 406690 and D3a 6397. In these cases we included the inclination as a second order fit parameter to bring the disk mass into a good match with the prior $M_{\rm baryon} = M_{\rm bulge} + M_{*,\rm disk} + M_{\rm gas,disk}$.

(2) Next we go back to the original data cube and extract position-velocity and position-velocity dispersion cuts along the best fit major axis by fitting Gaussian profiles in software slits typically four to five pixels perpendicular to, and two to three pixels along the line of nodes. This corresponds to about 1.1 and 0.5 resolution elements, respectively, and thus is approximately Nyquist sampled along the line of nodes. To include systematic uncertainties, we multiply all fit errors by 1.5 and introduce lower ceiling uncertainties of ±5 and ±10 km s^{-1} for velocity and velocity dispersion measurements, respectively. These scalings are derived from bootstrapping, as well as error scaling of the final reduced chi-squared $\chi^2_{\rm r}$ to about 1 for five of the six sources. We do not consider the additional information from deviations from Gaussian shape (the h_3 and h_4 components; Cappellari, 2016), as this does not add any useful information on the outer disks, and only on the details of the heavily beam-smeared data in the cores of the galaxies, which is of secondary interest in this paper. We next subtract in squares the instrumental line width to infer intrinsic velocity dispersions in each slit.

(3) Now we begin the fitting process to a model that consists of an $n = 1$ exponential disk (with effective radius $R_{1/2,\rm disk}$), a central bulge of $R_{\rm bulge} = 1$ kpc (with the B/T fit parameter giving the mass in the bulge relative to the total (disk+bulge) baryonic mass $M_{\rm baryon,disk}$), the rest being in the $n = 1$ disk), plus a dark matter halo. In those cases where we have a significant bulge, we assume that the Hα light distribution only traces the disk component, which is empirically justified (Wuyts et al., 2013; Nelson et al., 2016b). The assumption of exponential disk distributions ($n = 1$) is supported quite well for the 3D-HST star-forming population, which is characterized by $n = 0.5 - 2$ for most but the more bulge dominated systems (Lang et al., 2014; Wuyts et al., 2016b). We assume that the disk has a constant velocity dispersion, which we determine mainly in the outer parts of each galaxy where the beam-smeared rotation component is small. For the fitting we use a thin-exponential disk rotation curve (Freeman, 1970) but correct for the effects of the significant scale height ($h_z \approx (\sigma_0/v_{\rm rot}(R_{1/2}))R_{1/2}$) with models (Noordermeer, 2008) that assume a constant scale height. Near $R_{1/2}$ the Freeman disk rotates 15% faster than the corresponding spherical model, and the Noordermeer correction is about 0.9-0.97 so that the final rotation velocity is only 4-11% faster than the spherical model. For the dark matter halo, we use an NFW model (Navarro, Frenk, & White, 1996). We do not consider adiabatic contraction of the halo, such that the only parameter of the halo is its mass $M_{\rm virial} = M_{200,\rm NFW}$, where we fix the concentration parameter c to a typical value at the respective redshift (Bullock et al., 2001; Gao et al., 2008; Dutton

& Macciò, 2014). The angular momentum parameter of the halo is implicitly contained in $R_{1/2,\mathrm{disk}}$ and the assumption $j_{\mathrm{disk}} = j_{\mathrm{DM}}$ (Burkert et al., 2016). This yields 5 or 6 primary fit parameters, $R_{1/2,\mathrm{disk}}$, $M_{\mathrm{baryon,disk}}$, M_{virial}, B/T, σ_0 and in three cases, also the disk inclination. As for the data we determine velocity and velocity dispersion cuts for the model, convolve with the instrumental beam and then find the weighted best fit in the usual χ^2 minimization (using the DYSMAL tool; Förster Schreiber et al., 2009; Davies et al., 2011). For four or five of these parameters we have priors from independent data: Inclination, B/T and $R_{1/2}$ from the HST J, H imagery, $M_{\mathrm{baryon,disk}}$ from the sum of stellar disk mass in bulge and disk from the 3D-HST modelling and the (molecular) gas mass from the scaling relations between M_*, star formation rate and z and M_{molgas} (Genzel et al., 2015; Tacconi et al., 2018). We use these priors and their uncertainties to set upper and lower limits for the fitting range, as well as a constraint for inclination, as described above. The dark matter halo mass M_{virial} is a free parameter in the fitting, with only a fixed lower limit of $M_{\mathrm{virial}} = 10^7 M_\odot$.

(4) We include in our fitting a correction of the disk rotation for pressure effects due to the significant turbulent motions (asymmetric drift; Burkert et al., 2010, 2016; Wuyts et al., 2016b). This correction lowers the rotation velocity in the outer disk:

$$v_{\mathrm{rot}}^2 = v_c^2 + 2\sigma^2 \frac{\mathrm{d}(\ln \Sigma)}{\mathrm{d}(\ln R)} = v_c^2 - 2\sigma^2 \frac{R}{R_d}, \tag{4.1}$$

where Σ is the surface density distribution of the disk, which we assume to be an exponential with scale length $R_d = R_{1/2}/1.68$. The assumption of radially constant velocity dispersion likely is a simplification. In that case the thickness of the disk increases exponentially with radius. A superposition of a thin and thick disk could lead to a radially increasing dispersion and a more steeply falling rotation curve. This would create room for a somewhat higher dark matter fraction at $R_{1/2}$ and beyond than in the case of constant dispersion. In absence of any clear evidence we prefer to stay with the simplest assumption of a constant velocity dispersion.

Figure 4.5 shows the final χ_r^2 distributions for the most important parameter for our study, the dark matter fraction at $R_{1/2}$, $f_{\mathrm{DM}}(R_{1/2})$. The number of independent data points in the six galaxies varies between 30 and 54, and with the error-scaling described above the best fit in five of the 6 galaxies has a minimum of $\chi^2_{\mathrm{r,min}} = 0.98 - 1.7$. The one exception, D3a 15504 (black line in Figure 4.5) has $\chi^2_{\mathrm{r,min}} = 2.25$. This is caused mainly by the overshooting of the central velocity dispersion in two independent data sets that cannot be matched by the bulge plus disk data, as well as a second outlier point in velocity just north of the nucleus. We believe that the cause for these large near-nuclear deviations from the model is strong non-circular, or bar streaming in combination with outflows from the central AGN, which are well known to exist in this galaxy (Genzel et al., 2006;

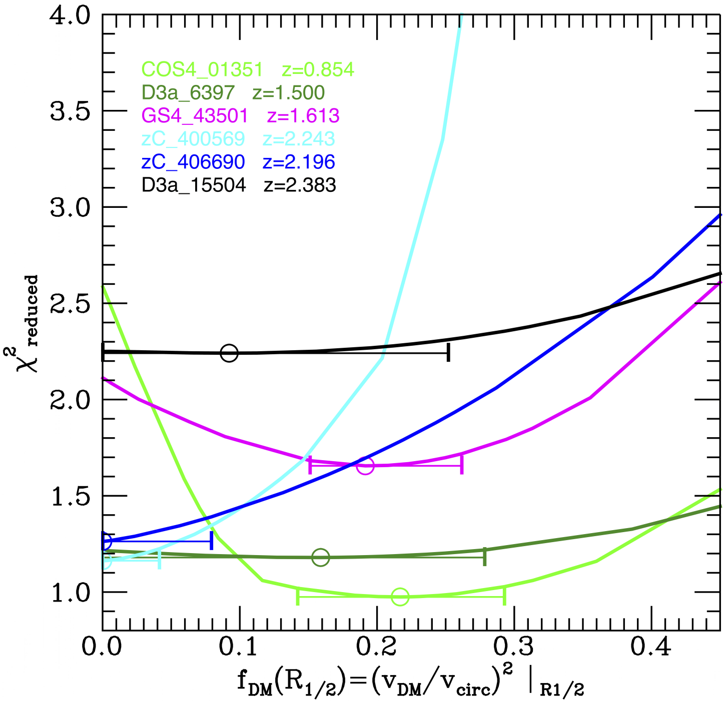

Figure 4.5: *The reduced chi-squared as a function of the dark-matter fraction $f_{\rm DM}$ at $R_{1/2}$ for the six galaxies in our sample, once the other parameters (x_0, y_0, the position angle of the kinematic major axis $PA_{\rm maj}$, i, σ_0, $R_{1/2}$ and B/T) are fixed at their best-fit values. Global minima are marked by circles; error bars give $\Delta\chi^2 \pm 4$ ranges, corresponding to confidence levels of 95% (2 r.m.s.) under the assumption of single-parameter Gaussian distributions. This is the most important parameter dependence for our dataset.*

Förster Schreiber et al., 2014). We will come briefly back to this issue when we discuss the two-dimensional residual maps below.

Parameter correlations and Dark Matter fractions From Figure 4.5 it becomes clear that the χ^2_r vs $f_{\rm DM}(R_{1/2})$ space is relatively flat for some of our galaxies, and it is therefore important to systematically test the dependence of $f_{\rm DM}(R_{1/2})$ on physical properties which constrain the rotation curve other than $M_{\rm baryon}$ and the mass of the dark matter halo $M_{\rm DM}$, namely $R_{1/2}$ and B/T. For galaxies with very low $f_{\rm DM}(R_{1/2})$ (zC 400569 and zC 406690), varying $R_{1/2}$ within the uncertainties, or B/T in steps of 0.05 or 0.1, does not significantly alter $f_{\rm DM}(R_{1/2})$. For the other galaxies, changing B/T has a larger effect than changing $R_{1/2}$. We find most extreme changes for galaxy D3a 6397, with $(\partial f_{\rm DM})/(\partial B/T) = 2.4$ when going from the best-fit $B/T = 0.35$ to $B/T = 0.3$ (that is, towards lower $f_{\rm DM}(R_{1/2})$), and with $(\partial f_{\rm DM})/(\partial R_{1/2}) = 0.6$ when going from the best-fit $R_{1/2} = 0.87$ to $R_{1/2} = 0.97$ (that is, towards higher $f_{\rm DM}(R_{1/2})$). We show

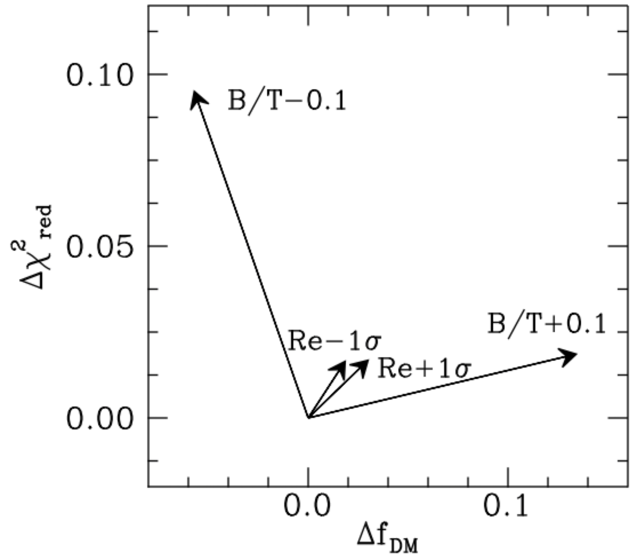

Figure 4.6: *Changes in B/T and $R_{1/2}$ are labelled '$B/T \pm 0.1$' and '$R_e \pm 1\sigma$', respectively, where 1σ is the uncertainty on $R_{1/2}$ given in Table 4.1; $\chi^2_{\rm red}$ is the reduced chi-squared.*

schematically in Figure 4.6 how $f_{\rm DM}$ and χ^2_r change for changes in these various parameters.

Generally, we find that increasing B/T leads to increased $f_{\rm DM}(R_{1/2})$, which can be understood in the sense that a higher fraction of the baryonic mass in the central bulge decreases the relative contribution of the baryons to $v_{\rm circ}$ at $R_{1/2}$. For changing $R_{1/2}$, the effects are less definite, but for the majority of cases we find that increasing $R_{1/2}$ again leads to increased $f_{\rm DM}(R_{1/2})$. For these cases, this can be understood in the sense that a larger $R_{1/2}$ distributes the baryonic mass onto a larger disk (i.e. less compact), leading to less relative contribution of the baryons to $v_{\rm circ}$ at $R_{1/2}$. Mean changes in $f_{\rm DM}(R_{1/2})$ when increasing/decreasing the best-fit B/T by the uncertainties given in Table 4.1, or increasing/decreasing the best-fit B/T by 0.1, are all below $\Delta f_{\rm DM} = 0.13$ (see also Figure 4.6).

The dark matter fraction depends also on the halo mass distribution. Our best-fit models do not include the possible adiabatic contraction of the dark matter halo as a response to the formation of the central galaxy. Simulations show that at high redshift ($z \approx 2$) adiabatic contraction can have an effect on the central dark matter density distribution (Johansson, Naab, & Ostriker, 2009; Dutton et al., 2015). Its net effect, however, is not well constrained and depends largely on the feedback implementation (Duffy et al., 2010), where strong supernova or AGN feedback can even create central dark matter cores (Pontzen & Governato, 2012; Martizzi, Teyssier, & Moore, 2013). Recent work (Dutton et al., 2016) constructs a toy model of repeated inflow and outflow cycles for dwarf to Milky Way type haloes to capture the various effects of baryons on the central dark matter

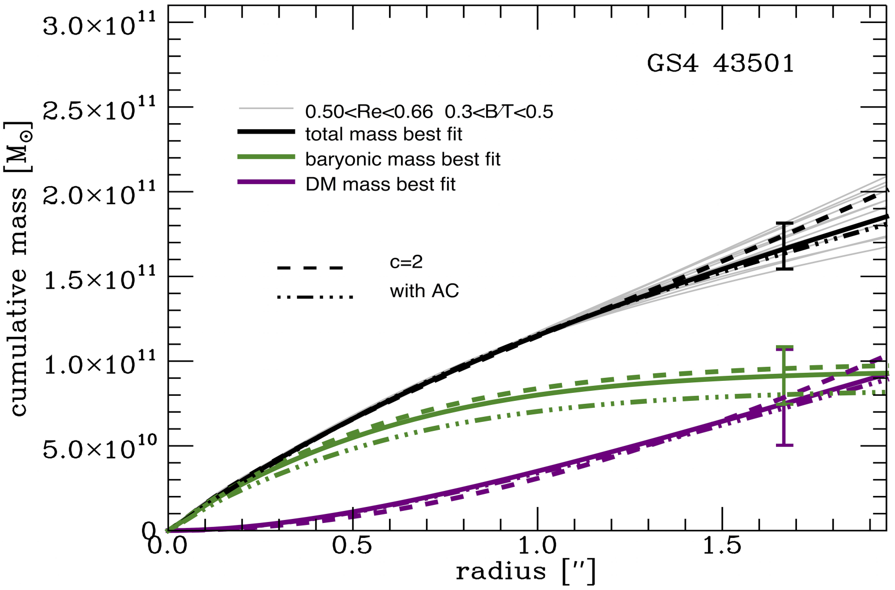

Figure 4.7: *Solid lines show the best fit; error bars show the variations in total (black, grey), baryonic (green) and dark-matter (DM; purple) mass at the outermost projected radius constrained by our data, if deviations from* B/T *and* $R_{1/2}$ *within the uncertainties are considered (only cases with* $\chi^2_{\rm red} < 1.75$ *are considered). Dashed lines show the best fit for a model with lower concentration parameter (*$c = 2$ *instead of* $c = 5$*); dashed-dotted lines show the best fit for a model with adiabatic contraction (AC; Blumenthal et al., 1986). Both modifications of the dark-matter profile lead to changes in the cumulative mass that are smaller than those obtained by varying* B/T *and* $R_{1/2}$ *within the above uncertainties. The grey lines encompass variations in the dark-matter fraction of* $f_{\rm DM}(R_{1/2}) = [0.14, 0.27]$ *(best-fit* $f_{\rm DM}(R_{1/2}) = 0.19$*).*

distribution. They find that high gas fractions and low star formation efficiencies favour halo expansion, as well as extended baryon distributions. Another possibility is 'baryonic gas-pile-up' at early times (Lilly et al., 2013). Since the star formation accretion rate scales as $(1+z)^{2-3}$ (Courteau et al., 2014) while the star formation efficiency scales as $(1+z)^{0.6}$ (Genzel et al., 2015), star formation may not be efficient enough at $z > 2-3$ to consume the incoming accreted baryonic gas, and gas might pile-up in the inner disk (Lilly et al., 2013).

We tested the effect of adiabatic contraction on an NFW halo (Blumenthal et al., 1986). Generally, for the constraints on the dark matter halo as set by our data, we find that the effects of adiabatic contraction (or of modest variations of

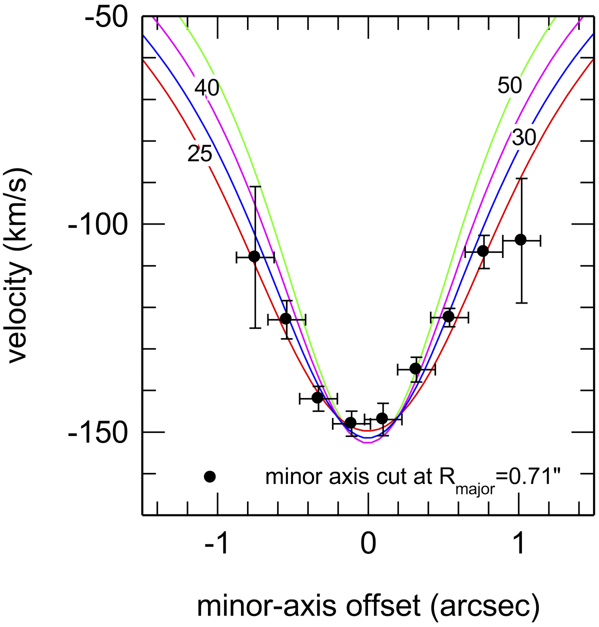

Figure 4.8: *Shown are the velocities (data points, with 1 r.m.s. error bars) and disk models for different inclinations (lines):* 25° *(red),* 30° *(blue),* 40° *(magenta) and* 50° *(green). The minor-axis cut favours a low inclination. In combination with the morphology of the stellar surface density distribution (Figure 4.1) and the constraint on the baryonic mass of the disk, this yields an overall inclination of* 34°±5° *(Table 4.1).* $R_{\rm major}$ *is the radial distance from the centre of the galaxy along the kinematic major axis.*

the concentration parameter) on $f_{\rm DM}$ are lower than the effects of changing $R_{1/2}$ or B/T within the uncertainties (Figure 4.7).

Two-dimensional Analysis Our analysis so far has used major axis cuts of velocity and velocity dispersion to characterize the mass distribution. We used the availability of the unique two dimensionality of integral field data to constrain x_0, y_0 and PA$_{\rm kin}$. The question is whether two dimensional fitting of the gas kinematics might provide additional constraints. It turns out that for the relatively low resolution data on compact high$-z$ disks (with $R_{1/2,\rm disk}/R_{\rm beam} \approx 2.7 - 4.5$) indeed most of the rotation curve information is encapsulated on/near the major axis. In deep AO data on moderate inclination, large disks, a kinematic estimate of inclination may be obtained from the off-axis data, in addition to centre and node direction. The 22h SINFONI AO data for D3a 15504 (Förster Schreiber et al., 2018) can be used in this way, and Figure 4.8 shows the result. The analysis of the minor axis cut data in this case support the evidence from the HST stellar distribution and the baryonic to dynamical mass constraint that the inclination of this galaxy is low, $34° \pm 5°$ (Table 4.1).

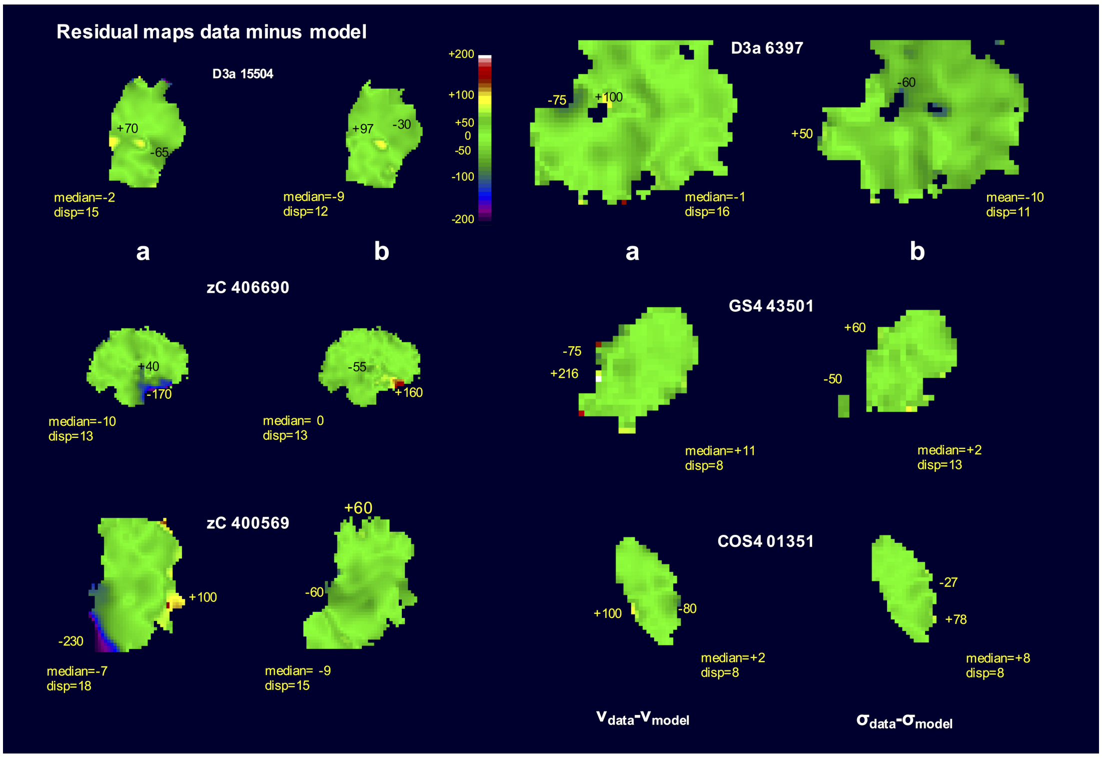

Figure 4.9: **(a), (b)** *Residual maps (data minus model) for velocity ((a); $v_{\mathrm{data}} - v_{\mathrm{model}}$) and velocity dispersion ((b); $\sigma_{\mathrm{data}} - \sigma_{\mathrm{model}}$), for the six galaxies studied here. The colour scale is the same in all maps (from -200 km s^{-1} (purple) to +200 km s^{-1} (white)). Minimum and maximum values are noted in each map, as are the median and median dispersion ('disp') values.*

Kinematic residual maps Another way of utilizing the full two-dimensional information is to construct two-dimension velocity and velocity dispersion residual maps (data minus model), constructed from the major-axis cut method, and then check whether systematic residuals appear (van der Kruit & Allen, 1978). Figure 4.9 shows the corresponding residual maps for all 6 galaxies.

The residual maps broadly show that the simple model of a compact bulge, plus $n = 1$ thick disk, plus NFW halo model does a fairly good job in accounting for the data. With two or three exceptions discussed below, most of the residual maps do not show large scale features or strong deviations that are comparable to the amplitudes in the original maps. Average values in the twelve residual maps range between -10 and +10 km s^{-1}, a few percent of the maximum data range. The median dispersions of the residuals range from 8-18 km s^{-1}, comparable to the measurement errors in most individual pixels, with two exceptions.

Kinematic anomalies: D3a 15504 One outlier is the galaxy D3a 15504 (top left in Figure 4.9). As already discussed in the first paper discussing this galaxy (Genzel et al., 2006), the strong (±65 km s^{-1}), velocity gradient near the nucleus but along the minor axis of the galaxy had been apparent, which the deeper data confirm. Related to this minor axis streaming, plus probably also influenced by a strong, broad nuclear outflow component (Förster Schreiber et al., 2014), is the high value of the nuclear velocity dispersion ($\approx$ 175 km s^{-1}), which cannot be accounted for by the best-fitting disk model and thus shows up as a large outlier in the velocity dispersion residual map. D3a 15504 has a small neighbour about 1.5$''$ NW of the nucleus (PA$= -450$, visible in the stellar density contour map in Figure 4.1), of mass $(2-3) \times 10^9 M_\odot$ – about 3% of the stellar mass of the main galaxy. Hα emission from the satellite is detected in our deep integral-field data at a projected velocity of around +10 km s^{-1} (relative to the systemic velocity of the main galaxy) – about 140 km s^{-1} redshifted relative to the projected rotation velocity of the main galaxy at this radius. The neighbour thus is a satellite. The position-velocity diagram of Hα emission shows that the satellite is connected back to the main galaxy, clearly indicating that the two are interacting. We have removed the well separated Hα emission of the satellite before fitting the rotation curve in Figure 4.1.

Kinematic anomalies: zC 406690 zC 406690, the second galaxy from the top in Figure 4.9, exhibits a significant anomaly in both velocity and velocity dispersion residual map as well, in the outer south-western part of the rotating ring structure, on and near 'clump B' (Genzel et al., 2011; Newman et al., 2012). This anomaly is caused by localized blue-shifted, very broad (up to -1000 km s^{-1}) Hα emission near that clump, and can probably be explained by star formation driven outflows. zC 406690 also has a companion located about 1.6$''$ W of the main ring galaxy, with $6 \times 10^9 M_\odot$ in stellar mass (14% of the main system). There is a marginal detection of Hα from that companion at around +100 km s^{-1} relative to the systemic velocity of the main galaxy, in which case it is an interacting satellite.

Kinematic anomalies: zC 400569 zC 400569, the third galaxy from the top in Figure 4.9, has two neighbours. Both are fairly prominent in Hα, but are not detected in [NII], plausibly because of their low mass and metallicity. The larger one, with a stellar mass of about $7 \times 10^9 M_\odot$ (5% of the mass of the main galaxy, $1.3 \times 10^{11} M_\odot$) is 1$''$ to the south-east of the nucleus of zC 400569, with a projected velocity in Hα of -330 km s^{-1}, appears to be edge on but does not exhibit much of a velocity gradient along its major axis. The second neighbour, 1.5$''$ to the south-east, has a stellar mass of $3 \times 10^9 M_\odot$ (2.3% of the main galaxy) and shows an east-west velocity gradient of ±20 km s^{-1} around the centre, which is blue-shifted by -410 km s^{-1} relative to the main galaxy. It thus appears that zC 400569 is situated in a group of gas rich, satellites galaxies of low mass and metallicity. The effect of the first galaxy on the line profiles is visible in the lower left of the velocity and velocity dispersion residuals in Figure 4.9, but does not very much affects the dynamical analysis in Figure 4.1.

Neighbours and Warps Our analysis of the HST and Hα data of the six galaxies shows that five sample galaxies have neighbours projected within $1''$ and $3.3''$ (8-25 kpc) of the main galaxy, and between 1% (GS4 43501, $4 \times 10^8 M_\odot$) and 20% (COS4 01351, $1.2 \times 10^{10} M_\odot$) of its mass. Of those five the detection of Hα emission from the companion in three (in D3a 15504, zC400690, zC400569) shows that these companions are indeed interacting satellites but probably not in the other two galaxies (COS4 01351, GS4 43501). The Jacobi (or Roche, or Hills) radius in a double galaxy system with mass M_1 and M_2, separated by R_{12}, defines the distance from the lower mass system M_2, within which tidal forces by the smaller system strongly perturb particles in the bigger system. This radius is given by (Binney & Tremaine, 2008, Chapter 8)

$$r_\mathrm{J} = \left(\frac{M_2}{3M_1}\right)^{1/3} R_{12} = 3\ \mathrm{kpc} \left(\frac{M_2/M_1}{0.05}\right)^{1/3} \frac{R_{12}}{12\ \mathrm{kpc}} \tag{4.2}$$

Here we have already inserted the typical mass ratios and separations for the satellite-main galaxy systems in our sample. This simple analysis shows that tidal perturbations or stripping by the satellite can be somewhat important in the outer parts of the main galaxies, if the satellite is within about $R_{1/2}$ of the main galaxy, as seems to be the case, for instance, for the north-western satellite of D3a 15504.

In addition to interactions, warping can be important in the outer disks and is frequently observed in the outer HI layers of $z \approx 0$ galaxies (including the Milky Way; van der Kruit & Freeman, 2011). Theoretically this type of buckling or firehose instability (with a predominant $m = 2$ mode) can occur in galaxy disks with surface density Σ, with radial wavelengths of $\lambda \leq \lambda_\mathrm{J} = \sigma_x^2/(G\Sigma)$, where σ_x is the in-plane velocity dispersion, (Binney & Tremaine, 2008, Chapter 6.6.1; Toomre, 1964) if the system is sufficiently cold in the vertical direction for the instability to grow, which requires (Toomre, 1964; Merritt & Sellwood, 1994) $h_z < \sigma_z^2/(G\Sigma)$ such that $\sigma_z/\sigma_x < 0.3 - 0.6$, where σ_x is the velocity dispersion in the galaxy plane and H_z is the disk scale-height. The current data for high$-z$ galaxies suggest that the velocity dispersion ellipsoid is isotropic (Genzel et al., 2011; van Dokkum et al., 2015) ($\sigma_x = \sigma_z$), such that warping should be suppressed.

If the warp has a sufficiently high amplitude, it could indeed introduce a radial dependence of the peak rotation velocity along the major axis. If the dominant mode is uneven $m = 1$ (or $m = 3$, as in the Milky Way; Levine, Blitz, & Heiles, 2006), warps would also introduce the same sign of the change in the absolute value of the peak rotation curve on the blue- and the redshifted side of the galaxy, which could mimic a radial decrease (or increase) in the rotation curve, with equal probability. However, no significant increase is seen in any of the galaxies of the SINS/zC-SINF or KMOS^{3D} samples. If the mode is even ($m = 2$), one should observe rotation curves that increase on one side, and decrease on the other. We do not observe this feature in any of the six galaxies presented here. Finally, the phase of the warp does not have to be aligned with the major axis and might change with radius. Such precessions could be observed in the residual maps. The data do not show any evidence for such an effect.

Comments on Overall Strategy This paper puts forward observational evidence for very high baryon fractions (and correspondingly low dark matter fractions) in several high mass disk galaxies at $z \approx 1 - 2$. First hints for this result came from Hα kinematics studies initially in the SINS sample (Förster Schreiber et al., 2009), and more robustly in the KMOS^{3D} sample (Wisnioski et al., 2015; Wuyts et al., 2016b) and, independently by others in compact high$-z$ star-forming galaxies (van Dokkum et al., 2015), as well as in the MOSDEF survey (Price et al., 2016). In these cases one infers the dynamical mass of the inner star-forming disks of $z \approx 1 - 2.5$ star-forming galaxies from the peak Hα rotation velocity (or velocity dispersion), and then compares it with the baryonic mass, that is, the sum of the stellar mass and the cold gas mass. The stellar mass is estimated from population synthesis fitting of the UV/optical SEDs, and the gas mass from CO or dust tracing the molecular hydrogen content (Förster Schreiber et al., 2009; van Dokkum et al., 2015; Genzel et al., 2015; Wuyts et al., 2016b; Price et al., 2016). Unfortunately this ‘inner disk dynamics’ technique, even in the best cases of spatially well resolved kinematics, requires strong assumptions on star formation histories, initial stellar mass functions and CO/dust emission to H$_2$-mass calibrations that are inherently not known better than ±0.2 to ±0.25 dex. Close to 50 years of experience of local Universe studies have taught that robust statements on dark matter content cannot be done solely, and certainly not robustly, from the ‘central disk dynamics’ technique (Courteau et al., 2014).

More robust statements on dark matter fractions are expected to come from rotation curves in the outer disk and inner halo. We detected a few cases of potentially falling Hα rotation curves in the best SINS/zC-SINF data a few years ago but it took several years to collect enough integration time to make a solid case for the six galaxies reported in this paper. However, these cases are biased from the outset as we invested additional integration time only in galaxies for which we already had prior evidence of falling rotation curves. In order to check that these galaxies are not outliers in a population of star-forming galaxies with primarily flat-rotation curves, we needed a statistical statement on the occurrence of falling rotation curves in the high$-z$, massive star-forming population, even if the individual rotation curves in these other galaxies were individually not good enough for study. As the KMOS^{3D} sample grew in size, we thus developed as a third element of our strategy a ‘rotation curve stacking’ technique on the overall sample to test for the hypothesis that the individual cases were (or were not) outliers. The results of this project (Lang et al., 2017) do confirm that falling rotation curves appear to be common at $z \approx 1 - 2.5$; see below for a summary, and Lang et al. (2017) for the exhaustive technical discussion of the methodology required to demonstrate the robustness of the result.

A fourth approach in this overall strategy is the measurement of the baryonic and stellar mass, Tully-Fisher relation, zero point offsets as a function of redshift. This ‘Tully-Fisher zero-point evolution’ approach is related to the ‘inner-disk dynamics’ method above, but uses the redshift dependence of a population-averaged property (the Tully-Fisher zero-point) instead of relying on the accurate determination of baryon fractions in individual galaxies. The results of the Tully-Fisher technique for the KMOS^{3D} sample (Übler et al., 2017) are in agreement with the other three tests.

Stacking Analysis In the following we summarize the stacking analysis of Lang et al. (2017) and refer the reader to that paper for a more detailed description.

Having established the properties of a few high quality outer disk rotation curves in star-forming galaxies with long integrations, the next step is to characterize the average rotation curve of a representative sample of $z \approx 0.6 - 2.6$ massive star-forming disks, as drawn from the seeing-limited KMOS^{3D} and AO-assisted SINS/zC-SINF datasets. For this purpose, Lang et al. (2017) employed a stacking approach to systematically determine the shape of outer rotation curves.

This stacking method is designed to leverage the faint outer ionized gas emission combining the signal of >100 massive star-forming galaxies at $0.6 < z < 2.6$. The methodology of this stacking technique first includes the normalization of each individual rotation curve by its observed maximum velocity $v_{\max}$ and the corresponding turnover-radius $R_{\max}$. Both $v_{\max}$ and $R_{\max}$ are determined by fitting the rotation curve with an exponential disk model convolved with the appropriate instrumental resolution of the data set. Values for $R_{\max}$ are also independently derived for each galaxy by converting intrinsic half-light radii measured on rest-frame optical HST images into observed turnover-radii, also taking into account the effect of beam smearing as well as the shape of the mass distribution (as parametrized by the Sérsic index). These independently derived $R_{\max}$ are in good agreement with the $R_{\max}$ values measured on the actual rotation curves and thus substantiate the validity of our $R_{\max}$ measurements using pure exponential disk models. Based on mock galaxy simulations, Lang et al. (2017) demonstrate that the above technique of normalizing and stacking rotation curves is able to reproduce both outer falling and rising rotation curves, with the latter being expected in case massive star-forming galaxies at high redshift are genuinely more dark-matter dominated.

With $R_{\max}$ and $v_{\max}$ derived for each galaxy, normalized position-velocity diagrams are generated which are then averaged into a stack from which a final combined rotation is curve is constructed. Due to field-of-view limitations for both KMOS and SINFONI AO observations, the number of galaxies available at a given galacto-centric radius drops with distance to the centre, such that the combined stacked rotation curve can be reliably determined out to about 2.4 R_{max}, corresponding to several effective radii. Within this radius, the shape of the resulting stack outlines a fall-off in rotation velocity beyond R_{max}, symmetric on either side from the center, reaching down to about 0.65 v_{max}. We show in the left panel of Figure 4.2 a slightly altered version of the original stack (Lang et al., 2017), where we remove D3a 15504, zC 400569 and GS4 43501, so that the remaining stack and the individual rotation curves are completely independent of each other. Lang et al. (2017) utilize template rotation curves of local spiral galaxies (Catinella, Giovanelli, & Haynes, 2006) and show that the outer fall-off in the stacked rotation curve deviates significantly from the (mildly rising) average rotation curves of local analogues of similar mass at the same galactocentric radii.

In addition, Lang et al. (2017) evaluate the outer drop in their stack by a comparison with models including baryons arranged in exponential disk configuration with added dark-matter NFW halos, taking into account pressure gradients in the outer disk resulting from a significant level of velocity dispersion. This comparison demonstrates that the stacked rotation curves can be explained by high baryonic disk mass fractions ($m_{\mathrm{d}} = M_{\mathrm{baryon}}/M_{\mathrm{DM}} \geq 0.05$), in combination with a significant level of pressure support in the outer disk. The latter is accounted for by considering a value $4.8 < v_{\mathrm{rot}}/\sigma_0 < 6.3$ depending on radius, as found to be the average for the sample of stacked galaxies. Considering galaxies with strong pressure support (represented by a low $v_{\mathrm{rot}}/\sigma_0$) for stacking, the resulting averaged outer rotation curve steepens compared to a stack made with only high $v_{\mathrm{rot}}/\sigma_0$ galaxies, which supports the conclusion that a significant part of the outer fall-off in the stacked rotation curve is driven by the presence of pressure effects in the outer disk.

Lang et al. (2017) furthermore demonstrate that the above results are largely independent of underlying model assumptions such as the presence or absence of a central stellar bulge, the halo concentration parameter c, and the possible adiabatic contraction of the host halo, since those do not appear to alter the shape of the expected rotation curve significantly.

The above results are in good agreement with the conclusion drawn from our six individual rotation curves. Most importantly, Lang et al. (2017) confirm that outer falling rotation curves are a common feature among a larger representative sample of massive star-forming galaxies at high redshift.

Comparison to Simulations In the following, we discuss how our results compared to state-of-the-art cosmological simulations of galaxy formation, and we briefly comment on the 'thick disk' phenomenon in local spiral galaxies.

Any quantitative comparison between observations and simulations is challenged by the fact that fundamental properties of high$-z$ galaxies are still not matched by the large-volume simulations that are needed in order to produce the observed diverse galaxy populations, as well as disk galaxies that are massive already at $z \approx 2$. Also the effective co-moving spatial resolutions in current simulations, such as Illustris and Eagle, are 1-3 kpc, which are not or only barely sufficient to resolve bulges, giant star-forming clumps and other intra-galactic structures, and the observed high star formation rates and gas fractions are under-predicted in these simulations (Genel et al., 2014; Schaye et al., 2015). Having said that, peaked rotation curves are produced in current simulations mostly as a result of weak (or no) feedback (Johansson, Naab, & Ostriker, 2012; Anglés-Alcázar et al., 2014). However, it is consensus now that stronger feedback descriptions (momentum feedback from supernovae, or from active galactic nuclei) are needed in order to match many other observed galaxy properties, like outflows, disk-like morphology, or angular momentum (Governato et al., 2007; Scannapieco et al., 2009, 2012; Agertz, Teyssier, & Moore, 2011; Brook et al., 2012b; Aumer et al., 2013; Hopkins et al., 2014; Marinacci, Pakmor, & Springel, 2014; Übler et al., 2014; Genel et al., 2015).

Given the limitations outlined above, a one-to-one comparison of our results to simulations is not feasible. To nevertheless perform a qualitative comparison to our $z \approx 2$ galaxies, we utilize results from the Illustris cosmological hydro-simulation as follows: we select galaxies at $z = 2$ with stellar masses of $10.9 < \log(M_*/M_\odot) < 11.3$, and SFR $> 55 M_\odot$/yr, a total of 80 galaxies. Their mean properties in terms of stellar size, stellar mass, and SFR are $<R_{1/2,*}> =$ 5.6 kpc, <SFR>=120 $M_\odot$/yr, $<M*> = 1.2 \times 10^{11} M_\odot$. We then inspect their two-dimensional distributions of velocity and velocity dispersion, where a cut of star formation rate surface density, $\Sigma_{\rm SFR} > 0.01 M_\odot$ yr^{-1} kpc^{-2}, has been applied. Galaxies are classified as rotationally supported if they exhibit a continuous velocity gradient along a single axis, and if the velocity dispersion map displays a central peak which coincides with the kinematic center of the galaxy. This if fulfilled for about 50% of the galaxies. Judging from the velocity and velocity dispersion maps, about 25% of the rotationally supported Illustris galaxies exhibit falling rotation curves, i.e. 10-15% of the parent sample of 80 $z = 2$ SFGs.

In other simulations falling rotation curves are seen typically for very compact systems, which do not represent the main population of simulated (or observed) SFGs. Most simulations find larger $v_{\rm rot}/\sigma_0$ than seen in the observed system, perhaps due to their still modest spatial resolutions not capturing all the necessary intra-galactic physics mentioned above. We note that typical intrinsic velocity dispersions of the Illustris sample discussed above are 30-40 km s^{-1}. A recent paper connects peaked rotation curves in zoom simulations at $z = 3$ to higher bulge-to-total fractions (Fiacconi, Feldmann, & Mayer, 2015). A significant fraction of our high$-z$ SFGs have indeed massive bulges. However, Lang et al. (2017)

find that the effect of a bulge on the shape of the outer rotation curve is negligible for our otherwise fairly extended SFGs. Although our observed galaxies are all star-forming and extended, these theoretical results give some support to our interpretation of the evolution of our galaxies with cosmic time: the massive, high$-z$ SFGs are likely soon to be quenched, and will afterwards evolve on the passive sequence into local, massive ETGs (Peng et al., 2010; Carollo et al., 2013).

There is an intriguing similarity between the turbulent high$-z$ disks and the 'thick disk'-phenomenon in local spiral galaxies (Bland-Hawthorn & Gerhard, 2016). The stellar population of the thick disk indicates a formation time of $z > 1 - 2$ while thin disk formation started at $z \approx 1$ and lasts until today. Thus, it is conceivable that our high redshift sample of disk galaxies shows the transition period from thick disk to thin disk formation.

Data availability The data discussed here are available on the archive of the European Southern Observatory (`http://archive.eso.org/eso/eso_archive_main.html`).

4.2 Ionized and molecular gas kinematics in a $z = 1.4$ star-forming galaxy

This Section is a reprint of the ApJL publication *Ionized and molecular gas kinematics in a $z = 1.4$ star-forming galaxy* by Übler et al. (2018); DOI:10.3847/2041-8213/aaacfa; ©AAS. Reproduced with permission.

This work is based on observations carried out with the IRAM Interferometer NOEMA. IRAM is supported by INSU/ CNRS (France), MPG (Germany) and IGN (Spain). Based on observations carried out with the LBT. The LBT is an international collaboration among institutions in the United States, Italy and Germany. LBT Corporation partners are: LBT Beteiligungsgesellschaft, Germany, representing the Max-Planck Society, The Leibniz Institute for Astrophysics Potsdam, and Heidelberg University; The University of Arizona on behalf of the Arizona Board of Regents; Istituto Nazionale di Astrofisica, Italy; The Ohio State University, and The Research Corporation, on behalf of The University of Notre Dame, University of Minnesota and University of Virginia.

Abstract – We present deep observations of a $z = 1.4$ massive, star-forming galaxy in molecular and ionized gas at comparable spatial resolution (CO 3-2, NOEMA; Hα, LBT). The kinematic tracers agree well, indicating that both gas phases are subject to the same gravitational potential and physical processes affecting the gas dynamics. We combine the one-dimensional velocity and velocity dispersion profiles in CO and Hα to forward-model the galaxy in a Bayesian framework, combining a thick exponential disk, a bulge, and a dark matter halo. We determine the dynamical support due to baryons and dark matter, and find a dark matter fraction within one effective radius of $f_{\rm DM}(\leq R_e) = 0.18^{+0.06}_{-0.04}$. Our result strengthens the evidence for strong baryon-dominance on galactic scales of massive $z \sim 1 - 3$ star-forming galaxies recently found based on ionized gas kinematics alone.

4.2.1 Introduction

Our knowledge of the kinematics of star-forming galaxies (SFGs) at $z = 1 - 3$ is dominated by large surveys targeting ionized gas emission (e.g. Förster Schreiber et al., 2009; Kriek et al., 2015; Wisnioski et al., 2015; Stott et al., 2016; Turner et al., 2017). There is strong evidence that the ionized gas kinematics of massive, high-redshift SFGs are dominated by ordered disk rotation, but a key question

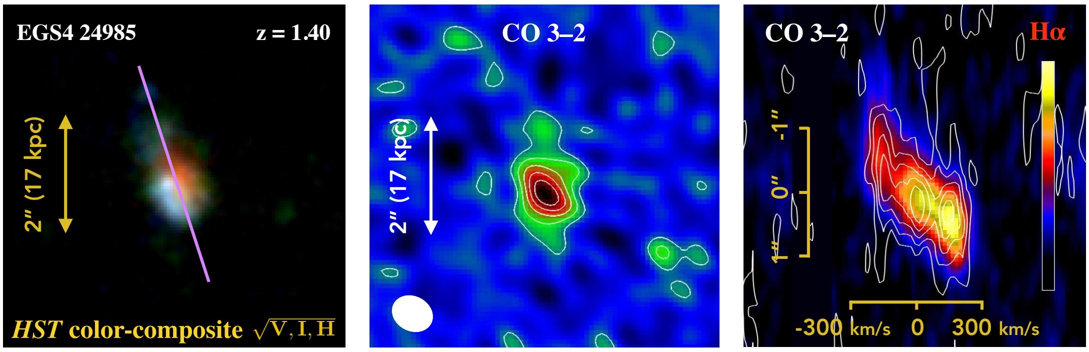

Figure 4.10: Left: *HST color-composite image of EGS4-24985. The magenta line shows the morphological position angle.* **Middle:** *Uniformly weighted CO(3-2) image. The white ellipse shows the clean beam.* **Right:** *Hα (intensity color scale) and CO (white intensity contours) PV diagram.*

remains: how do the ionized gas kinematics, particularly the rotation curve and intrinsic velocity dispersion, compare to that of neutral or molecular gas, which dominate the gas mass budget?

Multi-phase, spatially-resolved data exist only for a handful of high-redshift SFGs, where the kinematics of the different gas phases are found to agree (e.g. Chen et al., 2017), or not (e.g. Swinbank et al., 2011 *vs.* Olivares et al., 2016). Yet, deeper data are generally needed for at least one of the gas phases in these studies to compare the kinematics in detail, and to disentangle the contributions from baryons and dark matter. Genzel et al. (2013) showed through deep integrations of a $z = 1.5$ galaxy that its kinematics in Hα and CO(3-2) agree. However, this galaxy is undergoing a minor merger and is therefore not optimally suited to kinematically analyze the galaxy's baryon *vs.* dark matter content.

In this Letter, we analyze the Hα and CO(3-2) kinematics of a massive SFG at $z = 1.4$, EGS4-24985. We have obtained deep data, 21 and 45hrs on source, with the Large Binocular Telescope (LBT) and the NOrthern Extended Millimeter Array (NOEMA), making this an unprecedented data set of two important tracers of the gas kinematics in an SFG. We model the galaxy by combining a thick exponential disk, a bulge, and an NFW (Navarro, Frenk, & White, 1996) halo, using Markov chain Monte Carlo (MCMC) sampling. We discuss correlations among the model parameters and constrain the galaxy's dark matter fraction within one effective radius (R_e). Throughout, we adopt a Chabrier (2003) initial mass function and a flat ΛCDM cosmology with $H_0 = 70 \mathrm{kms}^{-1}\mathrm{Mpc}^{-1}$, $\Omega_\Lambda = 0.7$, and $\Omega_m = 0.3$.

4.2.2 Data

4.2.2.1 Physical Properties of EGS4-24985

EGS4-24985 (R.A. 14h19m26.66s, Dec. $+52°51'17.0''$) is a $z = 1.4$ galaxy with a stellar mass of $M_\star = 7.4 \times 10^{10} M_\odot$ and a star formation rate of SFR=$98.8 M_\odot \mathrm{yr}^{-1}$ (both derived following the techniques outlined by Wuyts et al., 2011b), placing it in the upper half of the main sequence at this redshift (Whitaker et al., 2014). The $V-, I-, H-$band ACS and WFC3 images reveal strong spatial color variations, indicative of a mixture of stellar populations, or varying dust obscuration that potentially hides a central mass concentration (Figure 4.10, left).

The morphological position angle $\mathrm{PA}_H = 18°$, minor-to-major axis ratio $q_H = 0.60$, $R_{e,H} = 0''52 = 4.4$kpc, and Sérsic index $n_{S,H} = 0.74$ are constrained from GALFIT (Peng et al., 2010) Sérsic models based on the 3D-HST team (Skelton et al., 2014) version of CANDELS H-band (F160W) imaging (Grogin et al., 2011; Koekemoer et al., 2011), presented by van der Wel et al. (2012). Assuming a ratio of scale height to scale length of $q_0 = 0.2$, typical for SFGs at this redshift (e.g. van der Wel et al., 2014a), the estimated inclination is $i = 55°$. There is a systematic change in q as derived from other filters, $q = 0.54 - 0.66$ from F125W (J-band) to F814W (I-band).

Assuming a bulge-to-disk decomposition with $n_{S,\mathrm{disk}} = 1$, $n_{S,\mathrm{bulge}} = 4$, we infer the bulge-to-total fraction from the stellar mass map to be $B/T = 0.13 \pm 0.15$ (Lang et al., 2014).

4.2.2.2 CO observations with NOEMA

To explore the kinematics of the cold gas, we observed the CO(3-2) line with the IRAM interferometer NOEMA. At the redshift of the source, the CO(3-2) line (rest frequency 345.796GHz) is shifted into the 2mm band. We observed EGS4-24985 in the D (compact) and A (extended) configurations with 7 or 8 antennas between November 2016 and April 2017. The total equivalent 8-antenna on-source integration time was 45hrs in the D+A configuration, with a resolution of $0''6 - 1''0$. Weather conditions during the observing periods were excellent, with typical system temperatures of ∼150K. The WiDEX spectral correlator provided 4GHz of bandwidth per polarization with a fixed channel spacing of 2MHz. For phase and amplitude calibration, every 20 minutes we alternated source observations with observations of a bright quasar within 15° of the source. The absolute flux calibration was done through bootstrapping from observations of LkHA-101 and MWC-349 (0.36Jy and 1.45Jy at 144GHz), resulting in a continuum flux of 70μJy.

The data were calibrated using the CLIC package of the IRAM GILDAS[2]

---

[2] `http://www.iram.fr/IRAMFR/GILDAS`

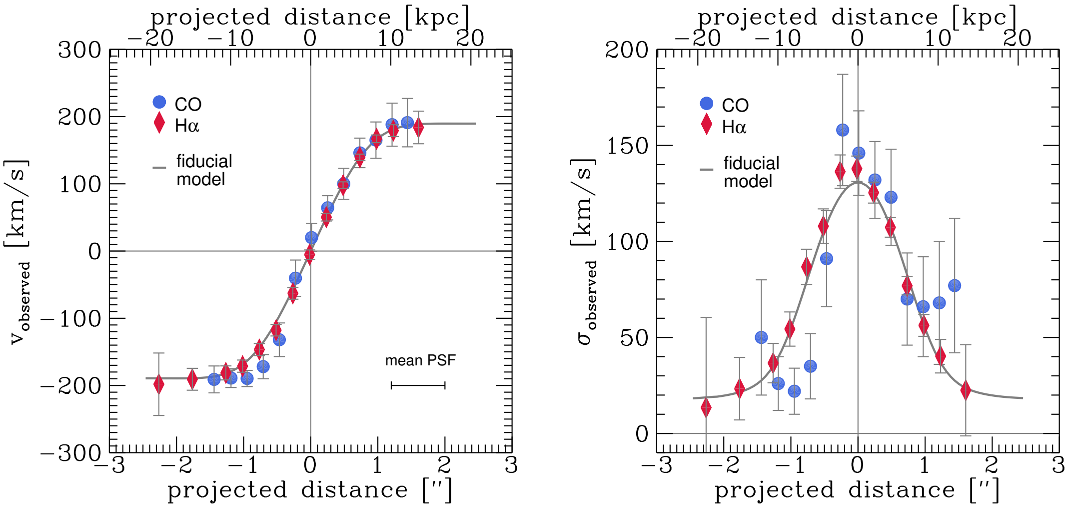

Figure 4.11: *One-dimensional velocity (left) and velocity dispersion (right) profiles along the kinematic major axis in CO(3-2) (blue circles) and Hα (red diamonds). Due to the spatial resolution of the observations, neighboring data points are not independent. The projected distance increases from NE to SW of the kinematic center of the galaxy. The extractions from the two tracers agree. In grey we show our fiducial model (see Section 4.2.4.1).*

software environment, and imaged and analyzed with the MAPPING routines in GILDAS. We applied a uniform weighting scheme to create the data cube, and then subtracted the 2mm continuum emission using channels free of line emission. The final cube was CLEANED with the CLARK version of CLEAN implemented in GILDAS, and reconstructed with a $0''67 \times 0''55$ (PA=62°) clean beam (Figure 4.10, middle), to a spectral resolution of 19kms^{-1} with an rms noise of 0.2mJy channel^{-1}synthesized beam^{-1}.

The molecular gas mass as measured from the CO(3-2) flux and using the α(CO) conversion function by Genzel et al. (2015) is $M_{\mathrm{mol}} = 6.9 \times 10^{10} M_{\odot}$. With a gas-to-baryonic mass fraction of $M_{\mathrm{mol}}/M_{\mathrm{bar}} = 0.48$, the galaxy is typical when compared to larger samples at the same redshift (Tacconi et al., 2018). The CO distribution has an approximate extent of $R_{e,\mathrm{CO}} \approx 0''26$ (measured from an exponential disk fit in the UV plane). The CO position-velocity (PV) diagram is shown in Figure 4.10 (right, white contours).

4.2.2.3 Hα observations with LUCI at LBT

We obtained seeing-limited near-infrared spectroscopy of EGS4-24985 using the LUCI1 and LUCI2 spectrographs in binocular mode (Buschkamp et al., 2012), mounted at the Bent Gregorian focus of the two 8.4m mirrors of the LBT (Hill, Green, & Slagle, 2006). The observations were carried out over five nights in

March 2017, in clear weather or thin clouds, with seeing $0.''6 - 1.''0$. We used a pixel scale of $0''25$, the 210 grating in $H-$band and a slit width of $1''0$, yielding a spectral resolution of $R \sim 3000$. We adopted a two-point dithering pattern and an exposure time of 5min per frame, for a total on-source time of 21hrs (summed from both spectrographs). To facilitate acquisition, we used a multi-object mask and chose PA= 20° to align the slit to the major axis of the galaxy (Section 4.2.2.1). The data were reduced using the `flame` pipeline (Belli, Contursi, & Davies, 2018), which outputs a rectified, sky-subtracted, wavelength-calibrated two-dimensional (2D) spectrum. The corresponding Hα PV diagram is shown in Figure 4.10 (right, color scale).

4.2.2.4 One-dimensional kinematic profiles

To create the one-dimensional (1D) velocity and dispersion profiles in CO, we proceed as described by Genzel et al. (2017): we first fit a Gaussian profile to the CO line emission in each spaxel of the data cube, smoothed over three spaxels to ensure sufficient S/N in the outer parts of the galaxy. Accounting for the galaxy's systemic velocity, this results in the 2D velocity map. From this we determine $\mathrm{PA_{kin}} = 23°$ as the axis with the steepest velocity gradient. It agrees with PA_H, and with the PA of the Hα slit observations (SectionSection 4.2.2.1, 4.2.2.3). The CO 1D velocity and dispersion profiles are then constructed from $0.''75$ diameter apertures (as a compromise between the CO data resolution and the seeing-limited Hα data) with the center spaced by $0.''24$ along $\mathrm{PA_{kin}}$.

To create the 1D profiles in Hα, we extract spectra in overlapping bins of two to four spatial pixels and fit a Gaussian profile to the Hα line emission. The choice of the number of spatial pixels used for the extraction of individual data points does not substantially affect the extracted values, but allows for increased S/N in the outer disk regions.

We trace Hα out to 19kpc (NE, $\sim 4.4R_{e,H}$) and 13kpc (SW, $\sim 3.1R_{e,H}$), and CO out to 12kpc ($\sim 2.8R_{e,H}$). These physical radii at $z \sim 1.4$ are equivalent to probing the rotation curve out to 23-35kpc for a galaxy of this stellar mass at $z \sim 0$ (van der Wel et al., 2014a). Figure 4.11 shows the 1D velocity and dispersion profiles in CO and Hα along $\mathrm{PA_{kin}}$ in observed space. The uncertainties are derived from the Gaussian fits described above where noise has been taken into account. The two tracers agree, indicating that they trace the same mass distribution, most reliably in the outer disk where beam-smearing effects become less important.

The galaxy's intrinsic velocity dispersion, ~15-30 km s^{-1}, is at the lower end of typical values of SFGs at this redshift (~45 km s^{-1}; Wisnioski et al., 2015; see also Di Teodoro, Fraternali, & Miller, 2016). This is evident from the outer regions of the 1D profile, where, under the assumption of constant intrinsic velocity dispersion, the effect of beam-smearing on the measured dispersion is low. Therefore, in the case of EGS4-24985, the correction for pressure support from the turbulent gas motions to the circular velocity is small (∼8 km s^{-1} at $2''3$), and thus does not lead to a significant drop in the observed outer rotation curve. Considering the limitations of the instrumental spectral resolution, the recovered dispersion values represent upper limits.

4.2.3 Modelling

Since the 1D kinematic profiles of ionized and molecular gas agree within their uncertainties, it is justified to combine them to improve constraints on our model parameters. We have also separately analyzed the Hα and CO data and found agreement of the results within the uncertainties (Table 4.2).

The kinematic modelling of our galaxy follows the methodology described by Wuyts et al. (2016b) and Genzel et al. (2017). We build a mass model consisting of a thick exponential disk ($n_S = 1$, $q_0 = 0.2$) a bulge ($n_S = 4$, $q_0 = 1$, $R_e = 1$kpc), and an NFW halo. We fit the mass model simultaneously to the 1D velocity and dispersion profiles of Hα+CO along $\mathrm{PA}_{\mathrm{kin}}$. For the baryonic mass distribution, we account for a finite flattening following Noordermeer (2008). Our choice of an $n_S = 1$ disk plus bulge is motivated by the bulge-to-disk decomposition and the likely high dust obscuration in the center of the galaxy.

The modelling uses an updated version of DYSMAL (Cresci et al., 2009; Davies et al., 2011; Wuyts et al., 2016b). This code accounts for spectral and spatial beam-smearing, and incorporates the effects of pressure support on the circular velocity from the turbulent gas motions of the kinematic tracer, as described by Burkert et al. (2010) and Wuyts et al. (2016b) (see also Dalcanton & Stilp, 2010, for a detailed discussion). The most important update to DYSMAL consists of the implementation of an MCMC sampling procedure using the EMCEE package (Foreman-Mackey et al., 2013).

Free parameters in our modelling are M_{bar}, R_e, B/T, i, σ_0, and the NFW halo mass M_{halo}. We choose the prior halo mass to be typical for the redshift and stellar mass of our galaxy (Moster, Naab, & White, 2013). The concentration parameter is fixed to a value typical for this halo mass and redshift, $c = 4.4$ (Dutton & Macciò, 2014). We verify that the typical concentration parameters for the range of halo masses derived from the MCMC sampling are broadly consistent with this value ($\Delta c \sim 0.2$ for the 1σ distribution of sampled halo masses). We explore setups with lower/higher concentrations ($c = 2; 8$), and consequently find lower/higher $f_{\mathrm{DM}}(\leq R_e)$ and higher/lower M_{halo}, consistent with our main results (Table 4.2). We do not consider adiabatic contraction since its net effect at high redshifts is not well constrained (e.g. Duffy et al., 2010).

Table 4.2: *Results from our fiducial model and additional setups. We first list the model priors ('G(x, y)': Gaussian(center x, width y); 'F[x; y]': flat prior in range [x; y]; 'f: x': fixed to x) and then the medians with 1σ confidence ranges of the marginalized probability distributions from the MCMC sampling.*

model	**fiducial Hα+CO**	only Hα	only CO	low c Hα+CO	high c Hα+CO	free halo, B/T Hα+CO	2 fixed disks Hα+CO
$M_{\rm bar}$	G(1.4; 0.7)	G(1.4; 0.7)	G(1.4; 0.7)	G(1.4; 0.7)	G(1.4; 0.7)	G(1.4; 0.7)	f: 0.74 + 0.69
$[10^{11} M_\odot]$	$1.1^{+0.5}_{-0.4}$	$1.1^{+0.5}_{-0.3}$	$1.2^{+0.5}_{-0.4}$	$1.2^{+0.4}_{-0.3}$	$1.2^{+0.5}_{-0.4}$	$1.0^{+0.5}_{-0.4}$	–
R_e [″]	G(0.52; 0.10)	G(0.52; 0.10)	G(0.52; 0.10)	G(0.52; 0.10)	G(0.52; 0.10)	G(0.52; 0.10)	f: 0.52; 0.26
	$0.49^{+0.10}_{-0.09}$	$0.51^{+0.10}_{-0.10}$	$0.50^{+0.10}_{-0.09}$	$0.53^{+0.09}_{-0.08}$	$0.48^{+0.11}_{-0.10}$	$0.50^{+0.10}_{-0.10}$	–
B/T	G(0.20; 0.15)	G(0.20; 0.15)	G(0.20; 0.15)	G(0.20; 0.15)	G(0.20; 0.15)	F[0;1]	–
	$0.27^{+0.10}_{-0.09}$	$0.28^{+0.10}_{-0.09}$	$0.22^{+0.12}_{-0.11}$	$0.23^{+0.08}_{-0.07}$	$0.29^{+0.11}_{-0.10}$	$0.43^{+0.28}_{-0.18}$	–
i [°]	G(55; 10)	G(55; 10)	G(55; 10)	G(55; 10)	G(55; 10)	G(55; 10)	f: 55
	44^{+8}_{-6}	44^{+9}_{-7}	47^{+9}_{-7}	50^{+8}_{-7}	39^{+9}_{-6}	40^{+11}_{-9}	–
σ_0 [kms^{-1}]	G(30; 10)	G(30; 10)	G(30; 10)	G(30; 10)	G(30; 10)	G(30; 10)	F[5;100]
	17^{+5}_{-6}	21^{+5}_{-6}	19^{+7}_{-7}	16^{+5}_{-6}	18^{+5}_{-6}	17^{+5}_{-6}	11^{+7}_{-4}
$M_{\rm halo}$	G(4.2; 2.0)	G(4.2; 2.0)	G(4.2; 2.0)	G(4.2; 2.0)	G(4.2; 2.0)	F[0.001;100]	F[0.01;100]
$[10^{12} M_\odot]$	$3.5^{+1.9}_{-1.7}$	$3.5^{+1.9}_{-1.7}$	$3.9^{+1.9}_{-1.8}$	$4.4^{+1.9}_{-1.9}$	$2.2^{+1.9}_{-1.3}$	$7.2^{+21}_{-5.1}$	$0.015^{+0.011}_{-0.004}$
c	f: 4.4	f: 4.4	f: 4.4	f: 2	f: 8	f: 4.4	F[1;10]
	–	–	–	–	–	–	$1.3^{+0.5}_{-0.2}$
inferred $f_{\rm DM}(\leq R_e)$	$0.18^{+0.06}_{-0.04}$	$0.19^{+0.06}_{-0.05}$	$0.20^{+0.08}_{-0.06}$	$0.11^{+0.04}_{-0.03}$	$0.25^{+0.07}_{-0.06}$	$0.22^{+0.08}_{-0.06}$	$0.008^{+0.002}_{-0.002}$

In calculating the model likelihood, we assume Gaussian measurement noise. For the purpose of parameter inference, we choose Gaussian priors for all model parameters that reflect our prior state of knowledge about their values and uncertainties (Table 4.2). As discussed in Section 4.2.2.1, q and R_e are independently constrained through GALFIT models. The adopted uncertainties of $\sigma_i = 10°$ and $\sigma_{R_e} = 0''10$ are conservative estimates (see van der Wel et al., 2012). Through our choice of narrow Gaussian priors for these parameters, we translate their uncertainties directly into the modelling. We choose $B/T = 0.2$ with $\sigma_{B/T} = 0.15$ to account for a possible bulge hidden by dust extinction. For $M_{\rm bar}$ and $M_{\rm halo}$, we adopt uncertainties of $\sim 50\%$. For σ_0, our estimate is roughly based on the outer values of the dispersion profile. If we adopt flat priors for $M_{\rm halo}$ and B/T, we find consistent results. We also explored a model with fixed stellar and gaseous exponential disks, no bulge, free σ_0, $M_{\rm halo}$, and c, leading to a central dark matter fraction of $< 1\%$ (Table 4.2).

For our fiducial model, we set up the MCMC sampling of the posterior probability function of the parameters with 180 walkers, a burn-in phase of 500 steps, and a running phase of 2000 steps. The length of the burn-in was designed to ensure convergence of the chains, while the length of the final run was designed to be >10 times the maximum autocorrelation time of the individual parameters. The acceptance fraction of the final run was 0.35.

4.2.4 Results

4.2.4.1 Parameter correlations and fiducial model

The MCMC sampling of the joint posterior probability distributions of the model parameters is visualized in the top rows of Figure 4.12. The median values and 1σ confidence ranges of the marginalized distributions are indicated by the dashed vertical lines in the 1D histograms (see also second column in Table 4.2).

For the 2D marginalized distributions, contours show the 1σ, 2σ, and 3σ confidence levels. The strongest correlation is between inclination and $M_{\rm bar}$. This is expected, since any inclination correction to the observed rotation velocity directly affects the inferred dynamical mass. This is also reflected to a smaller extent in the correlation between inclination and $M_{\rm halo}$.

Since the posterior distribution is well behaved, we choose our fiducial model to be represented by the median values of the individual marginalized distributions, with uncertainties represented by the 1σ confidence ranges. The median values are also shown as blue squares in the 2D histograms in Figure 4.12. Every median lies close to the mode of the posterior distribution in projection, indicating that they lie in the most likely parameter space.

The 1D profiles of velocity and dispersion corresponding to the fiducial model in observed space are shown as grey lines in Figure 4.11.

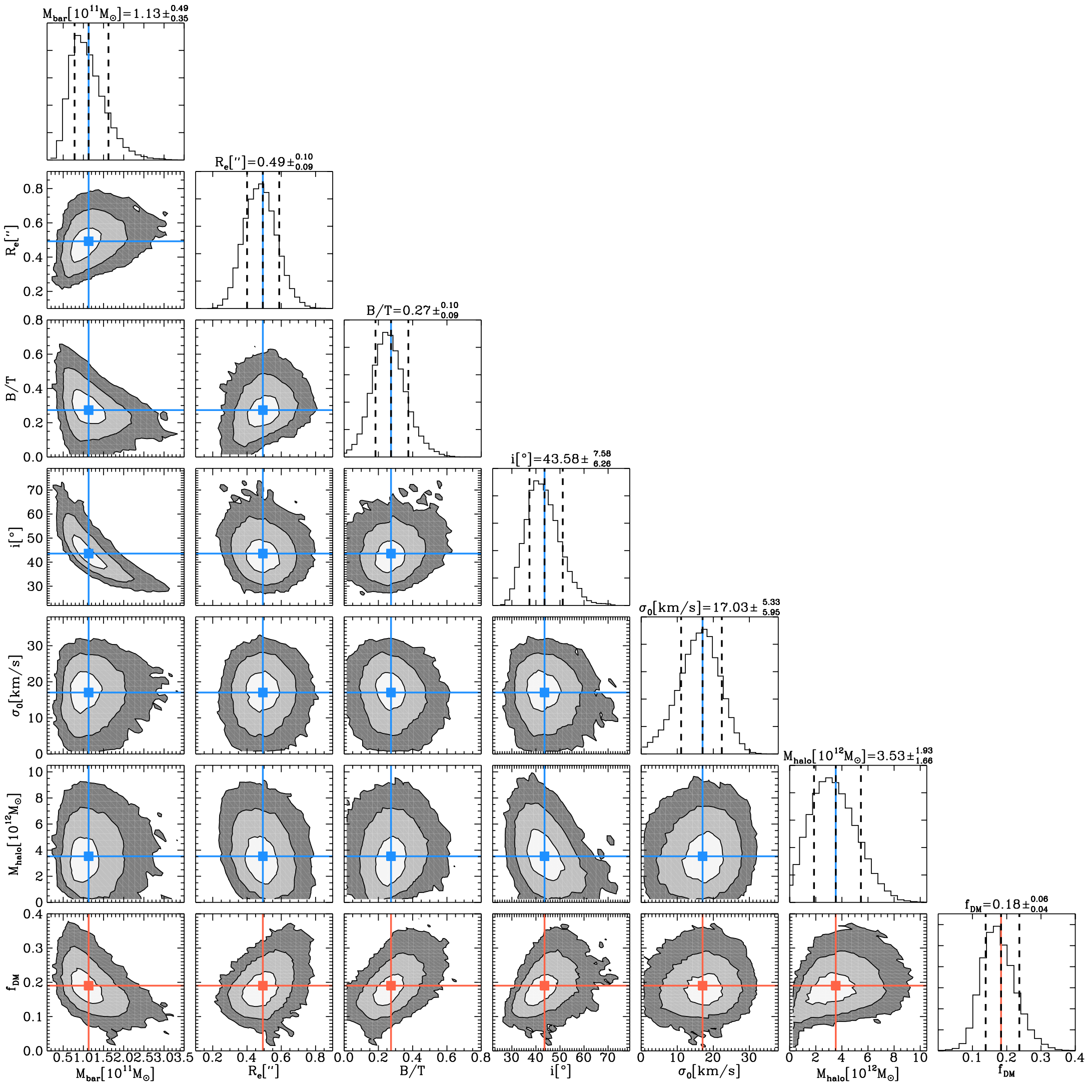

Figure 4.12: *MCMC sampling of the joint posterior probability distribution of the model parameters,* $M_{\rm bar}$, R_e, B/T, i, σ_0, *and* $M_{\rm halo}$ *(top rows) from a combined fitting to the Hα+CO data. The median values and 1σ confidence ranges of the marginalized distributions are indicated by the dashed vertical lines in the 1D histograms, and given on top of each histogram. The median values are also shown as blue squares on top of the 2D histograms. All of the median values lie close to the modes of the 2D histograms. The contours show the 1σ, 2σ, 3σ confidence levels of the 2D distributions. The bottom row histograms show* $f_{\rm DM}(\leq R_e)$, *calculated from the intrinsic models. Median values are indicated in red. For the sampled parameter space, dark matter is sub-dominant within* R_e.

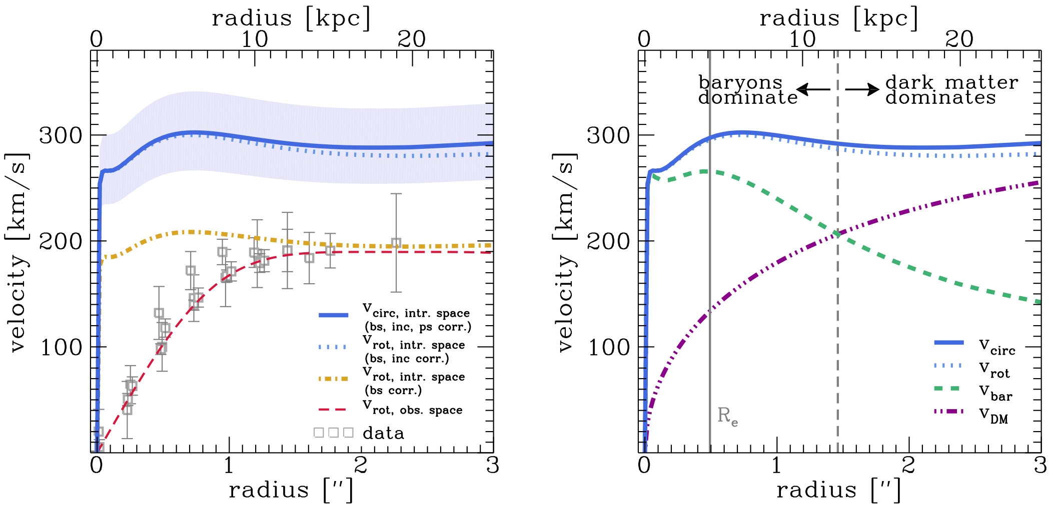

Figure 4.13: Left: *Rotation curve in observed vs. intrinsic space. The grey squares show the folded, observed velocity (Hα+CO) as a function of projected distance from the center. The red dashed line is our fiducial model in observed space. The dash-dotted yellow line shows the model rotation velocity in observed space, corrected for beam-smearing ('bs'). The dotted blue line shows the intrinsic model rotation velocity, further corrected for inclination ('inc'). The solid blue line shows the intrinsic model circular velocity, further corrected for pressure support ('ps'), and the shaded area shows the 1σ uncertainties of the inclination correction.* **Right:** *Intrinsic rotation curve of the fiducial model. The solid and dotted blue lines are as in the left panel. The baryonic contribution by the bulge and disk is shown as a dashed green line, and the dark matter contribution as a dash-dotted purple line. The inner solid and the outer dashed vertical grey lines respectively show R_e, and the radius where baryons and dark matter contribute equally to the potential.*

4.2.4.2 Central dark matter fraction

We measure the enclosed dark matter fraction at R_e from the intrinsic properties of the DYSMAL model defined by the median sampling results, and find $f_{\rm DM}(\leq R_e{=}0.''49) = v^2_{\rm DM}(R_e)/v^2_{\rm circ}(R_e) = 0.20$. $v_{\rm DM}$ is the contribution to the circular velocity of the dark matter halo, and $v_{\rm circ}$ is the total circular velocity. The galaxy is strongly baryon-dominated within R_e. This baryon-dominance prevails out to $r = 1.''46$ ($3R_e$). Our model agrees with the baryonic disk being 'maximal', $v_{\rm disk}(R_{\rm max})/v_{\rm circ}(R_{\rm max}) = 0.90$, where $R_{\rm max} = 0.''44$ is the radius where the disk velocity reaches its peak value (e.g. van Albada et al., 1985). The intrinsic model rotation curve and mass component curves are shown in Figure 4.13. The inferred baryon-to-total mass fraction $m_d = 0.03$ is compatible with predictions from abundance matching estimates that account for gas mass (Burkert et al., 2016).

Through the MCMC sampling, we also gather information on the probability distribution of $f_{\rm DM}(\leq R_e)$, which is not itself a model parameter but calculated from the intrinsic models. In Figure 4.12 (bottom row) we show the 1D and 2D histograms of the marginalized posterior distribution of the $f_{\rm DM}(\leq R_e)$ values associated with the sampled parameter space. While correlations with some of the model parameters are evident, particularly with $M_{\rm bar}$ and with the structural parameters R_e and B/T, dark matter is sub-dominant within R_e for the explored parameter space. We use the median and 1σ confidence ranges of the marginalized probability distribution to estimate $f_{\rm DM}(\leq R_e)$ and its uncertainties, and find $f_{\rm DM}(\leq R_e) = 0.18^{+0.06}_{-0.04}$.

4.2.5 Discussion and conclusions

We have presented kinematic data of a $z = 1.4$ SFG based on independent and deep Hα and CO(3-2) observations. We find that the ionized and molecular gas trace the same gravitational potential, as their kinematics agree within the uncertainties. Thus, we combine them to model the galaxy.

We use MCMC sampling to constrain a mass model consisting of a thick exponential disk, a bulge, and an NFW halo. We find that the galaxy's central region is baryon-dominated with a dark matter fraction of $f_{\rm DM}(\leq R_e) = 0.18^{+0.06}_{-0.04}$. This is in agreement with recent findings of low central dark matter fractions in high-redshift SFGs by several groups (Förster Schreiber et al., 2009; van Dokkum et al., 2015; Alcorn et al., 2016; Price et al., 2016; Stott et al., 2016; Wuyts et al., 2016b; Genzel et al., 2017; Lang et al., 2017).

Together with $v_{\rm circ}(R_e) = 296 {\rm kms}^{-1}$, this places EGS4-24985 into the same region of the $v_{\rm circ}$-$f_{\rm DM}$ parameter space as the two $z \sim 1.5 - 1.6$ galaxies observed in Hα by Genzel et al. (2017) – a region also populated by massive local SFGs (e.g. Persic & Salucci, 1988; Begeman, Broeils, & Sanders, 1991; de Blok et al., 2008; Lelli, McGaugh, & Schombert, 2016a) and early-type galaxies (e.g. Cappellari et al., 2013). The latter are the likely descendants of massive SFGs at $z \sim 1 - 3$. Our result supports the interpretation by Genzel et al. (2017) that the low central dark matter fractions observed during the peak epoch of cosmic star formation rate density might be preserved over the rest of cosmic history, as massive SFGs quench and evolve into passive galaxies. Also, this suggests that massive disks are baryon-dominated in their centers at all times.

The low pressure support in our galaxy results in a flat intrinsic rotation curve despite the low $f_{\rm DM}(\leq R_e)$, thus setting it apart from the galaxies presented by Genzel et al. (2017). It also implies that in this case the slope of the rotation curve in the outer disk region is a closer tracer of the relative contributions of baryons and dark matter to the rotational support of the galaxy. The low intrinsic dispersion further suggests that the galaxy is more settled than other galaxies at this redshift with otherwise comparable physical properties (Genzel et al., 2017), indicating that any potential dissipative condensation has happened at earlier times (e.g. Dekel & Burkert, 2014). Still, EGS4-24985 falls on the high-redshift Tully-Fisher relations (Übler et al., 2017).

The agreement of the deep Hα and CO data especially in the outer disk helps to alleviate concerns that ionized gas kinematics at high redshift might be unrepresentative of the galaxy kinematics, and could instead be circum-galactic or in-/outflowing gas in disguise. Future studies with high-quality resolved kinematics traced through multiple gas phases in SFGs at similar redshifts will be important to statistically corroborate our result.

Acknowledgements

We are grateful to the anonymous referee for a constructive report that helped to improve this manuscript. We thank the staff at IRAM and LBT for their helpful support with the NOEMA and LUCI observations for this work.

4.3 Detailed kinematics of IllustrisTNG50 massive, star-forming galaxies at $z \sim 2$ from the observer's perspective

This Section is based on a paper draft comparing in detail the mock-observed kinematics of massive, star-forming galaxies in the state-of-the-art IllustrisTNG50 cosmological simulation to the real galaxies presented in Section 4.1.

Abstract – We study the projected one- and two-dimensional kinematics of $M_* \approx 10^{11} M_\odot$, star-forming galaxies in the IllustrisTNG50 simulation from the observational perspective. Using standard observational techniques, we successfully recover the intrinsic kinematics of the star-forming gas from mock data cubes. We discuss several differences between the observed and simulated galaxies, most importantly: (i) the simulated galaxies have lower gas-to-stellar mass ratios than predicted by scaling relations. (ii) All simulated galaxies show clear signs of disk rotation but they appear more irregular compared to observations. We find large, asymmetric vertical and radial velocity components in all simulated galaxies. As a consequence, along different lines of sight the extracted circular kinematics can vary by up to 100 km s^{-1}. (iii) The rotation velocities of the simulated galaxies are higher than those of observed galaxies with comparable baryonic masses due to substantial amounts of dark matter in the central regions. For galaxies with sufficiently regular kinematics, we successfully recover the central dark matter fraction using standard dynamical modelling tools.

4.3.1 Introduction

Recent studies of massive ($M_* \approx 10^{11} M_\odot$) star-forming galaxies (SFGs) at redshift $z \sim 2$, near the peak of cosmic star-formation rate density, have demonstrated that these rapidly evolving galaxies differ from present-day systems in several fundamental ways. The $z \sim 2$ galaxies have higher gas-to-stellar mass ratios ($M_{\mathrm{gas}}/M_* \sim 1$; e.g. Genzel et al., 2015; Scoville et al., 2017; Tacconi et al., 2018), are forming stars more rapidly (with star-formation rates SFR$\gtrsim 100 M_\odot$ yr^{-1}; e.g. Whitaker et al., 2014; Speagle et al., 2014), and have higher intrinsic velocity dispersions relative to ordered rotational speeds ($\sigma_0/v_{\mathrm{rot}} \sim 0.2$; e.g. Förster Schreiber et al., 2006; Genzel et al., 2008, 2011; Wisnioski et al., 2015; Simons et al., 2017; Übler et al., 2019). Spatially resolved kinematic studies have revealed that the central regions of massive $z = 2$ SFGs are strongly baryon-dominated, with dark matter fractions much lower than typical SFGs at the current epoch (e.g. Martinsson et al., 2013a,b; Alcorn et al., 2016; Price et al., 2016; Wuyts et al., 2016b). Furthermore, the typical rotation curves of massive, high$-z$ SFGs drop beyond 1.3-1.5 effective radii, indicating the significant role of pressure gradients in partially supporting the disk structures due to high velocity dispersions (Lang et al., 2017; Genzel et al., 2017).

The IllustrisTNG simulations (e.g. Springel et al., 2018) have provided a high resolution computation of cosmologically evolving galaxy structures with sufficient detail that direct comparisons to the observed SFGs are now possible, particularly for the highest-resolution run TNG50 (Nelson et al., 2019; Pillepich et al., 2019).

The goal of this paper is to directly compare massive TNG50 SFGs at $z = 2$ to observed galaxies. Our main focus is on the rotational kinematics, the associated dark-matter distributions, and the properties and roles of non-ordered motions. For this purpose we apply the same data extraction pipeline and modelling tools to the TNG50 galaxies that were applied to the real galaxies in the observational study by Genzel et al. (2017). This approach enables several types of comparisons. First, since the internal structures of the simulated galaxies can be inspected directly, we can assess how accurately the observational pipelines recover these intrinsic structures. Second, given the observational results, e.g. the apparent role of pressure support as indicated by the declining rotation curves, we can ask whether the TNG50 galaxies successfully reproduce the observed properties, or not. The direct comparisons that we present in this paper will serve to inform both observers and simulators of possible caveats in the interpretation of real data and the reliability of the simulated galaxies.

4.3.2 The observational picture

Recent observational work revealed dropping rotation curves for a sample of six massive SFGs at $0.9 < z < 2.4$ (Genzel et al., 2017; Section 4.1). Through dynamical modelling of these deep and high-quality data, it was possible to infer the central dark matter fractions for these galaxies using a standard NFW halo (Navarro, Frenk, & White, 1996). This analysis showed that particularly the $z \gtrsim 2$ targets had very low to negligible central dark matter fractions of $f_{\rm DM}(R_e) = v^2_{\rm DM}(R_e)/v^2_{\rm circ}(R_e) \leq 0.15$. The results based on these individual targets were confirmed by Lang et al. (2017) for a representative sample of 101 SFGs through stacking, demonstrating that falling rotation curves are indeed common among the more massive $0.6 < z < 2.6$ SFG population, and in particular for systems with lower $v_{\rm rot}/\sigma_0$ which are more common at higher redshift.[3]

---

[3] We note that for SFGs with different physical properties, for instance lower baryonic masses and surface densities, smaller bulges, and lower$-z$ systems there exists a variety of outer rotation curve shapes.

4.3.2.1 Physical properties

The SFGs presented by Genzel et al. (2017) had been selected for follow-up observations based on previously available data from the SINS/zC-SINF and KMOS^{3D} integral-field spectroscopicsurveys (Förster Schreiber et al., 2009, 2018; Wisnioski et al., 2015, 2019). This selection was based on the quality of the available data, the kinematic properties of the galaxies ($v_{\rm rot}/\sigma_0 > 3$), and the extended galaxy sizes and high surface brightnesses (see Section 4.1.1 for more details).

All galaxies in the sample by Genzel et al. (2017) lie along or somewhat above the main sequence of SFGs at their respective redshifts, but their effective radii are slightly larger with respect to the main population due to the selection criteria. Their stellar masses are in the range $4 \times 10^{10} < M_*/M_\odot < 1.2 \times 10^{11}$. All galaxies have rotation velocities $v_{\rm rot} > 250$ km s^{-1} and high intrinsic velocity dispersions 34 km s$^{-1} < \sigma_0 < 76$ km s^{-1}.

4.3.2.2 Observational interpretation

The steep drop in the observed rotation curves can be explained by a combination of two effects: (i) the very low $f_{\rm DM}(R_e)$, and (ii) the high turbulent motions which counter-act part of the gravitational potential, thus leading to a reduction of the rotational speed as a function of radius. An important insight from this study was that the inferred central dark matter fractions are much lower than what would have been predicted from abundance matching techniques (Moster, Naab, & White, 2013, 2018).

Proposed reasons for this are connected to small-scale physical processes which might not be adequately capture in large-scale simulations: (i) high$-z$ SFGs are more gas-rich smaller than their equal-mass $z = 0$ counterparts, with dissipation processes efficiently channeling baryonic material to the central regions. (ii) Dark matter could be removed from the central galactic regions due to strong feedback (for which there is growing evidence from observations of gas outflows at high redshift, e.g. Förster Schreiber et al., 2018), or heating of the halo via dynamical friction caused by in-spiraling baryonic material. A consequence of this would be a change in the dark matter density profile with a less dense core, such as a Burkert (1995) or Einasto (1965) profile.

Based on comparison to the mass budget in local galaxies, and on the high baryonic masses already assembled in the high$-z$ galaxies, Genzel et al. (2017) concluded that the results are consistent with high$-z$ SFGs likely evolving into early-type systems by the present day, after further consumption and/or ejection of their available cold gas. This picture is supported by other lines of evidence, including clustering properties and abundance matching (e.g. Adelberger et al., 2005; Behroozi et al., 2013; Moster, Naab, & White, 2013, 2018; Papovich et al., 2015). Since present-day early-type galaxies have similarly low central dark matter fractions as the objects studied by Genzel et al. (2017), this suggests that the central mass budget is set early on in the evolution of the most massive galaxies.

We would like to emphasize a few more important points from the observational perspective:

(i) Dropping rotation curves require low dark matter fractions, but the reverse is not necessarily true. If the effect of pressure support is small due to low gas velocity dispersion, galaxies can still be baryon-dominated *and* have flat rotation curves (e.g. Übler et al., 2018).

(ii) However, it has been demonstrated through the work by Lang et al. (2017) based on more than 100 high$-z$ SFGs that the *typical* rotation curve of massive SFGs at $z > 1$ drops beyond $\sim 1.3 - 1.5R_e$. This drop is more pronounced for higher$-z$ galaxies due to their typically lower $v_{\rm rot}/\sigma_0$ ratios and therefore the more important role of pressure support.

(iii) Through the collection of additional, deep data sets of galaxies at lower z and with lower baryonic masses, a picture emerges where the central dark matter fraction depends on several physical properties, best captured in the baryonic surface density such that galaxies with higher baryonic surface densities have lower $f_{\rm DM}(R_e)$ (work in preparation). This reflects observations in the local Universe (e.g. Persic & Salucci, 1988; Begeman, Broeils, & Sanders, 1991; de Blok et al., 2008; Lelli, McGaugh, & Schombert, 2016b).

4.3.2.3 Note on modelling assumptions

For the baryonic mass distribution, Genzel et al. (2017) chose a combination of a thick exponential and axisymmetric disk and a compact, central bulge. These choices are well motivated by the typical structural properties of high$-z$ SFGs (Wuyts et al., 2011b; van der Wel et al., 2014b; Lang et al., 2014), and the available ancillary data for the targets (see Genzel et al., 2017, for details).

The dynamical analysis further accounts for the pressure support expected from the high turbulent motions as shown by Burkert et al. (2010, 2016). This is in line with other high$-z$ kinematic studies (e.g. Kassin et al., 2007, 2012; Wuyts et al., 2016b; Simons et al., 2016, 2017; Übler et al., 2017; Price et al., 2019).

For the dynamical modelling, Genzel et al. (2017) chose a standard NFW halo with a concentration parameter c fixed to the typical value predicted on basis of the stellar mass and redshift of the galaxies (based on the work by Moster, Naab, & White, 2013; Dutton & Macciò, 2014).

4.3.3 Simulated galaxies and methodology

4.3.3.1 The TNG50 simulation

The TNG50 simulation (Nelson et al., 2019; Pillepich et al., 2019) is the highest-resolution volume of the IllustrisTNG project, with a uniform periodic-boundary cube of 51.7 co-moving Mpc on a side, and 2×2160^3 total initial resolution elements, half dark-matter particles and half gas cells. The simulations are run with the unstructured moving-mesh code AREPO (Springel, 2010) and incorporate dark matter, gas, stars, black holes, and magnetic fields. The dark matter and baryonic mass resolutions are $4.5 \times 10^5 M_\odot$ and $8.5 \times 10^4 M_\odot$, respectively, and the gravitational softening lengths at $z = 2$ are 575 comoving pc for stars and dark matter, and adaptive for gas with a typical size of 100 pc. The simulations account for star formation, stellar population evolution, chemical enrichment following nine species through supernovae type Ia and II and through AGB stars, gas radiative processes, the formation, coalescence, and growth of supermassive black holes, and feedback from supernovae and black holes. TNG50 adopts a Planck Collaboration et al. (2016) cosmology with $h = 0.6774$, $\Omega_b = 0.0486$, $\Omega_m = 0.3089$, $\Omega_\Lambda = 0.6911$, and $\sigma_8 = 0.8159$.

4.3.3.2 Sample selection

To select simulated galaxies that most closely resemble the available deep observational data, we choose central galaxies in the same stellar mass range as for the observed sample, $4 \times 10^{10} < M_*/M_\odot < 1.2 \times 10^{11}$, and star-formation rates SFR $\gtrsim 50 M_\odot$ yr^{-1}. In total, 12 galaxies in the TNG50 volume meet these criteria at $z = 2$. Of those, we further exclude five galaxies that are either very compact, therefore hampering the extraction of kinematics out to sufficiently large radii, or clearly interacting or disturbed. We show projected maps of those dismissed galaxies in Appendix 4.3.7.

Figure 4.14 compares in terms of stellar mass, SFR, size, and gas-to-stellar-mass ratio our final sample to the observational sample by Genzel et al. (2017), on top of the underlying population of SFGs at $1.5 < z < 2.5$ based on the 3D-HST catalogue (Brammer et al., 2012; Skelton et al., 2014; Momcheva et al., 2016). The simulated galaxies are well matched in size, and have comparable but somewhat lower SFRs. Their gas-to-stellar-mass ratios are systematically lower by $\sim 20-30$ %. In Table 4.3 we list the physical properties of the selected TNG50 galaxies.

Table 4.3: *Physical properties of the selected TNG50 galaxies.*

ID	$M_*/M_\odot$	$M_{\rm gas}/M_\odot$	$R_{e,\rm disk}$/kpc[a]	B/T[a]	SFR/$M_\odot$ yr[b]
#1	1.0×10^{11}	5.5×10^{10}	4.4	0.33	71
#2	1.1×10^{11}	7.5×10^{10}	9.7	0.16	119
#3	1.5×10^{11}	1.0×10^{11}	8.9	0.19	113
#4	4.7×10^{10}	5.4×10^{10}	6.9	0.17	48
#5	1.2×10^{11}	5.5×10^{10}	5.0	0.19	92
#6	5.3×10^{10}	3.1×10^{10}	6.0	0.20	70
#7	6.2×10^{10}	3.7×10^{10}	4.4	0.22	50

[a] Measured from two-component Sérsic fits to the intrinsic, azimuthally averaged baryonic mass distribution.

[b] Instantaneous star-formation rate.

4.3.3.3 Mock Observations

For each selected galaxy we generate mock observations from a number of lines of sight. We first align the coordinate system of the galaxy using its moment of inertia tensor of the star-forming gas, such that the galactic plane approximately coincides with the $x-y-$plane, and the axis of rotation coincides with the shortest axis of the mass distribution. We then define a line of sight by an inclination angle with respect to the $z-$axis and an orientation angle with respect to the $x-$axis.

For each line of sight we then bin the star-forming gas cells into a cube in position-position-velocity space of dimensions 40 kpc × 40 kpc × 1600 km s^{-1}, where the size of each voxel is 0.5 kpc in the spatial directions and 40 km s^{-1} in the velocity direction. The cube is centered spatially on the potential minimum (which is also, in practice, the center of rotation) and along the velocity direction on the center-of-mass velocity of the stellar component of the galaxy (which differs insignificantly from that of the gas). Then it is convolved with a three-dimensional Gaussian with a FWHM of 2 kpc and 80 km s^{-1} in the spatial and velocity directions, respectively, to mimic the effects of the instrument point spread function (PSF) and line spread function (LSF; see Förster Schreiber et al., 2018).

We then convert the instantaneous SFR into Hα luminosity (Kennicutt, Jr., 1998). Note that the simulations do not account for extinction, and we therefore do not perform a dust correction. This should not importantly affect our results since we model the galaxy kinematics. To account for realistic noise properties, including from random and systematic sources, and in particular stemming from the strong and rapidly variable night sky line emission in the near-IR, we embed the mock data cube into a real noise cube from a SINFONI observation at $z \approx 2$. For this, we convert and interpolate the mock data cube to angular size and wavelength, such that our final cube sampling is $0.05'' \times 0.05'' \times 2.45$ Å. At $z = 2$,

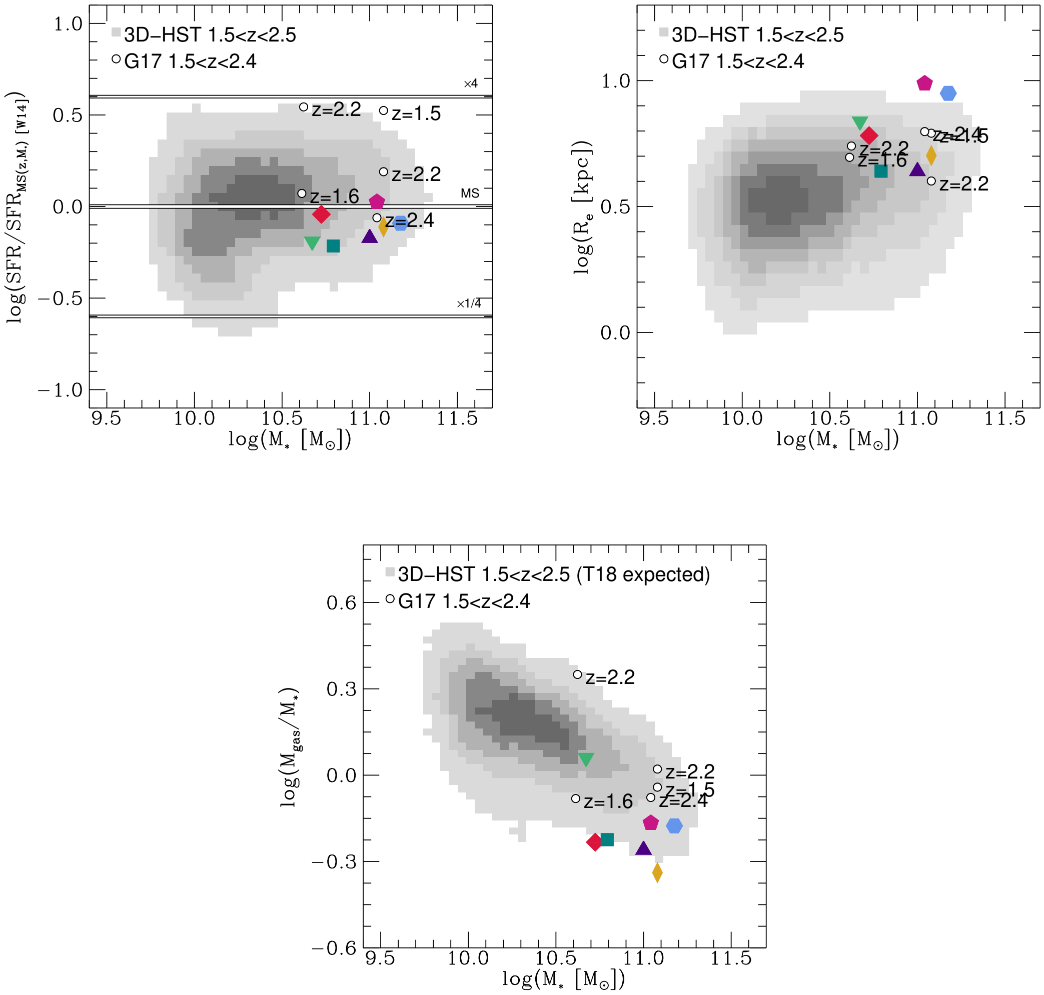

Figure 4.14: *Physical properties of TNG50 galaxies selected for kinematic analysis (colored symbols) in comparison to the observational reference sample by Genzel et al. (2017) (G17, white circles), and to the population of SFGs at* $1.5 < z < 2.5$ *based on the 3D-HST catalogue (grey scale; Brammer et al., 2012; Skelton et al., 2014; Momcheva et al., 2016). Offset from the main sequence (top left), effective radius (top right), and gas-to-stellar mass ratio (bottom) are shown as a function of stellar mass. In the top left panel, the SFR is normalized to the main sequence as derived by Whitaker et al. (2014) at the redshift and stellar mass of each galaxy, using the redshift-interpolated parametrization by Wisnioski et al. (2015). In the bottom panel, gas masses for the 3D-HST galaxies are computed from the scaling relation by Tacconi et al. (2018) (T18).The TNG50 galaxies lie along the main sequence, with a tendency towards lower star formation rates compared to the observed galaxies, have sizes similar to the reference sample by Genzel et al. (2017), but their gas-to-stellar mass ratios are lower by* $\sim 20 - 30$ *%.*

$1''$ corresponds to 8.01 kpc, and 1 Å corresponds to 15 km s^{-1}. The mock line emission is scaled to reproduce the typical signal-to-noise ratio (S/N) of the deep high$-z$ observations, with an average S/N per spaxel of $S/N \approx 3-5$ in the galaxy outskirts, and $S/N \gtrsim 20$ in the bright central regions.

Finally, we also generate for each galaxy and each line of sight a mock $K-$band image that has the same spatial dimensions and pixel resolution as the Hα cubes. These are based on the simulated stellar populations and are also dust-free.

4.3.3.4 Kinematic Extractions

With our mock data cubes in hand, we derive the kinematic properties of the simulated galaxies in the same way as was done for the real galaxies presented by Genzel et al. (2017). First, we derive the two-dimensional projected Hα velocity and velocity dispersion fields using LINEFIT (Davies et al., 2009, 2011; Förster Schreiber et al., 2009). This code takes into account the instrument line spread function and fits a Gaussian model for each spaxel of the data cube. For the extraction of one-dimensional kinematic profiles (the rotation curve and the dispersion profile), we go back to the mock data cube and place a pseudo-slit of width $0.24''$ on the kinematic major axis of the galaxies to generate a position-velocity diagram. Through horizontal cuts of width 4 pixels we then extract one-dimensional line profiles for different positions along the kinematic major axis. From those, we extract the velocity and velocity dispersion as a function of distance from the center using LINEFIT. Following Genzel et al. (2017), we introduce minimum uncertainties of ±5 km s^{-1} for the velocity and ±10 km s^{-1} for the velocity dispersion.

4.3.3.5 Modelling

For the modelling of our mock galaxies we use the dynamical fitting code DYSMAL (Cresci et al., 2009; Davies et al., 2011; Wuyts et al., 2016b; Übler et al., 2018), a forward-modelling code that allows for the combination of multiple mass components. It accounts for flattened spheroidal potentials (Noordermeer, 2008), includes the effects of pressure support on the rotation velocity, accounts for beam-smearing effects through convolving with the two-dimensional PSF of each galaxy, and for the instrument line-spread function. For our modelling, we use a thick exponential disk, a central bulge, and a dark matter halo. We assume a velocity dispersion that is isotropic and constant throughout the disk, and use a flat prior between 10 and 100 km s^{-1}.

Baryonic parameters Targets observed in kinematic studies often benefit from high-resolution ancillary imaging data that provide estimates on structural properties such as size, axis ratio (hence disk inclination), and bulge-to-total (B/T) fractions. The intrinsic baryonic components of the simulated galaxies are reasonably well fit by a double-exponential profile. We have verified through two-component Sérsic fits to the artificial $K-$band images of the simulated galaxies that we can recover the intrinsic effective radii R_e, bulge-to-total ratio B/T, and Sérsic indices n_S within the uncertainties.

For our fiducial modelling, we fix the Sérsic indices and the effective radii of the disk and bulge components, and use Gaussian priors on B/T and the baryonic mass, centered on the intrinsic values with standard deviations and hard bounds of 0.1 and typically ±0.3 for B/T, and 0.2 dex and ±0.5 dex of solar mass for the baryonic mass. With this approach, we fold into our modelling the typical uncertainties on those parameters expected from observational data, and allow for modelling solutions with somewhat deviant parameters, keeping in mind also the approximate measurement of the 'intrinsic' structural parameters.

We also explored models with a Gaussian prior on the disk effective radius R_e, but found that due to the highly asymmetric rotation curves of the simulated galaxies (see Section 4.3.4.2) R_e is poorly constrained for most galaxies and lines of sight. Because the central dark matter fraction $f_{\rm DM}(R_e)$ is naturally very sensitive to this value, we fix the disk effective radius for our fiducial models.

Dark matter density profile The results presented by Genzel et al. (2017) assume a standard NFW dark matter halo profile for the dynamical modelling (Navarro, Frenk, & White, 1996). The NFW model is a two-power-law density model of the form

$$\rho(r) = \frac{\rho_0}{(r/r_S)^{\alpha}(1+r/r_S)^{\beta-\alpha}}, \tag{4.3}$$

where $\alpha = 1$ and $\beta = 3$, and r_S is the halo scale radius.

Through modified NFW fits to the intrinsic dark matter density distributions, we find that all simulated haloes have a steeper inner slope with respect to a pure NFW halo, with individual values of $\alpha = 1.4 - 1.7$ (see also Lovell et al., 2018). An example is shown in Figure 4.15. We also constrain the halo concentration parameter $c = R_{200}/r_S$, where R_{200} is the innermost radius within which the mean density exceeds 200 times the critical density of the Universe. r_S is defined to be the radius where the slope of the density profile matches $-(\beta+\alpha)/2$. This is by definition -2 for an NFW halo, but varies for our modified NFW haloes with values ≤ -2, leading to larger scale radii. For our modified NFW fits, we find a range of concentration parameters $c = [2.4; 6.4]$. We note that the exact values of α, r_S, and correspondingly c are sensitive to the the radius out to which mass is included for the fit, and we always fit out to radii beyond R_{200}.

For the bulk of our modelling we adopt the modified NFW profiles for the dark matter distribution, and leave the total halo mass as a free parameter between $M_{\rm halo} = 10^{11} - 10^{13.5} M_{\odot}$, but we also perform modelling with standard NFW haloes for consistency with the modeling presented by Genzel et al. (2017),

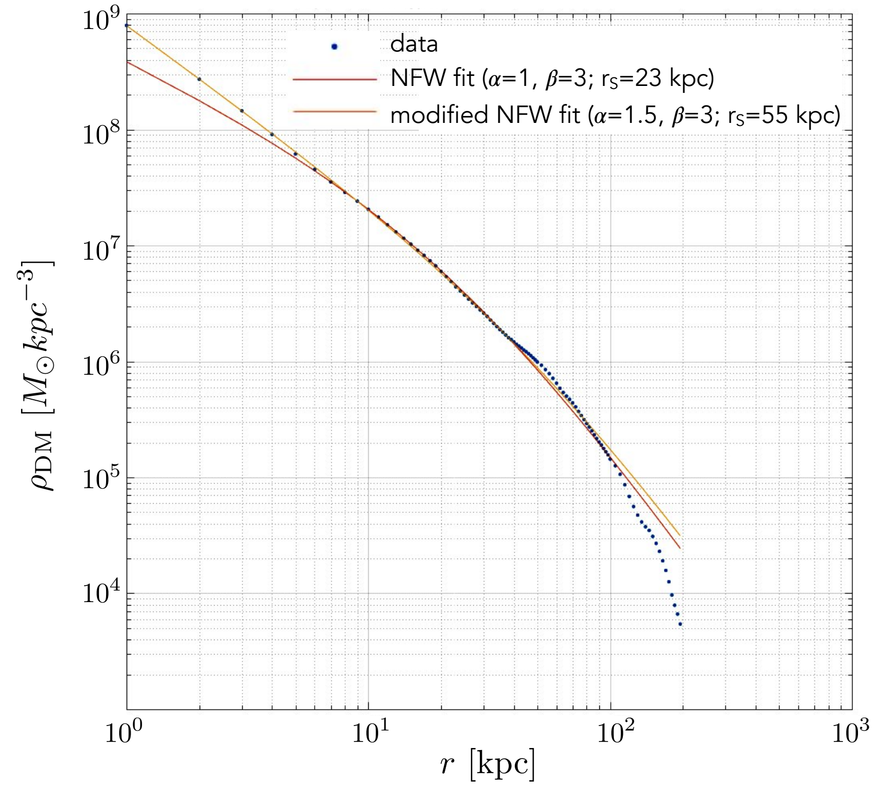

Figure 4.15: *Two-power-law density fit to the spherically averaged dark matter density distribution of the halo of galaxy #3. On the galaxy scale ($r \lesssim 30$ kpc), the dark matter density is well fit by a modified NFW halo with $\alpha = 1.5$, while a standard NFW fit with $\alpha = 1$ underestimates the central dark matter density. This halo has a virial radius $R_{200} \approx 174$ kpc with a total mass of $\log(M_{200}/M_\odot) = 12.70$. For our modified NFW fit we find a scale radius $r_S \approx 55$ kpc, corresponding to a concentration parameter of $c = 3.1$.*

and to assess the impact of the assumed dark matter halo profile on the inferred central dark matter fractions.

To summarize, in our standard modelling setup we leave the following four parameters free, using flat or truncated Gaussian priors: the total baryonic mass $M_{\rm bar}$, the baryonic bulge-to-total fraction B/T, the intrinsic velocity dispersion σ_0, and the total halo mass $M_{\rm halo}$. All other parameters are fixed, including the bulge and disk effective radii and Sérsic indices, inclination, and position angle.

Using DYSMAL, we simultaneously fit the extracted one-dimensional velocity and velocity dispersion profiles. We apply Markov chain Monte Carlo (MCMC) sampling to determine the model likelihood based on comparison to the extracted profiles, and assuming Gaussian measurement uncertainties. To ensure convergence of the MCMC chains, we model each galaxy with ≥ 200 walkers per free parameter, and a burn-in phase followed by a running phase of 100 steps each

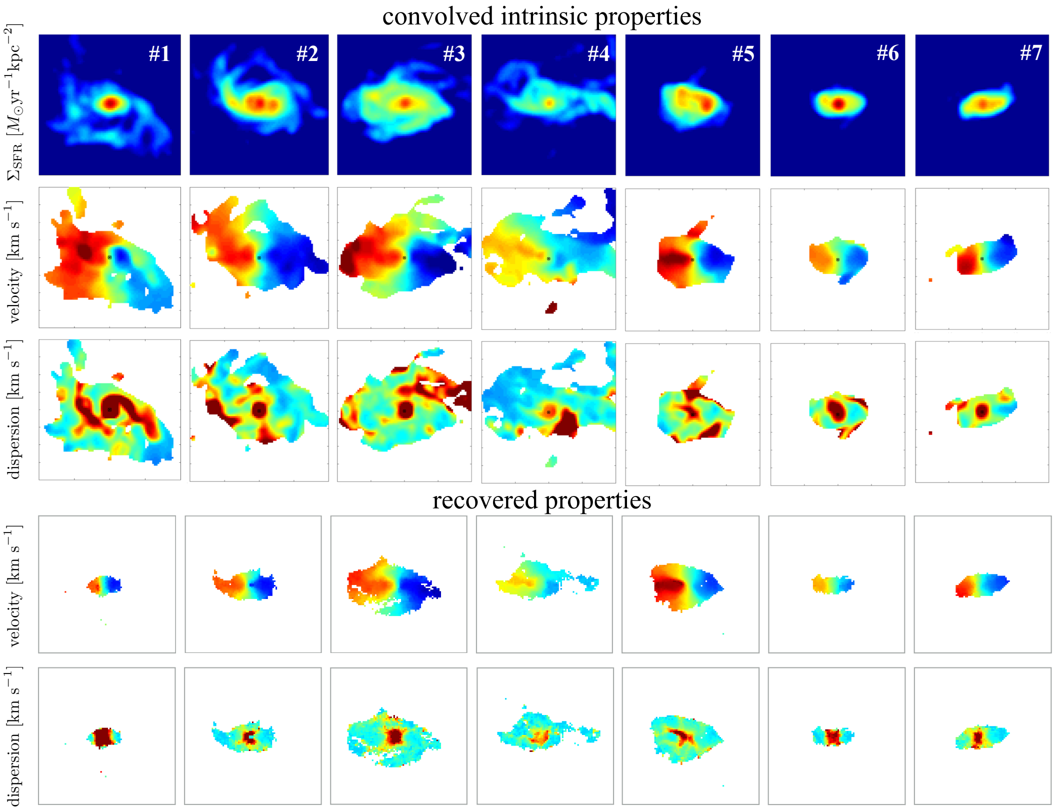

Figure 4.16: *Projected two-dimensional maps of the convolved intrinsic parameters (top row: $\Sigma_{\rm SFR}$; second row: velocity; third row: velocity dispersion) and recovered parameters from the mock observations with $S/N \geq 5$ (fourth row: velocity; bottom row: velocity dispersion) for the seven selected TNG50 galaxies (columns). The projections correspond to an inclination of $i = 60°$. The panels show 40 kpc × 40 kpc in projection, and the color scale shows [-2; 1] for $\log(\Sigma_{\rm SFR})$, [-400; 400] km s^{-1} for velocity, and [0; 150] km s^{-1} for velocity dispersion. The agreement between the intrinsic and the recovered kinematic properties in regions of high star-formation rate surface density is very good.*

(>10 times the maximum autocorrelation time of the individual parameters). For each free parameter, we adopt the median of all model realizations as our best fit value, with asymmetric uncertainties corresponding to the 68th percentile confidence ranges of the one-dimensional marginalized posterior distributions.

4.3.4 Results

4.3.4.1 Comparison of two-dimensional kinematics

In Figure 4.16 we compare the two-dimensional maps of velocity and velocity dispersion based on the kinematic properties after convolution with the PSF and LSF on the one hand, and on the other hand based on our mock observations

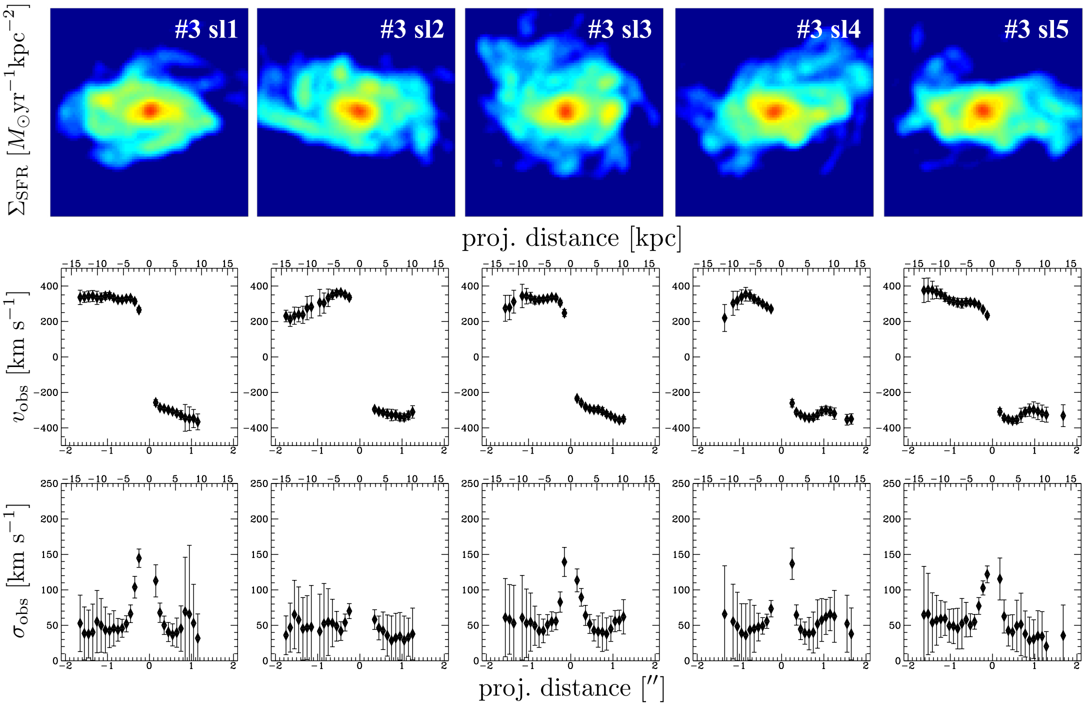

Figure 4.17: *Extracted kinematics along five different lines of sight (columns) for galaxy #3. Top row: star-formation rate surface density, 40 kpc × 40 kpc in projection; second row: extracted velocity along the kinematic major axis; bottom row: extracted velocity dispersion along the kinematic major axis, corrected for the 'instrument' LSF. Particularly the rotation velocities can differ substantially along different lines of sight. Variations in the velocity dispersion are more modest, and typically within the uncertainties. Not shown here are velocity and dispersion extractions for emission regions with highly non-Gaussian line profiles, typically found in the central* $0.2 - 0.5''$ *of the mock data.*

including noise. Through the addition of noise in the mock observation, the fainter emission in the outskirts of the galaxies can't be recovered, including low-surface brightness inflows and tidal features. However, above $S/N \geq 5$ the recovery of the intrinsic kinematics is very good.

4.3.4.2 Line-of-sight variations

The columns in Figure 4.16 show one line of sight per galaxy. In order to investigate the regularity of the simulated kinematics, we extract for each galaxy two- and one-dimensional kinematics from the mock observations along five random lines of sight, but keeping the inclination fixed. In Figure 4.17 we compare the one-dimensional velocity and velocity dispersion profiles extracted along the

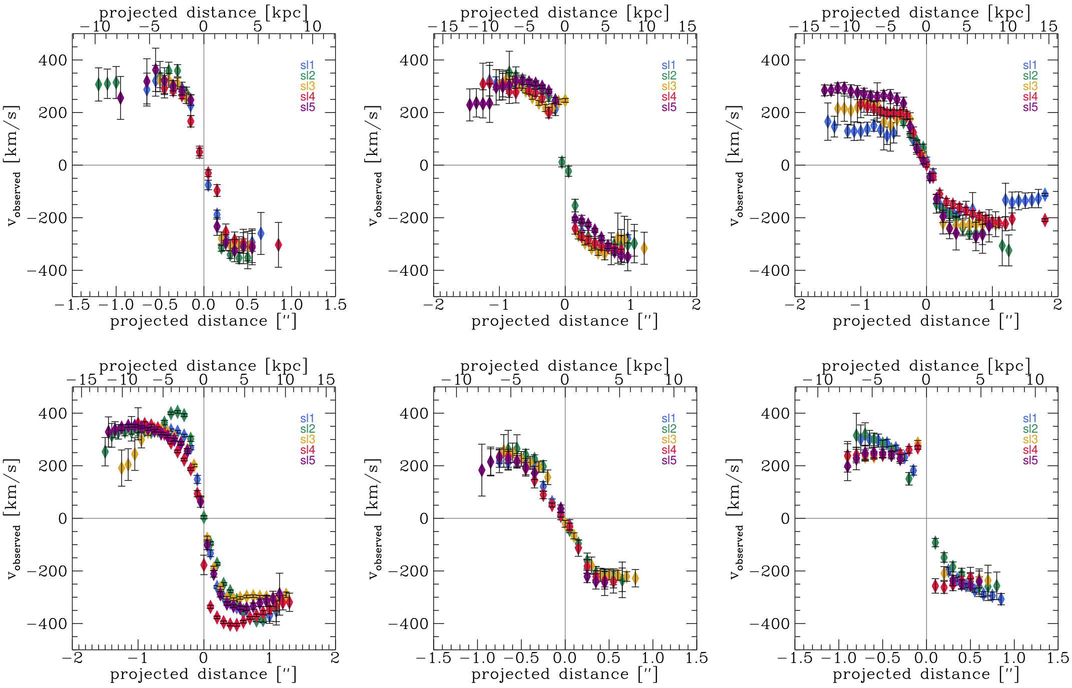

Figure 4.18: *Extracted rotation velocities along five different lines of sight (colors) for galaxies #1, #2, #4, #5, #6, and #7 (from left to right and top to bottom). We find large variations in extracted major axis velocities along different lines of sight for all simulated galaxies.*

different lines of sight for galaxy #3, for which the high surface brightness region is most extended. From this example it is evident that the kinematics can vary substantially between different lines of sight, with differences in the outer rotation velocities of ~ 150 km s^{-1}, much larger than the typical uncertainties of $\sim 30-50$ km s^{-1} in the outer regions. The velocity dispersions are generally more similar along different lines of sight, with maximum variations in the outer regions of ~ 30 km s^{-1} and typical uncertainties on the extracted values of $\sim 30-60$ km s^{-1}.

Furthermore, for each line of sight the extracted rotation curves are relatively asymmetric if comparing the approaching and receding side, to a degree that cannot be accounted for by fitting uncertainties. In fact, these asymmetries are seen in the intrinsic data. We find such asymmetries of individual lines of sight, and differences between lines of sight for all seven galaxies, as illustrated in the comparative plots for the major axis velocities of the other six galaxies in Figure 4.18.

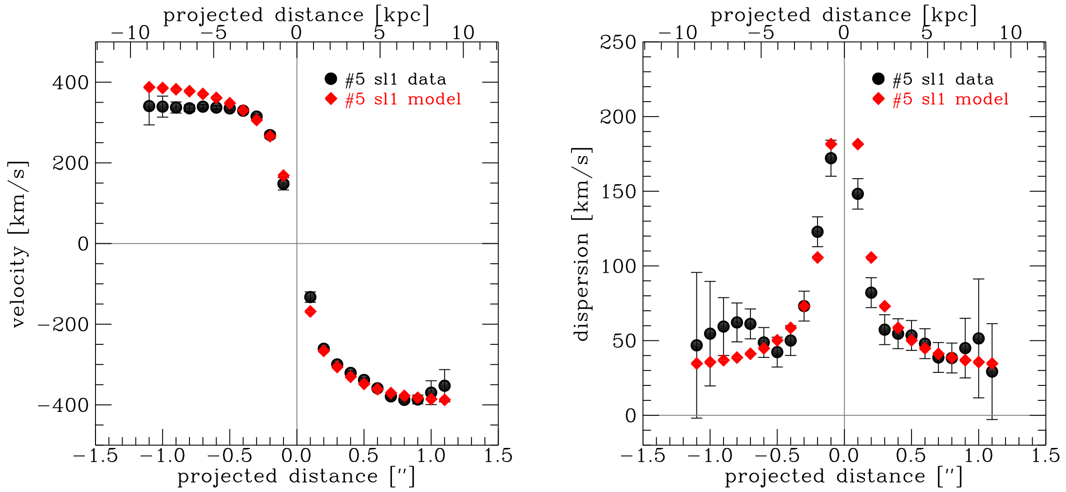

Figure 4.19: *One-dimensional velocity and velocity dispersion profiles for galaxy #5, sightline 1 (black circles with error bars) and the corresponding best-fit model (red diamonds). The model matches the data well within the uncertainties.*

4.3.4.3 Dynamical modelling and recovery of the central dark matter fraction

We model all seven galaxies with five lines of sight each with our fiducial modelling setup. Generally, the asymmetric kinematics along the major axis as discussed above hamper successfull modelling with DYSMAL because the code assumes axisymmetric mass distributions. One case with relatively symmetric one-dimensional kinematics is shown in Figure 4.19 (black points with errors) for galaxy #5, sightline 1, together with our best fit (red diamonds) as constrained through the medians of the posterior probability distributions from the MCMC chains (Figure 4.20). In Figure 4.20, best-fit parameters are indicated by the blue squares and vertical lines, while the true values are indicated by green stars and vertical dash-dotted lines or regions. In the bottom row we also show the corresponding histograms for the inferred dark matter fraction within the effective radius. We recover the central dark matter fraction $f_{\rm DM}(R_e)$ within one standard deviation. In Figure 4.20, we also see the typical (anti-)correlations between dark matter and baryonic mass, and its distribution.

In Table 4.4 we list the best-fit parameters for the simulated galaxy #5, including the inferred $f_{\rm DM}(R_e)$, for the five lines of sight, together with the corresponding intrinsic values. Generally, we recover the intrinsic parameters within one or two standard deviations. However, sightlines 2, 3, and 4, which give all relatively asymmetric one-dimensional kinematics, all overestimate the total baryonic mass, and underestimate the total dark matter halo mass. The central dark

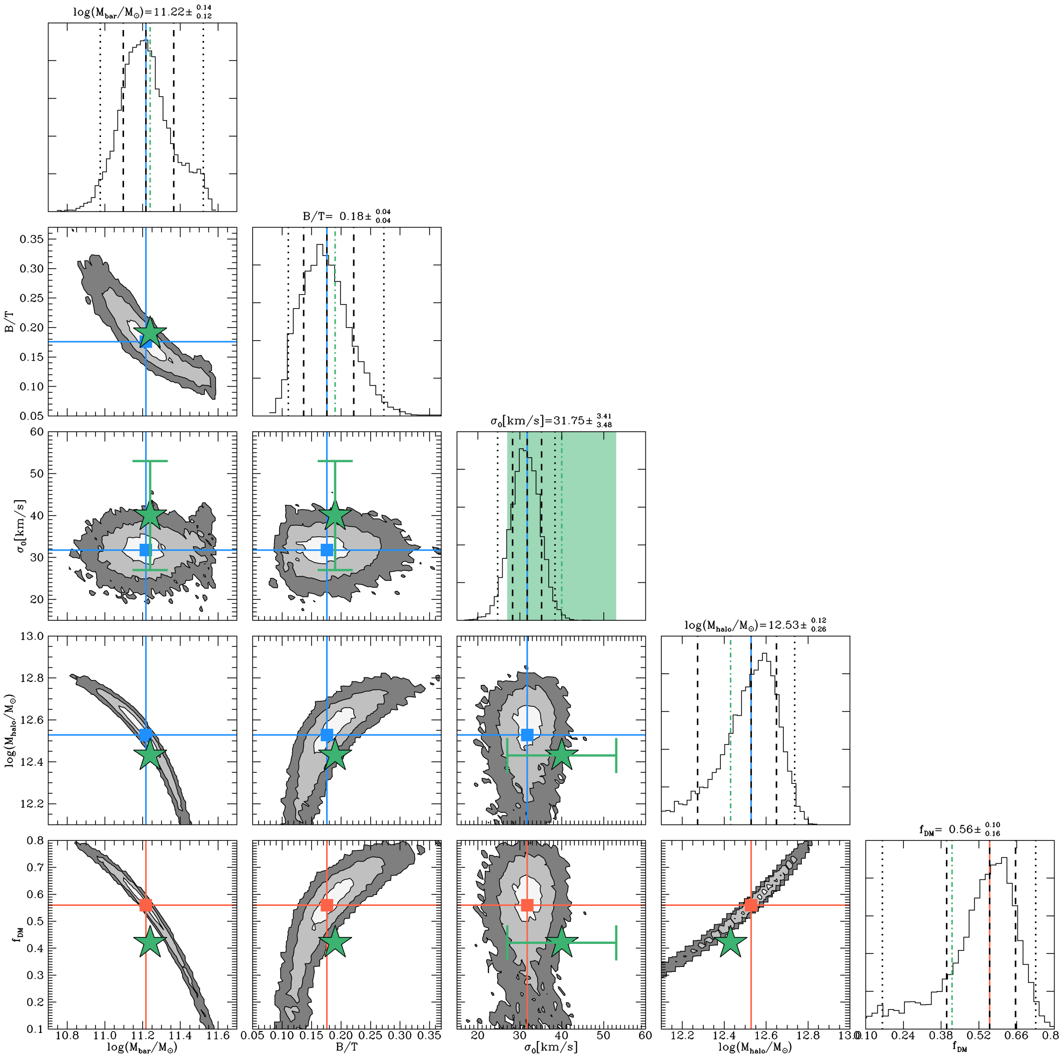

Figure 4.20: *MCMC sampling of the joint posterior probability distribution of the model parameters, $M_{\rm bar}$, B/T, σ_0, and $M_{\rm halo}$ (top rows) for galaxy #5, sightline 1. The median values and 1σ confidence ranges of the marginalized distributions are indicated by the dashed vertical lines in the one-dimensional histograms, and given on top of each histogram, and 2σ confidence ranges are indicated by the dotted vertical lines. The median values are also shown as blue squares on top of the two-dimensional histograms. All of the median values lie close to the modes of the two-dimensional histograms. The contours show the 1σ, 2σ, 3σ confidence levels of the two-dimensional distributions. The bottom row histograms show $f_{\rm DM}(\leq R_e)$, calculated from the MCMC realizations. Median values are indicated in red. As green stars we show the corresponding intrinsic parameters of the simulated galaxies for $M_{\rm bar}$, B/T, σ_0, and $f_{\rm DM}(\leq R_e)$. For σ_0 we give a range of values indicated by the shaded region in the one-dimensional histogram and by the error bars in the two-dimensional histograms, where the star simply indicates the midpoint. These regions encompass the range of σ_0 values as measured from the intrinsic azimuthally-averaged kinematics. We recover the dark matter fraction at $1R_{\rm e}$ within one standard deviation.*

matter fractions are poorly constrained for sightlines 2 and 3, and underestimated for sightline 4.

In Table 4.4 we also list our best fit for sightline 1 using a standard NFW halo instead of the modified, intrinsically constrained halo profile. This setup produces a higher baryonic mass compared to the modified NFW setup. Recall from Figure 4.15 that the NFW fit generally underestimates the dark matter density within the inner $\sim$ 10 kpc. In order to still reproduce the observed rotation curve shape, the baryonic mass has to be increased. In the present case, however, this effect is small if a very high concentration parameter is assumed – we use $c = 17$ for the NFW profile.

In Appendix 4.3.8 we list the best fit parameters for all galaxies and lines of sight for our fiducial modelling setup.

Dealing with asymmetries We have tested two approaches in dealing with the asymmetric kinematics: (i) 'symmetrization' of the one-dimensional extracted kinematics through rotating/folding and averaging, a method that can also be applied to real data, and (ii) 'equilibration' of the intrinsic kinematics before creating the mock data through artificially removing part of the non-circular motions, namely vertical motions perpendicular to the disk plane. In Appendix 4.3.9 we show examples of both approaches and discuss their effect.

4.3.4.4 Intrinsic kinematics of the simulated galaxies

The simulated galaxies differ in a number of ways from the systems observed by Genzel et al. (2017). To better understand the origin of these differences, we investigate the intrinsic kinematic properties of the galaxies. As for the different lines of sight, these properties are not accessible for real galaxies, but their study can highlight effects which are potentially relevant to observational work.

In Figure 4.21 we show different measures of the intrinsic, one-dimensional velocity and velocity dispersion profiles for all selected galaxies. While the circular velocity v_{circ} (black line) is calculated from the enclosed mass, resulting in a smooth curve, all other properties are measured from the azimuthally averaged star-forming gas.

Table 4.4: *Best-fit parameters for different lines of sight ('sl') and modelling setups for galaxy #5. We list the median together with the 1σ confidence ranges, or the upper 2σ value as upper limit if no reliable best-fit parameter could be constrained. If not specified otherwise, the standard setup uses Gaussian priors centered on the intrinsic values for $M_{\rm bar}$ and B/T, with standard deviations of 0.5 dex of solar masses and 0.1, respectively, flat priors for $M_{\rm halo}$ and σ_0, in the ranges log$(M_{\rm halo}/M_\odot) = [11; 13.5]$ and $\sigma_0 = [10; 100]$ km s^{-1}, respectively, and the halo density profile is fixed to the intrinsic, modified NFW profile.*

sightline & setup	$\log(M_{\rm bar}/M_\odot)$	B/T	σ_0 [km s^{-1}]	$\log(M_{\rm halo}/M_\odot)$	inferred $f_{\rm DM}(R_e = 5.0$ kpc)
sl1	$11.22^{+0.15}_{-0.12}$	0.18 ± 0.04	32^{+3}_{-4}	$12.53^{+0.12}_{-0.26}$	$0.56^{+0.09}_{-0.16}$
sl1 NFW	$11.29^{+0.09}_{-0.08}$	0.20 ± 0.04	32^{+3}_{-4}	$12.25^{+0.12}_{-0.18}$ ($c = 17$)	$0.47^{+0.08}_{-0.09}$
sl2	11.61 ± 0.02	$0.03^{+0.01}_{-0.00}$	44 ± 3	$11.30^{+0.29}_{-0.19}$	< 0.61
sl3	$11.42^{+0.01}_{-0.03}$	0.16 ± 0.01	31 ± 3	< 11.72	< 0.25
sl4	$11.41^{+0.07}_{-0.08}$	$0.21^{+0.04}_{-0.02}$	29 ± 3	$12.03^{+0.23}_{-0.28}$	$0.29^{+0.11}_{-0.09}$
sl5	$11.14^{+0.07}_{-0.08}$	$0.25^{+0.06}_{-0.04}$	38 ± 3	$12.43^{+0.08}_{-0.09}$	$0.56^{+0.06}_{-0.07}$
intrinsic values	11.24	0.19	$\sim 27 - 53$	12.43 ($c = 6.0$)	0.42

Three different measures of the intrinsic velocity dispersion are shown: the radial velocity dispersion σ_r (turquoise), the vertical velocity dispersion σ_z (green), and the three-dimensional velocity dispersion $\sigma_{\rm 3D}/\sqrt{3}$ (blue). All three measures agree extremely well, suggesting that the velocity dispersion is isotropic. Furthermore, beyond $r \sim 2$ kpc the velocity dispersion is remarkably constant, suggesting the existence of a galaxy-wide pressure floor. Generally, the dispersion values of $20 - 50$ km s^{-1} are in the lower part of the observed scatter at $z \sim 2$, which covers the range $\sim 20 - 100$ km s^{-1} for SFGs, with a median value of ~ 50 km s^{-1} (Wisnioski et al., 2015; Übler et al., 2019).

Out to $r \sim 10$ kpc and sometimes beyond, the gas rotation velocity $v_{\rm rot}$ (salmon) approximately traces the circular velocity. The light brown lines show the rotation velocity corrected for pressure support, often used in observations as an attempt to recover the circular velocity (e.g. Burkert et al., 2016; Wuyts et al., 2016b; Lang et al., 2017; Genzel et al., 2017; Übler et al., 2017, 2018). Due to the high rotation velocities ($\sim 300 - 400$ km s^{-1}) and the low velocity dispersion, the relative effect of the pressure support correction is comparably small for most simulated galaxies.

All galaxies show substantial amounts of vertical motions v_z (purple lines show $|v_z|$) and radial motions v_r (magenta). The magnitudes of these motions are often correlated (e.g., galaxy #1, top left panel), suggesting streaming motions diagonal to the galactic plane, potentially connected to minor mergers (as opposed to pure radial inflow triggered by a bar or disk instabilities). Adding these non-circular motions to the rotation velocity, together with the pressure correction, leads to the dark brown line which generally corresponds better to the total circular velocity than the light brown line, accounting only for pressure support. We note that the largest non-circular motions are seen for galaxies #6 and #7 (bottom panels) at distances $r \gtrsim 10$ kpc from the center, beyond the visible extent of these galaxies. These motions therefore most likely correspond to low-surface brightness, misaligned accretion streams.

4.3.5 Discussion

4.3.5.1 Recovery of intrinsic properties with the observational pipeline

Generally, the recovery of the simulated galaxy kinematics through the observational pipeline, i.e. the creation of two-dimensional kinematic maps and of one-dimensional major axis kinematics, works satisfactorily. Modulo accounting for random and correlated noise features, the recovered properties correspond well to the intrinsic kinematics.

The application of the dynamical modelling tool to recover the intrinsic mass profiles from the extracted kinematics proved more difficult. A limitation here is the assumed axisymmetry of the mass distribution and kinematics. While the azimuthally averaged mass profiles of the simulated galaxies are well fit by a

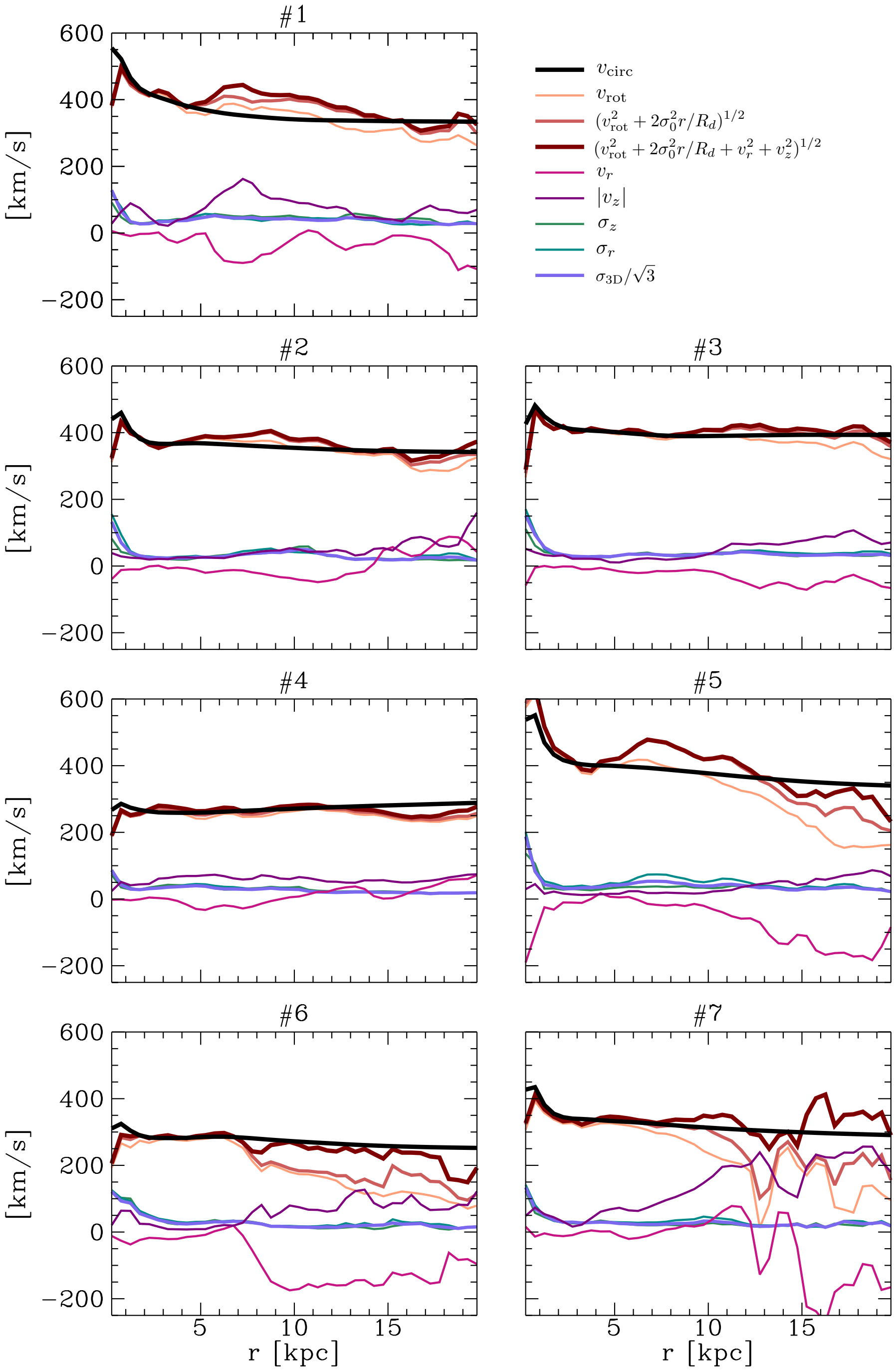

Figure 4.21: *Different measures of the intrinsic and azimuthally averaged velocity and velocity dispersion of the selected simulated galaxies, as indicated in the legend. Beyond $r \sim 2$ kpc, the velocity dispersion is approximately constant with radius (blue and green lines). All galaxies show substantial radial (magenta) and vertical motions (purple). Accounting for the turbulent and non-circular motions (light and dark brown), it is possible to approximately recover the intrinsic circular velocity (black).*

double-exponential for the baryonic component and a modified NFW halo, the projected two-dimensional and one-dimensional major axis kinematics as traced by the star-forming gas show clear deviations from axisymmetry. This is further reflected in the rotation velocities along different lines of sight (but with identical inclination) which can display large differences amongst each other, with up to $\Delta v_{\rm rot} > 100$ km s^{-1}. For the more symmetric cases of individual line-of-sight kinematics, however, we are able to recover the central dark matter fraction within the uncertainties constrained through our MCMC modelling.

It is crucial to realize that for the dynamical modelling we have fixed the density profile of the dark matter halo to a modified NFW profile with exponents as measured from the intrinsic data, leaving only the total mass of the halo free. Forcing a fit with a standard NFW profile typically leads to increased estimates of the total baryonic mass, and decreased estimates of the central dark matter fraction.

4.3.5.2 Comparison between simulated and real galaxies

As discussed in Section 4.3.3.2 the simulated galaxies lie in a similar parameter space of stellar mass, star formation properties, and sizes, compared to the galaxies observed by Genzel et al. (2017). With respect to their gaseous mass, one galaxy (#3) lies on the scaling relations by Tacconi et al. (2018), and one galaxy (#4) exceeds the predicted gas mass by 25%. The other four objects have gas masses between 60 and 90% of their predicted values. Correspondingly, the intrinsic velocity dispersions measured from the star-forming gas are in the lower half of the observed scatter for $z \sim 2$ SFGs (e.g. Übler et al., 2019).

The rotation velocities of the simulated galaxies, on the other hand, are higher than typical observed values, with $v_{\rm circ} \sim 300 - 400$ km s^{-1} for all galaxies, indicating a higher central mass concentration. In the simulations, this mass concentration is provided by dark matter. The intrinsic halo profiles are steeper than NFW, and more so due to the presence of baryons (Lovell et al., 2018). As a consequence of the somewhat lower velocity dispersions and the higher rotation velocities, the effects of pressure support, which can be substantial for observed galaxies (see Genzel et al., 2017; but also Übler et al., 2018), are not very important for the simulated galaxies.

For the dynamical modelling of the $z \sim 2$ galaxies presented by Genzel et al. (2017), a standard NFW halo was assumed. Our modelling of the simulated galaxies shows that the assumed halo profile has an effect on the inferred central dark matter fraction, and that in the particular case of the studied TNG50 galaxies an NFW halo profile systematically underestimates the central dark matter fractions. We note that in the case of the observed SFGs, any additional large central dark matter mass would have been reflected in higher rotation velocities (as we find it in this work for the simulated galaxies). Given the observed shape of the observed rotation curves, a higher central dark matter density would require a substantial decrease in baryonic mass of the observed galaxies.

Regarding the kinematic asymmetries in the simulated galaxies, it is important to realize that the galaxies discussed by Genzel et al. (2017) have been carefully selected to enable this challenging work. Certainly there exist real high$-z$ galaxies with asymmetric kinematics. Due to the low number statistics of the observed and simulated sample, we cannot conclusively determine how 'different' the simulated galaxies are in this respect. It is however noteworthy that *all* TNG50 galaxies in the explored $M_* - \mathrm{SFR} - R_e-$parameter space show kinematic asymmetries.

4.3.6 Conclusions

We have studied the detailed kinematics of massive, $z = 2$ SFGs from the IllustrisTNG50 simulation along different lines of sight. Our focus was on the observational perspective: through mock observations and application of the same observational tools for kinematic analysis and modelling, we have compared the simulated galaxies to those observed by Genzel et al. (2017) who found high baryonic surface densities and low central dark matter fractions for massive $z \sim 1-2$ SFGs.

Our main conclusions are as follows:

- All simulated galaxies show asymmetric kinematics particularly in the circular velocity fields and profiles, which can also vary by up to 100 km s^{-1} along different lines of sight. In addition, all galaxies show substantial vertical and radial velocity components.

- The extracted one- and two-dimensional kinematics from the mock data cubes, using the same observational tools, correspond well to the intrinsic galaxy kinematics.

- For the less asymmetric kinematics, we can recover the central dark matter fraction within the uncertainties.

- The simulated galaxies differ in a few important ways from the observed sample by Genzel et al. (2017): (i) their SFRs and gas masses are lower; (ii) their rotation velocities are higher, while their velocity dispersions are in the lower part of the observed scatter at $z \sim 2$; and (iii) their central dark matter fractions are higher.

Since real galaxies can ever only be observed from one line-of-sight, the substantial differences among different lines of sight in the simulated galaxy kinematics may serve as a caution to observers. However, considering the differences in other physical parameters between the simulated and observed sample, it is not ultimately clear that the features seen in the simulated galaxies would show up in real galaxies, since the simulated galaxies appear to *not* resemble the observed galaxies in various ways. This might also be due to low-number statistics from both the observational perspective (6 galaxies discussed by Genzel et al. (2017)) and the simulation perspective (only 12 TNG50 galaxies match the selection in stellar mass and SFRs).

From the observational perspective, work in progress is substantially extending the available outer rotation curve sample with constrained central dark matter fractions towards lower baryonic masses, velocities, and redshifts. It will be interesting to compare TNG50 or next-generation simulated galaxies to these systems for which better statistics will be available.

Our analysis shows that it may also be valuable to explore dynamical modelling with halo profiles that deviate from the standard NFW. For instance, if baryonic masses are allowed to decrease, a dark matter profile with a steeper inner slope can lead to higher central dark matter fractions.

4.3.7 Appendix A – Dismissed galaxies

In Figure 4.22 we show those 5/12 simulated galaxies that met the stellar mass and SFR selection cuts, but were dismissed from further kinematic analysis because they show signatures of strong interaction or disturbance, and/or they are too compact for a kinematic analysis using the standard observational tools (including noise).

4.3.8 Appendix B – Best-fit parameters

In Table 4.5 we list the best-fit parameters for all galaxies for our fiducial modelling setup.

For galaxy #1, the central dark matter fraction is not well constrained for all lines of sight but sl4. The 'emission line' profiles of this object are highly non-Gaussian in the central ±2 kpc for most lines of sight, and only for sl1 and sl4 we can extract reliable Gaussian fits to the central kinematics. The galaxy shows also high vertical and radial motions between $r = 5 - 10$ kpc, leading to uncertain measurements of the velocity dispersion, and is likely in a stage of rapid accretion.

For galaxy #2, we recover the intrinsic baryonic parameters reasonably well. The central dark matter fractions are somewhat too high for sl2, sl3, and sl5, but all agree within 2σ.

For galaxy #3, we find asymmetric rotation velocities. The best-fit baryonic mass and B/T are systematically over-estimated, while the central dark matter fraction is under-estimated.

Galaxy #4 appears to be in a stage of rapid assembly or post merger. It has relatively symmetric rotation curves but very asymmetric velocity dispersion pro-

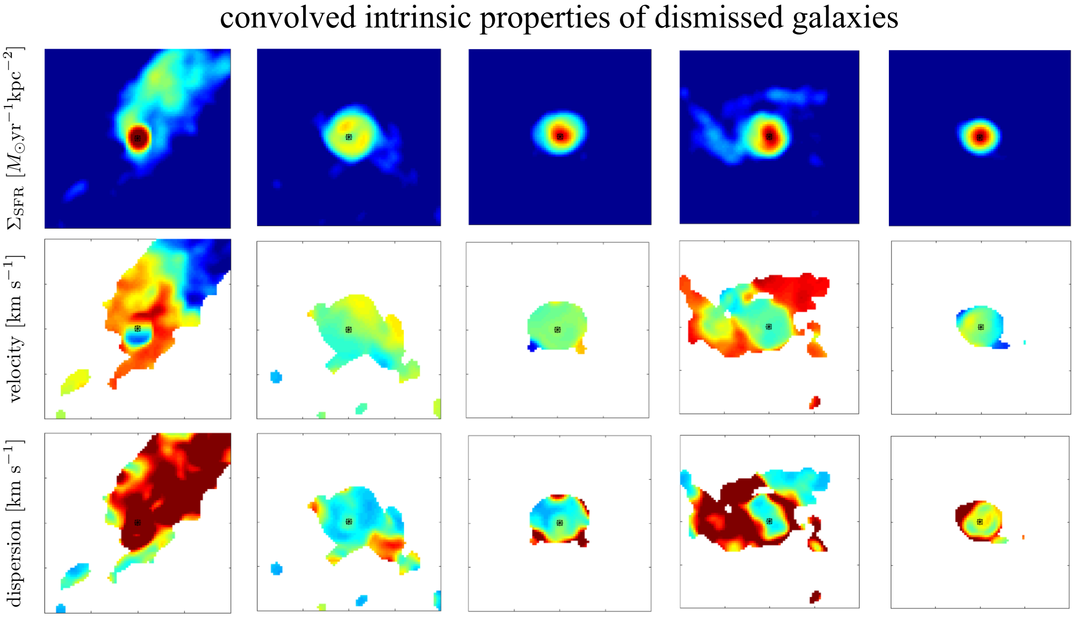

Figure 4.22: *Projected two-dimensional maps of the convolved intrinsic parameters (top row: $\Sigma_{\rm SFR}$; second row: velocity; third row: velocity dispersion) for the five dismissed TNG50 galaxies (columns). The projections correspond to face-on, i.e. an inclination of $i = 0°$. The panels show 40 kpc × 40 kpc in projection, and the color scale shows [-400; 400] km s^{-1} for velocity, and [0; 150] km s^{-1} for velocity dispersion. The galaxies were dismissed due to strong interaction/disturbance signatures and/or because they were too compact for a kinematic analysis with the standard observational tools.*

files, likely due to its high vertical motions. The different lines of sight, however, show rotation velocities with differences of up to $\Delta v_{\rm obs} \approx 150$ km s^{-1}. Particularly sl1 shows very low rotation velocities. For this sightline, we cannot recover the intrinsic parameters. The uncertainties in both the kinematic extractions and the best-fit dynamical modelling are relatively large, such that we can recover the central dark matter fraction for the other lines of sight within the uncertainties. We find the largest halo mass and central dark matter fraction for sl5 which shows also the highest rotation velocities.

Galaxy #5 shows very asymmetric rotation velocities and different kinematic profiles from different lines of sight. We find baryonic masses that differ by up to $\Delta(M_{\rm bar}/M_\odot) \approx 0.5$ dex, and halo masses that differ by up to $\Delta(M_{\rm halo}/M_\odot) \approx 1.3$ dex. The central dark matter fractions also differ by $> 30\%$. However, for sl1 and sl5 we get very good fits to the extracted one-dimensional kinematics. For those lines of sight, the best-fit values agree reasonably well with the intrinsic parameters.

For galaxy #6, we get poor fits to the extracted one-dimensional kinematics, except for sl3. For this line of sight, we also recover the intrinsic parameters within the uncertainties. The poor fits for the other lines of sight are mostly due to the velocity dispersion profiles, which are very asymmetric for these other cases. In this galaxy, the intrinsic, azimuthally averaged velocity dispersion is elevated in the central region and reaches a constant level only beyond $\sim 3-4$ kpc.

For galaxy #7, the extracted rotation curves are relatively symmetric, but very different between different lines of sight. We get reasonable fits for most lines of sight, but the central dark matter fraction is constrained only for sl1 and sl2 which show rising rotation curves, while the other lines of sight with flat rotation curves yield only upper limits.

Table 4.5: *Best-fit parameters for all simulated galaxies and lines of sight with the fiducial modelling setup. We list the median together with the 1σ confidence ranges, or the 2σ value as an upper/lower limit if no reliable best-fit parameter could be constrained. The fiducial modelling setup uses Gaussian priors centered on the intrinsic values for* $M_{\rm bar}$ *and* B/T*, with standard deviations of 0.5 dex of solar masses and 0.1, respectively, flat priors for* $M_{\rm halo}$ *and* σ_0*, in the ranges* $\log(M_{\rm halo}/M_\odot) = [11; 13.5]$ *and* $\sigma_0 = [10; 100]$ *km s*$^{-1}$*, respectively, and the halo density profiles is fixed to the intrinsic, modified NFW profile.*

galaxy	$\log(M_{\rm bar}/M_\odot)$	B/T	σ_0 [km s^{-1}]	$\log(M_{\rm halo}/M_\odot)$	$f_{\rm DM}(R_e)$
#1 sl1	11.29 ± 0.07	$0.40^{+0.13}_{-0.07}$	70^{+13}_{-14}	< 12.34	< 0.41
#1 sl2	$11.38^{+0.07}_{-0.09}$	$0.34^{+0.07}_{-0.05}$	29^{+12}_{-11}	$11.81^{+0.51}_{-0.53}$	< 0.51
#1 sl3	$11.26^{+0.09}_{-0.13}$	0.32 ± 0.06	45^{+15}_{-17}	$12.09^{+0.46}_{-0.66}$	< 0.71
#1 sl4	$11.12^{+0.13}_{-0.19}$	$0.26^{+0.06}_{-0.07}$	71^{+11}_{-12}	$12.29^{+0.37}_{-0.61}$	$0.45^{+0.22}_{-0.24}$
#1 sl5	$11.23^{+0.10}_{-0.14}$	$0.30^{+0.06}_{-0.05}$	31 ± 13	$12.11^{+0.44}_{-0.62}$	< 0.73
intrinsic	11.19	0.33	$\sim 27-51$	12.99 ($c = 3.5$)	0.40
#2 sl1	$11.49^{+0.15}_{-0.14}$	$0.25^{+0.08}_{-0.05}$	< 22	$12.39^{+0.22}_{-0.44}$	$0.45^{+0.14}_{-0.20}$
#2 sl2	$11.34^{+0.19}_{-0.15}$	$0.17^{+0.05}_{-0.04}$	16^{+5}_{-4}	$12.83^{+0.14}_{-0.27}$	$0.68^{+0.10}_{-0.17}$
#2 sl3	$11.24^{+0.15}_{-0.16}$	$0.15^{+0.05}_{-0.03}$	18^{+3}_{-2}	$12.87^{+0.10}_{-0.14}$	$0.75^{+0.07}_{-0.11}$
#2 sl4	$11.45^{+0.17}_{-0.15}$	$0.19^{+0.06}_{-0.04}$	< 40	$12.54^{+0.22}_{-0.43}$	$0.54^{+0.13}_{-0.23}$
#2 sl5	11.34 ± 0.11	0.20 ± 0.04	< 12	$12.73^{+0.09}_{-0.12}$	$0.65^{+0.07}_{-0.09}$
intrinsic	11.27	0.16	$\sim 18-50$	12.79 ($c = 3.1$)	0.51
#3 sl1	$11.59^{+0.10}_{-0.11}$	$0.24^{+0.06}_{-0.04}$	25 ± 6	$12.17^{+0.33}_{-0.57}$	$0.30^{+0.14}_{-0.16}$
#3 sl2	$11.64^{+0.04}_{-0.05}$	$0.30^{+0.05}_{-0.03}$	< 25	$11.47^{+0.38}_{-0.31}$	< 0.30
#3 sl3	$11.57^{+0.10}_{-0.12}$	$0.25^{+0.05}_{-0.04}$	24^{+6}_{-12}	$12.34^{+0.25}_{-0.45}$	$0.36^{+0.13}_{-0.16}$
#3 sl4	11.58 ± 0.11	$0.23^{+0.05}_{-0.04}$	19 ± 6	$12.33^{+0.28}_{-0.51}$	$0.35^{+0.14}_{-0.17}$
#3 sl5	$11.59^{+0.09}_{-0.11}$	$0.27^{+0.06}_{-0.05}$	< 32	$12.22^{+0.29}_{-0.51}$	$0.31^{+0.13}_{-0.15}$
intrinsic	11.40	0.19	$\sim 28-42$	12.70 ($c = 3.1$)	0.50
#4 sl1	$10.92^{+0.05}_{-0.08}$	$0.27^{+0.09}_{-0.05}$	55 ± 5	< 11.56	$0.23^{+0.07}_{-0.03}$
#4 sl2	$11.03^{+0.21}_{-0.24}$	< 0.12	32 ± 8	$12.42^{+0.22}_{-0.45}$	$0.57^{+0.17}_{-0.25}$
#4 sl3	$11.11^{+0.13}_{-0.15}$	0.19 ± 0.05	40 ± 10	$12.19^{+0.34}_{-0.56}$	$0.42^{+0.18}_{-0.20}$
#4 sl4	11.02 ± 0.11	0.12 ± 0.04	34^{+5}_{-6}	$11.96^{+0.19}_{-0.29}$	$0.42^{+0.11}_{-0.14}$
#4 sl5	$10.98^{+0.26}_{-0.23}$	$0.08^{+0.07}_{-0.05}$	37^{+7}_{-8}	$12.82^{+0.13}_{-0.31}$	$0.69^{+0.12}_{-0.22}$
intrinsic	11.00	0.17	$\sim 16-40$	12.60 (2.4)	0.58
#5 sl1	$11.22^{+0.15}_{-0.12}$	0.18 ± 0.04	32^{+3}_{-4}	$12.53^{+0.12}_{-0.26}$	$0.56^{+0.09}_{-0.16}$

#5 sl2	11.61 ± 0.02	$0.03^{+0.01}_{-0.00}$	44 ± 3	$11.30^{+0.29}_{-0.19}$	< 0.61
#5 sl3	$11.42^{+0.01}_{-0.03}$	0.16 ± 0.01	31 ± 3	< 11.72	< 0.25
#5 sl4	$11.41^{+0.07}_{-0.08}$	$0.21^{+0.04}_{-0.02}$	29 ± 3	$12.03^{+0.23}_{-0.28}$	$0.29^{+0.11}_{-0.09}$
#5 sl5	$11.14^{+0.07}_{-0.08}$	$0.25^{+0.06}_{-0.04}$	38 ± 3	$12.43^{+0.08}_{-0.09}$	$0.56^{+0.06}_{-0.07}$
intrinsic	11.24	0.19	$\sim 27 - 53$	12.43 ($c = 6.0$)	0.42
#6 sl1	$10.84^{+0.17}_{-0.20}$	$0.17^{+0.05}_{-0.07}$	58 ± 8	$12.12^{+0.19}_{-0.31}$	$0.66^{+0.13}_{-0.18}$
#6 sl2	10.89 ± 0.17	$0.19^{+0.06}_{-0.05}$	46^{+11}_{-13}	$12.24^{+0.21}_{-0.36}$	$0.66^{+0.13}_{-0.20}$
#6 sl3	$11.04^{+0.10}_{-0.12}$	$0.25^{+0.06}_{-0.05}$	40^{+10}_{-11}	$11.67^{+0.31}_{-0.40}$	$0.39^{+0.16}_{-0.15}$
#6 sl4	$11.20^{+0.06}_{-0.19}$	< 0.03	69 ± 7	< 12.06	$0.27^{+0.22}_{-0.10}$
#6 sl5	$11.13^{+0.09}_{-0.11}$	$0.31^{+0.12}_{-0.07}$	53^{+13}_{-14}	$11.45^{+0.38}_{-0.31}$	$0.27^{+0.16}_{-0.09}$
intrinsic	10.92	0.20	$\sim 11 - 32$	12.22 ($c = 6.4$)	0.47
#7 sl1	$10.90^{+0.16}_{-0.19}$	0.16 ± 0.05	38 ± 5	$12.28^{+0.15}_{-0.22}$	$0.63^{+0.12}_{-0.16}$
#7 sl2	$11.09^{+0.20}_{-0.27}$	< 0.18	57^{+7}_{-8}	$12.13^{+0.28}_{-0.53}$	$0.49^{+0.23}_{-0.25}$
#7 sl3	11.05 ± 0.04	> 0.31	34^{+6}_{-7}	< 11.66	$0.19^{+0.07}_{-0.04}$
#7 sl4	$11.09^{+0.06}_{-0.07}$	0.38 ± 0.07	< 16	$11.47^{+0.27}_{-0.26}$	$0.24^{+0.11}_{-0.07}$
#7 sl5	$11.06^{+0.07}_{-0.12}$	0.23 ± 0.06	30 ± 10	$11.59^{+0.35}_{-0.38}$	$0.31^{+0.17}_{-0.13}$
intrinsic	11.00	0.22	$\sim 14 - 33$	12.25 ($c = 6.2$)	0.46

4.3.9 Appendix C – Approaches to dealing with kinematic asymmetries

Here we show examples of our two approaches to dealing with asymmetric kinematics as discussed in Section 4.3.4.3, 'symmetrization' and 'equilibration'.

Symmetrization In Figure 4.23 we show the original one-dimensional kinematic extractions for galaxy #5, sightline 2 (red) and the corresponding 'symmetrized' profiles (blue). To symmetrize the one-dimensional extractions, the profiles are rotated (for the velocity) or folded (for the dispersion) around the kinematic center, interpolated onto a common grid, and averaged, with uncertainties added in quadrature. In the example shown the symmetrization helps to make the rotation velocity regular, and to smooth out the noise spike at a projected distance of $\sim 1''$. Otherwise, the S/N is not affected.

Equilibration In Figure 4.24 we show the intrinsic convolved and projected two-dimensional kinematics for galaxy #3, sightline 2 before (left) and after (right) removing vertical and radial motions. Clearly, this leads to more symmetric and smoother velocity and velocity dispersion maps, emphasizing the impact of these non-circular motions. In Figure 4.25 we compare the corresponding one-dimensional kinematic extractions after creating mock data cubes for the processed galaxy with the original extractions. Note that for this exercise we use the identical noise cube in order to ensure a consistent comparison. In good agreement with the intrinsic two-dimensional kinematics shown in Figure 4.24,

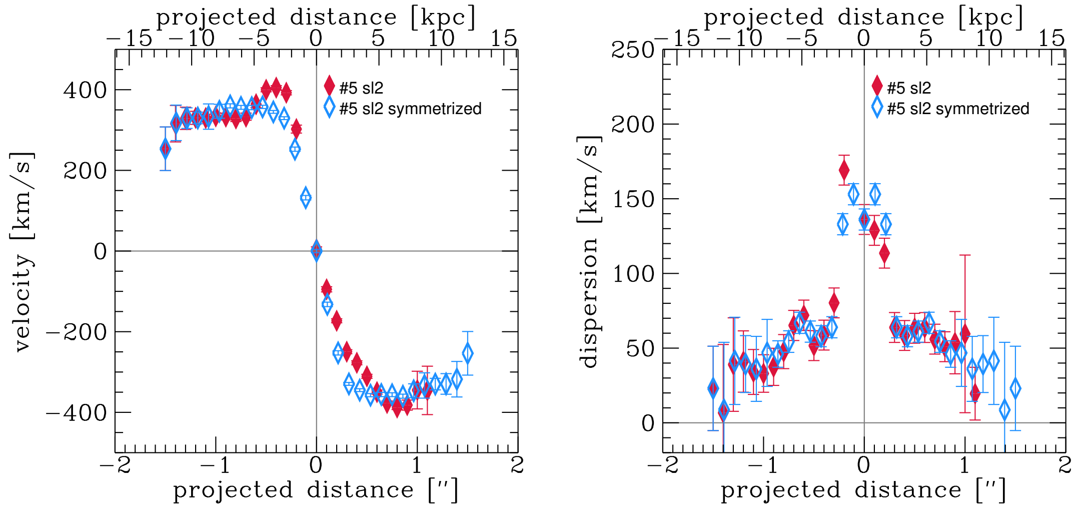

Figure 4.23: *One-dimensional kinematic extractions from the mock data cubes before (red) and after (blue) 'symmetrization' for galaxy #5, sightline 2. The kinematics become symmetric, and features such as the noise spike at projected distance* $\sim 1''$ *get smoothed out.*

the fall-off on the receding side of the rotation curve is less extreme after equilibration, while the velocity dispersion along the kinematic major axis is not much affected. The more regular behaviour of the kinematics facilitates the line fitting and results in higher S/N on average ($\Delta S/N \approx 0.07$ for the full two-dimensional map, with $\Delta S/N \sim 10$ in the center) such that the uncertainties on the extracted kinematics are smaller, and extractions out to larger distances from the center are possible.

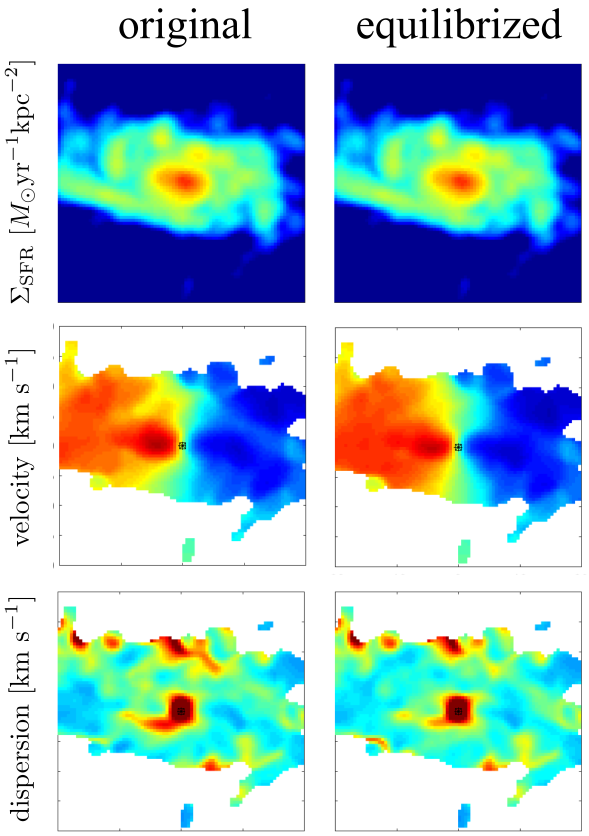

Figure 4.24: *Intrinsic projected SFR surface density, velocity, and velocity dispersion maps before (left) and after (right) removing velocity components vertical and radial with respect to the disk plane ('equilibrized') for galaxy #3, sightline 2. The projections correspond to an inclination of* $i = 60°$*. The panels show 40 kpc × 40 kpc in projection, and the color scale shows [-400; 400] km* s^{-1} *for velocity, and [0; 150] km* s^{-1} *for velocity dispersion. Both the velocity and velocity dispersion fields become smoother and more regular with the vertical motions removed.*

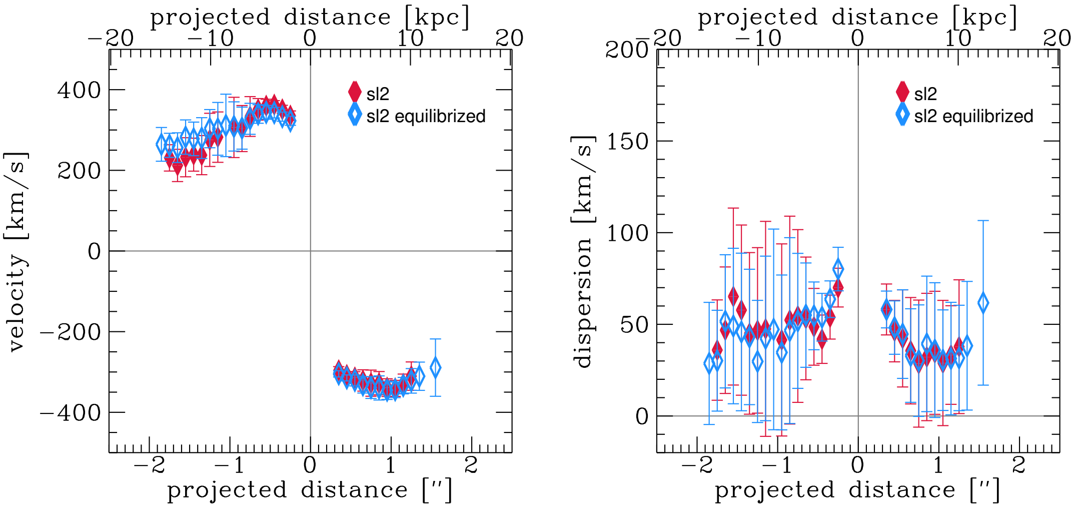

Figure 4.25: *One-dimensional kinematic extractions from the mock data cubes before (red) and after (blue) removing velocity components vertical to the disk plane for galaxy #3, sightline 2. The rotation curve becomes less asymmetric, and through increased S/N extractions at larger galactocentric distances are possible. The velocity dispersion is less affected.*

Chapter 5

Conclusions

This thesis presents the kinematics of star-forming galaxies (SFGs) during the peak epoch of cosmic star formation rate density and shortly after, at $0.5 < z < 2.5$, both in a population-averaged sense and with greater detail for individual systems. This is done based on the highest-quality and deepest data currently available from the ground, taken with integral-field instruments such as SINFONI and particularly the efficient multi-IFU KMOS, but also longslit observations and radio interferometry.

Together, the presented work tackles important questions in galaxy evolution that can now be addressed for the first time to such an extent. In the study of the Tully-Fisher relation (Chapter 2) we investigate how the average dynamical support of star-forming galaxies is distributed between gas, stars, and dark matter at different cosmic times, and how this fits into a cosmological context. In Chapter 3 we quantify the redshift evolution of the velocity dispersion, which encompasses the turbulent, non-circular motions in galaxies. These turbulent motions create a pressure term counter-acting part of the gravitational potential, and are therefore crucial in order to trace back the dynamical potential the galaxy is embedded in. In Chapter 4 we present the deepest and most detailed observations currently available of high$-z$ galaxy kinematics out to ~ 3 effective radii and for one object in two different gas phases (Sections 4.1 and 4.2). This work reveals very low central dark matter fractions in these massive SFGs, in tension with standard NFW dark matter halo models. To investigate this tension in more detail, we analyze in Section 4.3 the kinematics of corresponding simulated galaxies from the state-of-the-art IllustrisTNG50 simulation, and identify several differences between the simulated and observed objects, suggesting that the observed galaxies have no counterpart in the simulation. The simulated objects appear to be out of equilibrium, have lower gas masses and gas velocity dispersions, but much higher central concentrations of dark matter.

Coming back to the questions posed in Section 1.4, we can now conclude:

- *Do kinematic galaxy scaling relations known from the local Universe exist at $z \sim 1-2$? If so, how do they compare, and what drives their evolution?* Yes, kinematic scaling relations such as the Tully-Fisher relation exist already at $z \sim 2.3$. Its evolution with cosmic time can be explained through the interplay of baryonic and dark matter on galaxy scales, and through the conversion of gas into stars. To accurately recover kinematic scaling relations, it is important to take into account the contribution from turbulent motions, which steadily increase with increasing redshift, to the total dynamical support.

- *What dominates the dynamical support of SFGs over cosmic time, and why?* The presented work unambiguously shows that on galaxy scales the average, dominant source of dynamical support changes with redshift: for massive, high$-z$ galaxies, the potential created through gas and stars dominates over the contribution from dark matter, while for typical SFGs in the local Universe dark matter dominates.
  We emphasize, however, that this is not determined through a simple redshift-dependence, but in detail depends also on other factors such as the galaxy mass. Reflecting observations in the local Universe, a good proxy for the central dark matter fraction also of high$-z$ SGFs is the baryonic surface density, as we will show in future work.

- *What is the interplay of baryonic and dark matter on galaxy scales, and is our theoretical understanding of the structure evolution of dark matter reconcilable with observations?* The high-quality observations discussed in this thesis reveal a tension with predictions from theoretical models, suggesting the the interplay of baryonic and dark matter on galaxy scales is more complex than currently captured in simulations. While many present-day properties of simulated galaxies correspond well to observations, it is possible that details of, for instance, feedback implementations are responsible for the mismatch at higher redshift.
  During the peak epoch of cosmic star formation rapid baryonic assembly, high gas fractions, and high star formation rates define galactic evolution. More numerous and even more detailed observational studies will help to pin down the physical processes in need of refinement in cosmological simulations.

Future studies with next-generation instruments such as ERIS (the Enhanced Resolution Imager and Spectrograph) in adaptive-optics mode on the VLT, or HARMONI (the High Angular Resolution Monolithic Optical and Near-infrared Integral field spectrograph) on the *Extremely Large Telescope* (ELT) will push beyond currently available spatial and spectral resolutions, enabling systematic and statistic studies of detailed galaxy kinematics. Multi-phase studies will be crucial in pinning down baryonic conversion and feedback processes at high$-z$ to guide sub-grid models needed in cosmological simulations. Subsequent comparisons between next-generation simulations and observations are warranted to ensure that we can make progress in the field of galaxy evolution in the early Universe.

Danksagung

I am deeply grateful to my advisor Reinhard Genzel for his mentorship, purposefulness, sincerity, and generosity. As a young scientist I was privileged to become part of the MPE IR research group that, under his leadership, is continuously striving for scientific excellence. His knowledge and dedication to science have inspired me throughout the PhD. Despite his many responsibilities his door was always open, and he was never too busy to sit down with me and go over my questions. I am also very thankful for his hospitality in Munich and Berkeley.

I am deeply grateful to Natascha Förster Schreiber who is an unmatched role model for accuracy and thoroughness in science. With her usual consideration, patience, and vast knowledge she helped me make the transition from simulations to observational science. I am also grateful for those occasions during the PhD when she told me to take a day off, and not to worry so much.

My thanks go to many former and current members of the IR group who supported me in various ways during my PhD. I am very grateful to Linda Tacconi for encouraging me to aim high. Her experience and foresight made many challenges easier for me. I thank Eva Wuyts for guiding me during my first months. I thank my former office mate Philipp Lang for answering my questions and ordering pizza with me during late-night office shifts. I thank Emily Wisnioski who taught me about observing with KMOS, for her support, and for becoming a good friend. I thank Taro Shimizu for his tremendous help with all kinds of coding problems, and for his friendship. I thank Stefan Gillessen for encouraging me to apply to the IR group. My thanks go to Michi, Sirio, and Taro for chess and Go, to Alex for birthday beers, to Dieter and the lunch and coffee crew, and to Lothar for the morning chats.

I thank Thorsten for his friendship and advice since many years. I thank Shy for his support. I thank Amiel for his friendship and his hospitality in Tel Aviv and New York.

Von ganzem Herzen danke ich meinen Eltern Dagmar und Karl, und meinen Geschwistern Rebekka und Benedikt. Liebe Eltern, ohne eure Förderung, Großzügigkeit und fortwährende Unterstützung hätte ich es nicht so weit schaffen können. Danke, dass ihr so viel in mich investiert habt!

Ich empfinde große Dankbarkeit gegenüber meiner Patin Hanna. Ihre Begeis-

terung für die Naturwissenschaften hat in mir den Wunsch geweckt, meinen jetzigen Weg einzuschlagen.

Ich danke meiner Patin Elisabeth für ihre große Unterstützung in persönlichen Belangen, und dass sie meinen Weg bis zum Beginn der Doktorarbeit begleitet hat.

Ich danke außerdem meinen Freunden hier in München, die mich stetig unterstützt haben, und deren Annahme mir hier eine zweite Heimat geschaffen hat – Sina und Judith, Johannes, Hanna, Andrea, Kathi, Lukas und Hannes. Danke!

Bibliography

K. N. Abazajian et al., *The First Data Release of the Sloan Digital Sky Survey*, AJ, 126, 2081–2086 (2003).

K. N. Abazajian et al., *The Seventh Data Release of the Sloan Digital Sky Survey*, ApJS, 182, 543–558 (2009).

K. L. Adelberger et al., *The Spatial Clustering of Star-forming Galaxies at Redshifts* $1.4 \lesssim z \lesssim 3.5$, ApJ, 619(2), 697–713 (2005).

O. Agertz, R. Teyssier, & B. Moore, *Disc formation and the origin of clumpy galaxies at high redshift*, MNRAS, 397, L64–L68 (2009).

O. Agertz, R. Teyssier, & B. Moore, *The formation of disc galaxies in a* Λ*CDM universe*, MNRAS, 410, 1391–1408 (2011).

O. Agertz et al., *Large-scale galactic turbulence: can self-gravity drive the observed HI velocity dispersions?*, MNRAS, 392, 294–308 (2009).

D. S. Aguado et al., *The Fifteenth Data Release of the Sloan Digital Sky Surveys: First Release of MaNGA-derived Quantities, Data Visualization Tools, and Stellar Library*, ApJS, 240, 23 (2019).

L. Y. Alcorn et al., *ZFIRE: The Kinematics of Star-forming Galaxies as a Function of Environment at* $z \sim 2$, ApJL, 825, L2 (2016).

D. Anglés-Alcázar et al., *Cosmological Zoom Simulations of* $z = 2$ *Galaxies: The Impact of Galactic Outflows*, ApJ, 782, 84 (2014).

R. E. Angulo et al., *Scaling relations for galaxy clusters in the Millennium-XXL simulation*, MNRAS, 426, 2046–2062 (2012).

E. Athanassoula & J. A. Sellwood, *Bi-symmetric instabilities of the Kuz'min/Toomre disc.*, MNRAS, 221, 213–232 (1986).

M. Aumer & J. Binney, *The structural evolution of galaxies with both thin and thick discs*, MNRAS, 470, 2113–2132 (2017).

M. AUMER, J. BINNEY, & R. SCHÖNRICH, *Age-velocity dispersion relations and heating histories in disc galaxies*, MNRAS, 462, 1697–1713 (2016).

M. AUMER et al., *The Structure of Gravitationally Unstable Gas-rich Disk Galaxies*, ApJ, 719, 1230–1243 (2010).

M. AUMER et al., *Towards a more realistic population of bright spiral galaxies in cosmological simulations*, MNRAS, 434, 3142–3164 (2013).

V. AVILA-REESE et al., *On the Baryonic, Stellar, and Luminous Scaling Relations of Disk Galaxies*, AJ, 136, 1340–1360 (2008).

G. BARRO et al., *Sub-kiloparsec ALMA Imaging of Compact Star-forming Galaxies at* $z \sim 2.5$*: Revealing the Formation of Dense Galactic Cores in the Progenitors of Compact Quiescent Galaxies*, ApJ, 827, L32 (2016).

V. BAUMGARTNER & D. BREITSCHWERDT, *Superbubble evolution in disk galaxies. I. Study of blow-out by analytical models*, A&A, 557, A140 (2013).

K. G. BEGEMAN, A. H. BROEILS, & R. H. SANDERS, *Extended rotation curves of spiral galaxies - Dark haloes and modified dynamics*, MNRAS, 249, 523–537 (1991).

M. BEHRENDT, A. BURKERT, & M. SCHARTMANN, *Structure formation in gas-rich galactic discs with finite thickness: from discs to rings*, MNRAS, 448, 1007–1019 (2015).

P. S. BEHROOZI et al., *Using Cumulative Number Densities to Compare Galaxies across Cosmic Time*, ApJL, 777, L10 (2013).

E. F. BELL & R. S. DE JONG, *Stellar Mass-to-Light Ratios and the Tully-Fisher Relation*, ApJ, 550, 212–229 (2001).

E. F. BELL et al., *What Turns Galaxies Off? The Different Morphologies of Star-forming and Quiescent Galaxies since* $z \sim 2$ *from CANDELS*, ApJ, 753, 167 (2012).

S. BELLI, A. CONTURSI, & R. I. DAVIES, *Flame : A flexible data reduction pipeline for near-infrared and optical spectroscopy*, MNRAS, 478(2), 2097–2112 (2018).

C. L. BENNETT et al., *Four-Year COBE DMR Cosmic Microwave Background Observations: Maps and Basic Results*, ApJ, 464, L1 (1996).

C. L. BENNETT et al., *First-Year Wilkinson Microwave Anisotropy Probe (WMAP) Observations: Preliminary Maps and Basic Results*, ApJS, 148, 1–27 (2003).

M. Béthermin et al., *Evolution of the dust emission of massive galaxies up to $z = 4$ and constraints on their dominant mode of star formation*, A&A, 573, A113 (2015).

F. Bigiel & L. Blitz, *A Universal Neutral Gas Profile for nearby Disk Galaxies*, ApJ, 756, 183 (2012).

J. Binney & S. Tremaine, *Galactic Dynamics: Second Edition*, Princeton University Press (2008).

J. Bland-Hawthorn & O. Gerhard, *The Galaxy in Context: Structural, Kinematic, and Integrated Properties*, ARAA, 54, 529–596 (2016).

M. R. Blanton & J. Moustakas, *Physical Properties and Environments of Nearby Galaxies*, ARAA, 47, 159–210 (2009).

G. R. Blumenthal et al., *Contraction of Dark Matter Galactic Halos Due to Baryonic Infall*, ApJ, 301, 27 (1986).

A. D. Bolatto et al., *The EDGE-CALIFA Survey: Interferometric Observations of 126 Galaxies with CARMA*, ApJ, 846, 159 (2017).

H. Bonnet et al., *First light of SINFONI at the VLT*, The Messenger, 117, 17–24 (2004).

R. Bottema, *Simulations of normal spiral galaxies*, MNRAS, 344, 358–384 (2003).

N. Bouché et al., *The Impact of Cold Gas Accretion Above a Mass Floor on Galaxy Scaling Relations*, ApJ, 718, 1001–1018 (2010).

F. Boulanger & F. Viallefond, *Observational study of the spiral gaalxy NGC 6946. I. HI and radio continuum observations.*, A&A, 266, 37 (1992).

J. Bovy et al., *The Spatial Structure of Mono-abundance Sub-populations of the Milky Way Disk*, ApJ, 753, 148 (2012).

J. Bovy et al., *The Stellar Population Structure of the Galactic Disk*, ApJ, 823, 30 (2016).

J. D. Bradford, M. C. Geha, & F. C. van den Bosch, *A Slippery Slope: Systematic Uncertainties in the Line Width Baryonic Tully-Fisher Relation*, ApJ, 832, 11 (2016).

G. B. Brammer et al., *The Number Density and Mass Density of Star-forming and Quiescent Galaxies at* $0.4 \leq z \leq 2.2$, ApJ, 739, 24 (2011).

G. B. Brammer et al., *3D-HST: A Wide-field Grism Spectroscopic Survey with the Hubble Space Telescope*, ApJS, 200, 13 (2012).

J. Brinchmann et al., *The physical properties of star-forming galaxies in the low-redshift Universe*, MNRAS, 351(4), 1151–1179 (2004).

A. H. Broeils & M.-H. Rhee, *Short 21-cm WSRT observations of spiral and irregular galaxies. HI properties.*, A&A, 324, 877–887 (1997).

C. B. Brook et al., *Hierarchical formation of bulgeless galaxies - II. Redistribution of angular momentum via galactic fountains*, MNRAS, 419, 771–779 (2012a).

C. B. Brook et al., *MaGICC discs: matching observed galaxy relationships over a wide stellar mass range*, MNRAS, 424, 1275–1283 (2012b).

V. A. Bruce et al., *The bulge-disc decomposed evolution of massive galaxies at* $1 < z < 3$ *in CANDELS*, MNRAS, 444, 1001–1033 (2014a).

V. A. Bruce et al., *The decomposed bulge and disc size-mass relations of massive galaxies at* $1 < z < 3$ *in CANDELS*, MNRAS, 444(2), 1660–1673 (2014b).

C. M. Brunt, M. H. Heyer, & M. M. Mac Low, *Turbulent driving scales in molecular clouds*, A&A, 504, 883–890 (2009).

G. Bruzual & S. Charlot, *Stellar population synthesis at the resolution of 2003*, MNRAS, 344, 1000–1028 (2003).

J. J. Bryant et al., *The SAMI Galaxy Survey: instrument specification and target selection*, MNRAS, 447(3), 2857–2879 (2015).

J. S. Bullock et al., *Strong Evolution in the Luminosity-Velocity Relation at* $z \gtrsim 1$*?*, ApJ, 550, 21–25 (2001).

A. Burkert, *The Structure of Dark Matter Halos in Dwarf Galaxies*, ApJ, 447, L25–L28 (1995).

A. Burkert, J. W. Truran, & G. Hensler, *The Collapse of Our Galaxy and the Formation of the Galactic Disk*, ApJ, 391, 651 (1992).

A. Burkert et al., *High-redshift Star-forming Galaxies: Angular Momentum and Baryon Fraction, Turbulent Pressure Effects, and the Origin of Turbulence*, ApJ, 725, 2324–2332 (2010).

A. Burkert et al., *The Angular Momentum Distribution and Baryon Content of Star-forming Galaxies at* $z \sim 1-3$, ApJ, 826, 214 (2016).

P. Buschkamp et al., *LUCI in the sky: performance and lessons learned in the first two years of near-infrared multi-object spectroscopy at the LBT*, in: *Ground-based and Airborne Instrumentation for Astronomy IV*, vol. 8446 of *Proceedings of the SPIE*, page 84465L (2012).

M. Cacciato, A. Dekel, & S. Genel, *Evolution of violent gravitational disc instability in galaxies: late stabilization by transition from gas to stellar dominance*, MNRAS, 421, 818–831 (2012).

A. Caldú-Primo & A. Schruba, *Molecular Gas Velocity Dispersions in the Andromeda Galaxy*, AJ, 151, 34 (2016).

A. Caldú-Primo et al., *A High-dispersion Molecular Gas Component in Nearby Galaxies*, AJ, 146, 150 (2013).

D. Calzetti et al., *The Dust Content and Opacity of Actively Star-forming Galaxies*, ApJ, 533, 682–695 (2000).

M. Cappellari, *Structure and Kinematics of Early-Type Galaxies from Integral Field Spectroscopy*, ARAA, 54, 597–665 (2016).

M. Cappellari et al., *The ATLAS^{3D} project - XV. Benchmark for early-type galaxies scaling relations from 260 dynamical models: mass-to-light ratio, dark matter, Fundamental Plane and Mass Plane*, MNRAS, 432, 1709–1741 (2013).

C. Carignan et al., *The Extended H I Rotation Curve and Mass Distribution of M31*, ApJ, 641, L109–L112 (2006).

C. L. Carilli & F. Walter, *Cool Gas in High-Redshift Galaxies*, ARAA, 51, 105–161 (2013).

C. M. Carollo et al., *Newly Quenched Galaxies as the Cause for the Apparent Evolution in Average Size of the Population*, ApJ, 773, 112 (2013).

R. J. Carroll et al., *Measurement Error in Nonlinear Models: A Modern Perspective*, Mongraphs on Statistics and Applied Probability 105, Chapman and Hall/CRC, second ed. (2006).

S. Casertano & J. H. van Gorkom, *Declining Rotation Curves: The End of a Conspiracy?*, AJ, 101, 1231 (1991).

B. Catinella, R. Giovanelli, & M. P. Haynes, *Template Rotation Curves for Disk Galaxies*, ApJ, 640, 751–761 (2006).

D. Ceverino, A. Dekel, & F. Bournaud, *High-redshift clumpy discs and bulges in cosmological simulations*, MNRAS, 404, 2151–2169 (2010).

G. CHABRIER, *Galactic Stellar and Substellar Initial Mass Function*, Publications of the Astronomical Society of the Pacific, 115, 763–795 (2003).

C.-C. CHEN et al., *A Spatially Resolved Study of Cold Dust, Molecular Gas, H*II *Regions, and Stars in the z = 2.12 Submillimeter Galaxy ALESS67.1*, ApJ, 846, 108 (2017).

F. CIVANO et al., *The Chandra COSMOS Survey. III. Optical and Infrared Identification of X-Ray Point Sources*, ApJS, 201, 30 (2012).

S. COLE et al., *The 2dF Galaxy Redshift Survey: power-spectrum analysis of the final data set and cosmological implications*, MNRAS, 362, 505–534 (2005).

M. COLLESS et al., *The 2dF Galaxy Redshift Survey: spectra and redshifts*, MNRAS, 328, 1039–1063 (2001).

F. COMBES et al., *Galaxy evolution and star formation efficiency at* $0.2 < z < 0.6$, A&A, 528, A124 (2011).

C. J. CONSELICE et al., *Evolution of the Near-Infrared Tully-Fisher Relation: Constraints on the Relationship between the Stellar and Total Masses of Disk Galaxies since* $z \sim 1$, ApJ, 628, 160–168 (2005).

T. CONTINI et al., *MASSIV: Mass Assemby Survey with SINFONI in VVDS. I. Survey description and global properties of the* $0.9 < z < 1.8$ *galaxy sample*, A&A, 539, A91 (2012).

T. CONTINI et al., *Deep MUSE observations in the HDFS. Morpho-kinematics of distant star-forming galaxies down to* $10^8 M_\odot$, A&A, 591, A49 (2016).

L. CORTESE, B. CATINELLA, & S. JANOWIECKI, *ALMA Shows that Gas Reservoirs of Star-forming Disks over the Past 3 Billion Years Are Not Predominantly Molecular*, ApJL, 848(1), L7 (2017).

S. COURTEAU, *Optical Rotation Curves and Linewidths for Tully-Fisher Applications*, AJ, 114, 2402 (1997).

S. COURTEAU & A. A. DUTTON, *On the Global Mass Distribution in Disk Galaxies*, ApJL, 801, L20 (2015).

S. COURTEAU & H.-W. RIX, *Maximal Disks and the Tully-Fisher Relation*, ApJ, 513, 561–571 (1999).

S. COURTEAU et al., *Scaling Relations of Spiral Galaxies*, ApJ, 671, 203–225 (2007).

S. COURTEAU et al., *Galaxy masses*, Reviews of Modern Physics, 86, 47–119 (2014).

M. D. COVINGTON et al., *Evolution of the Stellar Mass Tully-Fisher Relation in Disk Galaxy Merger Simulations*, ApJ, 710, 279–288 (2010).

G. CRESCI et al., *The SINS Survey: Modeling the Dynamics of $z \sim 2$ Galaxies and the High-z Tully-Fisher Relation*, ApJ, 697, 115–132 (2009).

E. DADDI et al., *Multiwavelength Study of Massive Galaxies at $z \sim 2$. I. Star Formation and Galaxy Growth*, ApJ, 670(1), 156–172 (2007).

E. DADDI et al., *Very High Gas Fractions and Extended Gas Reservoirs in $z = 1.5$ Disk Galaxies*, ApJ, 713, 686–707 (2010).

J. J. DALCANTON & R. A. BERNSTEIN, *A Structural and Dynamical Study of Late-Type, Edge-on Galaxies. II. Vertical Color Gradients and the Detection of Ubiquitous Thick Disks*, AJ, 124, 1328–1359 (2002).

J. J. DALCANTON, D. N. SPERGEL, & F. J. SUMMERS, *The Formation of Disk Galaxies*, ApJ, 482, 659–676 (1997).

J. J. DALCANTON & A. M. STILP, *Pressure Support in Galaxy Disks: Impact on Rotation Curves and Dark Matter Density Profiles*, ApJ, 721, 547–561 (2010).

M. DANOVICH et al., *Four phases of angular-momentum buildup in high-z galaxies: from cosmic-web streams through an extended ring to disc and bulge*, MNRAS, 449, 2087–2111 (2015).

R. DAVÉ, K. FINLATOR, & B. D. OPPENHEIMER, *An analytic model for the evolution of the stellar, gas and metal content of galaxies*, MNRAS, 421, 98–107 (2012).

R. I. DAVIES et al., *Stellar and Molecular Gas Kinematics Of NGC 1097: Inflow Driven by a Nuclear Spiral*, ApJ, 702, 114–128 (2009).

R. I. DAVIES et al., *How Well Can We Measure the Intrinsic Velocity Dispersion of Distant Disk Galaxies?*, ApJ, 741, 69 (2011).

R. I. DAVIES et al., *The Software Package for Astronomical Reductions with KMOS: SPARK*, A&A, 558, A56 (2013).

M. DAVIS et al., *Science Objectives and Early Results of the DEEP2 Redshift Survey*, in: P. GUHATHAKURTA, ed., *Discoveries and Research Prospects from 6- to 10-Meter-Class Telescopes II*, vol. 4834 of *Society of Photo-Optical Instrumentation Engineers (SPIE) Conference Series*, pages 161–172 (2003).

W. J. G. DE BLOK et al., *High-Resolution Rotation Curves and Galaxy Mass Models from THINGS*, AJ, 136, 2648-2719 (2008).

A. Dekel & A. Burkert, *Wet disc contraction to galactic blue nuggets and quenching to red nuggets*, MNRAS, 438, 1870–1879 (2014).

A. Dekel, R. Sari, & D. Ceverino, *Formation of Massive Galaxies at High Redshift: Cold Streams, Clumpy Disks, and Compact Spheroids*, ApJ, 703, 785–801 (2009).

A. Dekel et al., *Cold streams in early massive hot haloes as the main mode of galaxy formation*, Nature, 457, 451–454 (2009).

E. M. Di Teodoro, F. Fraternali, & S. H. Miller, *Flat rotation curves and low velocity dispersions in KMOS star-forming galaxies at* $z \sim 1$, A&A, 594, A77 (2016).

S. Dib, E. Bell, & A. Burkert, *The Supernova Rate–Velocity Dispersion Relation in the Interstellar Medium*, ApJ, 638, 797–810 (2006).

R. H. Dicke et al., *Cosmic Black-Body Radiation.*, ApJ, 142, 414–419 (1965).

J. M. Dickey, M. M. Hanson, & G. Helou, *NGC 1058: Gas Motions in an Extended, Quiescent Spiral Disk*, ApJ, 352, 522 (1990).

C. Druard et al., *The IRAM M 33 CO(2-1) survey. A complete census of molecular gas out to 7 kpc*, A&A, 567, A118 (2014).

A. R. Duffy et al., *Impact of baryon physics on dark matter structures: a detailed simulation study of halo density profiles*, MNRAS, 405, 2161–2178 (2010).

A. A. Dutton & A. V. Macciò, *Cold dark matter haloes in the Planck era: evolution of structural parameters for Einasto and NFW profiles*, MNRAS, 441, 3359–3374 (2014).

A. A. Dutton et al., *A Revised Model for the Formation of Disk Galaxies: Low Spin and Dark Halo Expansion*, ApJ, 654, 27–52 (2007).

A. A. Dutton et al., *On the evolution of the velocity-mass-size relations of disc-dominated galaxies over the past 10 billion years*, MNRAS, 410, 1660–1676 (2011).

A. A. Dutton et al., *The response of dark matter haloes to elliptical galaxy formation: a new test for quenching scenarios*, MNRAS, 453, 2447–2464 (2015).

A. A. Dutton et al., *NIHAO IX: the role of gas inflows and outflows in driving the contraction and expansion of cold dark matter haloes*, MNRAS, 461, 2658–2675 (2016).

J. Einasto, *On the Construction of a Composite Model for the Galaxy and on the Determination of the System of Galactic Parameters*, Trudy Astrofizicheskogo Instituta Alma-Ata, 5, 87–100 (1965).

F. Eisenhauer et al., *SINFONI - Integral field spectroscopy at 50 milli-arcsecond resolution with the ESO VLT*, in: M. Iye & A. F. M. Moorwood, eds., *Instrument Design and Performance for Optical/Infrared Ground-based Telescopes*, vol. 4841 of *Proceedings of the SPIE*, pages 1548–1561 (2003).

D. J. Eisenstein et al., *Detection of the Baryon Acoustic Peak in the Large-Scale Correlation Function of SDSS Luminous Red Galaxies*, ApJ, 633, 560–574 (2005).

B. G. Elmegreen & A. Burkert, *Accretion-Driven Turbulence and the Transition to Global Instability in Young Galaxy Disks*, ApJ, 712, 294–302 (2010).

B. G. Elmegreen & D. M. Elmegreen, *Observations of Thick Disks in the Hubble Space Telescope Ultra Deep Field*, ApJ, 650, 644–660 (2006).

B. G. Elmegreen & J. Scalo, *Interstellar Turbulence I: Observations and Processes*, ARAA, 42, 211–273 (2004).

D. M. Elmegreen, B. G. Elmegreen, & A. C. Hirst, *Discovery of Face-on Counterparts of Chain Galaxies in the Tadpole Advanced Camera for Surveys Field*, ApJ, 604, L21–L23 (2004).

D. M. Elmegreen, B. G. Elmegreen, & C. M. Sheets, *Chain Galaxies in the Tadpole Advanced Camera for Surveys Field*, ApJ, 603, 74–81 (2004).

D. M. Elmegreen et al., *Galaxy Morphologies in the Hubble Ultra Deep Field: Dominance of Linear Structures at the Detection Limit*, ApJ, 631, 85–100 (2005).

D. M. Elmegreen et al., *Resolved Galaxies in the Hubble Ultra Deep Field: Star Formation in Disks at High Redshift*, ApJ, 658, 763–777 (2007).

B. Epinat, P. Amram, & M. Marcelin, *GHASP: an Hα kinematic survey of 203 spiral and irregular galaxies - VII. Revisiting the analysis of Hα data cubes for 97 galaxies*, MNRAS, 390, 466–504 (2008).

B. Epinat et al., *Integral field spectroscopy with SINFONI of VVDS galaxies. I. Galaxy dynamics and mass assembly at* $1.2 < z < 1.6$, A&A, 504, 789–805 (2009).

B. Epinat et al., *Evidence for strong dynamical evolution in disc galaxies through the last 11 Gyr. GHASP VIII - a local reference sample of rotating disc galaxies for high-redshift studies*, MNRAS, 401, 2113–2147 (2010).

B. EPINAT et al., *MASSIV: Mass Assembly Survey with SINFONI in VVDS. II. Kinematics and close environment classification*, A&A, 539, A92 (2012).

D. K. ERB et al., *The Mass-Metallicity Relation at* $z \gtrsim 2$, ApJ, 644, 813–828 (2006).

A. ESCALA & R. B. LARSON, *Stability of Galactic Gas Disks and the Formation of Massive Clusters*, ApJ, 685, L31 (2008).

S. M. FABER & J. S. GALLAGHER, *Masses and mass-to-light ratios of galaxies*, ARAA, 17, 135–187 (1979).

S. M. FALL & G. EFSTATHIOU, *Formation and rotation of disc galaxies with haloes*, MNRAS, 193, 189–206 (1980).

D. FIACCONI, R. FELDMANN, & L. MAYER, *The Argo simulation - II. The early build-up of the Hubble sequence*, MNRAS, 446, 1957–1972 (2015).

D. B. FISHER et al., *Connecting Clump Sizes in Turbulent Disk Galaxies to Instability Theory*, ApJ, 839, L5 (2017).

D. B. FISHER et al., *Testing Feedback-regulated Star Formation in Gas-rich, Turbulent Disk Galaxies*, ApJ, 870, 46 (2019).

D. J. FIXSEN et al., *The Cosmic Microwave Background Spectrum from the Full COBE FIRAS Data Set*, ApJ, 473, 576 (1996).

H. FLORES et al., *3D spectroscopy with VLT/GIRAFFE. I. The true Tully Fisher relationship at* $z \sim 0.6$, A&A, 455, 107–118 (2006).

D. FOREMAN-MACKEY et al., *emcee: The MCMC Hammer*, Publications of the ASP, 125, 306 (2013).

N. M. FÖRSTER SCHREIBER et al., *A Substantial Population of Red Galaxies at* $z > 2$*: Modeling of the Spectral Energy Distributions of an Extended Sample*, ApJ, 616, 40–62 (2004).

N. M. FÖRSTER SCHREIBER et al., *SINFONI Integral Field Spectroscopy of* $z \sim 2$ *UV-selected Galaxies: Rotation Curves and Dynamical Evolution*, ApJ, 645, 1062–1075 (2006).

N. M. FÖRSTER SCHREIBER et al., *The SINS Survey: SINFONI Integral Field Spectroscopy of* $z \sim 2$ *Star-forming Galaxies*, ApJ, 706, 1364–1428 (2009).

N. M. FÖRSTER SCHREIBER et al., *Constraints on the Assembly and Dynamics of Galaxies. I. Detailed Rest-frame Optical Morphologies on Kiloparsec Scale of* $z \sim 2$ *Star-forming Galaxies*, ApJ, 731, 65 (2011a).

N. M. FÖRSTER SCHREIBER et al., *Constraints on the Assembly and Dynamics of Galaxies. II. Properties of Kiloparsec-scale Clumps in Rest-frame Optical Emission of $z \sim 2$ Star-forming Galaxies*, ApJ, 739, 45 (2011b).

N. M. FÖRSTER SCHREIBER et al., *The SINS/zC-SINF Survey of $z \sim 2$ Galaxy Kinematics: Evidence for Powerful Active Galactic Nucleus-Driven Nuclear Outflows in Massive Star-Forming Galaxies*, ApJ, 787, 38 (2014).

N. M. FÖRSTER SCHREIBER et al., *The SINS/zC-SINF Survey of z ∼ 2 Galaxy Kinematics: SINFONI Adaptive Optics-assisted Data and Kiloparsec-scale Emission-line Properties*, ApJS, 238, 21 (2018).

M. FOSSATI et al., *Galaxy Environment in the 3D-HST Fields: Witnessing the Onset of Satellite Quenching at $z \sim 1-2$*, ApJ, 835, 153 (2017).

K. C. FREEMAN, *On the Disks of Spiral and S0 Galaxies*, ApJ, 160, 811 (1970).

J. FREUNDLICH et al., *PHIBSS2: survey design and z = 0.5 - 0.8 results. Molecular gas reservoirs during the winding-down of star formation*, A&A, 622, A105 (2019).

A. FRIEDMANN, *Über die Krümmung des Raumes*, Zeitschrift für Physik, 10, 377–386 (1922).

J. FU et al., *The effect of star formation on the redshift evolution of interstellar metals, atomic and molecular gas in galaxies*, MNRAS, 424, 2701–2714 (2012).

Y. FUKUI et al., *Molecular and Atomic Gas in the Large Magellanic Cloud. II. Three-dimensional Correlation Between CO and H I*, ApJ, 705, 144–155 (2009).

L. GAO et al., *The redshift dependence of the structure of massive Λ cold dark matter haloes*, MNRAS, 387, 536–544 (2008).

A. GATTO et al., *Modelling the supernova-driven ISM in different environments*, MNRAS, 449, 1057–1075 (2015).

S. GENEL, A. DEKEL, & M. CACCIATO, *On the effect of cosmological inflow on turbulence and instability in galactic discs*, MNRAS, 425, 788–800 (2012).

S. GENEL et al., *Short-lived Star-forming Giant Clumps in Cosmological Simulations of z ≈ 2 Disks*, ApJ, 745, 11 (2012).

S. GENEL et al., *Introducing the Illustris project: the evolution of galaxy populations across cosmic time*, MNRAS, 445, 175–200 (2014).

S. GENEL et al., *Galactic Angular Momentum in the Illustris Simulation: Feedback and the Hubble Sequence*, ApJL, 804, L40 (2015).

R. GENZEL et al., *The rapid formation of a large rotating disk galaxy three billion years after the Big Bang*, Nature, 442, 786–789 (2006).

R. GENZEL et al., *From Rings to Bulges: Evidence for Rapid Secular Galaxy Evolution at $z \sim 2$ from Integral Field Spectroscopy in the SINS Survey*, ApJ, 687, 59-77 (2008).

R. GENZEL et al., *A study of the gas-star formation relation over cosmic time*, MNRAS, 407, 2091–2108 (2010).

R. GENZEL et al., *The SINS Survey of $z \sim 2$ Galaxy Kinematics: Properties of the Giant Star-forming Clumps*, ApJ, 733, 101 (2011).

R. GENZEL et al., *Phibss: Molecular Gas, Extinction, Star Formation, and Kinematics in the z = 1.5 Star-forming Galaxy EGS13011166*, ApJ, 773, 68 (2013).

R. GENZEL et al., *Evidence for Wide-spread Active Galactic Nucleus-driven Outflows in the Most Massive $z \sim 1-2$ Star-forming Galaxies*, ApJ, 796, 7 (2014a).

R. GENZEL et al., *The SINS/zC-SINF Survey of $z \sim 2$ Galaxy Kinematics: Evidence for Gravitational Quenching*, ApJ, 785, 75 (2014b).

R. GENZEL et al., *Combined CO and Dust Scaling Relations of Depletion Time and Molecular Gas Fractions with Cosmic Time, Specific Star-formation Rate, and Stellar Mass*, ApJ, 800, 20 (2015).

R. GENZEL et al., *Strongly baryon-dominated disk galaxies at the peak of galaxy formation ten billion years ago*, Nature, 543, 397–401 (2017).

G. GILMORE & N. REID, *New light on faint stars - III. Galactic structure towards the South Pole and the Galactic thick disc.*, MNRAS, 202, 1025–1047 (1983).

M. GIRARD et al., *KMOS LENsing Survey (KLENS): Morpho-kinematic analysis of star-forming galaxies at $z \sim 2$*, A&A, 613, A72 (2018).

K. GLAZEBROOK, *The Dawes Review 1: Kinematic Studies of Star-Forming Galaxies Across Cosmic Time*, Publications of the Astronomical Society of Australia, 30, e056 (2013).

O. Y. GNEDIN et al., *Dark Matter Halos of Disk Galaxies: Constraints from the Tully-Fisher Relation*, ApJ, 671, 1115–1134 (2007).

A. GNERUCCI et al., *Dynamical properties of AMAZE and LSD galaxies from gas kinematics and the Tully-Fisher relation at $z \sim 3$*, A&A, 528, A88 (2011).

P. GOLDREICH & D. LYNDEN-BELL, *I. Gravitational stability of uniformly rotating disks*, MNRAS, 130, 97 (1965).

F. GOVERNATO et al., *Forming disc galaxies in* Λ*CDM simulations*, MNRAS, 374, 1479–1494 (2007).

R. J. J. GRAND et al., *Vertical disc heating in Milky Way-sized galaxies in a cosmological context*, MNRAS, 459, 199–219 (2016).

A. W. GREEN et al., *High star formation rates as the origin of turbulence in early and modern disk galaxies*, Nature, 467, 684–686 (2010).

A. W. GREEN et al., *DYNAMO - I. A sample of H*α*-luminous galaxies with resolved kinematics*, MNRAS, 437, 1070–1095 (2014).

N. A. GROGIN et al., *CANDELS: The Cosmic Assembly Near-infrared Deep Extragalactic Legacy Survey*, ApJS, 197, 35 (2011).

J. E. GUNN & J. R. GOTT, III, *On the Infall of Matter Into Clusters of Galaxies and Some Effects on Their Evolution*, ApJ, 176, 1 (1972).

Q. GUO & S. D. M. WHITE, *Galaxy growth in the concordance* Λ*CDM cosmology*, MNRAS, 384, 2–10 (2008).

S. GUROVICH et al., *The Slope of the Baryonic Tully-Fisher Relation*, AJ, 140, 663–676 (2010).

F. HAMMER et al., *The Milky Way, an Exceptionally Quiet Galaxy: Implications for the Formation of Spiral Galaxies*, ApJ, 662, 322–334 (2007).

M. HEYER & T. M. DAME, *Molecular Clouds in the Milky Way*, ARAA, 53, 583–629 (2015).

M. H. HEYER & C. M. BRUNT, *The Universality of Turbulence in Galactic Molecular Clouds*, ApJ, 615, L45–L48 (2004).

J. M. HILL, R. F. GREEN, & J. H. SLAGLE, *The Large Binocular Telescope*, in: *Society of Photo-Optical Instrumentation Engineers (SPIE) Conference Series*, vol. 6267 of *Proceedings of the SPIE*, page 62670Y (2006).

G. HINSHAW et al., *Nine-year Wilkinson Microwave Anisotropy Probe (WMAP) Observations: Cosmological Parameter Results*, ApJS, 208, 19 (2013).

F. HOHL, *Numerical Experiments with a Disk of Stars*, ApJ, 168, 343 (1971).

M. HONMA & Y. SOFUE, *On the Keplerian Rotation Curves of Galaxies*, Publications of the Astronomical Society of Japan, 49, 539–545 (1997).

P. F. HOPKINS, E. QUATAERT, & N. MURRAY, *Self-regulated star formation in galaxies via momentum input from massive stars*, MNRAS, 417, 950–973 (2011).

P. F. HOPKINS et al., *Galaxies on FIRE (Feedback In Realistic Environments): stellar feedback explains cosmologically inefficient star formation*, MNRAS, 445, 581–603 (2014).

E. P. HUBBLE, *Extragalactic nebulae.*, ApJ, 64, 321–369 (1926).

C.-L. HUNG et al., *What drives the evolution of gas kinematics in star-forming galaxies?*, MNRAS, 482, 5125–5137 (2019).

R. IANJAMASIMANANA et al., *The Shapes of the H I Velocity Profiles of the THINGS Galaxies*, AJ, 144, 96 (2012).

R. IANJAMASIMANANA et al., *The Radial Variation of H I Velocity Dispersions in Dwarfs and Spirals*, AJ, 150(2), 47 (2015).

A. IMMELI et al., *Gas physics, disk fragmentation, and bulge formation in young galaxies*, A&A, 413, 547–561 (2004a).

A. IMMELI et al., *Subgalactic Clumps at High Redshift: A Fragmentation Origin?*, ApJ, 611, 20–25 (2004b).

S. INOUE et al., *Non-linear violent disc instability with high Toomre's Q in high-redshift clumpy disc galaxies*, MNRAS, 456, 2052–2069 (2016).

P. H. JOHANSSON, T. NAAB, & J. P. OSTRIKER, *Gravitational Heating Helps Make Massive Galaxies Red and Dead*, ApJ, 697, L38–L43 (2009).

P. H. JOHANSSON, T. NAAB, & J. P. OSTRIKER, *Forming Early-type Galaxies in ΛCDM Simulations. I. Assembly Histories*, ApJ, 754, 115 (2012).

H. L. JOHNSON et al., *The KMOS Redshift One Spectroscopic Survey (KROSS): the origin of disc turbulence in $z \approx 1$ star-forming galaxies*, MNRAS, 474, 5076–5104 (2018).

T. A. JONES et al., *Resolved spectroscopy of gravitationally lensed galaxies: recovering coherent velocity fields in sublum inous $z \sim 2-3$ galaxies*, MNRAS, 404, 1247–1262 (2010).

T. A. JONES et al., *The Origin and Evolution of Metallicity Gradients: Probing the Mode of Mass Assembly at $z \simeq 2$*, ApJ, 765, 48 (2013).

M. R. JOUNG, M.-M. MAC LOW, & G. L. BRYAN, *Dependence of Interstellar Turbulent Pressure on Supernova Rate*, ApJ, 704, 137–149 (2009).

M. JURIĆ et al., *The Milky Way Tomography with SDSS. I. Stellar Number Density Distribution*, ApJ, 673, 864–914 (2008).

J. Kamphuis & R. Sancisi, *Widespread high velocity gas in the spiral galaxy NGC 6946.*, A&A, 273, L31–L34 (1993).

S. J. Kannappan, D. G. Fabricant, & M. Franx, *Physical Sources of Scatter in the Tully-Fisher Relation*, AJ, 123, 2358–2386 (2002).

S. A. Kassin et al., *The Stellar Mass Tully-Fisher Relation to $z = 1.2$ from AEGIS*, ApJL, 660, L35–L38 (2007).

S. A. Kassin et al., *The Epoch of Disk Settling: $z \sim 1$ to Now*, ApJ, 758, 106 (2012).

B. C. Kelly, *Some Aspects of Measurement Error in Linear Regression of Astronomical Data*, ApJ, 665, 1489–1506 (2007).

R. C. Kennicutt, Jr., *The Global Schmidt Law in Star-forming Galaxies*, ApJ, 498, 541–552 (1998).

L. J. Kewley et al., *Theoretical Evolution of Optical Strong Lines across Cosmic Time*, ApJ, 774, 100 (2013).

C.-G. Kim & E. C. Ostriker, *Numerical Simulations of Multiphase Winds and Fountains from Star-forming Galactic Disks. I. Solar Neighborhood TIGRESS Model*, ApJ, 853, 173 (2018).

C.-G. Kim, E. C. Ostriker, & W.-T. Kim, *Three-dimensional Hydrodynamic Simulations of Multiphase Galactic Disks with Star Formation Feedback. I. Regulation of Star Formation Rates*, ApJ, 776, 1 (2013).

W.-T. Kim & E. C. Ostriker, *Gravitational Runaway and Turbulence Driving in Star-Gas Galactic Disks*, ApJ, 660, 1232–1245 (2007).

A. A. Klypin, S. Trujillo-Gomez, & J. Primack, *Dark Matter Halos in the Standard Cosmological Model: Results from the Bolshoi Simulation*, ApJ, 740, 102 (2011).

E. W. Koch et al., *Relationship between the line width of the atomic and molecular ISM in M33*, MNRAS, 485(2), 2324–2342 (2019).

A. M. Koekemoer et al., *CANDELS: The Cosmic Assembly Near-infrared Deep Extragalactic Legacy Survey—The Hubble Space Telescope Observations, Imaging Data Products, and Mosaics*, ApJS, 197, 36 (2011).

E. Komatsu et al., *Five-Year Wilkinson Microwave Anisotropy Probe Observations: Cosmological Interpretation*, ApJS, 180, 330–376 (2009).

E. Komatsu et al., *Seven-year Wilkinson Microwave Anisotropy Probe (WMAP) Observations: Cosmological Interpretation*, ApJS, 192, 18 (2011).

X. KONG et al., *A Wide Area Survey for High-Redshift Massive Galaxies. I. Number Counts and Clustering of BzKs and EROs*, ApJ, 638, 72–87 (2006).

M. KRIEK et al., *The MOSFIRE Deep Evolution Field (MOSDEF) Survey: Rest-frame Optical Spectroscopy for* ~ 1500 $H-$*selected Galaxies at* $1.37 \leq z \leq 3.8$, ApJS, 218, 15 (2015).

P. KROUPA, *On the variation of the initial mass function*, MNRAS, 322, 231–246 (2001).

M. R. KRUMHOLZ & A. BURKERT, *On the Dynamics and Evolution of Gravitational Instability-dominated Disks*, ApJ, 724, 895–907 (2010).

M. R. KRUMHOLZ & B. BURKHART, *Is turbulence in the interstellar medium driven by feedback or gravity? An observational test*, MNRAS, 458, 1671–1677 (2016).

M. R. KRUMHOLZ et al., *A unified model for galactic discs: star formation, turbulence driving, and mass transport*, MNRAS, 477, 2716–2740 (2018).

I. LABBÉ et al., *Large Disklike Galaxies at High Redshift*, ApJL, 591, L95–L98 (2003).

C. D. P. LAGOS et al., *Cosmic evolution of the atomic and molecular gas contents of galaxies*, MNRAS, 418, 1649–1667 (2011).

P. LANG et al., *Bulge Growth and Quenching since z = 2.5 in CANDELS/3D-HST*, ApJ, 788, 11 (2014).

P. LANG et al., *Falling Outer Rotation Curves of Star-forming Galaxies at* $0.6 \lesssim z \lesssim 2.6$ *Probed with KMOS*^{3D} *and SINS/zC-SINF*, ApJ, 840, 92 (2017).

R. B. LARSON, *Turbulence and star formation in molecular clouds.*, MNRAS, 194, 809–826 (1981).

D. R. LAW et al., *Integral Field Spectroscopy of High-Redshift Star-forming Galaxies with Laser-guided Adaptive Optics: Evidence for Dispersion-dominated Kinematics*, ApJ, 669, 929–946 (2007).

D. R. LAW et al., *The Kiloparsec-scale Kinematics of High-redshift Star-forming Galaxies*, ApJ, 697, 2057–2082 (2009).

D. R. LAW et al., *A HST/WFC3-IR Morphological Survey of Galaxies at z = 1.5-3.6. II. The Relation between Morphology and Gas-phase Kinematics*, ApJ, 759, 29 (2012).

R. LEAMAN et al., *A unified model for age-velocity dispersion relations in Local Group galaxies: disentangling ISM turbulence and latent dynamical heating*, MNRAS, 472, 1879–1896 (2017).

M. D. LEHNERT et al., *Physical Conditions in the Interstellar Medium of Intensely Star-Forming Galaxies at Redshift* ~ 2, ApJ, 699, 1660–1678 (2009).

M. D. LEHNERT et al., *On the self-regulation of intense star-formation in galaxies at* z *= 1-3*, A&A, 555, A72 (2013).

F. LELLI, S. S. MCGAUGH, & J. M. SCHOMBERT, *SPARC: Mass Models for 175 Disk Galaxies with Spitzer Photometry and Accurate Rotation Curves*, AJ, 152, 157 (2016a).

F. LELLI, S. S. MCGAUGH, & J. M. SCHOMBERT, *The Small Scatter of the Baryonic Tully-Fisher Relation*, ApJL, 816, L14 (2016b).

G. LEMAÎTRE, *Un Univers homogène de masse constante et de rayon croissant rendant compte de la vitesse radiale des nébuleuses extra-galactiques*, Annales de la Société Scientifique de Bruxelles, 47, 49–59 (1927).

A. K. LEROY et al., *The Star Formation Efficiency in Nearby Galaxies: Measuring Where Gas Forms Stars Effectively*, AJ, 136, 2782–2845 (2008).

A. K. LEROY et al., *Heracles: The HERA CO Line Extragalactic Survey*, AJ, 137, 4670–4696 (2009).

E. S. LEVINE, L. BLITZ, & C. HEILES, *The Vertical Structure of the Outer Milky Way H I Disk*, ApJ, 643, 881–896 (2006).

R. C. LEVY et al., *The EDGE-CALIFA Survey: Molecular and Ionized Gas Kinematics in Nearby Galaxies*, ApJ, 860, 92 (2018).

S. J. LILLY et al., *Gas Regulation of Galaxies: The Evolution of the Cosmic Specific Star Formation Rate, the Metallicity-Mass-Star-formation Rate Relation, and the Stellar Content of Halos*, ApJ, 772, 119 (2013).

R. C. LIVERMORE et al., *Resolved spectroscopy of gravitationally lensed galaxies: global dynamics and star-forming clumps on* ~ 100 *pc scales at* $1 < z < 4$, MNRAS, 450, 1812–1835 (2015).

M. R. LOVELL et al., *The fraction of dark matter within galaxies from the IllustrisTNG simulations*, MNRAS, 481(2), 1950–1975 (2018).

D. LUTZ et al., *PACS Evolutionary Probe (PEP) - A Herschel key program*, A&A, 532, A90 (2011).

M.-M. MAC LOW & R. S. KLESSEN, *Control of star formation by supersonic turbulence*, Reviews of Modern Physics, 76, 125–194 (2004).

M.-M. MAC LOW, R. MCCRAY, & M. L. NORMAN, *Superbubble Blowout Dynamics*, ApJ, 337, 141 (1989).

M.-M. MAC LOW et al., *Kinetic Energy Decay Rates of Supersonic and Super-Alfvénic Turbulence in Star-Forming Clouds*, Physical Review Letters, 80, 2754–2757 (1998).

P. MADAU & M. DICKINSON, *Cosmic Star-Formation History*, ARAA, 52, 415–486 (2014).

G. E. MAGDIS et al., *The Evolving Interstellar Medium of Star-forming Galaxies since $z = 2$ as Probed by Their Infrared Spectral Energy Distributions*, ApJ, 760, 6 (2012).

B. MAGNELLI et al., *The deepest Herschel-PACS far-infrared survey: number counts and infrared luminosity functions from combined PEP/GOODS-H observations*, A&A, 553, A132 (2013).

C. MANCINI et al., *The zCOSMOS-SINFONI Project. I. Sample Selection and Natural-seeing Observations*, ApJ, 743, 86 (2011).

N. MANDELKER et al., *The population of giant clumps in simulated high-z galaxies: in situ and ex situ migration and survival*, MNRAS, 443, 3675–3702 (2014).

C. MARASTON et al., *Star formation rates and masses of $z \sim 2$ galaxies from multicolour photometry*, MNRAS, 407, 830–845 (2010).

F. MARINACCI, R. PAKMOR, & V. SPRINGEL, *The formation of disc galaxies in high-resolution moving-mesh cosmological simulations*, MNRAS, 437, 1750–1775 (2014).

C. B. MARKWARDT, *Non-linear Least-squares Fitting in IDL with MPFIT*, in: D. A. BOHLENDER, D. DURAND, & P. DOWLER, eds., *Astronomical Data Analysis Software and Systems XVIII*, vol. 411 of *Astronomical Society of the Pacific Conference Series*, page 251 (2009).

T. P. K. MARTINSSON et al., *The DiskMass Survey. VI. Gas and stellar kinematics in spiral galaxies from PPak integral-field spectroscopy*, A&A, 557, A130 (2013a).

T. P. K. MARTINSSON et al., *The DiskMass Survey. VII. The distribution of luminous and dark matter in spiral galaxies*, A&A, 557, A131 (2013b).

D. Martizzi, R. Teyssier, & B. Moore, *Cusp-core transformations induced by AGN feedback in the progenitors of cluster galaxies*, MNRAS, 432, 1947–1954 (2013).

C. A. Mason et al., *First Results from the KMOS Lens-Amplified Spectroscopic Survey (KLASS): Kinematics of Lensed Galaxies at Cosmic Noon*, ApJ, 838, 14 (2017).

J. C. Mather et al., *Measurement of the Cosmic Microwave Background Spectrum by the COBE FIRAS Instrument*, ApJ, 420, 439 (1994).

R. M. McDermid et al., *The ATLAS^{3D} Project - XXX. Star formation histories and stellar population scaling relations of early-type galaxies*, MNRAS, 448, 3484–3513 (2015).

S. S. McGaugh, *The Baryonic Tully-Fisher Relation of Galaxies with Extended Rotation Curves and the Stellar Mass of Rotating Galaxies*, ApJ, 632, 859–871 (2005).

S. S. McGaugh & J. M. Schombert, *Weighing Galaxy Disks With the Baryonic Tully-Fisher Relation*, ApJ, 802, 18 (2015).

S. S. McGaugh et al., *The Baryonic Tully-Fisher Relation*, ApJL, 533, L99–L102 (2000).

C. F. McKee & E. C. Ostriker, *Theory of Star Formation*, ARAA, 45, 565–687 (2007).

C. F. McKee, A. Parravano, & D. J. Hollenbach, *Stars, Gas, and Dark Matter in the Solar Neighborhood*, ApJ, 814, 13 (2015).

X. Meng, O. Y. Gnedin, & H. Li, *Structure and stability of high-redshift galaxies in cosmological simulations*, MNRAS, 486(2), 1574–1589 (2019).

D. Merritt & J. A. Sellwood, *Bending Instabilities in Stellar Systems*, ApJ, 425, 551 (1994).

G. R. Meurer et al., *NGC 2915.II.A Dark Spiral Galaxy With a Blue Compact Dwarf Core*, AJ, 111, 1551 (1996).

E. Middelberg et al., *Wide-field VLBA observations of the Chandra deep field South*, A&A, 526, A74 (2011).

N. A. Miller et al., *The Very Large Array 1.4 GHz Survey of the Extended Chandra Deep Field South: Second Data Release*, ApJS, 205(2), 13 (2013).

S. H. Miller, M. Sullivan, & R. S. Ellis, *Uncovering Drivers of Disk Assembly: Bulgeless Galaxies and the Stellar Mass Tully-Fisher Relation*, ApJL, 762, L11 (2013).

S. H. Miller et al., *The Assembly History of Disk Galaxies. I. The Tully-Fisher Relation to* $z \simeq 1.3$ *from Deep Exposures with DEIMOS*, ApJ, 741, 115 (2011).

S. H. Miller et al., *The Assembly History of Disk Galaxies. II. Probing the Emerging Tully-Fisher Relation during* $1 < z < 1.7$, ApJ, 753, 74 (2012).

H. J. Mo, S. Mao, & S. D. M. White, *The formation of galactic discs*, MNRAS, 295, 319–336 (1998).

K. M. Mogotsi et al., *H I and CO Velocity Dispersions in Nearby Galaxies*, AJ, 151, 15 (2016).

A. V. Moiseev, A. V. Tikhonov, & A. Klypin, *What controls the ionized gas turbulent motions in dwarf galaxies?*, MNRAS, 449, 3568–3580 (2015).

J. Molina et al., *SINFONI-HiZELS: the dynamics, merger rates and metallicity gradients of 'typical' star-forming galaxies at z = 0.8-2.2*, MNRAS, 466, 892–905 (2017).

I. G. Momcheva et al., *The 3D-HST Survey: Hubble Space Telescope WFC3/G141 Grism Spectra, Redshifts, and Emission Line Measurements for ˜ 100,000 Galaxies*, ApJS, 225, 27 (2016).

B. P. Moster, T. Naab, & S. D. M. White, *Galactic star formation and accretion histories from matching galaxies to dark matter haloes*, MNRAS, 428, 3121–3138 (2013).

B. P. Moster, T. Naab, & S. D. M. White, *EMERGE - an empirical model for the formation of galaxies since* $z \sim 10$, MNRAS, 477, 1822–1852 (2018).

T. Naab & J. P. Ostriker, *Theoretical Challenges in Galaxy Formation*, ARAA, 55, 59–109 (2017).

J. F. Navarro, C. S. Frenk, & S. D. M. White, *The Structure of Cold Dark Matter Halos*, ApJ, 462, 563 (1996).

D. Nelson et al., *First Results from the TNG50 Simulation: Galactic outflows driven by supernovae and black hole feedback*, arXiv e-prints, arXiv:1902.05554 (2019).

E. J. Nelson et al., *Spatially Resolved Hα Maps and Sizes of 57 Strongly Star-forming Galaxies at* $z \sim 1$ *from 3D-HST: Evidence for Rapid Inside-out Assembly of Disk Galaxies*, ApJL, 747, L28 (2012).

E. J. NELSON et al., *Spatially Resolved Dust Maps from Balmer Decrements in Galaxies at* $z \sim 1.4$, ApJL, 817, L9 (2016a).

E. J. NELSON et al., *Where Stars Form: Inside-out Growth and Coherent Star Formation from HST Hα Maps of 3200 Galaxies across the Main Sequence at* $0.7 < z < 1.5$, ApJ, 828, 27 (2016b).

S. F. NEWMAN et al., *Shocked Superwinds from the* $z \sim 2$ *Clumpy Star-forming Galaxy, ZC406690*, ApJ, 752, 111 (2012).

S. F. NEWMAN et al., *The SINS/zC-SINF Survey of* $z \sim 2$ *Galaxy Kinematics: The Nature of Dispersion-dominated Galaxies*, ApJ, 767, 104 (2013).

M. NOGUCHI, *Early Evolution of Disk Galaxies: Formation of Bulges in Clumpy Young Galactic Disks*, ApJ, 514, 77–95 (1999).

E. NOORDERMEER, *The rotation curves of flattened Sérsic bulges*, MNRAS, 385, 1359–1364 (2008).

P. NOTERDAEME et al., *Evolution of the cosmological mass density of neutral gas from Sloan Digital Sky Survey II - Data Release 7*, A&A, 505, 1087–1098 (2009).

D. OBRESCHKOW et al., *Low Angular Momentum in Clumpy, Turbulent Disk Galaxies*, ApJ, 815, 97 (2015).

V. OLIVARES et al., *Spatially Resolved Spectroscopy of Submillimeter Galaxies at* $z \simeq 2$, ApJ, 827, 57 (2016).

L. OSER et al., *The Two Phases of Galaxy Formation*, ApJ, 725, 2312–2323 (2010).

E. C. OSTRIKER & R. SHETTY, *Maximally Star-forming Galactic Disks. I. Starburst Regulation Via Feedback-driven Turbulence*, ApJ, 731, 41 (2011).

E. PAPASTERGIS, E. A. K. ADAMS, & J. M. VAN DER HULST, *An accurate measurement of the baryonic Tully-Fisher relation with heavily gas-dominated ALFALFA galaxies*, A&A, 593, A39 (2016).

C. PAPOVICH et al., *ZFOURGE/CANDELS: On the Evolution of M* Galaxy Progenitors from* $z = 3$ *to 0.5*, ApJ, 803(1), 26 (2015).

V. PATRÍCIO et al., *Kinematics, turbulence, and star formation of* $z \sim 1$ *strongly lensed galaxies seen with MUSE*, MNRAS, 477, 18–44 (2018).

W. J. PEARSON et al., *Main sequence of star forming galaxies beyond the Herschel confusion limit*, A&A, 615, A146 (2018).

D. Pelliccia et al., *HR-COSMOS: Kinematics of star-forming galaxies at* $z \sim 0.9$, A&A, 599, A25 (2017).

C. Y. Peng et al., *Detailed Decomposition of Galaxy Images. II. Beyond Axisymmetric Models*, AJ, 139, 2097–2129 (2010).

A. A. Penzias & R. W. Wilson, *A Measurement of Excess Antenna Temperature at 4080 Mc/s.*, ApJ, 142, 419–421 (1965).

W. J. Percival et al., *The 2dF Galaxy Redshift Survey: the power spectrum and the matter content of the Universe*, MNRAS, 327, 1297–1306 (2001).

C. Péroux et al., *A homogeneous sample of sub-damped Lyman* α *systems - III. Total gas mass* $\Omega_{HI+HeII}$ *at* $z > 2$, MNRAS, 363, 479–495 (2005).

M. Persic & P. Salucci, *Dark and visible matter in spiral galaxies*, MNRAS, 234, 131–154 (1988).

A. O. Petric & M. P. Rupen, *H I Velocity Dispersion in NGC 1058*, AJ, 134, 1952–1962 (2007).

A. Pillepich et al., *First Results from the TNG50 Simulation: The evolution of stellar and gaseous disks across cosmic time*, arXiv e-prints, arXiv:1902.05553 (2019).

J. Pizagno et al., *Dark Matter and Stellar Mass in the Luminous Regions of Disk Galaxies*, ApJ, 633, 844–856 (2005).

J. Pizagno et al., *The Tully-Fisher Relation and its Residuals for a Broadly Selected Sample of Galaxies*, AJ, 134, 945–972 (2007).

Planck Collaboration et al., *Planck 2013 results. XVI. Cosmological parameters*, A&A, 571, A16 (2014).

Planck Collaboration et al., *Planck 2015 results. XIII. Cosmological parameters*, A&A, 594, A13 (2016).

Planck Collaboration et al., *Planck 2018 results. I. Overview and the cosmological legacy of Planck*, arXiv e-prints, arXiv:1807.06205 (2018a).

Planck Collaboration et al., *Planck 2018 results. VI. Cosmological parameters*, arXiv e-prints, arXiv:1807.06209 (2018b).

A. Pontzen & F. Governato, *How supernova feedback turns dark matter cusps into cores*, MNRAS, 421, 3464–3471 (2012).

G. Popping et al., *The inferred evolution of the cold gas properties of CANDELS galaxies at* $0.5 < z < 3.0$, MNRAS, 454, 2258–2276 (2015).

S. H. PRICE et al., *The MOSDEF Survey: Dynamical and Baryonic Masses and Kinematic Structures of Star-forming Galaxies at* $1.4 \leq z \leq 2.6$, ApJ, 819, 80 (2016).

S. H. PRICE et al., *The MOSDEF Survey: Kinematic and Structural Evolution of Star-Forming Galaxies at* $1.4 \leq z \leq 3.8$, arXiv e-prints, arXiv:1902.09554 (2019).

M. PUECH et al., *IMAGES. III. The evolution of the near-infrared Tully-Fisher relation over the last 6 Gyr*, A&A, 484, 173–187 (2008).

M. PUECH et al., *The baryonic content and Tully-Fisher relation at* $z \sim 0.6$, A&A, 510, A68 (2010).

B. RATHAUS & A. STERNBERG, *Stellar and gaseous disc structures in cosmological galaxy equilibrium models*, MNRAS, 458, 3168–3180 (2016).

R. REYES et al., *Calibrated Tully-Fisher relations for improved estimates of disc rotation velocities*, MNRAS, 417, 2347–2386 (2011).

A. G. RIESS et al., *Type Ia Supernova Discoveries at* $z > 1$ *from the Hubble Space Telescope: Evidence for Past Deceleration and Constraints on Dark Energy Evolution*, ApJ, 607(2), 665–687 (2004).

H.-W. RIX & J. BOVY, *The Milky Way's stellar disk. Mapping and modeling the Galactic disk*, Astronomy and Astrophysics Review, 21, 61 (2013).

G. RODIGHIERO et al., *The Lesser Role of Starbursts in Star Formation at* $z = 2$, ApJ, 739(2), L40 (2011).

M. RODRIGUES et al., *Morpho-kinematics of* $z \sim 1$ *galaxies probe the hierarchical scenario*, MNRAS, 465, 1157–1180 (2017).

A. B. ROMEO & O. AGERTZ, *Larson's scaling laws, and the gravitational instability of clumpy discs at high redshift*, MNRAS, 442(2), 1230–1238 (2014).

A. B. ROMEO & N. FALSTAD, *A simple and accurate approximation for the Q stability parameter in multicomponent and realistically thick discs*, MNRAS, 433(2), 1389–1397 (2013).

A. SAINTONGE et al., *COLD GASS, an IRAM legacy survey of molecular gas in massive galaxies - I. Relations between* H_2*, H I, stellar content and structural properties*, MNRAS, 415, 32–60 (2011).

A. SAINTONGE et al., *Validation of the Equilibrium Model for Galaxy Evolution to* $z \sim 3$ *through Molecular Gas and Dust Observations of Lensed Star-forming Galaxies*, ApJ, 778, 2 (2013).

R. L. Sanders et al., *The MOSDEF Survey: Mass, Metallicity, and Star-formation Rate at* $z \sim 2.3$, ApJ, 799(2), 138 (2015).

P. Santini et al., *The Star Formation Main Sequence in the Hubble Space Telescope Frontier Fields*, ApJ, 847, 76 (2017).

M. T. Sargent et al., *Regularity Underlying Complexity: A Redshift-independent Description of the Continuous Variation of Galaxy-scale Molecular Gas Properties in the Mass-star Formation Rate Plane*, ApJ, 793, 19 (2014).

C. Scannapieco et al., *The formation and survival of discs in a* ΛCDM *universe*, MNRAS, 396, 696–708 (2009).

C. Scannapieco et al., *The Aquila comparison project: the effects of feedback and numerical methods on simulations of galaxy formation*, MNRAS, 423, 1726–1749 (2012).

J. Schaye et al., *The EAGLE project: simulating the evolution and assembly of galaxies and their environments*, MNRAS, 446, 521–554 (2015).

M. Schmidt, *The Rate of Star Formation.*, ApJ, 129, 243 (1959).

N. Scoville et al., *Evolution of Interstellar Medium, Star Formation, and Accretion at High Redshift*, ApJ, 837, 150 (2017).

K. L. Shapiro et al., *Kinemetry of SINS High-Redshift Star-Forming Galaxies: Distinguishing Rotating Disks from Major Mergers*, ApJ, 682, 231–251 (2008).

A. E. Shapley et al., *Chemical Abundances of DEEP2 Star-forming Galaxies at* $z \sim 1.0 - 1.5$, ApJ, 635, 1006–1021 (2005).

R. Sharples et al., *First Light for the KMOS Multi-Object Integral-Field Spectrometer*, The Messenger, 151, 21–23 (2013).

R. M. Sharples et al., *KMOS: an infrared multiple-object integral field spectrograph for the ESO VLT*, in: A. F. M. Moorwood & M. Iye, eds., *Ground-based Instrumentation for Astronomy*, vol. 5492 of *Society of Photo-Optical Instrumentation Engineers (SPIE) Conference Series*, pages 1179–1186 (2004).

R. Shetty & E. C. Ostriker, *Maximally Star-forming Galactic Disks. II. Vertically Resolved Hydrodynamic Simulations of Starburst Regulation*, ApJ, 754, 2 (2012).

G. A. Shields, *Extragalactic HII regions.*, ARAA, 28, 525–560 (1990).

J. Silk, *The formation of galaxy discs*, MNRAS, 324, 313–318 (2001).

R. C. Simons et al., *Kinematic Downsizing at* $z \sim 2$, ApJ, 830, 14 (2016).

R. C. Simons et al., $z \sim 2$*: An Epoch of Disk Assembly*, ApJ, 843, 46 (2017).

R. E. Skelton et al., *3D-HST WFC3-selected Photometric Catalogs in the Five CANDELS/3D-HST Fields: Photometry, Photometric Redshifts, and Stellar Masses*, ApJS, 214, 24 (2014).

V. M. Slipher, *The radial velocity of the Andromeda Nebula*, Lowell Observatory Bulletin, 1, 56–57 (1913).

G. F. Smoot et al., *Structure in the COBE Differential Microwave Radiometer First-Year Maps*, ApJ, 396, L1 (1992).

Y. Sofue & V. Rubin, *Rotation Curves of Spiral Galaxies*, ARAA, 39, 137–174 (2001).

R. S. Somerville et al., *An Explanation for the Observed Weak Size Evolution of Disk Galaxies*, ApJ, 672, 776-786 (2008).

J. S. Speagle et al., *A Highly Consistent Framework for the Evolution of the Star-Forming "Main Sequence" from* $z \sim 0-6$, The Astrophysical Journal Supplement Series, 214, 15 (2014).

D. N. Spergel et al., *First-Year Wilkinson Microwave Anisotropy Probe (WMAP) Observations: Determination of Cosmological Parameters*, ApJS, 148, 175–194 (2003).

D. N. Spergel et al., *Three-Year Wilkinson Microwave Anisotropy Probe (WMAP) Observations: Implications for Cosmology*, ApJS, 170, 377–408 (2007).

V. Springel, *E pur si muove: Galilean-invariant cosmological hydrodynamical simulations on a moving mesh*, MNRAS, 401(2), 791–851 (2010).

V. Springel et al., *Simulations of the formation, evolution and clustering of galaxies and quasars*, Nature, 435, 629–636 (2005).

V. Springel et al., *First results from the IllustrisTNG simulations: matter and galaxy clustering*, MNRAS, 475(1), 676–698 (2018).

D. P. Stark et al., *The formation and assembly of a typical star-forming galaxy at redshift* $z \sim 3$, Nature, 455, 775–777 (2008).

D. V. Stark, S. S. McGaugh, & R. A. Swaters, *A First Attempt to Calibrate the Baryonic Tully-Fisher Relation with Gas-Dominated Galaxies*, AJ, 138, 392–401 (2009).

C. C. Steidel et al., *Strong Nebular Line Ratios in the Spectra of* $z \sim 2-3$ *Star Forming Galaxies: First Results from KBSS-MOSFIRE*, ApJ, 795, 165 (2014).

J. M. Stone, E. C. Ostriker, & C. F. Gammie, *Dissipation in Compressible Magnetohydrodynamic Turbulence*, ApJ, 508, L99–L102 (1998).

J. P. Stott et al., *A fundamental metallicity relation for galaxies at $z = 0.84$-1.47 from HiZELS*, MNRAS, 436, 1130–1141 (2013).

J. P. Stott et al., *The KMOS Redshift One Spectroscopic Survey (KROSS): dynamical properties, gas and dark matter fractions of typical $z \sim 1$ star-forming galaxies*, MNRAS, 457, 1888–1904 (2016).

C. M. S. Straatman et al., *ZFIRE: The Evolution of the Stellar Mass Tully-Fisher Relation to Redshift ~ 2.2*, ApJ, 839, 57 (2017).

J. Sun et al., *Cloud-scale Molecular Gas Properties in 15 Nearby Galaxies*, ApJ, 860(2), 172 (2018).

A. M. Swinbank et al., *The Interstellar Medium in Distant Star-forming Galaxies: Turbulent Pressure, Fragmentation, and Cloud Scaling Relations in a Dense Gas Disk at $z = 2.3$*, ApJ, 742, 11 (2011).

A. M. Swinbank et al., *The Properties of the Star-forming Interstellar Medium at $z = 0.8$-2.2 from HiZELS: Star Formation and Clump Scaling Laws in Gas-rich, Turbulent Disks*, ApJ, 760, 130 (2012a).

A. M. Swinbank et al., *The properties of the star-forming interstellar medium at $z = 0.84$-2.23 from HiZELS: mapping the internal dynamics and metallicity gradients in high-redshift disc galaxies*, MNRAS, 426, 935–950 (2012b).

A. M. Swinbank et al., *Angular momentum evolution of galaxies over the past 10 Gyr: a MUSE and KMOS dynamical survey of 400 star-forming galaxies from $z = 0.3$ to 1.7*, MNRAS, 467, 3140–3159 (2017).

S. Tacchella et al., *Evidence for mature bulges and an inside-out quenching phase 3 billion years after the Big Bang*, Science, 348, 314–317 (2015a).

S. Tacchella et al., *SINS/zC-SINF Survey of $z \sim 2$ Galaxy Kinematics: Rest-frame Morphology, Structure, and Colors from Near-infrared Hubble Space Telescope Imaging*, ApJ, 802, 101 (2015b).

S. Tacchella et al., *Evolution of density profiles in high-z galaxies: compaction and quenching inside-out*, MNRAS, 458, 242–263 (2016a).

S. Tacchella et al., *The confinement of star-forming galaxies into a main sequence through episodes of gas compaction, depletion and replenishment*, MNRAS, 457, 2790–2813 (2016b).

L. J. Tacconi et al., *High molecular gas fractions in normal massive star-forming galaxies in the young Universe*, Nature, 463, 781–784 (2010).

L. J. Tacconi et al., *PHIBSS: Molecular Gas Content and Scaling Relations in* $z \sim 1-3$ *Massive, Main-sequence Star-forming Galaxies*, ApJ, 768, 74 (2013).

L. J. Tacconi et al., *PHIBSS: Unified Scaling Relations of Gas Depletion Time and Molecular Gas Fractions*, ApJ, 853, 179 (2018).

K. Tadaki et al., *The gravitationally unstable gas disk of a starburst galaxy 12 billion years ago*, Nature, 560, 613–616 (2018).

K.-i. Tadaki et al., *SXDF-ALMA 1.5 arcmin*^{2} *Deep Survey: A Compact Dusty Star-forming Galaxy at* $z = 2.5$, ApJ, 811, L3 (2015).

K.-i. Tadaki et al., *Bulge-forming Galaxies with an Extended Rotating Disk at* $z \sim 2$, ApJ, 834, 135 (2017).

D. Tamburro et al., *What is Driving the H I Velocity Dispersion?*, AJ, 137, 4424–4435 (2009).

J. Thomas, *Schwarzschild Modelling of Elliptical Galaxies and Their Black Holes*, in: R. von Berlepsch, ed., *Reviews in Modern Astronomy*, vol. 22 of *Reviews in Modern Astronomy*, pages 143–154 (2010).

A. L. Tiley et al., *The KMOS Redshift One Spectroscopic Survey (KROSS): the Tully-Fisher relation at* $z \sim 1$, MNRAS, 460, 103–129 (2016).

A. L. Tiley et al., *KROSS-SAMI: a direct IFS comparison of the Tully-Fisher relation across 8 Gyr since* $z \approx 1$, MNRAS, 482(2), 2166–2188 (2019).

A. R. Tomczak et al., *The SFR-*M_* *Relation and Empirical Star-Formation Histories from ZFOURGE* at* $0.5 < z < 4$, ApJ, 817, 118 (2016).

A. Toomre, *On the gravitational stability of a disk of stars*, ApJ, 139, 1217–1238 (1964).

S. Torres-Flores et al., *GHASP: an H*α *kinematic survey of spiral and irregular galaxies - IX. The near-infrared, stellar and baryonic Tully-Fisher relations*, MNRAS, 416, 1936–1948 (2011).

C. Trachternach et al., *The baryonic Tully-Fisher relation and its implication for dark matter halos*, A&A, 505, 577–587 (2009).

S. Tremaine et al., *The Slope of the Black Hole Mass versus Velocity Dispersion Correlation*, ApJ, 574, 740–753 (2002).

R. B. Tully & J. R. Fisher, *A new method of determining distances to galaxies*, A&A, 54, 661–673 (1977).

O. J. Turner et al., *The KMOS Deep Survey (KDS) - I. Dynamical measurements of typical star-forming galaxies at* $z \simeq 3.5$, MNRAS, 471, 1280–1320 (2017).

H. D. N. Übler et al., *Why stellar feedback promotes disc formation in simulated galaxies*, MNRAS, 443, 2092–2111 (2014).

H. D. N. Übler et al., *The Evolution of the Tully-Fisher Relation between* $z \sim 2.3$ *and* $z \sim 0.9$ *with KMOS*^{3D}, ApJ, 842, 121 (2017).

H. D. N. Übler et al., *Ionized and Molecular Gas Kinematics in a* $z = 1.4$ *Star-forming Galaxy*, ApJL, 854, L24 (2018).

H. D. N. Übler et al., *The Evolution and Origin of Ionized Gas Velocity Dispersion from* $z \sim 2.6$ *to* $z \sim 0.6$ *with KMOS*^{3D}, ApJ, 880(1), 48 (2019).

Y. Ueda et al., *The Subaru/XMM-Newton Deep Survey (SXDS). III. X-Ray Data*, ApJS, 179, 124–141 (2008).

D. Utomo, L. Blitz, & E. Falgarone, *The Origin of Interstellar Turbulence in M33*, ApJ, 871(1), 17 (2019).

T. S. van Albada et al., *Distribution of dark matter in the spiral galaxy NGC 3198*, ApJ, 295, 305–313 (1985).

P. C. van der Kruit & R. J. Allen, *The kinematics of spiral and irregular galaxies.*, ARAA, 16, 103–139 (1978).

P. C. van der Kruit & K. C. Freeman, *The vertical velocity dispersions of the stars in the disks of two spiral galaxies.*, ApJ, 278, 81–88 (1984).

P. C. van der Kruit & K. C. Freeman, *Galaxy Disks*, ARAA, 49, 301–371 (2011).

A. van der Wel et al., *Structural Parameters of Galaxies in CANDELS*, ApJS, 203, 24 (2012).

A. van der Wel et al., *3D-HST+CANDELS: The Evolution of the Galaxy Size-Mass Distribution since* $z = 3$, ApJ, 788, 28 (2014a).

A. van der Wel et al., *Geometry of Star-forming Galaxies from SDSS, 3D-HST, and CANDELS*, ApJ, 792, L6 (2014b).

P. G. van Dokkum et al., *The Growth of Massive Galaxies Since* $z = 2$, ApJ, 709, 1018–1041 (2010).

P. G. VAN DOKKUM et al., *First Results from the 3D-HST Survey: The Striking Diversity of Massive Galaxies at* $z > 1$, ApJ, 743, L15 (2011).

P. G. VAN DOKKUM et al., *Forming Compact Massive Galaxies*, ApJ, 813, 23 (2015).

M. VARIDEL et al., *Resolved Gas Kinematics in a Sample of Low-Redshift High Star-Formation Rate Galaxies*, Publications of the Astronomical Society of Australia, 33, e006 (2016).

M. R. VARIDEL et al., *The SAMI Galaxy Survey: Bayesian inference for gas disc kinematics using a hierarchical Gaussian mixture model*, MNRAS, 485(3), 4024–4044 (2019).

M. VELLISCIG et al., *The impact of galaxy formation on the total mass, mass profile and abundance of haloes*, MNRAS, 442, 2641–2658 (2014).

D. VERGANI et al., *MASSIV: Mass Assembly Survey with SINFONI in VVDS. IV. Fundamental relations of star-forming galaxies at* $1 < z < 1.6$, A&A, 546, A118 (2012).

M. A. W. VERHEIJEN, *The Ursa Major Cluster of Galaxies*, Ph.D. thesis, University of Groningen (1997).

M. A. W. VERHEIJEN, *The Ursa Major Cluster of Galaxies. V. H I Rotation Curve Shapes and the Tully-Fisher Relations*, ApJ, 563, 694–715 (2001).

M. VOGELSBERGER et al., *Introducing the Illustris Project: simulating the coevolution of dark and visible matter in the Universe*, MNRAS, 444, 1518–1547 (2014).

F. WALTER et al., *THINGS: The H I Nearby Galaxy Survey*, AJ, 136, 2563–2647 (2008).

B. WANG & J. SILK, *Gravitational Instability and Disk Star Formation*, ApJ, 427, 759 (1994).

H.-H. WANG et al., *Equilibrium initialization and stability of three-dimensional gas discs*, MNRAS, 407, 705–720 (2010).

B. J. WEINER et al., *A Survey of Galaxy Kinematics to* $z \sim 1$ *in the TKRS/GOODS-N Field. I. Rotation and Dispersion Properties*, ApJ, 653, 1027–1048 (2006).

J. K. WERK et al., *The COS-Halos Survey: Physical Conditions and Baryonic Mass in the Low-redshift Circumgalactic Medium*, ApJ, 792, 8 (2014).

K. E. Whitaker et al., *Constraining the Low-mass Slope of the Star Formation Sequence at* $0.5 < z < 2.5$, ApJ, 795, 104 (2014).

H. A. White et al., *Gas Content and Kinematics in Clumpy, Turbulent Star-forming Disks*, ApJ, 846, 35 (2017).

S. D. M. White & M. J. Rees, *Core condensation in heavy halos: a two-stage theory for galaxy formation and clustering.*, MNRAS, 183, 341–358 (1978).

M. J. Williams, M. Bureau, & M. Cappellari, *The Tully-Fisher relations of early-type spiral and S0 galaxies*, MNRAS, 409, 1330–1346 (2010).

C. D. Wilson et al., *The JCMT Nearby Galaxies Legacy Survey - IV. Velocity dispersions in the molecular interstellar medium in spiral galaxies*, MNRAS, 410, 1409–1422 (2011).

E. Wisnioski et al., *The WiggleZ Dark Energy Survey: high-resolution kinematics of luminous star-forming galaxies*, MNRAS, 417, 2601–2623 (2011).

E. Wisnioski et al., *Scaling relations of star-forming regions: from kpc-sized clumps to H II regions*, MNRAS, 422, 3339–3355 (2012).

E. Wisnioski et al., *The KMOS^{3D} Survey: Design, First Results, and the Evolution of Galaxy Kinematics from* $0.7 \leq z \leq 2.7$, ApJ, 799, 209 (2015).

E. Wisnioski et al., *The KMOS^{3D} Survey: Rotating Compact Star-forming Galaxies and the Decomposition of Integrated Line Widths*, ApJ, 855, 97 (2018).

E. Wisnioski et al., *The KMOS^{3D} Survey: Data Release and Final Survey Paper*, submitted to ApJ (2019).

A. M. Wolfe, E. Gawiser, & J. X. Prochaska, *Damped Ly α Systems*, ARAA, 43, 861–918 (2005).

T. Wong et al., *Molecular and Atomic Gas in the Large Magellanic Cloud. I. Conditions for CO Detection*, ApJ, 696(1), 370–384 (2009).

S. A. Wright et al., *Dynamics of Galactic Disks and Mergers at* $z \sim 1.6$*: Spatially Resolved Spectroscopy with Keck Laser Guide Star Adaptive Optics*, ApJ, 699, 421–440 (2009).

E. Wuyts et al., *A Consistent Study of Metallicity Evolution at* $0.8 < z < 2.6$, ApJ, 789, L40 (2014).

E. Wuyts et al., *The Evolution of Metallicity and Metallicity Gradients from z = 2.7 to 0.6 with KMOS^{3D}*, ApJ, 827(1), 74 (2016a).

S. Wuyts et al., *What Do We Learn from IRAC Observations of Galaxies at* $2 < z < 3.5$*?*, ApJ, 655, 51–65 (2007).

S. Wuyts et al., *Recovering Stellar Population Properties and Redshifts from Broadband Photometry of Simulated Galaxies: Lessons for SED Modeling*, ApJ, 696, 348–369 (2009).

S. Wuyts et al., *Galaxy Structure and Mode of Star Formation in the SFR-Mass Plane from* $z \sim 2.5$ *to* $z \sim 0.1$, ApJ, 742, 96 (2011a).

S. Wuyts et al., *On Star Formation Rates and Star Formation Histories of Galaxies Out to* $z \sim 3$, ApJ, 738, 106 (2011b).

S. Wuyts et al., *Smooth(er) Stellar Mass Maps in CANDELS: Constraints on the Longevity of Clumps in High-redshift Star-forming Galaxies*, ApJ, 753, 114 (2012).

S. Wuyts et al., *A CANDELS-3D-HST synergy: Resolved Star Formation Patterns at* $0.7 < z < 1.5$, ApJ, 779, 135 (2013).

S. Wuyts et al., *KMOS*$^{\rm 3D}$*: Dynamical Constraints on the Mass Budget in Early Star-forming Disks*, ApJ, 831, 149 (2016b).

Y. Q. Xue et al., *The Chandra Deep Field-South Survey: 4 Ms Source Catalogs*, ApJS, 195, 10 (2011).

P. Yoachim & J. J. Dalcanton, *Structural Parameters of Thin and Thick Disks in Edge-on Disk Galaxies*, AJ, 131, 226–249 (2006).

D. G. York et al., *The Sloan Digital Sky Survey: Technical Summary*, AJ, 120, 1579–1587 (2000).

H. J. Zahid, L. J. Kewley, & F. Bresolin, *The Mass-Metallicity and Luminosity-Metallicity Relations from DEEP2 at* $z \sim 0.8$, ApJ, 730, 137 (2011).

H. J. Zahid et al., *The FMOS-COSMOS Survey of Star-forming Galaxies at* $z \sim 1.6$*. II. The Mass-Metallicity Relation and the Dependence on Star Formation Rate and Dust Extinction*, ApJ, 792, 75 (2014).

D. Zaritsky et al., *The Baryonic Tully-Fisher Relationship for* S^4G *Galaxies and the "Condensed" Baryon Fraction of Galaxies*, AJ, 147, 134 (2014).

L. Zhou et al., *The SAMI Galaxy Survey: energy sources of the turbulent velocity dispersion in spatially resolved local star-forming galaxies*, MNRAS, 470, 4573–4582 (2017).

A. Zolotov et al., *Compaction and quenching of high-z galaxies in cosmological simulations: blue and red nuggets*, MNRAS, 450, 2327–2353 (2015).